UNIVERSIDADE DE LISBOA
FACULDADE DE CIÊNCIAS

Exhumation of anatectic complexes through shear zones: petrological and geochemical constraints on the evolution of the Figueira de Castelo Rodrigo – Lumbrales Anatectic Complex

"Documento Definitivo"

Doutoramento em Geologia
Especialidade de Geoquímica

Joana Alexandra dos Santos Ferreira

Tese orientada por:
Professor Doutor Telmo M. Bento dos Santos
Professor Doutor João Mata

Documento especialmente elaborado para a obtenção do grau de doutor

2020

UNIVERSIDADE DE LISBOA

FACULDADE DE CIÊNCIAS

Exhumation of anatectic complexes through shear zones: petrological and geochemical constraints on the evolution of the Figueira de Castelo Rodrigo – Lumbrales Anatectic Complex

Doutoramento em Geologia

Especialidade de Geoquímica

Joana Alexandra dos Santos Ferreira

Tese orientada por:

Professor Doutor Telmo M. Bento dos Santos

Professor Doutor João Mata

Júri:

Presidente:

- Doutora Maria da Conceição Pombo de Freitas, Professora Catedrática e Presidente do Departamento de Geologia da Faculdade de Ciências da Universidade de Lisboa.

Vogais:

- Doutor Carlos Villaseca González, Profesor Catedrático, Facultad de Ciências Geológicas da Universidad Complutense de Madrid;
- Doutora Maria do Rosário Mascarenhas de Almeida Azevedo, Professora Associada, Departamento de Geociências da Universidade de Aveiro;
- Doutora Maria Elisa Preto Gomes, Professora Catedrática, Escola de Ciências da Vida e do Ambiente da Universidade de Trás-os-Montes e Alto Douro;
- Doutor Telmo Manuel Bento dos Santos, Professor Auxiliar, Faculdade de Ciências da Universidade de Lisboa (orientador);
- Doutor Ícaro Frois Dias da Silva, Investigador Doutorado Contratado, Faculdade Ciências da Universidade de Lisboa.

Documento especialmente elaborado para a obtenção do grau de doutor

Bolsa de doutoramento financiada pela Fundação para a Ciência e a Tecnologia

(PD/BD/114486/2016)

2020

AGRADECIMENTOS

Tal como um edifício é sustentado por vários pilares também o é este trabalho e são vários os pilares a quem devo um agradecimento e gratidão.

Primeiro, quero agradecer aos meus orientadores, Telmo Bentos dos Santos e João Mata, por apostarem em mim para a execução deste projeto, por todo o apoio e confiança depositada, e, sobretudo, por todos os ensinamentos e orientação que me deram ao longo destes 4 anos.

À Inês Pereira que me deu a possibilidade de obter mais dados para este trabalho e criou todas as condições para eu ser recebida na Universidade de Portsmouth. Ao longo destes 4 anos foi uma excelente parceira, sempre presente e empenhada na partilha de conhecimento e troca de ideias. Além disto, tornou-se uma grande amiga e conselheira. Já perdi a conta das vezes que lhe agradeci por tudo o que fez por mim e por este trabalho, mas mais uma vez OBRIGADA!

Quero agradecer às professoras Maria dos Anjos Ribeiro e Helena Cristina Brites Martins, que não estiveram diretamente relacionadas com este trabalho, mas sempre acreditaram em mim, foram as minhas primeiras mentoras e deram-me o empurrão para o meio académico.

Agradeço à Cyntia Mourão que tão bem me recebeu nos laboratórios do departamento, com boa disposição, sempre uma palavra de incentivo, e sempre disposta a ajudar.

Agradeço também ao João Cascalho pelos ensinamentos laboratoriais e à Vera Lopes que tão prontamente me deu acesso aos laboratórios do terceiro piso do departamento e me ajudou na minha demanda das separações gravimétricas.

Um grande agradecimento à professora Isabel Fernandes, por quem tenho estima e admiração, pelas palavras de incentivo e força cada vez que nos encontrávamos.

Ao Ícaro Dias da Silva agradeço as partilhas de conhecimento, as sugestões, os conselhos, e as conversas incentivadoras e inspiradoras. Obrigada pela tua humildade e por seres bom ouvinte!

Obrigada Sofia Pereira, Cristiana Esteves, e Jorge Colmenar por me acolherem no Paleolab, pelas boas risadas e boas conversas durante o trabalho árduo de separar minerais.

À Adriana Abreu agradeço por me dar abrigo durante a minha estadia em Portsmouth. Obrigada por me receberes tão bem e por teres ido comigo à descoberta de alguns locais.

Agradeço à Carolina, à Maria, à Winner, ao Ilisio, ao Nuno, e ao Óscar pela ajuda que me deram no laboratório.

Agradeço ao quarteto da vida airada, José Roseiro, Ivo Martins, André Cravinho Santos, e Eduardo Soares a amizade que me disponibilizaram, os bons momentos durante a minha estada em Lisboa, e todo o apoio quando a vida corria menos bem.

Agradeço ao meu grupo de amigos do *Earthsystems2016*, João, Riccardo, Alessandro, Filipa e Dorota que embarcaram juntamente comigo nesta aventura que é o doutoramento e com quem passei muitos bons momentos.

À minha amiga de longa data, Sara Leal, agradeço todo o apoio e as palavras de incentivo e força que me deste em todas as fases da minha vida.

Um gigante agradecimento às minhas *partners in crime*, Andreia Ribeiro e Joana Carvalho, sem elas era impossível aguentar. À Andreia Ribeiro agradeço toda a paciência e compreensão, e por ser das poucas que consegue me acalmar nos meus momentos mais temperamentais. Para a Joana Carvalho não há palavras que consigam descrever o que nos une, como já mencionaste parece que estava destinado, o meu braço direito nestes 4 anos, sempre que eu começava a descambar para o lado negro sempre me chamaste à atenção e me puxaste para a luz.

Às minhas queridas Rita Ferraz e Isa Braz agradeço a amizade, o companheirismo, a paciência, e o apoio durante todo o tempo que vivemos juntas e mesmo depois dessa fase que nos uniu.

Agradeço aos meus amigos Joana Rocha, Hugo Novais, Iolanda Lino e Liliana Ferreira por acreditarem em mim e por ouvirem os meus desabafos e frustrações.

Ao meu avô Manuel, que partiu durante a execução deste projeto, agradeço o orgulho que ele sentia em mim. Apesar de ter sido um homem de poucas palavras eu sentia esse orgulho.

Ao meu irmão Vitor e à minha cunhada Flávia agradeço toda a força e positivismo que me deram nesta fase através de telefonemas, e das fotos e vídeos que me mandavam dos meninos e que alegravam mais os meus dias.

A ti, Miguel, agradeço todo o companheirismo e apoio incondicional nesta aventura, mesmo colocando a nossa vida em *stand-by*. Se não fosse pelo teu apoio tinha desistido no primeiro dia que pus os pés em Lisboa, e tu sabes.

À minha irmã Rita agradeço as palhaçadas que me fazem rir, e, acima de tudo, a admiração que ela tem por mim, irmã mais velha, e que me inspira a fazer sempre mais e melhor.

Aos meus meninos, Gonçalo e Simão, obrigada por existirem na vida da tia e por me darem tanta alegria e amor.

Ao meu pai, apesar das divergências, agradeço por acreditar em mim até mais do que eu, de se orgulhar de todas as minhas conquistas, e, por sempre, relembrar-me onde são as minhas raízes onde posso ir buscar forças para as minhas lutas.

À minha mãe agradeço o facto de ela ser uma mãe lutadora e de pôr as necessidades dos filhos sempre em primeiro lugar, sempre os apoiando na perseguição dos seus sonhos sem nunca os deixar cair. OBRIGADA MÃE!

ABSTRACT

The Figueira de Castelo Rodrigo–Lumbrales Anatectic Complex (FCR-LAC) is an example of a granite-migmatite complex formed during the Variscan Orogeny located within the autochthonous terrane of the Central Iberian Zone. The FCR-LAC contacts with an Ediacaran–Cambrian metasedimentary sequence (Douro–Beiras Supergroup – DBSG) through the Huebra and Juzbado–Penalva do Castelo shear zones.

New U–Pb zircon and apatite ages constrain emplacement and migmatization ages, inherited ages and unprecedented cooling rates for the FCR–LAC lithologies. The granites emplacement ages cluster around 313–317 Ma while the migmatization age constrains the prograde metamorphic path (344 – 315 Ma) and the metamorphic peak at 316.8 ± 2.0 Ma. The migmatization/peak metamorphic ages suggest that the anatexis started during the D_2 and culminated during the D_3 Variscan phase, concomitantly with the emplacement of the S-type granites. The cooling (7 to 54 ºC/Ma) and exhumation rates (0.2 and 1.3 mm a^{-1}) of the FCR–LAC imply fast cooling/exhumation conditions which are compatible with a tectonically-assisted mechanism where the shear zones have an important role.

The elemental composition of the FCR-LAC reveals the existence of two distinct diatexite groups: diatexites type-1 produced via dehydration-melting of muscovite; and the diatexites type-2 formed by a fluid-present melting reaction. These two diatexite groups evolved in different stages of the prograde metamorphic path: 343.7 ± 2.5 Ma for diatexite type-2, 328.8 ± 3.4 Ma for a diatexite type-1, culminating in the metamorphic peak at 318.8 ± 2.6 Ma with a diatexite type-1. The different melting reactions justify the isotopic variability observed in the FCR-LAC.

The U-Pb detrital zircon ages of the FCR-LAC and the DBSG reveal an important input of the Cadomian sediments. The zircon distribution ages of the Pinhão Formation (Douro Group) compared to the Beiras Group reinforce the existence of a physical barrier at south of the FCR-LAC. Younger inherited zircon from the anatectic rocks can be linked to the Ollo de Sapo magmatic rocks indicating that they melted alongside the DBSG showing the existence of source heterogeneity. This fact is also supported by the Sr-Nd isotopic compositions of the FCR-LAC and explains the existence of two groups with distinct initial isotopic compositions, both composed by metatexites, diatexites and granites.

KEYWORDS: Variscan Orogeny; crustal anatexis; granitogenesis; migmatization; granite-migmatite complex

RESUMO

A orogenia Varisca foi responsável pela formação de diversos complexos metamórficos ao longo de toda a cadeia orogénica. Na Cadeia Varisca Ibérica, particularmente na Zona Centro Ibérica, é característico a profusão de corpos graníticos por vezes associados a rochas migmatíticas. O Complexo Anatéctico de Figueira de Castelo Rodrigo-Lumbrales (CAFCR-L) é um exemplo de um complexo granito-migmatítico que aflora no autóctone da Zona Centro Ibérica. Este é composto por metatexitos, diatexitos, e granitos de duas-micas do tipo-S. O CAFCR-L complexo contacta a norte e a sul com rochas metassedimentares de baixo grau metamórfico de idade Ediacariana-Câmbrico pertencentes ao Supergrupo Dúrico-Beirão. Este contacto é materializado pela zona de cisalhamento do Huebra, a norte, e pela zona de cisalhamento Juzbado-Penalva do Castelo, a sul, ambas de cinemática esquerda.

Através do estudo do CAFRC-L, este projeto de doutoramento tem como principal objetivo contribuir para aumentar o conhecimento sobre a interdependência entre migmatização, granito-génese, deformação e exumação de complexos anatécticos na Cadeia Varisca Ibérica.

A concretização deste estudo envolveu a aplicação de diversos métodos analíticos tais como: caracterização petrográfica, geocronologia U-Pb em zircão e apatite, geoquímica elementar em rocha total, geoquímica isotópica em rocha total (Sr-Nd-Hf-Pb), e análises de elementos traço em zircão e apatite.

Novas idades U-Pb em zircão e apatite permitiram obter idades de instalação, idades de migmatização, idades herdadas em zircão, e taxas de arrefecimento para as litologias do complexo anatéctico. A instalação/cristalização dos granitos ocorreu entre os 313 e os 317 Ma para os granitos sin-tectónicos e, também, foi obtida uma idade de 300 Ma para uma fácies granítica tardi-tectónica. As idades de migmatização obtidas a partir dos migmatitos (metatexitos e diatexitos) do complexo anatéctico restringem o intervalo de tempo em que ocorreu o percurso de metamorfismo prógrado até ao pico metamórfico (344 – 315 Ma). O metatexito analisado regista uma idade de pico metamórfico de 314.8 ± 1.3 Ma enquanto que nos diatexitos é obtida uma idade de 318.8 ± 2.6. A partir destas idades é estimada a idade de 316.8 ± 2.0 Ma para o pico metamórfico da região. Estas idades de migmatização e do pico metamórfico indicam que a anatexia crustal começou durante a segunda fase de deformação Varisca (D_2) e atingiu o seu clímax na terceira fase de deformação Varisca (D_3) em simultâneo com a instalação dos granitos sin-tectónicos. As idades U-Pb em apatite sugerem que o arrefecimento do complexo anatéctico, até aproximadamente 500 ºC, ocorreu no intervalo entre os 301 e os 314 Ma.

A integração das idades U-Pb em zircão e apatite com as respetivas temperaturas de fecho permitiram, pela primeira vez, determinar as condições de arrefecimento e exumação do CAFCR-L. As taxas de arrefecimento do complex anatéctico variam entre 7 e 54 ºC/Ma, enquanto que as taxas de exumação apresentam valores entre 0.2 e 1.3 mm a^{-1}. Considerando as taxas de arrefecimento dos granitos sin-tectónicos e dos migmatitos que representam o pico metamórfico (13 – 54 ºC) é estimada uma taxa de arrefecimento média de 31 ºC/Ma. Estas taxas implicam condições de arrefecimento e exumação rápidas para o complexo anatéctico que são compatíveis com um mecanismo de exumação assistido pela tectónica onde as zonas de cisalhamento do Huebra e Juzbado-Penalva do Castelo tiveram um papel importante.

As idades U-Pb em zircões detríticos do complexo anatéctico e do Supergrupo Dúrico-Beirão (SGDB) revelam um importante contributo detrítico de idade Cadomiana, e um menor aporte de sedimentos de idade Neo- a Mesoproterozóico até ao Arcaico. As rochas anatécticas exibem uma distribuição das idades herdadas semelhante à distribuição das idades dos zircões detríticos da Formação de Excomungada do SGDB localizada a sul do complexo anatéctico. A distribuição das idades dos zircões detríticos da Formação de Pinhão (Grupo do Douro – SGDB) é comparada com as distribuições dos grauvaques do Grupo das Beiras (SGDB) onde se destaca um contraste nas fontes nos domínio norte e sul do Supergrupo Dúrico-Beirão. Este contraste reforça a existência de uma barreira física durante o Ediacariano e o Câmbrico Inferior, a sul da área em estudo, que inibiu o aporte de sedimentos antigos para a bacia do Douro.

A presença de zircões herdados com idades entre os 450 Ma e os 500 Ma nas rochas anatécticas está relacionada com o magmatismo do Ollo de Sapo, o que indica que estas rochas fundiram juntamente com os metassedimentos do Supergrupo Dúrico-Beirão para dar origem ao CAFCR-L, mostrando assim a existência de uma fonte heterogénea. Esta heterogeneidade na fonte é também confirmada pela composição isotópicas das litologias do complexo anatéctico que mostram afinidade com o Supergrupo Dúrico-Beirão e o domínio do Ollo de Sapo.

A composição química das rochas anatécticas revela a existência de dois grupos de diatexitos, os diatexitos tipo-1 e os diatexitos tipo-2. Os diatexitos tipo-1 caracterizam-se por elevados teores de Rb e elementos de terras raras pesadas fracionadas, e são composicionalmente semelhantes aos granitos, o oposto é observado para os diatexitos tipo-2. Os diatexitos tipo-1 e os granitos foram gerados por reações de fusão por desidratação da moscovite. A reação de fusão parcial por desidratação da biotite também ocorreu numa fase final, mas foi incipiente. Os diatexitos tipo-2 geraram-se pela reação de fusão hidratada da moscovite sendo que no caso da geração dos metatexitos foi a mesma reação, mas com maior consumo de plagioclase relativamente à moscovite. No caso dos diatexitos, a divisão em dois tipos e a reação de fusão

parcial modelada para cada tipo é congruente com as idades de migmatização. Isto é, considerando que as reações de fusão hidratadas ocorrem a mais baixa temperatura relativamente às reações de fusão desidratadas, as idades de migmatização mostram a relação temperatura-tempo caracterizando o percurso do metamorfismo prógrado da seguinte forma: 343.7 ± 2.5 Ma para o diatexite type-2 e 328.8 ± 3.4 Ma para o diatexito tipo-1, culminando no pico metamórfico aos 318.8 ± 2.6 Ma para o diatexito tipo-1.

A intervenção de diferentes reações de fusão parcial identificadas na formação do CAFCR-L juntamente com a participação dos diferentes minerais principais e acessórios (zircão e apatite) justifica a variabilidade isotópica (Sr-Nd-Hf-Pb) observada nas litologias do complexo anatéctico. Além disto, os dados isotópicos das rochas anatécticas revelam a existência de dois grupos com composições isotópicas iniciais distintas, ambos incluem metatexitos, diatexitos e granitos. A distinção destes dois grupos deve-se à heterogeneidade observada na fonte.

PALAVRAS-CHAVE: Orogenia Varisca; anatexia crustal; granito-génese; migmatização; complexo granito-migmatítico

TABLE OF CONTENTS

LIST OF FIGURES

LIST OF TABLES

LIST OF ABBREVIATIONS, ACRONYMS, AND SYMBOLS

A – numerical constant depending on the geometry of the grain

a – effective diffusion dimension

AFC – Assimilation Fractional Crystallization

ASI – Aluminium Saturation Index

BSE – Backscattered Electron

Bt – biotite

CAD – Cadomian

CDF – Cumulative Distribution Function

CIZ – Central Iberian Zone

CL – Cathodoluminescence

D – daughter isotope

D_0 – the diffusion coefficient at infinitely high temperature

DBSG – Douro-Beiras Supergroup

DG-FCUL – Department of Geology – Faculty of Sciences, University of Lisbon

dT/dt – cooling rate

DTX – diatexite

E – activation energy for the diffusion process

FCR-LAC – Figueira de Castelo Rodrigo -Lumbrales Anatectic Complex

Fm. – formation

HFSE – High Field Strength Elements

HREE – Heavy Rare Earth Elements

ICP-MS – Inductively Coupled Plasma Mass Spectrometry

IM – Iberian Massif

IVB – Iberian Variscan Belt

JPCSZ – Juzbado-Penalva do Castelo Shear Zone

KDE – Kernel Density Estimate

Kfs – K-feldspar

LA-ICP-MS – Laser Ablation Inductively Coupled Plasma Mass Spectrometry

LILE – Large Ion Lithophile Elements

LP-HT – Low Pressure-High Temperature

LREE – Light Rare Earth Elements

Mc – microcline

MC-ICP-MS – Multi-Collector Inductively Coupled Mass Spectrometry

MDA – Maximum Depositional Age

Ms – muscovite

MSWD – Mean Square Weighted Deviation

MTX – metatexite

My – myrmequite

N// – parallel nicols

NX – crossed nicols

Or – orthoclase

P – parent isotope

P-T-t – Pressure-Temperature-time

Pbcm – common Pb

PDP – Probability Density Function

Pl – plagioclase

Qtz – quartz

R – ideal gas constant

R^2 – cross-correlation of PDPs coefficient

REE – Rare Earth Elements

SEM – Scanning Electron Microscope

SHRIMP – Sensitive High-Resolution Ion Microprobe

Sil – sillimanite

T-t – temperature-time

Tc – closure temperature

TDM_2 – two-stage model age

TW – Tera-Wasserburg

TZircsat – zircon saturation temperature

T_{Zr} – zircon saturation temperature

UoP – University of Portsmouth

USGS – United States Geological Survey

wt.% – weight percentage

CHAPTER 1. INTRODUCTION

1.1. STATE OF THE ART

The formation of large granite-migmatite complexes by crustal melting (anatexis) during orogenic processes is a process still debated, particularly because of the deep, unreachable location of their production sites (Ledru et al., 2001). Deep anatexis in the continental crust causes weakening and deformation of the rocks (Zhang et al., 2014), which induces chemical differentiation and rapid exhumation of thick mountain belts (Rey et al., 2001). Moreover, in the cores of orogenic mountain belts (e.g. Variscan Orogeny) are commonly observed structural and metamorphic core complexes bounded by shear zones and are inferred that these complexes have formed during or after the late stages of collision (Bertrand et al., 2017).

In the Variscan orogen, the petrogenetic association of S-type granitic rocks with migmatites has been defended and demonstrated combining geological, geochronological and geochemical (elemental and isotopic) data, for instance in the Apalaches (Maine, USA) (Solar and Brown, 2001), the Armorican Massif (St. Malo, France) (Milord et al., 2001), the Massif Central (France) (Ledru et al., 2001; Roger et al., 2015), and the Bohemian Massif (Austria) (Vanderhaeghe, 2009). In the Iberian Variscan Belt (IVB; the southwestern sector of the European Variscan orogen), precisely in Portugal, several authors evidenced the association between anatectic granites and gneiss-migmatitic rocks in the following works:

- Carríngton da Costa and Teixeira (1957) mentioned the existence of migmatitic rocks associated with the Porto granite massif;

- Ribeiro (1978) referred the existence of metasediments affected by the high-grade regional metamorphism in the surroundings of the granite massifs of the Tourém region;

- Esteves (2006) defined the Mundão Migmatitic Complex (Viseu) which exhibits metatexites and diatexites in the NW flank of the Porto-Viseu Metamorphic Belt. The Mundão Migmatitic Complex is limited by the Viseu-Cota late- to post-tectonic granitic massif, a syn-tectonic two-mica granite, and the Douro-Beirão Supergroup metasediments;

- Moita et al. (2009) discussed the relationships between granitoids and migmatites within the Évora Massif (southwest of IVB) and evaluated the interplay between mantle and crustal derived magmas;

- Bento dos Santos et al. (2010) performed a geothermobarometric study in the Berlengas Archipelago. The Berlenga island and the Estelas islets are mainly composed of a biotitic granite, whereas the Farilhões islets correspond to an anatectic complex composed of diatexites, metatexites and small-scale granulite relics (Bento dos Santos et al., 2019);

- Ribeiro et al. (2011) described metatexitic and diatexitic rocks in the Lavadores-Madalena coastal area (Porto, northwest of IVB) which are intruded by a post-tectonic biotitic granite (Lavadores granite);

- In the Porto-Viseu Metamorphic Belt is demonstrated the occurrence of high-grade metamorphic rocks, such as migmatites, and Variscan granitoids in its core (Rodrigues et al., 2013; Valle Aguado et al., 2005);

- Areias et al. (2014) studied the Mindelo Migmatitic Complex which is located on the NW part of the Porto-Viseu Metamorphic Belt and where it is visible the association between migmatites (metatexites and diatexites), two-mica granites, and the Douro-Beiras Supergroup metasediments.

- Ferreira et al. (2014) described a migmatitic outcrop (Pedregal) adjacent to synorogenic granites of different facies at north of the Douro river in the Porto metropolitan area.

- The Serra da Estrela Anatectic Complex is another example of migmatitic rocks spatially associated to Variscan granites in contact with the low-grade metamorphic metasediments of the Douro-Beiras Supergroup (Amaro et al., 2016);

- Damas et al. (2016) depicted the Bemposta Migmatitic Complex located at north of the Central Iberian Zone (NE Portugal) which are composed by stromatic migmatites and Variscan granites, which are hosted by the Douro-Beiras Supergroup metasediments (Douro Group).

The target area of this PhD project is the Figueira de Castelo Rodrigo-Lumbrales Anatectic Complex (FCR-LAC), as renamed by Pereira et al. (2014). It is framed in the Central Iberian

Zone autochthonous terrains and is also an example of the spatial association between granites and migmatites formed during the Variscan Orogeny. Previous work on this complex include:

- Carvalhosa (1960) was one of the first to refer the existence of high-grade metamorphic rocks in the Figueira de Castelo Rodrigo region, identifying a migmatitic border of 4 km north of the Marofa syncline, where outcrops of schists, gneisses and granites were intercalated.

- Ribeiro (2001) referred the existence of a metamorphic discontinuity between the migmatitic belt and the low metamorphic grade rocks from the Ordovician and Precambrian/Cambrian and named the complex by Lamego-Penedono-Escalhão antiform. This discontinuity is defined by the Juzbado-Penalva do Castelo shear zone (Iglesias and Ribeiro, 1981) that divides terrains with extremely different metamorphic grades.

- Recently, Pereira et al. (2017) constrained the exhumation conditions of the FCR-LAC from structural and geothermobarometric data. The structural analysis allowed to constrain two major deformation stages during the Variscan deformation phase D_3: a D_{3a} ductile deformation event and a D_{3b} thrusting ductile-brittle deformation event. The geothermobarometric estimations point to minimum metamorphic peak conditions of T = 761 ± 50 ºC and P = 5.0 ± 1.0 kbar. These observations led the authors to propose a model where the FCR-LAC exhumed vertically some 5-8 km during the 65-100 km horizontal displacement caused by a simple shear-dominated transpression mechanism during D_3.

1.2. THESIS GOALS

More than 60% in area of the outcropping rocks of Portugal mainland were affected and/or formed by the Variscan Orogeny. The study of Variscan (*s.l.*) rocks is, thus, of primordial importance to the understanding of the geological evolution of Portugal. The axial zones of orogens are usually marked by the occurrence of migmatization processes, ultimately leading to the genesis of large volumes of granites and to significant intracrustal heat and mass transfer responsible for continental crust differentiation. The Central Iberian Zone (CIZ), the axial sector of the Iberian Variscan segment, is known by the abundance of granitic intrusions, sometimes clearly associated in space, to migmatitic rocks. By the reasons above mentioned (see also 1.1)

such migmatite/granite complexes are paramount to understand the crustal evolution of the orogenic cores.

The FCR-LAC was chosen as study case of this PhD project due to the outstanding quality of their lithological exposure that allows the characterization of the interference patterns between the structures associated with the different Variscan tectonometamorphic events and a comparative petrological, geochemical (elemental and isotopic) analysis of lithotypes from different crustal levels. In addition, this thesis is intended to contribute to an increased knowledge concerning the interdependence between migmatization, granitogenesis, deformation and exhumation of the anatectic complexes generated at deep crustal levels, as well as the characterization of the exhumation conditions of this anatectic complex in the IVB, with implications for the evolution of axial zones of orogens elsewhere. Accordingly, the main goal of the PhD project is divided in the following objectives/steps:

- to acquire of new petrological, geochemical and geochronological data which will allow a better definition of the time and conditions of the Variscan deformation, metamorphism and granite emplacement;

- to obtain new petrological, whole-rock and isotopic (Sr, Nd, Hf and Pb) geochemical data, which will allow to assess the role of crustal anatexis in the genesis and evolution of the anatectic complex;

- to determine novel U-Pb zircon ages that will contribute to a better constraint of the time of granite emplacement, migmatization and peak metamorphic ages in the anatectic complex, but also a better definition of the deformation phases in the IVB;

- to apply thermochronological methods (U-Pb zircon and apatite ages; Ti-in-Zircon geothermometer) to quantify the duration of the deformation events, the cooling and exhumation rates of the FCR-LAC, and thereby the exhumation conditions of the anatectic complex;

- to provide U-Pb detrital zircon age patterns of the host rocks of the FCR-LAC for source rock assessment and characterization of its ages distribution;

- to integrate the obtained data into a consistent geodynamic model for the evolution of the Central Iberian Zone in the framework of the Iberian Variscan Orogeny.

1.3. THESIS OUTLINE

This PhD thesis entitled "Exhumation of anatectic complexes through shear zones: petrological and geochemical constraints on the evolution of the Figueira de Castelo Rodrigo – Lumbrales Anatectic Complex" is organized in 8 chapters, including 3 chapters (5, 6, and 7) reproducing scientific articles performed during this PhD thesis and that, presently, are published, under review or in preparation for submission. The reproducibility of the scientific articles on chapters 5, 6, and 7 is done in full except to the geological setting and the lithological description to avoid repetitions. The content of each chapter can be summarized as follow:

- **Chapter 1** corresponds to the introduction where the motivation, goals and thesis structure is described.

- **Chapter 2** includes a description from the regional to local-scale of the geological setting where the target area is framed.

- **Chapter 3** presents the sampling points and the number of samples. In this chapter is also described the sample preparation before performing the different analytical methods. Each specific analytical method is described in chapters 5, 6 and 7.

- **Chapter 4** includes a petrographic characterization for each group of the sampled lithologies in the study area.

- **Chapter 5** is a scientific article published in International Journal of Earth Sciences (2019 Impact Factor:2.295) entitled "Tectonically assisted exhumation and cooling of Variscan granites in an anatectic complex of the Central Iberian Zone, Portugal: constraints from LA-ICP-MS zircon and apatite U–Pb ages" (Ferreira et al., 2019). This study presents new U–Pb zircon and apatite ages for distinct FCR–LAC granite facies to constrain their crystallization ages and cooling rates, and, therefore, their emplacement conditions within the framework of the Variscan Orogeny.

- **Chapter 6** consists of an article submitted to Precambrian Research (2019 Impact Factor: 3.834). The main objective of this work is to present new U-Pb zircon and apatite ages for the anatectic rocks of the FCR-LAC to constrain their migmatization and metamorphic peak ages, as well as the retrograde path ages and their cooling rates, thus defining their emplacement conditions within the framework of the Iberian Variscan Belt. Additionally, it is presented new U-Pb detrital zircon data from the main hosting stratigraphic unit of the studied anatectic complex. A comparison between the detrital zircon populations of the hosting metasedimentary units and the inherited zircon ages retrieved from the anatectic complex lithologies (metatexites, diatexites and granites) is done in order to explore their genetic links. These new detrital zircon ages of metasedimentary units are also compared to published detrital zircon data from potential stratigraphic equivalents in the Spanish sector and in the Beiras Group, and from the overlying Ordovician metasedimentary units. This approach allows the assessment of the evolution of the sediment sources during the Ediacaran – Cambrian – Ordovician, with implications on the geodynamic evolution of the CIZ.

- **Chapter 7** comprises an article published in Lithos (2019 Impact Factor: 3.913) entitled "The role of melting on the geochemical evolution and isotopic variability of an anatectic complex in the Iberian Variscides". This study is supported on isotope (Sr, Nd, Hf, and Pb), elemental whole-rock compositions and trace-element zircon and apatite analyses from the FCR-LAC to assess the melting reactions that led to the formation of its different lithotypes; provide insights onto the causes of isotopic variability characterizing the anatectic complex, and explore the geochemical link between the different stages of anatexis from migmatites to granites, besides defining potential metapelitic protoliths.

- **Chapter 8** closes the thesis with a discussion and the main conclusions combining the outcomes presented in each chapter. The future steps of this research project are also approached in this chapter.

CHAPTER 2. GEOLOGICAL SETTING

2.1. REGIONAL GEOLOGY

The opening of the Rheic Ocean defined the beginning of the Variscan Cycle, whereas the continental collision of major paleocontinents Gondwana and Laurussia led to the end of this cycle and the Variscan Orogeny (560 – 245 Ma). This orogeny was responsible for the deformation of the pre-Mesozoic terranes during the Devonian and Carboniferous periods (Simancas, 2019 and references therein). The Variscan Belt has a length of over 3000 km from Appalachian Mountains (North America, East coast) until the northeast of Bohemia Massif (Central Europe) comprising the North Africa (Morocco, Anti-Atlas) and the Iberia Peninsula where the maximum curvature of the belt (Ibero-Armorican Arc) is exhibited. The Iberian Massif (IM) represents the westernmost part of the European Variscan Belt, exposing the largest segment in Iberia with pre-Mesozoic rocks where the Variscan Orogeny produced macrostructures resultant from three main deformation phases (Ribeiro, 2013).

The highly variable stratigraphic, structural, magmatic, and metamorphic characteristics of the IM led to its division in six tectono-stratigraphic zones, from northeast to southwest (Figure 2.1; Farias et al., 1987; Julivert et al., 1972; Lotze, 1945):

- Cantabrian Zone;
- West Asturian-Leonese Zone;
- Galicia-Trás-os-Montes Zone;
- Central Iberian Zone;
- Ossa-Morena Zone;
- South Portuguese Zone.

The first five tectono-stratigraphic zones (Cantabrian, West Asturian-Leonese, Galicia-Trás-os-Montes, Central Iberian and Ossa-Morena Zone) were part of the northern continental margin of Gondwana during the Neoproterozoic, whereas the South Portuguese Zone was part of the Avalonia continent (Pérez-Cáceres et al., 2017). The IM zoning reflects the complex evolution since the Cadomian collision (Neoproterozoic), the Lower Palaeozoic extensional tectonic activity and the Upper Palaeozoic Variscan Orogeny (Upper Palaeozoic) (Figure 2.1.; Dias et al., 2016). The study area is located in the Central Iberian Zone (CIZ), therefore the geology of this tectono-stratigraphic zone will be described in the next subchapter.

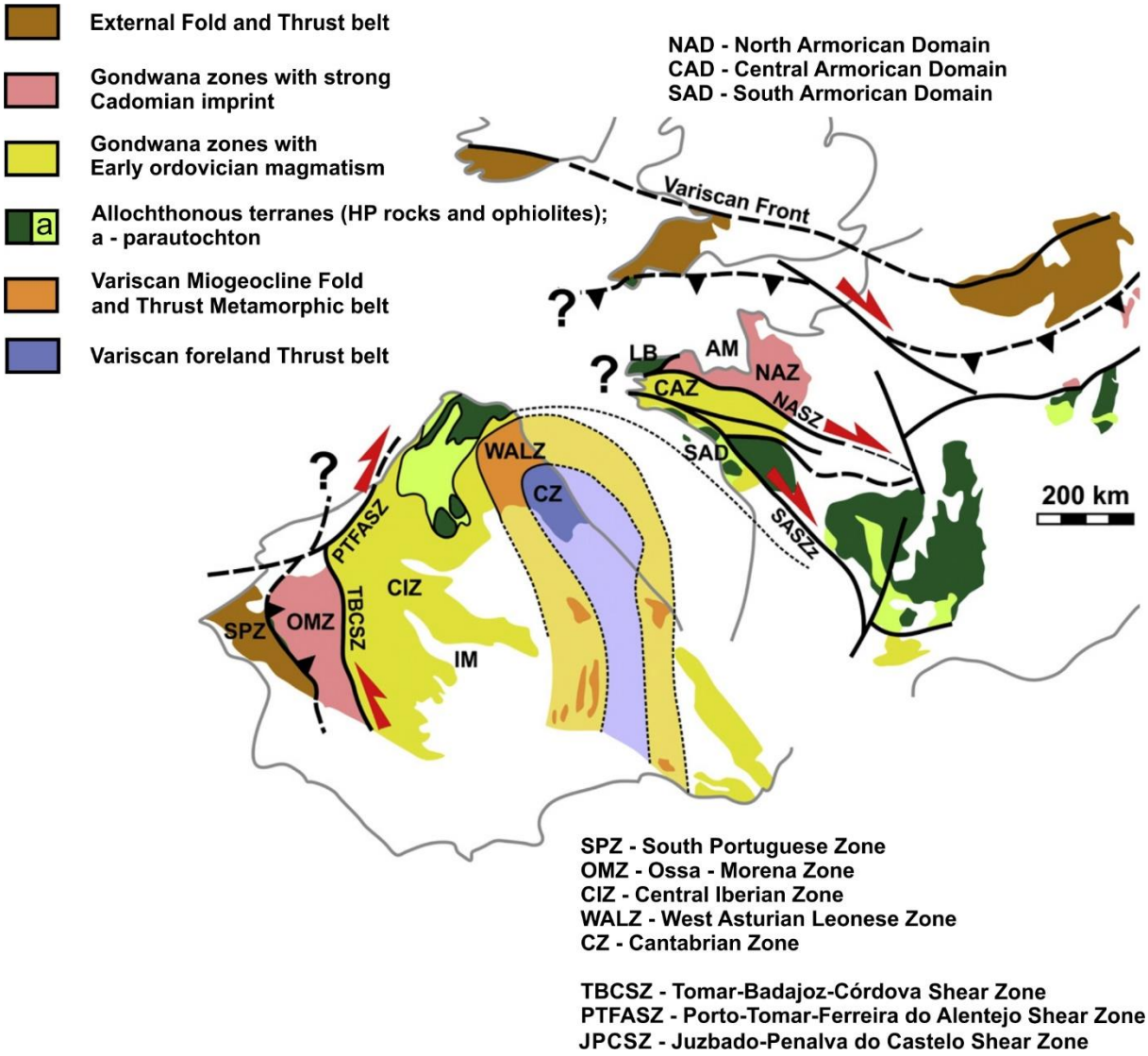

Figure 2.1 – Iberian Massif tectonostratigraphic units in the framework of the European Variscan Belt (Dias et al., 2016).

2.1.1. Central Iberian Zone

The CIZ is the axial domain of the Iberian Variscan Belt (IVB) and is characterized by an autochthonous domain that reveals particular lithostratigraphic features which led to individualize it as a zone, and it is overlaid by an allochthonous domain, the Galicia-Trás-os-Montes Zone (Julivert et al., 1972). The autochthonous of the CIZ is marked by the predominance of Pre-Ordovician sequences (Douro-Beiras Supergroup), Lower Ordovician quartzites with transgressive character, and the presence of an unconformity separating the Lower Ordovician from Precambrian-Cambrian rocks. Additionally are also exposed a profusion of granitic plutons and low- to high-grade metamorphic rocks (Martínez Catalán et al., 2014).

The autochthonous of the CIZ is bounded at north by the Olho-de-Sapo antiform (Julivert et al., 1972). At west and south, the CIZ is limited by the Porto-Tomar-Ferreira do Alentejo and Tomar-Badajoz-Córdoba shear zones, respectively (Dias et al., 2016; and references therein).
The Central Iberian autochthonous is subdivided in three domains (Martínez Catalán et al., 2004): Ollo de Sapo domain, Douro-Beiras Supergroup domain, and Meridional domain. The Ollo de Sapo domain located at the northern part of the CIZ is related to Cambro-Ordovician magmatism (García-Arias et al., 2018). The Douro-Beiras Supergroup domain (Oliveira et al., 1992; Sousa and Sequeira, 1993) is the most predominant domain in the CIZ which is composed by a flyschoid sequence of Neoproterozoic-Cambrian age. In the south CIZ, the Meridional domain is represented by Upper Neoproterozoic – Lower Cambrian rocks that have tight affinities with the Ossa-Morena Zone (Martínez Catalán et al., 2004).
Due to the dominance of the Douro-Beiras Supergroup in the CIZ and because of its role as host unit of the anatectic complex in study, this lithostratigraphic domain is described in the next chapter.

Lithostratigraphy: Douro-Beiras Supergroup

The Douro-Beiras Supergroup (DBSG) is characterized by a thick and relatively monotonous metasedimentary sequence of Upper Neoproterozoic – Lower Cambrian age composed of layers of phyllites and greywackes (Complexo Xisto-Grauváquico of Carríngton da Costa, 1950 and Teixeira, 1955). The DBSG is divided in three groups: Beiras Group, Douro Group, and Arda-Marofa Group. The Douro Group is represented at north of the CIZ, being particularly well exposed along the Douro river, while the Beiras Group occur at south of the S. João da Madeira, Viseu and Serra da Malcata alignment (Oliveira et al., 1992). The Douro Group depositional age range from the Late Ediacaran to Lower Cambrian (Stage 4) (Dias da Silva et al., 2014; Rebelo and Romano, 1986) while the Beiras Group has Ediacaran – Lower Cambrian (Stage 3) depositional ages (Romão et al., 2010 and references within). The DBSG sedimentation culminates with the Arda-Marofa Group where its depositional age interval range from the Upper Ediacarian to the Upper Cambrian (Silva et al., 1995). This group occurs in the northern part of the CIZ namely in the following regions: Coimbra, Porto, Viana do Castelo, Guarda and Trás-os-Montes.

- BEIRAS GROUP

The Beiras Group of Ediacaran age is composed, from the base to the top, by the Malpica do Tejo, Perais, Rosmaninhal (Silva et al., 1988) and Almaceda formations (Romão, 1991). The

Malpica do Tejo Fm. is predominantly characterized by greywackes and it is divided in two Members. The Lower Member comprises alternations of centimetric to millimetric pelitic layers with metric layers of greywackes. The passage to the Upper Member is characterized by the thickness/frequency increasing of the greywacke layers. The Perais Fm. shows phyllites and metagreywackes in similar proportions. The Rosmaninhal Fm. exhibits a thick pelitic sequence composed by microconglomerates, conglomerates and metric layers of greywackes. Similar to the Upper Member of the Malpica do Tejo Fm., the Almaceda Fm. is mainly composed by greywackes, with metric thickness, containing, at times, clay clasts.

- DOURO GROUP

Sousa (1982) established six formations for the Douro Group sequence: Bateiras, Ervedosa do Douro, Rio Pinhão, Pinhão, Desejosa and S. Domingos (Figure 2.2). The existence of a syn-sedimentary thrust of Cambrian age, Senhora do Viso thrust, caused the duplication of some formations of the Douro Group (Silva and Ribeiro, 1985). Thus, the Douro formations were organized in two sequences, the autochthonous (Bateiras and Ervedosa do Douro Formation Fm.) and the allochthonous sequence (Rio Pinhão, Pinhão, Desejosa and S. Domingos Fm.).

The Bateiras Fm. is composed by a bottom member and an upper member. The bottom member is represented by graphite-bearing phyllites and metagreywackes, while the upper member has limestones, grey phyllites and metagreywackes. A thickness above 800 m was estimated for this formation (Sousa, 1982). The Ervedosa do Douro Fm. exhibits greenish chlorite-bearing phyllites, quartzphyllites and metagreywackes with 250 ± 50 m of thickness. The contact between this formation and the Rio Pinhão Fm. is expressed by the Senhora do Viso thrust.

The Rio Pinhão Fm. is the base of the allochthonous sequence, and it is predominantly composed by a thick metagreywacke sequence alternating with thin dark phyllites. In the Vila Nova de Foz Côa region was estimated at 900 ± 100 m of thickness for this formation (Silva and Ribeiro, 1991), whereas in Freixo de Espada à Cinta thickness is only 85 m (Silva and Ribeiro, 1994). The Pinhão Fm. presents alternations of psammitic (e.g. metaquartz-wackes) and pelitic (e.g. phyllites) thin layers (10 to 20 cm of thickness) (Sousa, 1982). This formation is akin to its autochthonous counterpart, the Ervedosa do Douro Formation. The thickness of the Pinhão unit is 700 ± 100 m in the Vila Nova de Foz Côa region (Silva and Ribeiro, 1991) while in the Freixo de Espada à Cinta area is up to 250 ± 50 m (Silva and Ribeiro, 1994). The Desejosa Fm. comprises alternations of thin layers (millimetric to centimetric scale) of phyllites and psammites, where, rarely, intercalations of metagreywackes and calcsilicate rocks occur. The thickness of this formation is up to 800 ± 100 m (Silva and Ribeiro, 1991). Dias da Silva

(2013) attributed a Cambrian (Stage 3) age to the top of the Desejosa unit. Ribeiro (2001) assumes the Desejosa Fm. as an equivalent unit of the Excomungada Fm. which belongs to the Arda-Marofa Group and it occurs in the study area.

The Montes Ermos Fm. was recently identified in Freixo de Espada à Cinta and Mazouco with a thickness of 150 m and an age constrained between the Desejosa Fm. and the Ordovician (Dias da Silva, 2013). This unit is formed by a regressive turbiditic sequence which is composed by intercalations of fine sandstones and mudstones, sometimes, with iron oxide levels. The S. Domingos Fm. occur on the top of the Douro Group and it is characterized by the occurrence of conglomerates and metaquartz-sandstones, as well as by the absence of pelitic material (unit thickness around 50 m. Martins et al. (2012) estimated an maximum depositional age of 524 ± 20 Ma (Lower Cambrian) to the S. Domingos Fm. Overlying the Desejosa Fm., over an angular unconformity, occurs a unit of pure quartzites with Early Ordovician age and designated by Armorican Quartzites (Oliveira et al., 1992; Sousa, 1984).

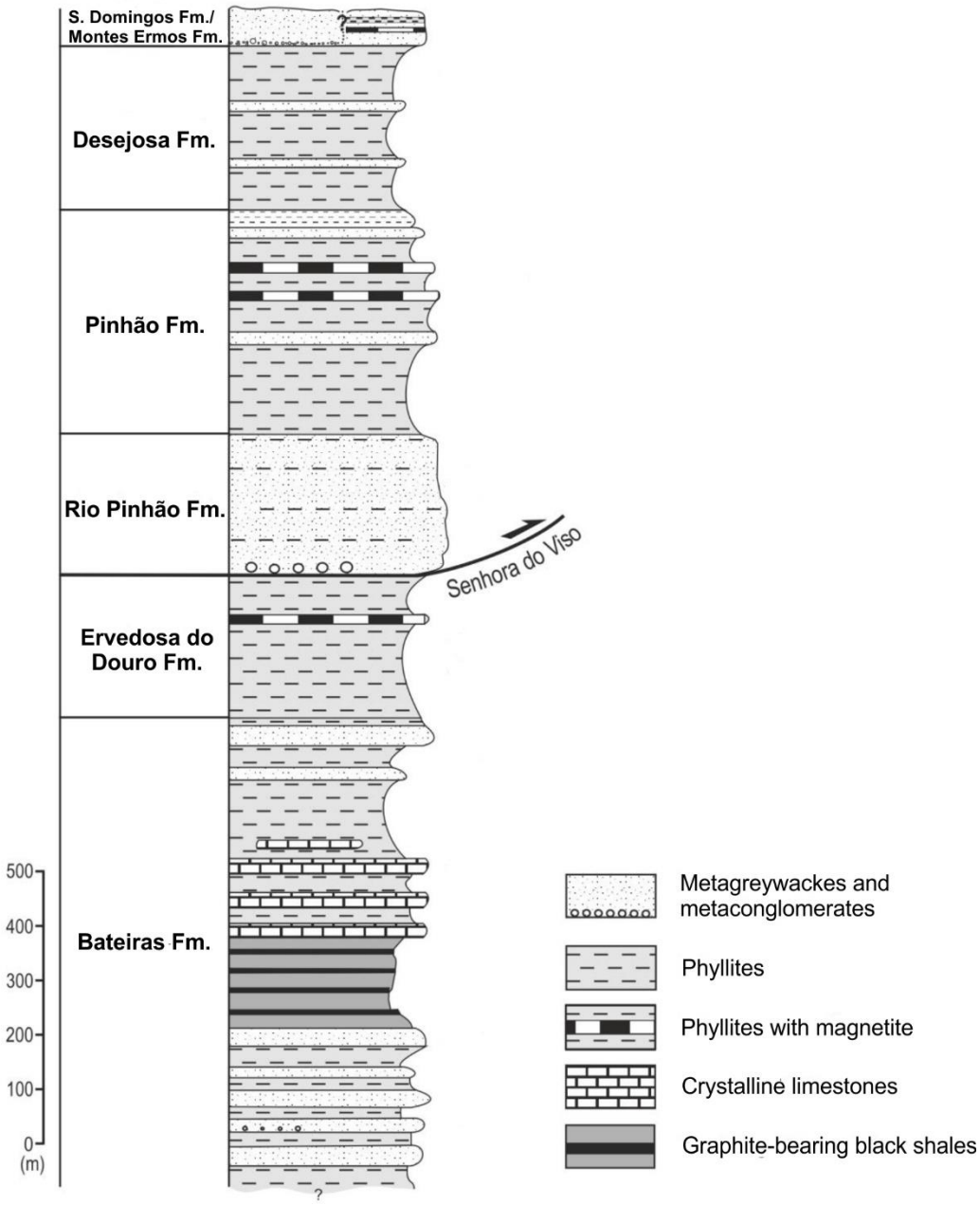

Figure 2.2 – Stratigraphic sequence of the Douro Group (adapted from Dias et al., 2013).

- ARDA-MAROFA GROUP

Initially, Silva et al. (1995) defined the Arda-Marofa Group sequence with the Póvoa-Sátão and the Excomungada-Ribeira do Colmeal formations. Later, Silva (2005) revised this sequence including more units as follows: Póvoa, Real, Sátão, Excomungada-Ribeira do Colmeal, Queiriga, Desejosa, S. Gabriel and S. Domingos formations.

The Póvoa Fm. is composed of chlorite-bearing phyllites intercalated with metaquartz-sandstones, impure quartzites, meta-microconglomerates, metasiltstones and meta-arkoses. The Real Fm. exhibit chlorite-bearing phyllites and quartzphyllites and micaschists intercalated with

micaceous metasiltstones, micaceous metasandstones, micaceous quartzites, meta-microconglomerates and, rarely, metagreywackes and pelitic hornfels. This unit occurs frequently deformed and, locally, migmatized. The Sátão Fm. is characterized by alternations of micaceous metapelites, graphite-bearing phyllites, micaceous quartzites and/or micaceous metasandstones. In the contact of this unit with the Variscan granitoids occurs gneiss-migmatitic rocks and two-micas micaschists. The most prevalent lithologies in the Excomungada-Ribeira do Colmeal Fm. are the grey to greenish chlorite-bearing phyllites frequently intercalated with thick layers of metasiltstones, metasandstones, impure quartzites and metaconglomerates (Silva, 2005; Sousa, 1989). At north of the Marofa syncline, the migmatitic rocks exhibit paleosome of micaschist composition and another metasediments which not only correspond to this migmatized unit. The Queiriga Fm. is formed by grey to greenish chlorite-bearing phyllites intercalated with metasiltstones, metasandstones and metaconglomerates.

The Desejosa Fm. is correlated with the Excomungada-Ribeira do Colmeal Fm. and it is mainly composed by an alternance of dark grey chlorite-bearing phyllites, metapsammitic rocks (metagreywackes and metasiltstones), calc-silicate rocks and, rarely, limestones. The São Gabriel Fm. corresponds to a volcano-clastic sequence composed by metatuffs and basic and acid metatuffites in alternance with metapelites, metasiltstones and metasandstones (Coke et al., 2000; Silva, 2005). The São Domingos Fm. reveals metapelitic layers with fine levels of quartz-sandstone which increase of thickness in the direction of the top where gives place to conglomeratic intercalations (Silva, 2005; Sousa, 1982).

Variscan Deformation

The Variscan Orogeny was responsible for the action of three compressive deformation phases in the ZCI (D_1, D_2 and D_3; Noronha et al., 1979). It is important to clarify that D_1, D_2 and D_3 deformation phases are equivalent to the Martínez Catalán et al. (2014) nomenclature C1, C2 and C3 (Figure 2.3).

The major structures of the autochthonous of the ZCI result, essentially, of the D_1 deformation phase which is more widespread at the regional scale (Noronha et al., 1979; Ribeiro et al., 1990). In general, the D_1 produced overturned to recumbent folds with axial planar cleavage (S_1) that assumes an E-W direction at east changing to the NW-SE orientation next to the coast, in this way shaping the south branch of the Ibero-Armorican Arc (Dias et al., 2013; Ribeiro et al., 1990). The D_1 took place between 359–347 Ma (Alcock et al., 2015; Dallmeyer et al., 1997).

The D_2 deformation phase is associated to the emplacement of the allochthonous nappe stack at NW of Iberia (Alcock et al., 2015; Dias et al., 2013). Thus, the D_2 is well represented at the base of the allochthonous and parauthocthonous units, being responsible for the generation of recumbent folds with crenulation cleavage or axial planar schistosity (S_2) (Ribeiro et al., 1990). This deformation phase is less pervasive/intense than the D_1, although it deformed the structures acquired in previous tectonic events in a limited way. In the autochthonous domain, the main D_2 structures are NNE-SSW normal faults dipping 60-20ºW (Ribeiro et al., 1990). The D_2 activity occurred in the 345–335 Ma age interval (Alcock et al., 2015; Dallmeyer et al., 1997). After the allochthonous complexes emplacement occurred a period of thermal relaxation of a heated thickened crust which triggered the synorogenic extensional collapse arising the first extensional event (E1; Alcock et al., 2015; Martínez Catalán et al., 2014). This extensional event is associated to decompression, crustal partial melting and voluminous granitic magmatism. The middle and lower crust was deformed by ductile flow that produced anatectic domes composed by a gneissic or migmatitic cores, bounded by extensional detachments. The E1 extensional event in the internal zones of the CIZ occurred between 340–327 Ma (Rubio Pascual et al., 2013; Valverde-Vaquero et al., 2007). The E_1 phase has been considered coeval with the migmatization which yielded ages around 329–316 Ma (Figure 2.3; Rubio Pascual et al., 2013; Valverde-Vaquero et al., 2007). In this thesis new data on the migmatization age will be discussed on Chapter 6.

Vertical or steeply inclined folds were produced during the D_3 Variscan phase associated with a crenulation cleavage (S_3) formed where the previous regional foliation (S_1 and S_2) was subhorizontal, The folding and the shear zones associated to the D_3 deformation phase contributed to the definition of the Ibero-Armorican Arc (Dias et al., 2013; Ribeiro et al., 1990). The D_3 folds occur frequently related with ductile strike-slip shear zones and are coeval with the emplacement of syn-tectonic granites (315–305 Ma; (Gutiérrez-Alonso et al., 2011; Valle Aguado et al., 2005). The late stages of crustal extension (E2) continued during and after D_3, producing new migmatitic domes with brittle–ductile faults developed at their limits. The 315–305 Ma age interval mentioned before overlaps the migmatization developed during the E2 extensional event (Figure 2.3; Alcock et al., 2015 and references therein; Martínez Catalán et al., 2014).

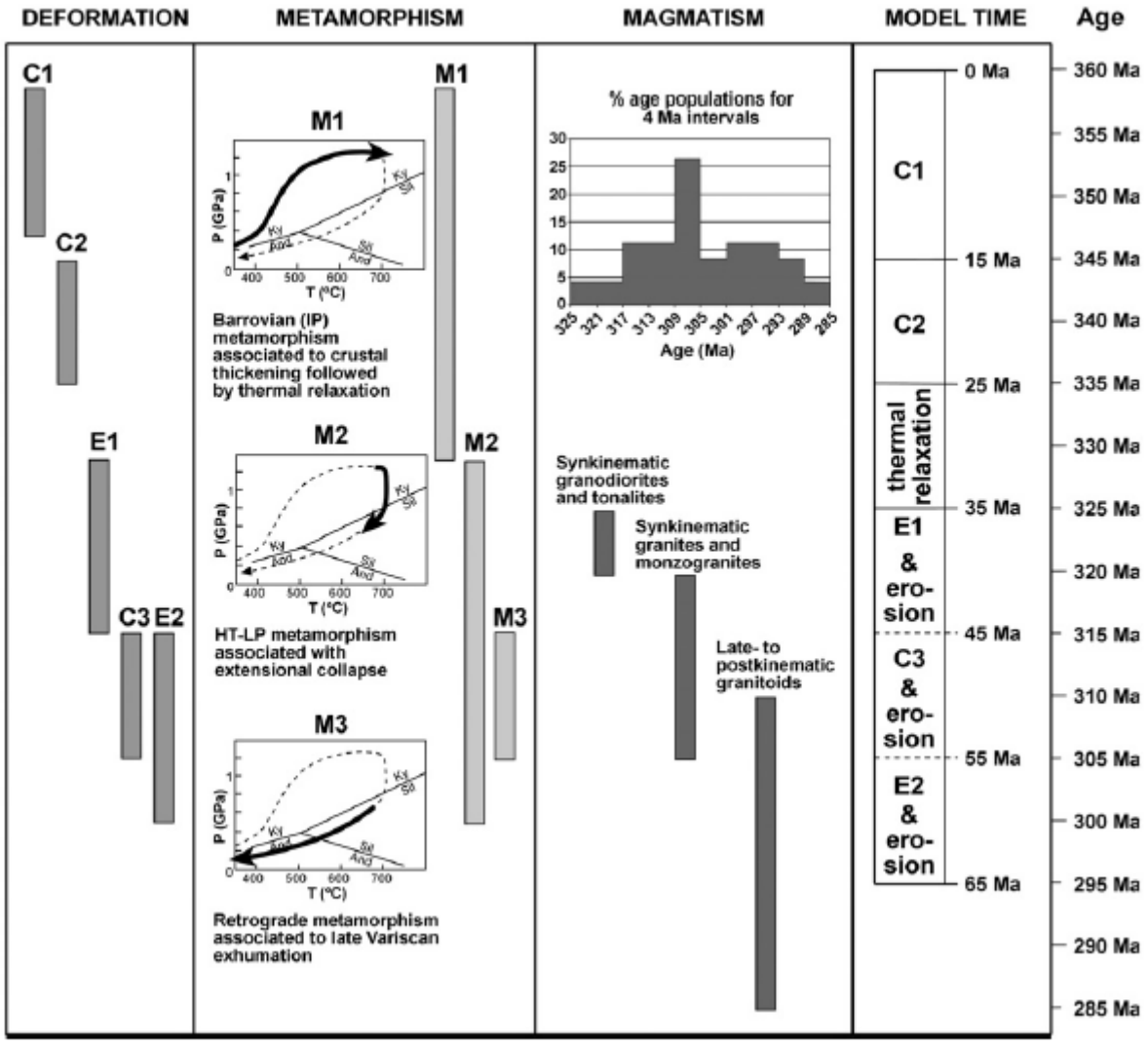

Figure 2.3 – Age distribution synthesis of the Variscan deformation, metamorphic, and magmatic phases in the internal zones of NW and Central Iberia (Alcock et al., 2015 and references therein).

Variscan Metamorphism

In the CIZ, migmatitic terrains occur in elongated metamorphic belts associated with syn-tectonic Variscan granitoids (e.g. Porto-Viseu and Meda-Penedono-Lumbrales) (Alcock et al., 2015; Martínez Catalán et al., 2014). The metamorphism in the CIZ metamorphic belts reached the granulite facies and is defined by thermal domes nearly related with structural antiformal-dome like structures. Far from the thermal domes, the metamorphic grade decreases quickly to greenschist facies in few kilometres (Ribeiro et al., 2019 and references therein).

The Variscan metamorphism comprises three phases (M1, M2 and M3; Figure 2.3) which starts with the prograde event, M1, developed under an intermediate to higher pressure, Barrovian-type gradient, during deformational events D_1 and D_2, associated with crustal thickening followed by thermal relaxation. Exceptionally, it was observed mid-temperatures eclogite

facies conditions in the retrogressed eclogites from the Sierra de Guadarrama (725–775 ºC, 1.4 GPa; Barbero and Villaseca, 2000).

The M2 is a high-temperature and low-pressure metamorphic event (HT–LP), coeval with exhumation during the extension phases (E1 and E2) and associated with extensional collapse. Several authors restrict this event to the D_2 deformation phase (Ábalos, 1992; Escuder Viruete et al., 1995; Valle Aguado et al., 2005). Although, Valverde-Vaquero et al. (2006) presented monazite ages for the Lumbrales Antiform (Salamanca; 316-314 Ma) suggesting that the HT–LP metamorphism is not exclusive of the D_2 phase being also associated with the D_3 folding phase/magmatism. This subject is also debated in this thesis (see chapter 6). The M2 metamorphic phase reached the high-temperature granulite facies as testified by the occurrence of sillimanite – K-feldspar – muscovite out zone (e.g. Toledo dome; Barbero, 1995).

M3 is involved a retrograde metamorphic path characterized by a regional decreasing of temperature and pressure, simultaneously with the development of D_3 structures, partially overlapping in time with M2 in the youngest thermal domes and associated with late Variscan exhumation (Figure 2.3; 315-300 Ma; Alcock et al., 2015; Martínez Catalán et al., 2014).

Variscan Granitic Magmatism

Variscan granitic magmatism is widespread in the central part of the CIZ and it is associated with the D_3 ductile deformation phase (Figure 2.4). Based on petrographic and geochemical features, Capdevila and Floor (1970) divided the granitoids in the following groups:

- ✓ S-type, peraluminous two-mica granites closely associated with migmatites in high-grade metamorphic terrains;
- ✓ Granodiorites and calc-alkaline biotitic granites (syn- to late-post-tectonic) frequently associated with intermediate and mafic igneous rocks.

Schermerhorn (1956) and Oen (1958) using structural and geochronological criteria classified the Variscan granites of north Portugal in *Older* (syn- to late-tectonic) and *Younger* granites (post-tectonic). The *Older* granites group include the two-mica granites, granodiorites and earlier biotitic granites from calc-alkaline series. The *Younger* granites comprise the late to post-tectonic granodiorites and biotitic granites also from the calc-alkaline series.

The fact that the Variscan granites are related with the D_3 phase led Ferreira et al. (1987) to group the granites in pre-D_3, syn-D_3, late-D_3 and post-D_3. The pre-D_3 granites have similar compositional features to the syn-D_3 granites but are less representative in the Iberian Massif.

The syn-D_3 granites group consists of peraluminous, two-mica granites and leucogranites, and a few granodiorites and biotitic granites outcrops. The late- and post-D_3 group is characterized by undeformed granodiorites and biotitic granites, weak to moderately peraluminous, occasionally associated with rocks of intermediate to basic composition. This group is frequently surrounded by a contact metamorphic aureole. Thus, these different granitoid groups present the following emplacement chronology during the D_3 ductile deformation phase (Dias et al., 1998; Ferreira et al., 1987):

- ✓ syn-D_3 granitoids, 321–312 Ma (two-mica granites, biotite granites and leucogranites);
- ✓ late-to post-D_3 granitoids, 312–300 Ma (biotite or dominant-biotite granites, sometimes associated with basic rocks, and some leucogranites);
- ✓ granitoids post-D_3, 290–299 Ma (mainly biotite to biotite-muscovite granites).

The geochronological data reveal that the granite intrusions were emplaced continuously in the CIZ during a short time interval around 30 Ma, corresponding to the latest stages of the Variscan Orogeny. Additionally, the D_3 and the late Variscan fragile deformation phase were active in the age intervals of 321–300 Ma and 299–290 Ma, respectively (Ribeiro et al., 2019).

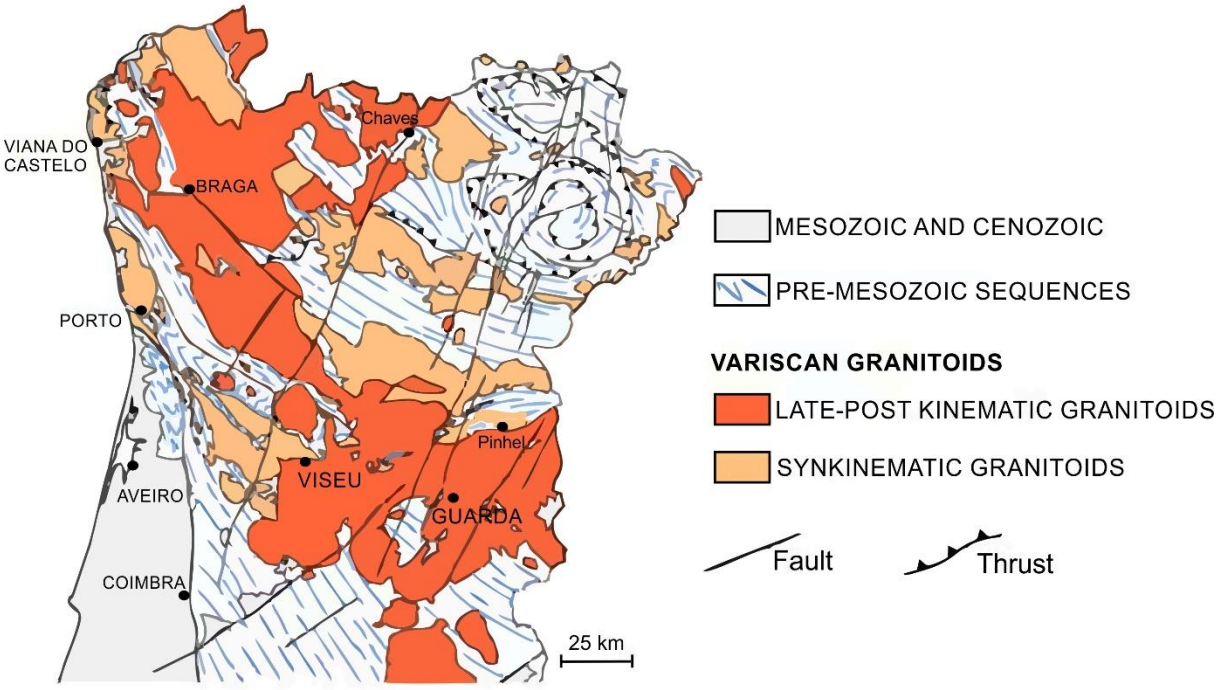

Figure 2.4 – Variscan granitoids distribution in the northern Portugal and its temporal relation with the D3 deformation phase (adapted from Azevedo et al., 2005).

2.2. LOCAL GEOLOGY

The Figueira de Castelo Rodrigo-Lumbrales Anatectic Complex (FCR-LAC) is located within the autochthonous terrains of the CIZ and is an example of a granite-migmatite complex generated during the Variscan Orogeny. This anatectic complex is composed by migmatites (metatexites and diatexites) closely associated in space with syn-tectonic granites of different facies (Figure 2.5).

The FCR-LAC contacts to the North and South with the low-grade metamorphic units of Douro-Beiras Supergroup (Douro Group) and the Ordovician formations (e.g. Marofa syncline). The contacts between the FCR-LAC and the low-grade metamorphic units are delimited by the Huebra (HSZ) and the Juzbado-Penalva do Castelo (JPCSZ) shear zones, respectively (Pereira et al., 2017). The JPCSZ defines a metamorphic discontinuity between high-grade, at north, and low-grade metamorphism, at south, placing side by side terrains with significantly different metamorphic grades (Ribeiro, 2001). The sinistral JPCSZ extends for 200 km, from Juzbado (Spain) to Penalva do Castelo (Portugal), with a displacement of 65 to 100 km that took place during the D_3 intracontinental collision stage (Iglesias and Ribeiro, 1981; Pereira et al., 2017; Villar Alonso et al., 2000). In this region, the shear zone is decomposed into two E-W to ENE-WSW, sinistral and steeply-dipping shear zones that bound the anatectic complex. The northern HSZ exhibits a D_{3a} stretching lineation plunging 10 to 30° W, and boudins showing vertical stretching (Pereira et al., 2017). A later stretching lineation D_{3b}, gently plunging to the E affects melt feeding channels and some of the granites (Pereira et al., 2017). The activity of this strike-slip shear zone appears to have been diachronic from east to west, being dated at 309 ± 2.5 Ma ($^{40}Ar/^{39}Ar$ on syn-kinematic white micas) in Juzbado (Gutiérrez-Alonso et al., 2015), and at *ca.* 299.4 ± 0.4 Ma (U-Pb zircon ages) in Penalva do Castelo (Viseu granite, Valle Aguado et al., 2017). We also discuss this subject in Chapter 5.

The exhumation conditions of the FCR-LAC were constrained using structural and geothermobarometric data by Pereira et al. (2017). The authors propose a model where a 5 to 8 km vertical exhumation occurred during the 65-100 km horizontal displacement caused in a simple shear-dominated transpression mechanism during the early D_3. However, other authors propose orogenic collapse as the most likely exhumation mechanism, due to extensional detachment faults that produce a sub-horizontal S_2 foliation that was later transposed and verticalized by the later D_3 stage (Díez Fernández and Pereira, 2016; Pereira et al., 2018).

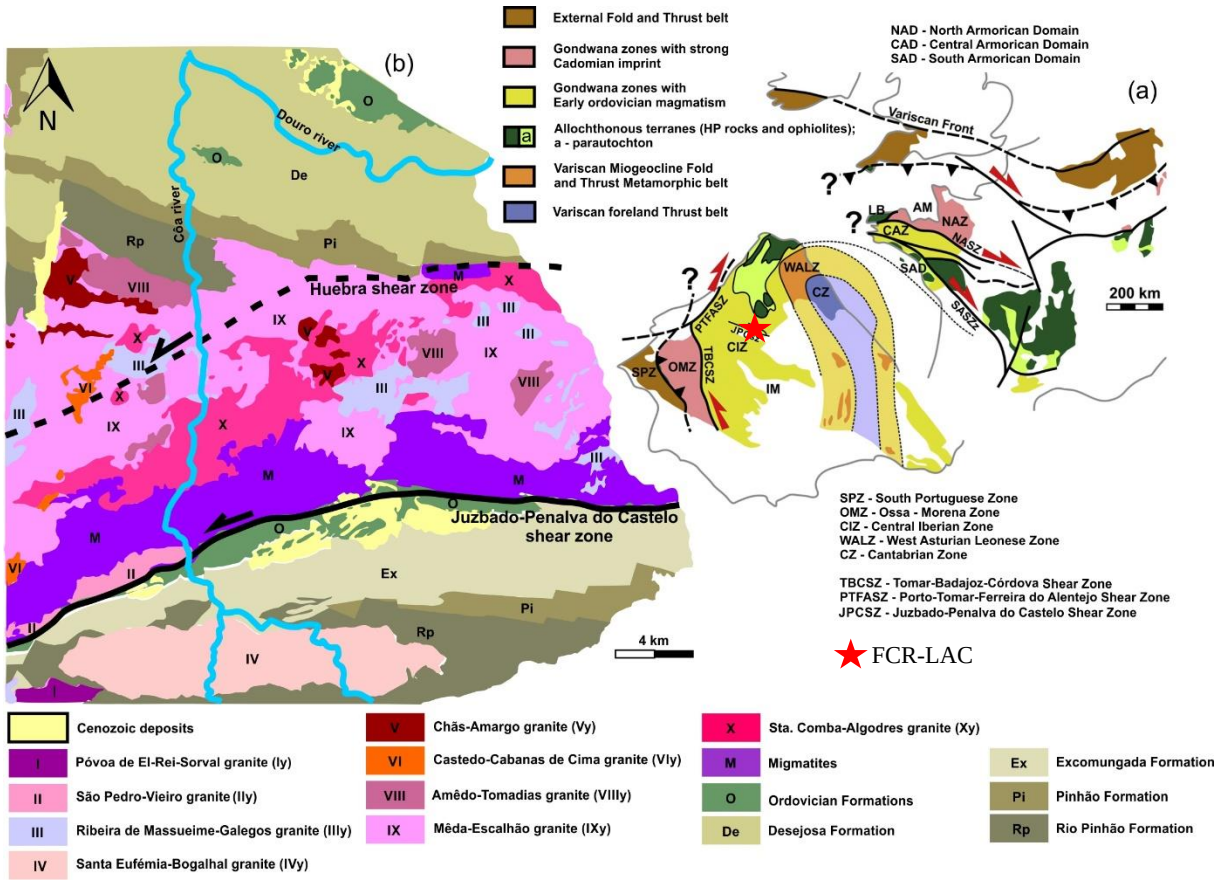

Figure 2.5 – (a) Location of the studied area in the Iberian Massif (adapted from Dias et al., 2016); (b) geological map of the Figueira de Castelo Rodrigo-Lumbrales Anatectic Complex (adapted from Silva and Ribeiro, 2000).

2.2.1. Lithological description

The low-grade metamorphic units, preserved in the chlorite to biotite metamorphic zones, are represented by phyllites and quartzphyllites (Figure 2.6A) that, generally, show schistosity nearly E-W (N90-100º; subvertical). These metasediments appear deformed close to the Huebra shear zone (Figure 2.6B). Phyllites in the vicinity of granites show post-deformation andalusite porphyroblasts (Figure 2.6C), usually formed by contact metamorphism. They are often pseudomorphosed.

The metatexites exhibit stromatic textures where the banded orientation is inherited/coincident with the phyllites' schistosity (E-W; subvertical). Occasionally, in the metatexites stand out centimetric or millimetric bands of peritectic sillimanite associated with muscovite (Figure 2.7A). At times, the leucosomes of centimetric dimension occur boudinated with E-W orientation (Figure 2.7B). In some outcrops leucosomatic pockets occur in association with the leucosome veins (Figure 2.7C). The majority of leucosomatic veins are parallel to the pre-migmatization structures (schistosity; Figure 2.7B) in their host, but some are cross-cutting (Figure. 2.7C).

The diatexites show structures such as restitic nodules (Figure 2.8A), schlieren structures (Figure 2.8B), and, occasionally, ptygmatic folds. The diatexitic outcrops when near the shear zones reveals shear deformation planes (ductile deformation) nearly oriented E-W, subvertical (Figure 2.8C). The other structures seen in these outcrops are the pegmatitic and the leucosomatic veins forming vein-structured diatexites. Nebulitic textures are also observed in diatexites (Figure 2.8D).

The granites are essentially two-mica type, with biotite and muscovite appearing in different proportions giving origin to different granite facies (Silva and Ribeiro, 2000). The grain size of these granites is also diverse in the different outcrops (Figure 2.9A and 2.9B). Some granitic outcrops reveal deformation which match the movement of the JPCSZ (Figure 2.9C).

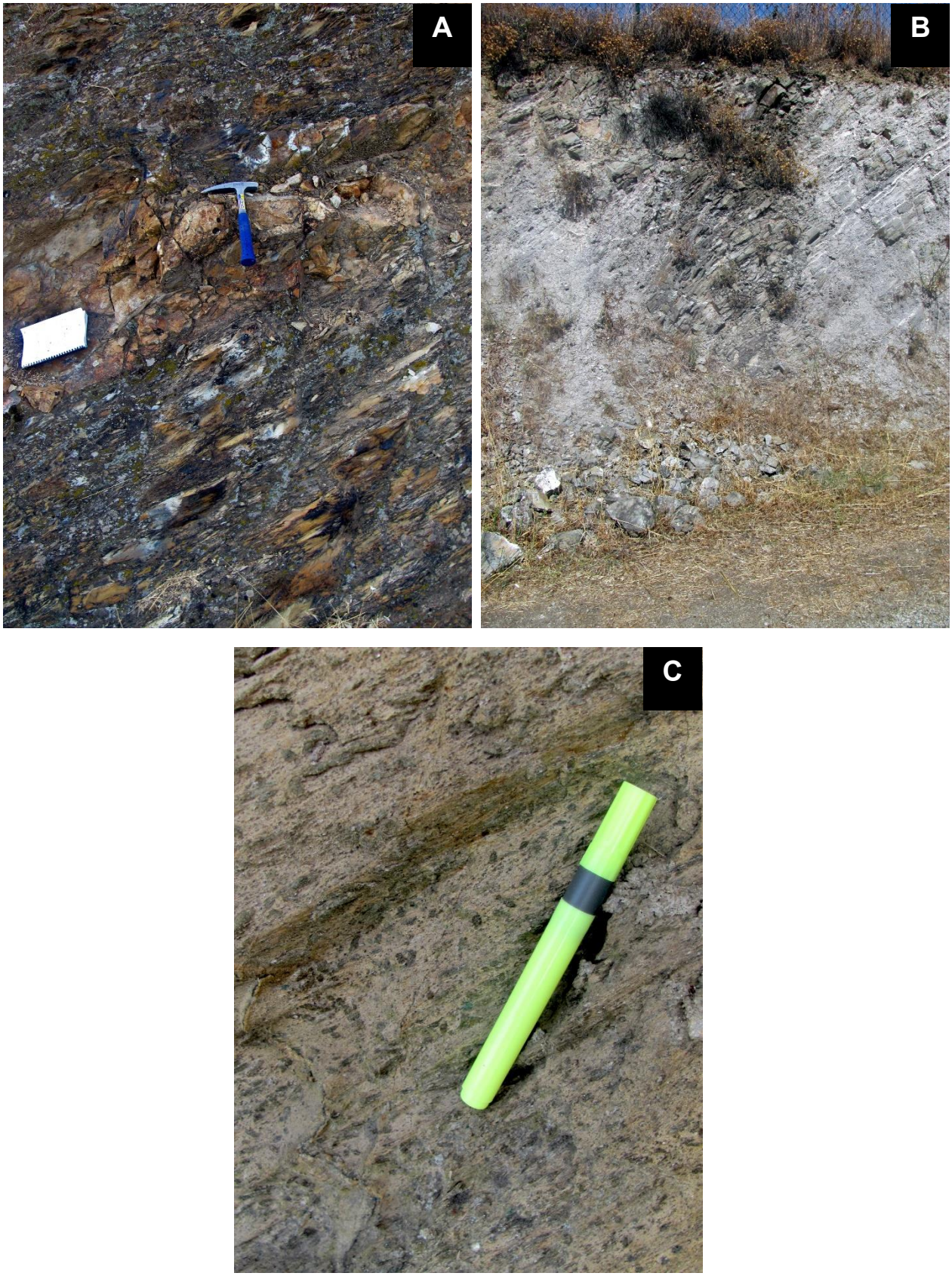

Figure 2.6 – Lithological description: A – quartzphyllites; B – deformation of metasediments close to the Huebra shear zone; C – phyllites with andalusite porphyroblasts.

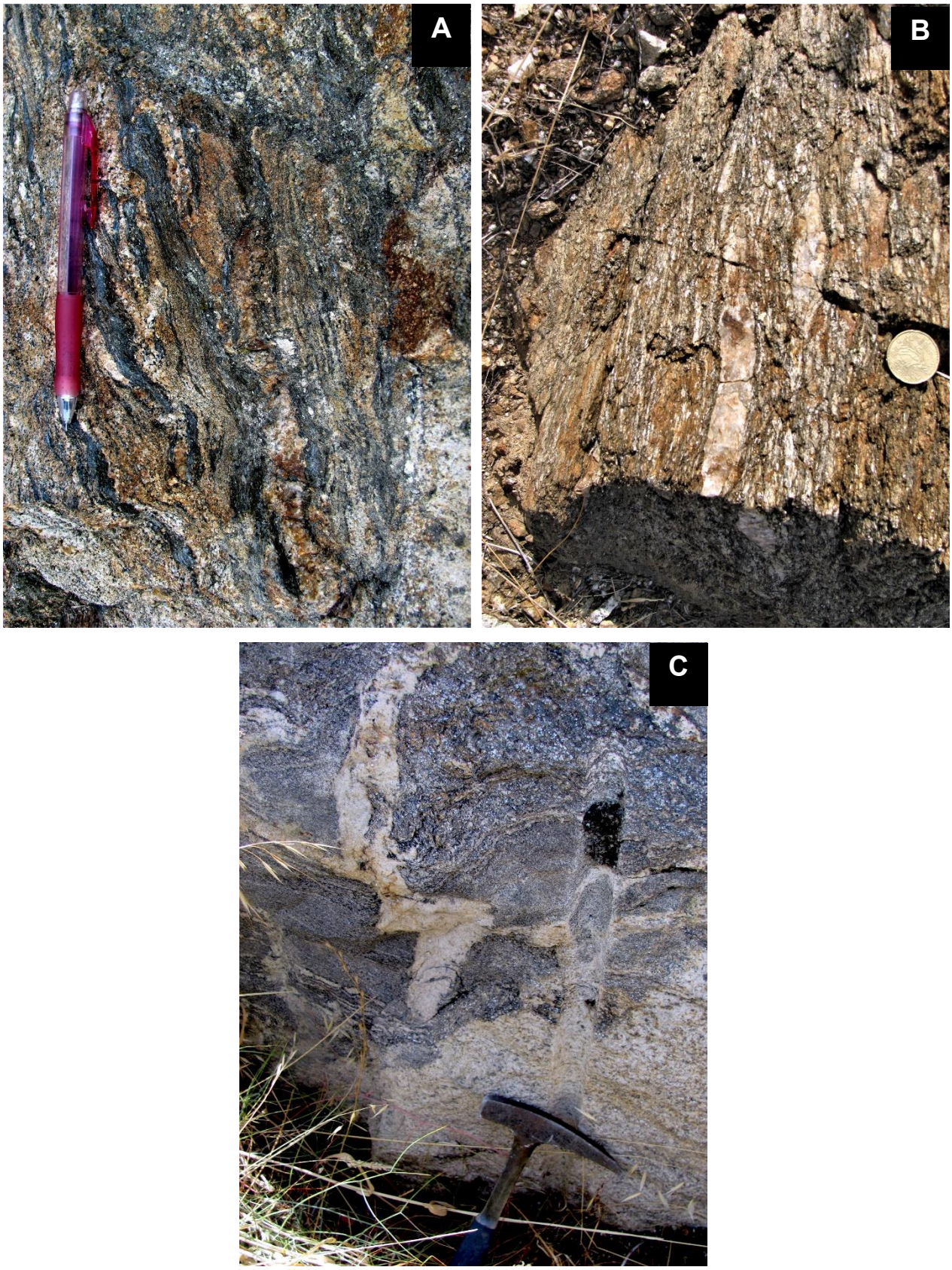

Figure 2.7 – Lithological description: A – metatexite with bands of peritectic sillimanite associated with muscovite; B – metatexite with boudinated leucosome veins; C – leucosome pocket associated to metatexite.

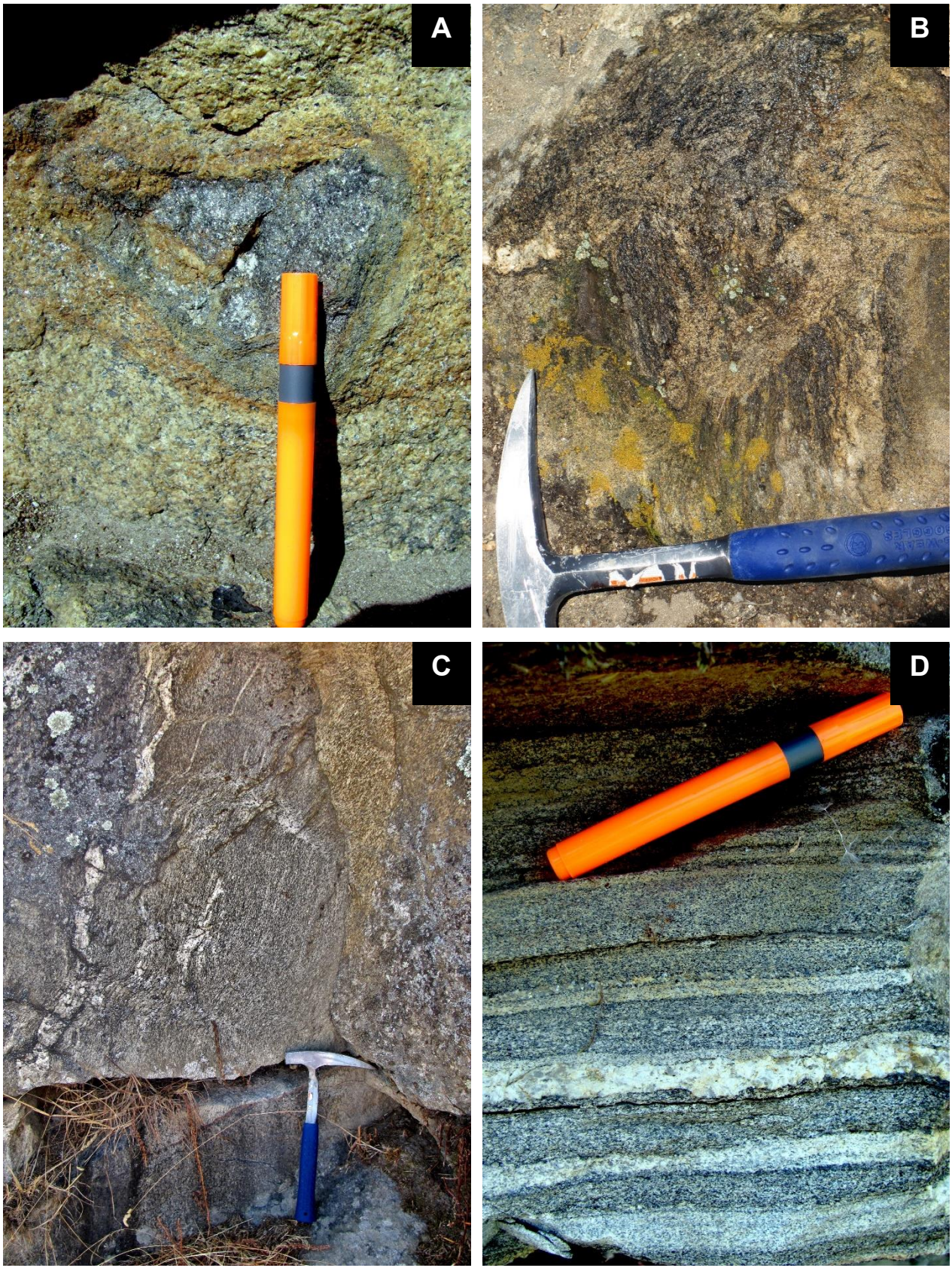

Figure 2.8 – Lithological description: A – restitic nodule in diatexite; B – schlieren structures in diatexite; C – deformation planes (ductile deformation) in diatexite; D – nebulitic texture in diatexite.

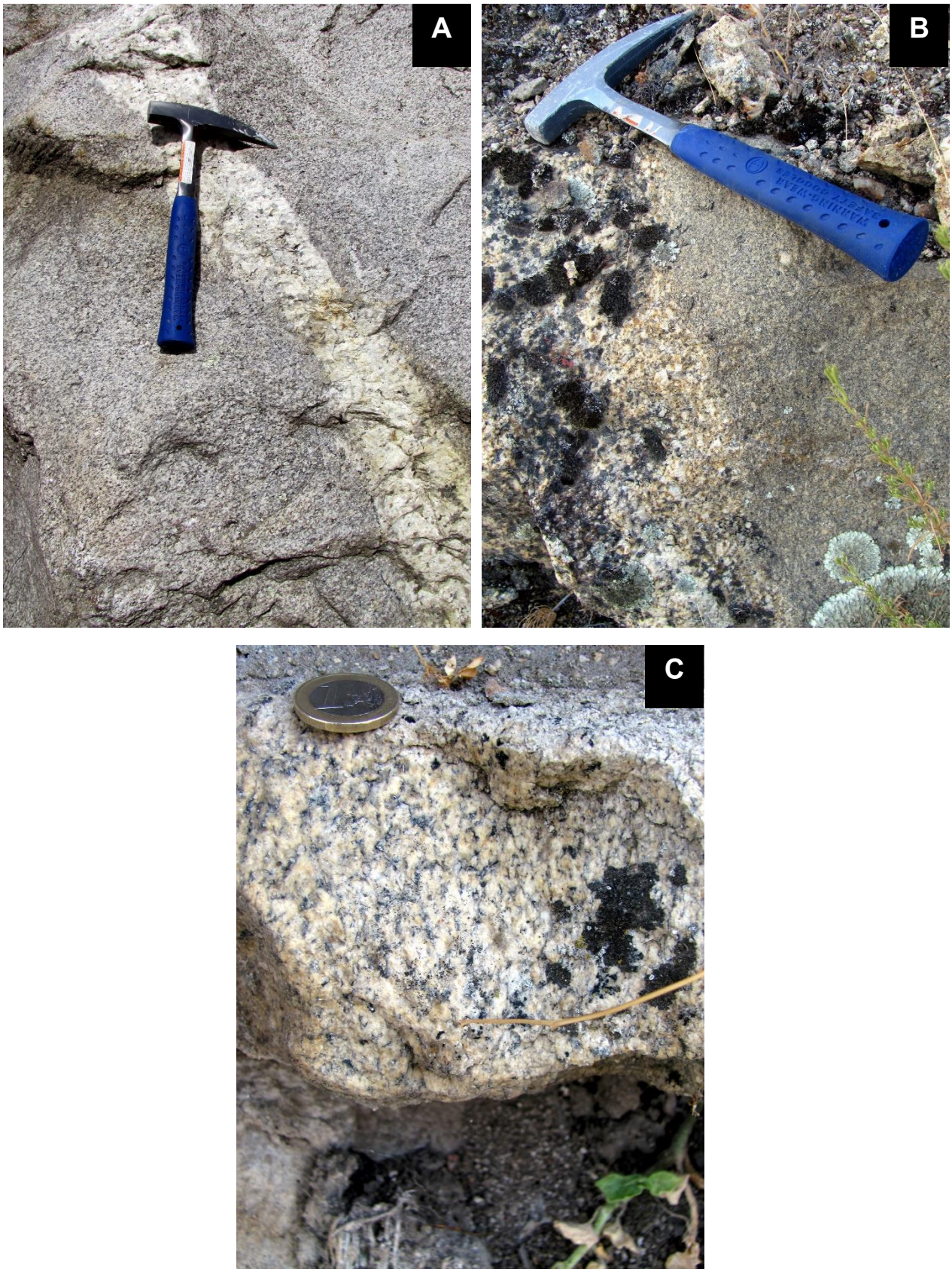

Figure 2.9 – Lithological description: A and B – two-mica granites with variable grain size; C – Evidence of deformation in granite.

CHAPTER 3. SAMPLING AND SAMPLE PREPARATION

3.1. SAMPLING

The study area is localized mainly in the Guarda district (Pinhel, Figueira de Castelo Rodrigo and Vila Nova de Foz Côa municipalities) and south of the district of Bragança (Freixo de Espada à Cinta municipality). The anatectic complex in study is mapped in the following geological maps of Portugal at 1:50 000 scale, edited by Serviços Geológicos de Portugal, Instituto Geológico e Mineiro and Laboratório Nacional de Energia e Geologia: 15-A (Vila Nova de Foz de Côa), 15-B (Freixo de Espada à Cinta), 15-C (Pinhel, not published) and 15-D (Figueira de Castelo Rodrigo).

Sampling and field recognition were supported by the geological map of the Vale do Côa Archaeological Park at 1:80 000 scale (Figure 3.1) and unpublished mapping done by T. Bento dos Santos during 2011-2014. A total of 80 samples were collected for all following methodologies (Appendix A).

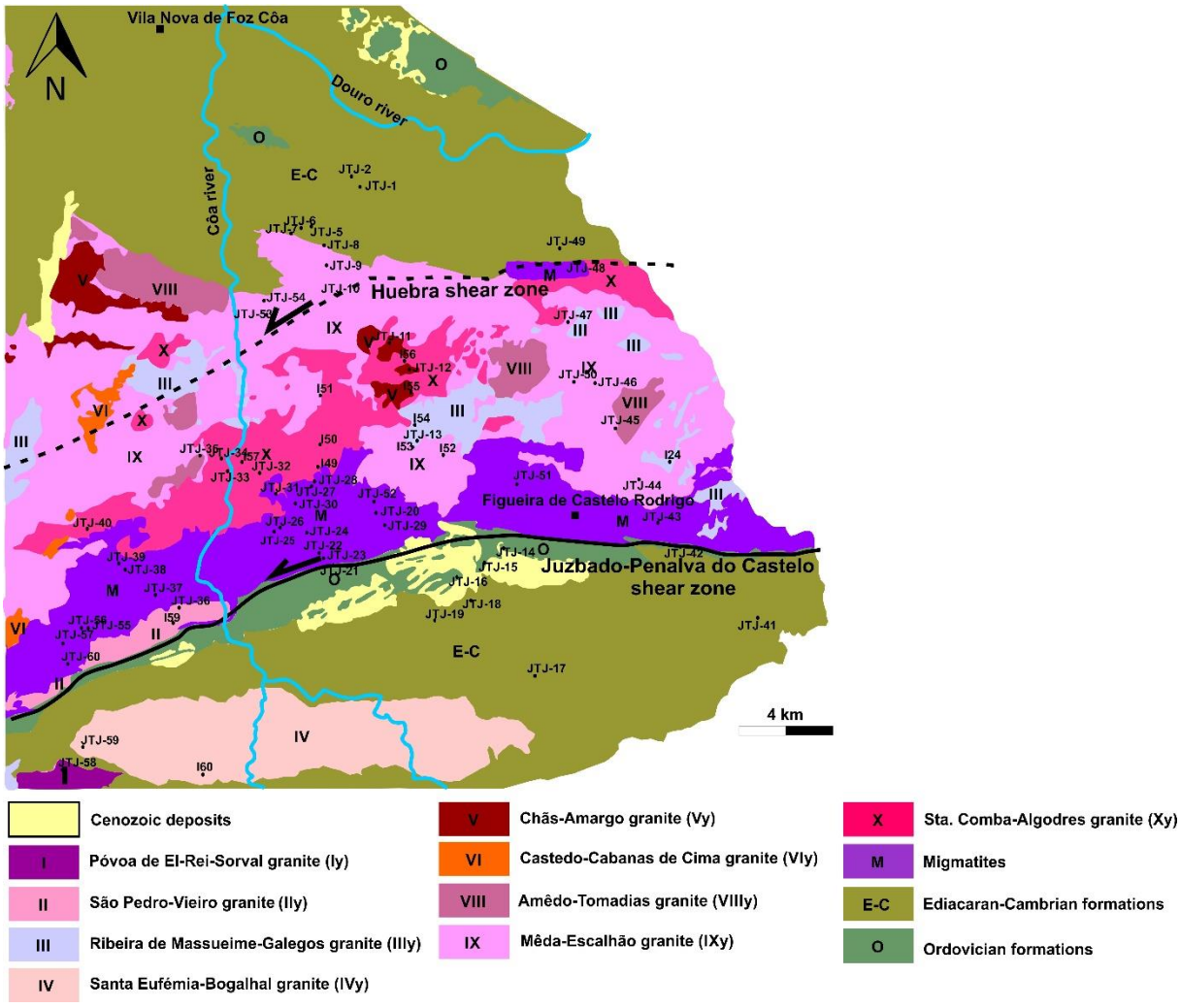

Figure 3.1 – Simplified geological map adapted from Silva and Ribeiro (2000) with the sample distribution.

3.2. SAMPLE PREPARATION

From the 80 collected samples, all of them were processed for petrographic characterization, 55 samples for whole-rock geochemistry, 15 samples for Sr-Nd-Hf-Pb whole-rock isotope geochemistry and 20 samples for U-Pb geochronological analyses (Appendix A). Rock processing took place in the laboratories of DG-FCUL – Department of Geology, Faculty of Sciences, University of Lisbon, involving the following steps for different purposes (Figure 3.2):

- ✓ All rock samples were sawed to take off the weathered parts and to reduce the sample size for milling and to perform 82 thin sections for petrographic characterisation.

- ✓ The selected samples, for whole-rock and isotopic geochemistry analysis, were crushed in the jaw crusher to reduce their size, and then milled in the agate mill to reduce the samples to powder;

- ✓ For U-Pb geochronology analyses, it was necessary to obtain zircon and apatite concentrates which involved four mineral separation techniques: dry sieving, density separation, magnetic separation and picking/grain selection.

    - After crushing and milling, the rock samples were sieved in a vibrating sieve machine using the following sieves column: 63 – 125 – 250 – 425 μm. From the sieved samples it was chosen the 63 – 250 μm fractions, because zircons tend to concentrate between these dimensions. The fractions were washed and dried in the oven at 30 ºC;

    - Since zircon and apatite are heavy minerals with 4.6 - 4.7 g/cm^3 and 3.1 - 3.2 g/cm^3 of density, respectively, it was necessary to apply a density separation technique. In this separation was used bromoform, a heavy liquid with 2.89 g/cm^3 density, to separate relatively lighter and heavier minerals on a funnel;

    - The heavy minerals previously concentrated were submitted to the magnetic separation using the Frantz Isodynamic Separator that separates minerals according to their magnetic susceptibility, dividing them in magnetic and non-magnetic minerals. Zircon and apatite are non-magnetic minerals, so the

magnetic separation allowed to separate them from the heavy magnetic minerals. The equipment was set up with a slope of 20º, a tilt of -10º, and each sample was run at 0.5, 1 and 1.5 A, always retaining the magnetic fraction;

- All the accessory mineral separation techniques described before were important to obtain a refined mineral concentrate, to facilitate grain selection. The grain selection was made by hand picking using a binocular magnifier. For each sample it was selected around 120 grains based on their purity and crystal integrity.

It is important to mention that the methodology inherent to each analytical method is described in detail in the respective chapter: whole-rock and isotopic (Sr, Nd, Hf and Pb) geochemistry in chapter 7 and U-Pb geochronology in chapters 5 and 6.

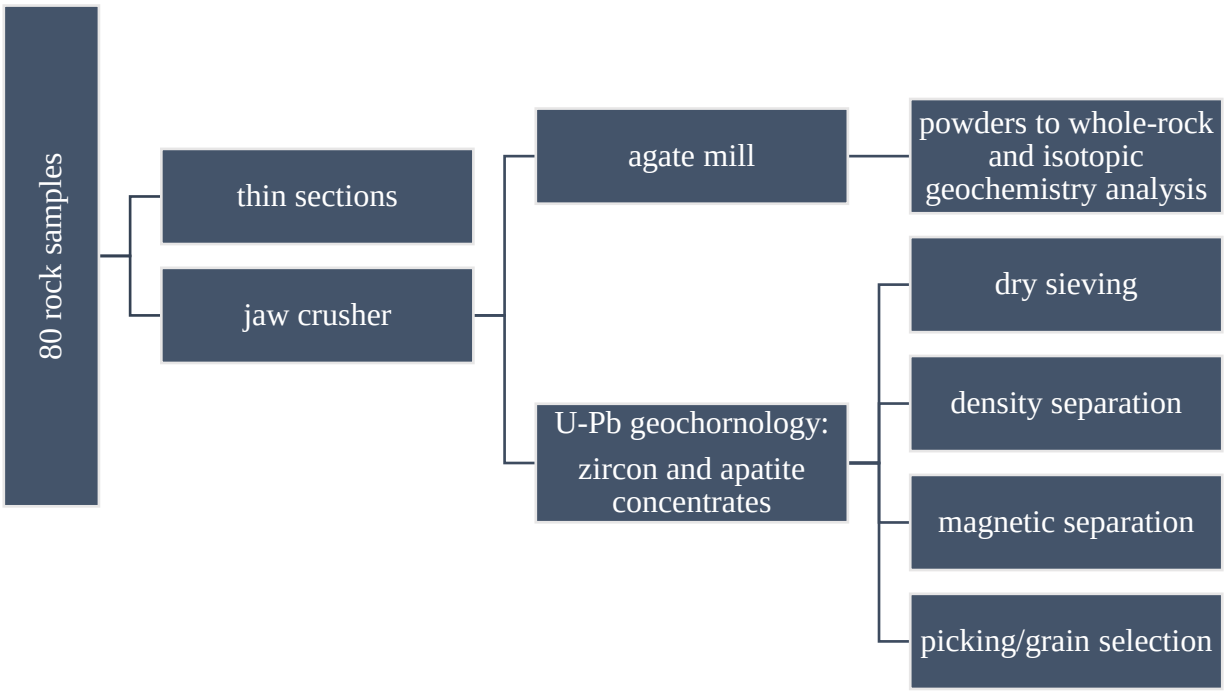

Figure 3.2 – Schematics for the sample preparation procedures.

CHAPTER 4. PETROGRAPHIC CHARACTERIZATION

The petrographic analysis was based on the observation of 82 thin sections of the low-grade metamorphic rocks (phyllites, quartzphyllites, and quartzites) and from the anatectic complex (metatexites, individual leucosomes, diatexites, and granites).

4.1. LOW-GRADE METAMORPHIC ROCKS

4.1.1. Phyllites and Quartzphyllites

The majority of the phyllites and quartzphyllites exhibit a granolepidoblastic texture (Figure 4.1C) with lepidogranoblastic tendency in some samples, and a few samples show a mylonitic texture. The phyllites are fine-grained, while the quartzphyllites are medium grain size. Regarding the structural features, the foliation of these lithologies is defined by the micas alignment (biotite and muscovite) and it is essentially spaced, sometimes appearing crenulated (Figure 4.1B) and anastomosed (Figure 4.1A). In some samples, the foliation is continuous. Sometimes, the structure is crossed by veins composed of quartz and feldspar which occasionally are folded. The main mineral assemblage observed in these metasediments is quartz + biotite + muscovite ± plagioclase ± chlorite. The present accessory phases are titanite, zircon, apatite, staurolite, and opaque minerals.

Looking to the mineral's features, quartz is predominantly subhedral, but when the samples reveal some deformation, it appears with a sigmoidal shape. The undulose extinction is frequent in quartz. Locally, it is observed dynamic recrystallization (e.g. bulging).

Biotite is mainly subhedral with common inclusions of quartz and, rarely, apatite. The biotite chloritization is frequent in these lithologies. Moreover, in some samples, biotite has tendency to occur oriented. Muscovite is also subhedral and it is relevant in the definition of the crenulated foliation in the samples where this type of foliation appears. When muscovite appears deformed, it exhibits mica-fish shapes.

Sometimes, it is also visible porphyroblasts of chlorite surrounded by the foliation. Another rare aspect is the occurrence of pseudomorphs of andalusite filled by quartz and muscovite (Figure 4.1D).

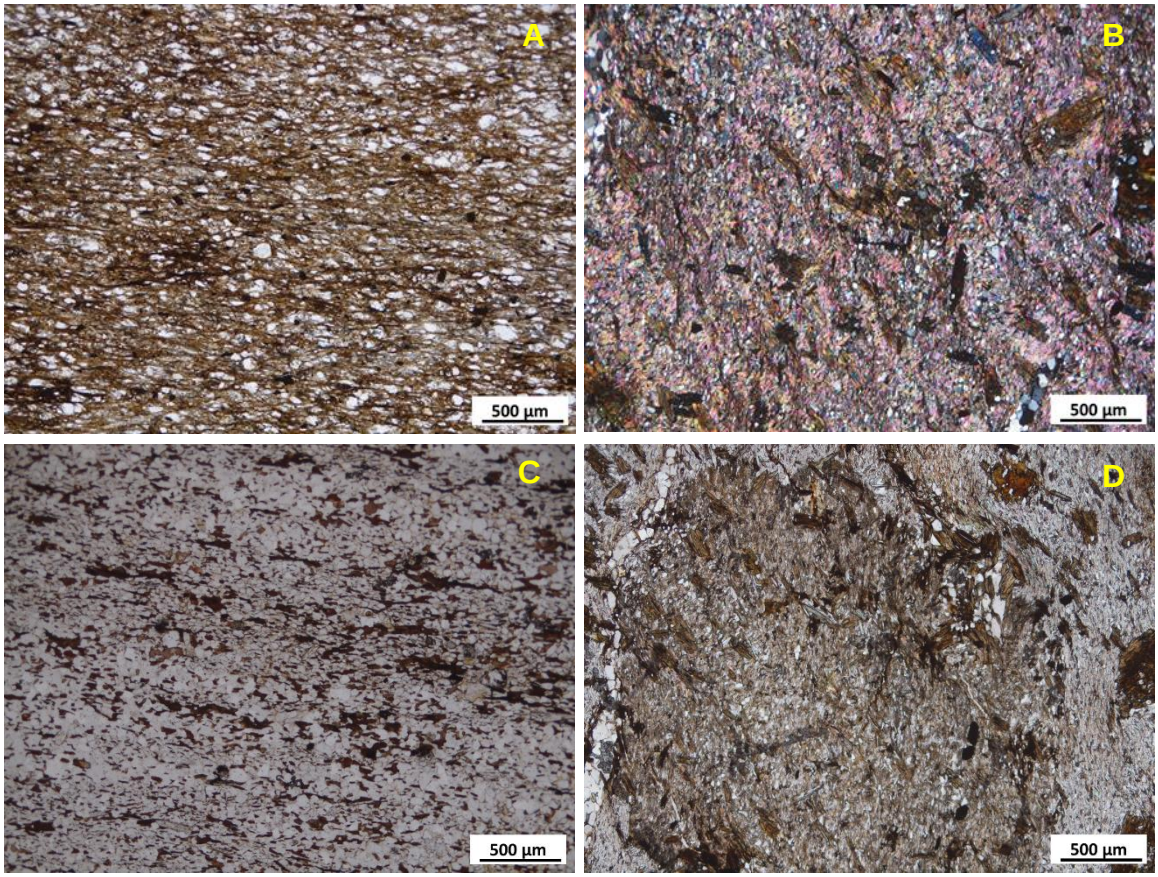

Figure 4.1 – Phyllites petrographic features: A – lepidogranoblastic texture with anastomosing cleavage foliation (N//); B – lepidogranoblastic texture with crenulation cleavage foliation (NX); C – granolepidoblastic texture (N//); D – andalusite pseudomorph (N//).

4.1.2. Quartzites

Most of the quartzites have a granoblastic and isogranular texture with medium grain-size. The grains of quartz are subhedral with irregular and sutured borders. The deformation is visible in the quartz grains through frequent undulose extinction and, less frequently, subgranulation. The dynamic recrystallization of quartz (e.g. bulging and grain boundary migration) is common in the quartzites (Figure 4.2A).

Sometimes, fine lamellar crystals of muscovite occur subordinated by the quartz grains limits, but they appear oriented (Figure 4.2B). Occasionally, it is also visible biotite and sericitized plagioclase. So, the mineral assemblage is essentially composed by quartz ± muscovite ± plagioclase ± biotite. The accessory minerals present in the quartzites are titanite, tourmaline, zircon, apatite, and opaque minerals.

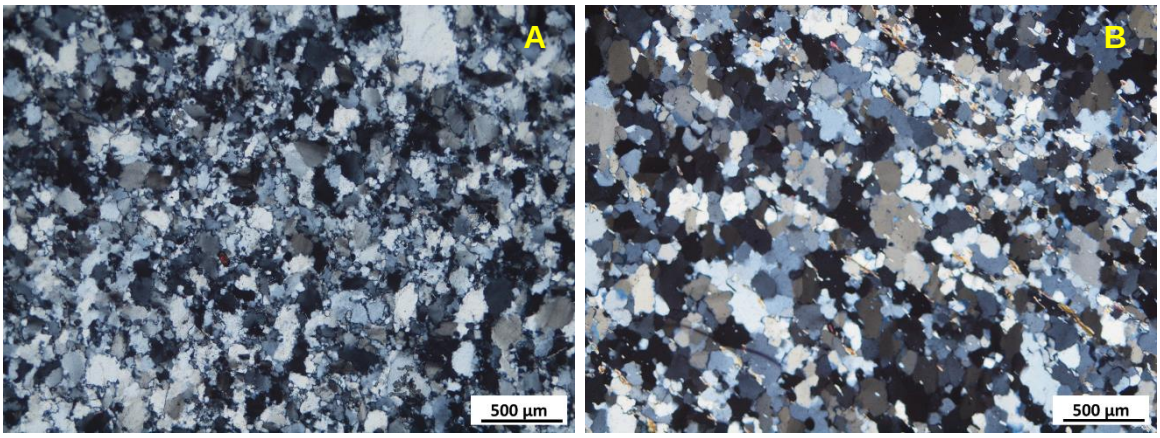

Figure 4.2 – Quartzite petrographic features: A – granoblastic texture with evidences of intense dynamic recrystallization (N//); B – Muscovite alignments (N//).

4.2. FCR-LAC LITHOLOGIES

4.2.1. Metatexites

The metatexites have a granolepidoblastic texture with medium to coarse grain-size. The paleosome of the metatexites is predominantly composed of biotite, muscovite and, at times, chlorite, preserving the anisotropic features of the country rocks (phyllites). In contrast, the neosome present in the metatexites has a quartz-feldspar dominant mineralogy (Figure 4.3A). The metatexites mineral assemblage is defined by quartz + plagioclase + K-feldspar + biotite + secondary muscovite ± fibrolitic sillimanite. The present accessory minerals are zircon, apatite, tourmaline, staurolite, and opaque minerals.

Quartz is subhedral where the undulose extinction and dynamic recrystallization aspects are regularly visible. When quartz is included in other minerals like feldspars, it assumes a droplet shape. Veinlets and lenses of cataclastic quartz appear in a few samples. Plagioclase and K-feldspar are subhedral and, sometimes, both minerals show a slight sericitization. K-feldspar grains show perthites, besides inclusions of quartz, muscovite, biotite and fibrolitic sillimanite. Plagioclase shows inclusions of quartz, biotite, and muscovite.

Biotite is subhedral and is aligned with the foliation or perpendicular to the structure. Sometimes, biotite occurs intergrown with muscovite grains and as porphyroblasts resulting from retrogression (Figure 4.3B). Chloritization and muscovitization affect biotite in some samples. Biotite also presents inclusions of quartz, muscovite, zircon, apatite, rutile needles, and opaque minerals. From time to time, biotite reveals some deformational features, like cleavage bending.

Muscovite has a typical subhedral form and it is common to appear slightly sericitized. Occasionally, it is observed muscovite in optical continuity with biotite. Moreover, muscovite reveals secondary character because it is observed as symplectic borders and, rarely, relics of biotite in the muscovite cleavages in optical continuity with it. Some aspects of deformation are noticeable in the muscovite crystals, like the cleavages bending and, less commonly, kink-like structures (only around cataclastic zones). Muscovite has common inclusions of fibrolitic sillimanite (several times as aggregates; Figure 4.3C), zircon, and quartz. Related with the relation blastesis-deformation, it was observed in a sample of metatexite an aspect of mimetic blastesis which is characterized by the static recrystallization of biotite on a previous folded foliation (Figure 4.3D).

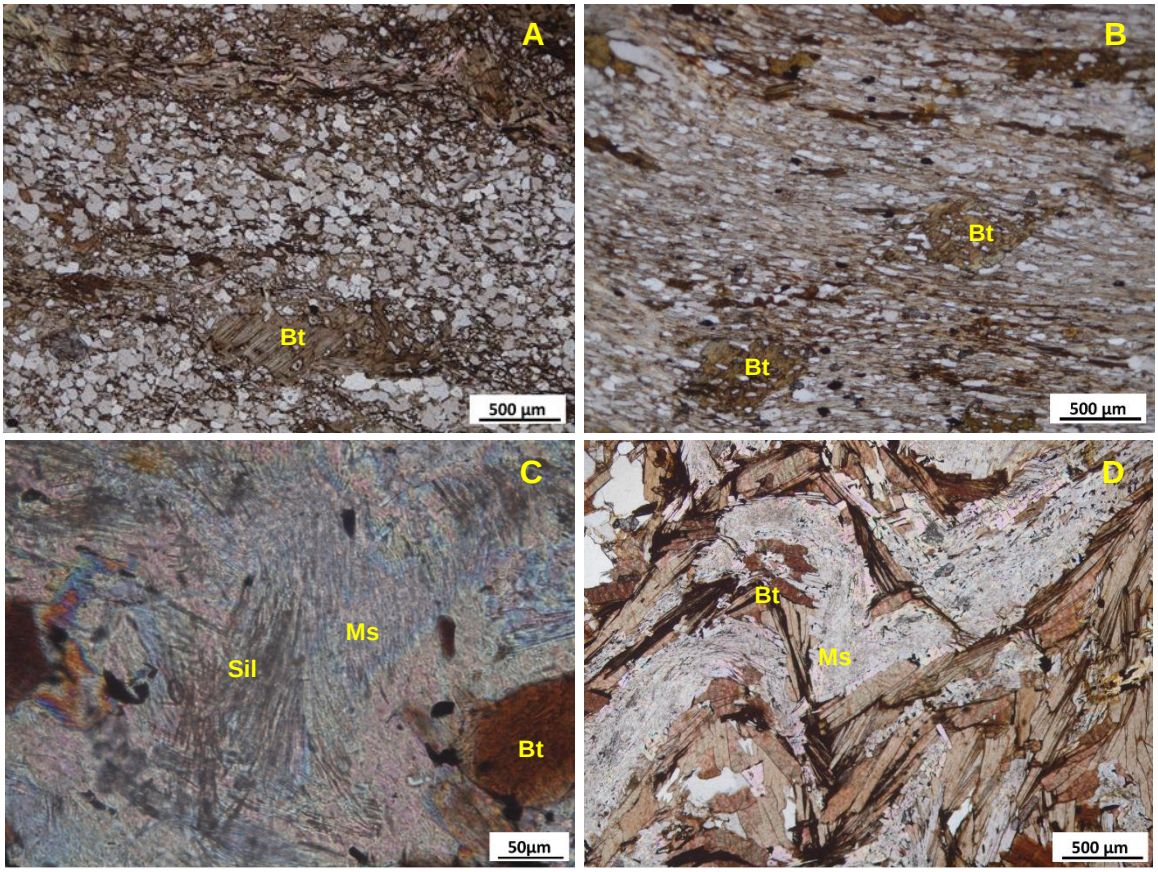

Figure 4.3 – Metatexite petrographic features: A – granolepidoblastic texture (N//); B – Biotite porphyroblasts with poikiloblastic texture (N//); C – Sillimanite aggregates included in muscovite (N//); D – Mimetic blastesis of biotite (N//). Bt – biotite; Ms – muscovite; Sil – sillimanite.

4.2.2. Individual Leucosomes

Leucosomes have a granoblastic texture (Figure 4.4A) with coarse grain-size. The leucosome mineral assemblage (Figure 4.4B) is quartz + plagioclase + muscovite ± K-feldspar. Tourmaline appears as an accessory mineral.

In general, quartz is subhedral and it reveals some aspects related with deformation like undulose extinction and subgranulation. It is also visible dynamic recrystallization evidences in quartz. The subhedral plagioclase and K-feldspar occurs frequently muscovitized and slightly sericitized. Sometimes, plagioclase has quartz inclusions and exhibits undulose extinction. Large subhedral crystals of muscovite appear with symplectic borders, slightly sericitized, and with quartz inclusions. Fine-grained muscovite grew in the limits of the large crystals of muscovite.

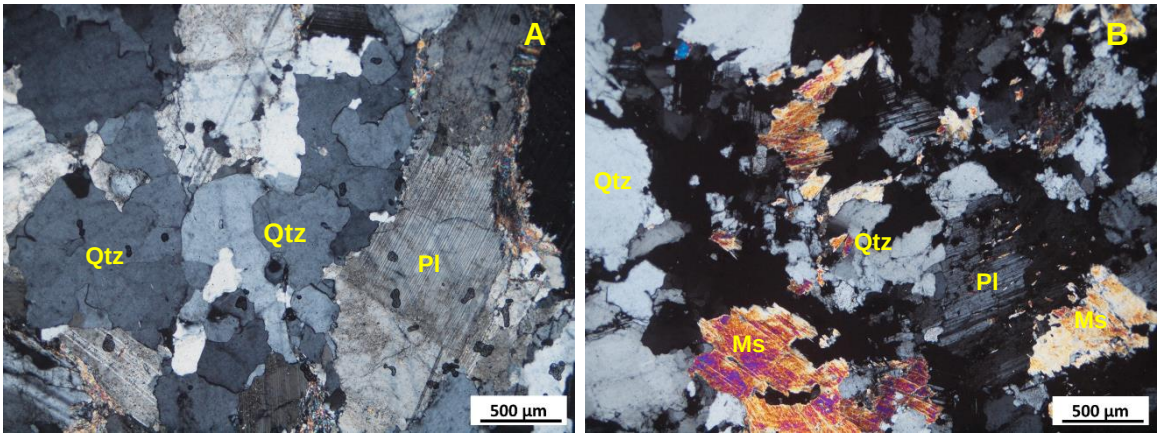

Figure 4.4 – Leucosome petrographic features: A – granoblastic texture with some dynamic recrystallization of quartz (NX); B – quartz, muscovite and plagioclase association (NX). Qtz – quartz; Pl – plagioclase; Ms – muscovite.

4.2.3. Diatexites

The diatexites texture range from granoblastic (Figure 4.5A) to granolepidoblastic, with coarse and medium grain-size. The granolepidoblastic texture is mainly present in the nebulitic diatexites and in the samples that show a transition from metatexite do diatexite. In general, the diatexites mineral assemblage (Figure 4.5A and 4.5B) is defined by quartz + plagioclase + K-feldspar + biotite + secondary muscovite ± fibrolitic sillimanite. Although the proportion of plagioclase and K-feldspar is different between samples. The accessory minerals present in diatexites are zircon, apatite, tourmaline, retrograde staurolite, and opaque minerals.

Quartz is mainly subhedral and it shows some deformation evidences such as undulose extinction and subgranulation. The dynamic recrystallization of quartz is also present (e.g. bulging and grain boundary migration), sometimes in the grain limits between quartz and K-feldspar. Quartz has inclusions of rutile needles, muscovite and fibrolitic sillimanite.

Plagioclase is subhedral and it occurs with alteration aspects like muscovitization and slightly sericitized (Figure 4.5B). Occasionally, plagioclase shows undulose extinction. The plagioclase inclusions are essentially quartz and muscovite, and, rarely, tourmaline. K-feldspar have some aspects similar to plagioclase like the subhedral form and the alteration aspects (sericitization

and muscovitization). At times, it is visible albitization and microclinization on the borders of the K-feldspars grains. The frequency of perthite veinlets in the K-feldspar and the occurrence of myrmekites are variable in the different diatexite samples. K-feldspar shows inclusions of quartz, muscovite and biotite.

Muscovite is mostly subhedral, it assumes a euhedral form when included in feldspars. In some samples, muscovite defines an alignment. Muscovite grains normally appear associated to quartz and feldspar and slightly sericitized. The secondary character of muscovite is defined by the occurrence of symplectic borders, relics of biotite in optical continuity (Figure 4.5C). Muscovite has inclusions of quartz, fibrolitic sillimanite (Figure 4.5D), zircon, apatite, biotite, and opaque minerals.

Biotite is subhedral, sometimes occurring with corroded borders. Chloritization and muscovitization of biotite are observed (Figure 4.5A). Biotite is much more common than muscovite in the nebulitic diatexites. This mica shows inclusions of quartz, zircon, apatite, rutile needles when chloritized, and opaque minerals.

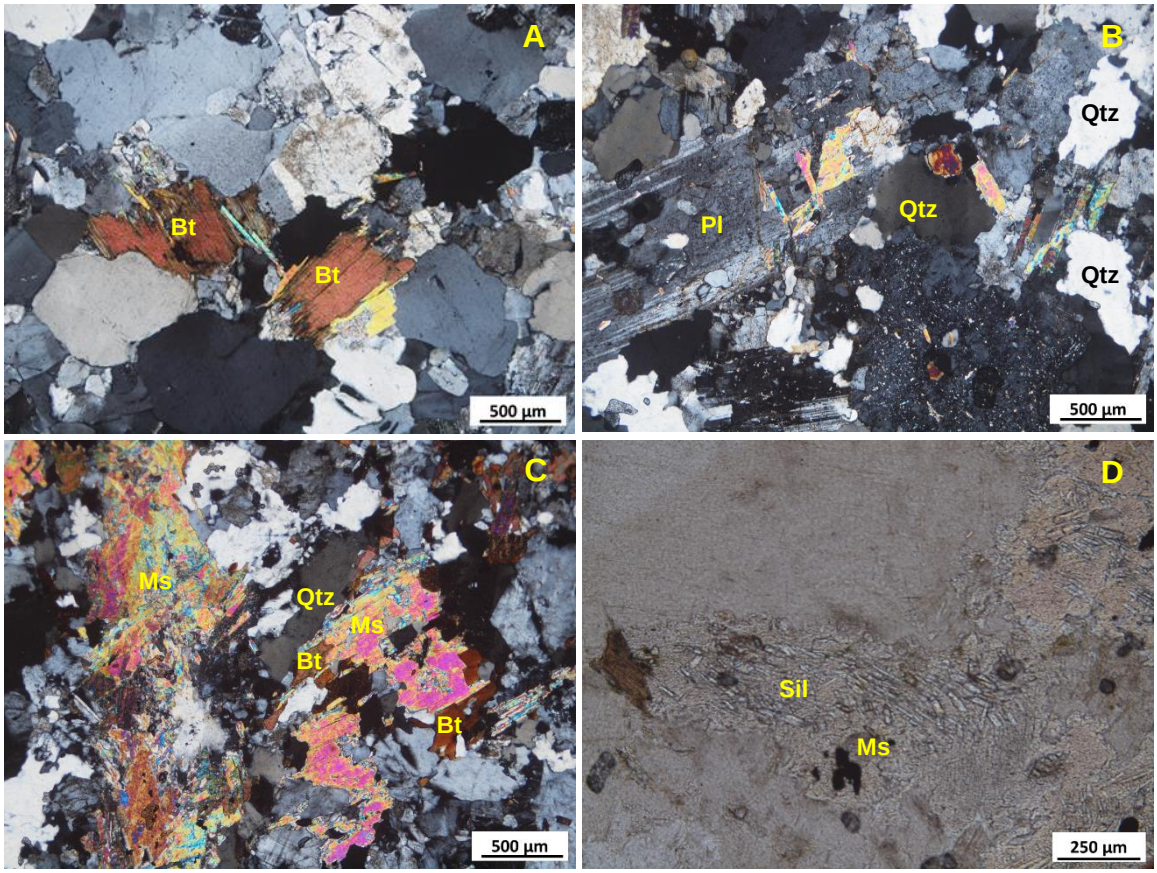

Figure 4.5 – Diatexites petrographic features: A – granoblastic texture and evidences of biotite muscovitization (NX); B – quartz and plagioclase association with the sericitization and muscovitization of plagioclase (NX); C – Muscovite secondary character (NX); D – Sillimanite inclusions on muscovite (N//). Qtz – quartz; Pl – plagioclase; Bt – biotite; Ms – muscovite; Sil – sillimanite.

4.2.4. Sta. Comba-Algodres granite (Xγ)

The Sta. Comba-Algodres granite has an inequigranular texture (Figure 4.6A) with medium to coarse grain-size. The mineral assemblage (Figure 4.6A) of this granite is quartz + plagioclase + microcline + biotite + muscovite ± orthoclase ± fibrolitic sillimanite. The accessory minerals are zircon, apatite, rutile needles, and opaque minerals.

Quartz is subhedral with evidences of deformation, such as undulose extinction, subgranulation, and dynamic recrystallization (e.g. bulging and grain boundary migration). In general, the feldspars are subhedral, exhibit muscovitization and sericitization, and, sometimes, they have inclusions of biotite, muscovite, and quartz. The K-feldspars show perthitic veinlets. Orthoclase endured some albitization (Figure 4.6B) and intensive microclinization.

The subhedral biotite most of the times is chloritized, and, it endured muscovitization. Biotite shows inclusions of zircon, apatite, and rutile needles when chloritized. Occasionally, biotite and muscovite occur together as aggregates.

Muscovite is mainly subhedral exhibiting symplectic borders and a slight sericitization. This mineral occurs frequently associated to quartz and feldspar and seems that muscovite grew conditioned by these minerals. Muscovite has inclusions of fibrolitic sillimanite, zircon, and quartz.

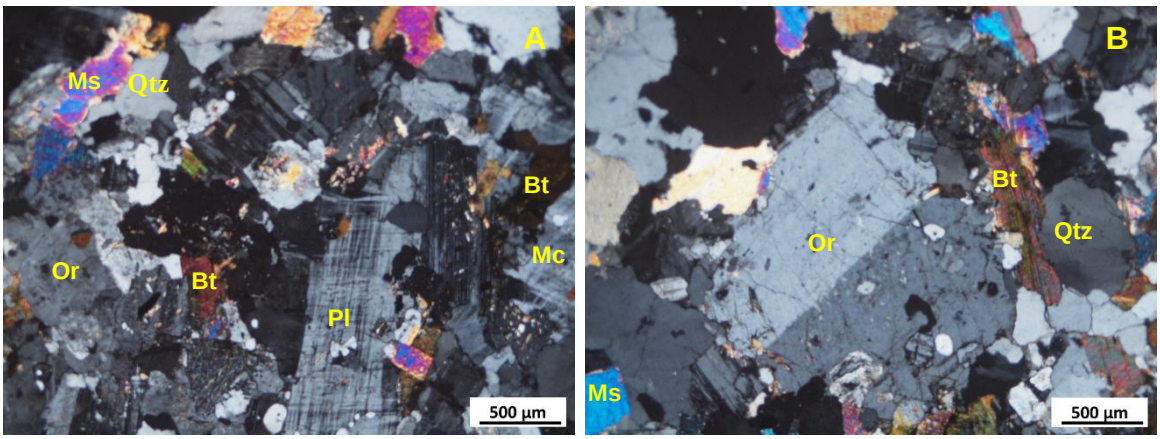

Figure 4.6 – Granite Xγ petrographic features: A – inequigranular texture and general mineral assemblage aspect (NX); B –. orthoclase crystal (NX). Qtz – quartz; Pl – plagioclase; Bt – biotite; Ms – muscovite; Or – Orthoclase; Mc – microcline.

4.2.5. Mêda-Escalhão granite (IXγ)

The Mêda-Escalhão granite has an inequigranular texture with medium grain-size. The mineral assemblage of the IXγ granite is quartz + plagioclase + K-feldspar + biotite + muscovite ± fibrolitic sillimanite. The accessory minerals are zircon, apatite, rutile needles, and opaque minerals.

Quartz varies between subhedral and anhedral shape. The undulose extinction, subgranulation, and dynamic recrystallization (Figure 4.7A) are present in quartz grains.

Feldspars are subhedral with a slight sericitization and muscovitization. Sporadically, orthoclase grains show albitization and microclinization evidences. K-feldspars exhibit also perthite veinlets. Feldspars have inclusions of quartz and muscovite.

The subhedral biotite is often chloritized and, occasionally, shows some muscovitization. Biotite occur associated to muscovite and some grains appear corroded. This mica has inclusions of zircon, apatite, rutile needles, quartz, and opaque minerals. Muscovite is subhedral, sometimes appear with symplectic borders. Occasionally, muscovite exhibit relics of biotite in optical continuity. In few samples, muscovite occurs between the crystal boundaries and conditioned by them. The muscovite inclusions are zircon, apatite, fibrolitic sillimanite (less frequent; Figure 4.7B) and quartz.

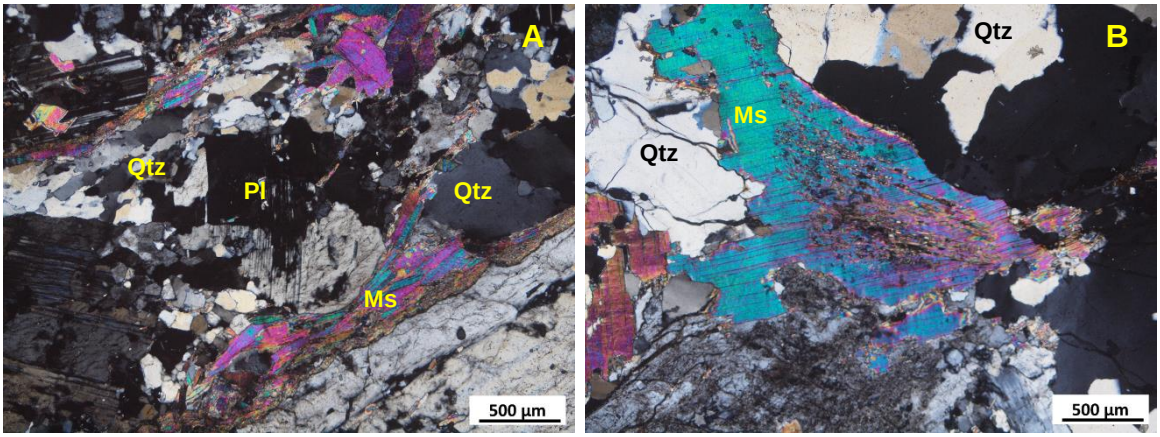

Figure 4.7 – Granite IXγ petrographic features: A: Inequigranular texture, deformation aspect of muscovite and dynamic recrystallization of quartz (NX); B – Secondary muscovite with inclusions of fibrolitic sillimanite (NX). Qtz -quartz; Pl – plagioclase; Ms – muscovite.

4.2.6. Amêdo-Tomadias granite (VIIIγ)

The Amêdo-Tomadias granite has an inequigranular texture (Figure 4.8A) with medium grain-size. The mineral assemblage of this granite is quartz + plagioclase + orthoclase + microcline + biotite + muscovite ± chlorite. The accessory minerals are zircon, apatite, and opaque minerals.

Quartz varies between subhedral and anhedral shape and exhibits some dynamic recrystallization and subgranulation. Rutile needles occur as inclusions in quartz.

Orthoclase appears with perthite veinlets, slightly sericitized and microclinized, and with inclusions of quartz, muscovite, and biotite. Occasionally, orthoclase occurs as a megacrystal.

Microcline is subhedral, slightly sericitized and, sometimes, with quartz inclusions. Plagioclase is subhedral and occurs sericitized. Myrmekites are also present in these granites (Figure 4.8B). Biotite is occasionally subhedral, exhibits corroded borders, and inclusions of zircon and apatite. Subhedral muscovite occurs with symplectic borders, and enclosed zircon, apatite and quartz. Rarely, chlorite occurs with rutile needles inclusions.

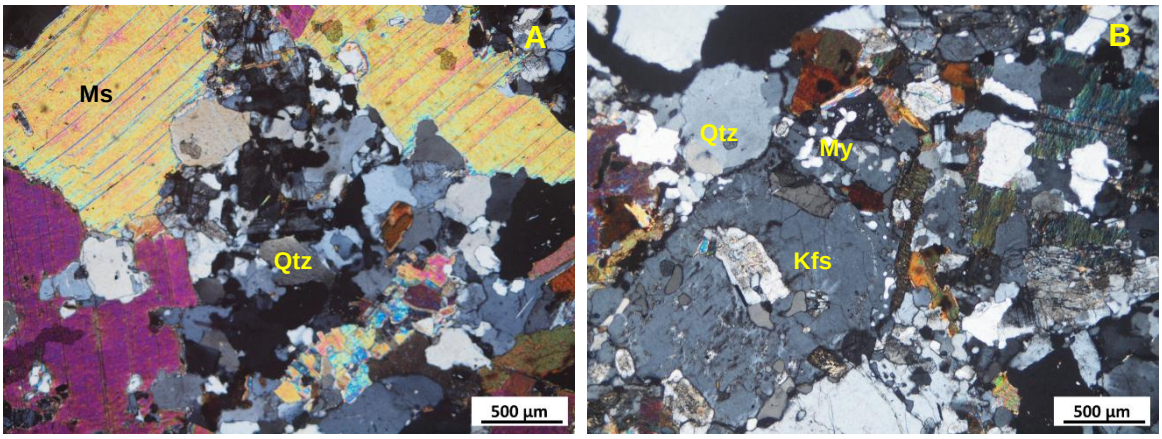

Figure 4.8 – Granite VIIIγ petrographic features: A – Inequigranular texture with large crystals of muscovite (NX); B – occurrence of myrmekites and dynamic recrystallization of quartz (NX). Qtz -quartz; Ms – muscovite; Bt – biotite; Kfs – K-feldspar; My – Myrmequite.

4.2.7. Chãs-Amargo granite (Vγ)

The Chãs-Amargo granite has an inequigranular texture with fine to coarse grain-size. In general, this granite reveals less deformation aspects than the granite facies described before. The mineral assemblage of Vγ granite is quartz + plagioclase + K-feldspar ± chlorite ± fibrolitic sillimanite. The present accessory minerals are zircon, apatite, and opaque minerals.

Quartz is subhedral with visible undulose extinction and some dynamic recrystallization. The feldspars are subhedral, frequently muscovitized and slightly sericitized. K-feldspar is sporadically albitized and microclinized. The feldspars sometimes have inclusions of anhedral quartz.

Biotite is subhedral with frequent inclusions of zircon, apatite and some opaque minerals. Muscovitization and chloritization of biotite (Figure 4.9A) is also visible. Muscovite is subhedral, sometimes with symplectic borders. It has inclusions of quartz, apatite, and fibrolitic sillimanite (Figure 4.9B).

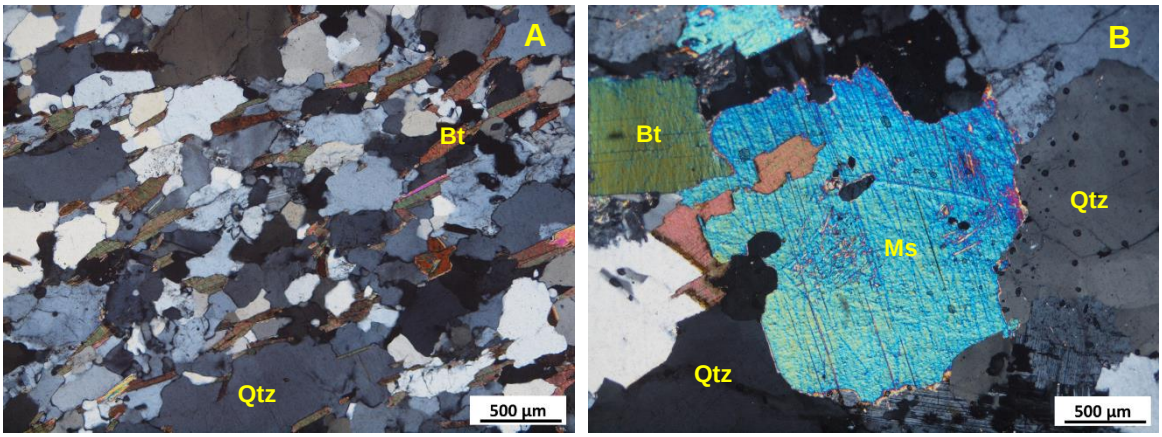

Figure 4.9 – Granite Vγ petrographic features: A – inequigranular texture, biotite alignment, and muscovitization and chloritization of biotite (NX); B – muscovite with inclusions of fibrolitic sillimanite (NX). Qtz -quartz; Ms – muscovite; Bt – biotite.

4.2.8. Santa Eufémia-Bogalhal granite (IVγ)

The Santa Eufémia-Bogalhal granite has an inequigranular texture (Figure 4.10A) with medium grain-size. The mineral assemblage of this granite is quartz + plagioclase + K-feldspar + biotite + muscovite. The accessory minerals are zircon, apatite, and opaque minerals.

Quartz is subhedral with visible undulose extinction and dynamic recrystallization too. Orthoclase is subhedral and its dimension varies from large to medium size crystals. This K-feldspar occurs with some inclusions of quartz and muscovite. Perthite veinlets are observed in orthoclase. Sometimes, orthoclase and microcline occur as aggregates. Plagioclase is subhedral, sometimes slightly sericitized (Figure 4.10A) and muscovitized.

Biotite is subhedral showing a slight chloritization and muscovitization in some grains. Apatite, zircon and opaque minerals appear as biotite inclusions. Subhedral muscovite reveals some symplectic borders, sometimes with relics of biotite in optical continuity (Figure 4.10B). At times, biotite and muscovite exhibit incipient deformation trough the occurrence of bent crystals.

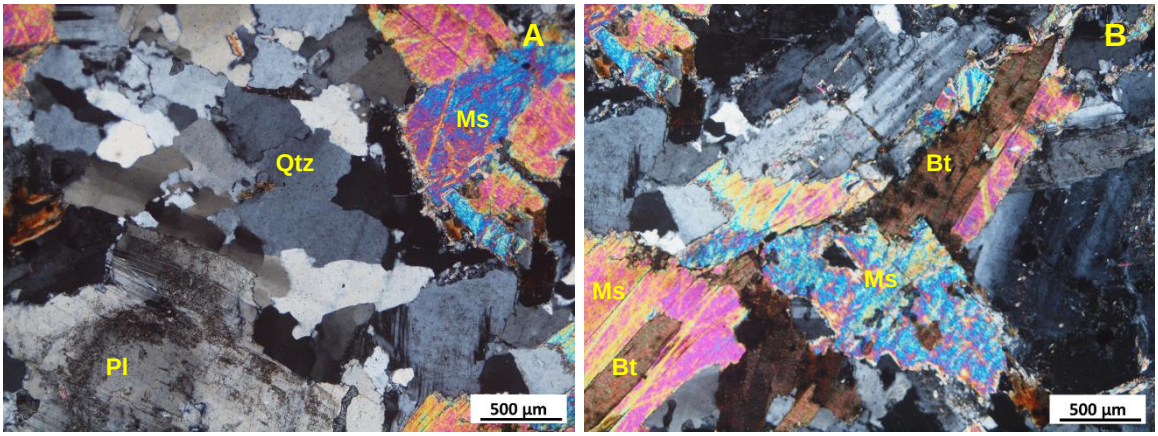

Figure 4.10 – Granite IVγ petrographic features: A – inequigranular texture, sericitized plagioclase, and some dynamic recrystallization of quartz (NX); B – association of muscovite and biotite, with biotite in optical continuity (muscovite of bottom left border; NX). Qtz – quartz; Pl – plagioclase; Ms – muscovite; Bt – biotite.

4.2.9. Ribeira de Massueime-Galegos granite (IIIγ)

The Ribeira de Massueime-Galegos granite has an inequigranular texture with coarsed grain-size. The IIIγ granite mineral assemblage is quartz + plagioclase + microcline + biotite + muscovite ± orthoclase. The accessory minerals are zircon, apatite, and opaque minerals.

Quartz is essentially subhedral showing evidences for subgranulation. Subhedral microcline occurs slightly sericitized and with quartz inclusions. Orthoclase is subhedral also, it exhibits perthite veinlets and some sericitization, albitization and microclinization. Subhedral plagioclase occurs muscovitized and sericitized.

Micas show subhedral crystals, in the case of biotite, sometimes with corroded borders. Biotite appears with some muscovitization and with zircon, apatite, and opaque minerals inclusions. Muscovite has symplectic borders and, less frequent, relics of biotite in optical continuity (Figure 4.11A). The minerals included on muscovite are zircon, apatite, quartz, and opaque minerals.

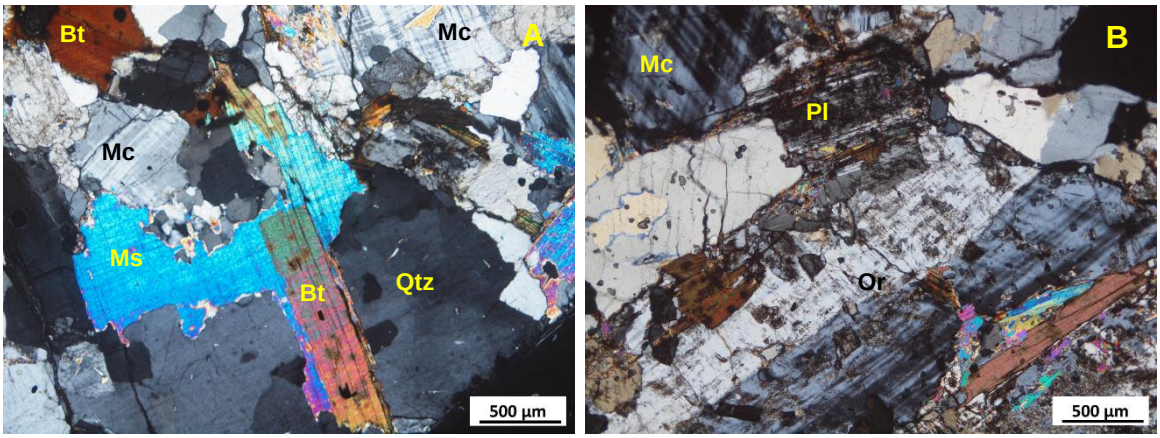

Figure 4.11 – Granite IIIγ petrographic features: A – Inequigranular texture and biotite in optical continuity with muscovite (NX); B – microclinization of orthoclase (NX). Qtz – quartz; Pl – plagioclase; Ms – muscovite; Bt – biotite; Mc – microcline; Or – orthoclase.

4.2.10. São Pedro-Vieiro granite (IIγ)

The São Pedro-Vieiro granite has an inequigranular texture with medium grain-size. This granite facies appears to be considerably deformed (Figure 4.12A). The mineral assemblage of this granite is defined by quartz + plagioclase + biotite + muscovite ± orthoclase ± chlorite. The accessory minerals are zircon, apatite, and opaque minerals.

Quartz grains varies between subhedral and anhedral. The quartz deformation is too clear through the intense undulose extinction, subgranulation, and dynamic recrystallization (e.g. bulging and grain boundary migration) (Figure 4.12B). Subhedral plagioclase is the feldspar in larger proportion relatively to orthoclase, and, at times, it occurs muscovitized and sericitized. Micas are subhedral and they occur with frequent undulose extinction and bent crystals. Aggregates of muscovite and biotite are visible. Biotite crystals appear with chloritized bands and with inclusions of zircon and apatite. Muscovite occurs in fractures and cross-cutting minerals and, sometimes, with symplectic borders.

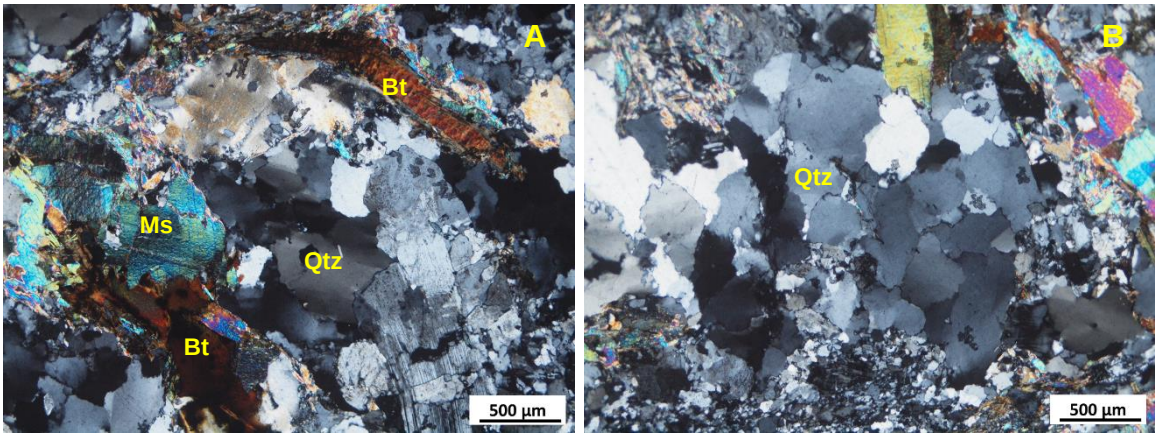

Figure 4.12 – Granite IIγ petrographic features: A – deformation evidences (minerals undulose extinction and biotite bending; NX); B – quartz dynamic recrystallization (NX). Qtz -quartz; Ms – muscovite; Bt – biotite.

CHAPTER 5. TECTONICALLY ASSISTED EXHUMATION AND COOLING OF VARISCAN GRANITES IN AN ANATECTIC COMPLEX OF THE CENTRAL IBERIAN ZONE, PORTUGAL: CONSTRAINTS FROM LA-ICP-MS ZIRCON AND APATITE U–PB AGES

J. A. Ferreira[1], T. Bento dos Santos[1], I. Pereira[2], J. Mata[1]

[1] IDL-Instituto Dom Luiz, Faculdade de Ciências, Universidade de Lisboa, Campo Grande, 1749-016 Lisbon, Portugal

[2] School of Earth and Environmental Sciences, University of Portsmouth, Building Burnaby Rd, Portsmouth P01 3QL, UK

Ferreira, J.A., Bento dos Santos, T., Pereira, I., Mata, J., 2019. Tectonically assisted exhumation and cooling of Variscan granites in an anatectic complex of the Central Iberian Zone, Portugal: constraints from LA - ICP - MS zircon and apatite U – Pb ages. Int. J. Earth Sci. https://doi.org/10.1007/s00531-019-01755-1

Abstract: Understanding the exhumation of middle to lower crustal rocks is of utmost importance to unravel intracrustal mass transfer processes during orogenic build-up. The Figueira de Castelo Rodrigo–Lumbrales Anatectic Complex (FCR–LAC) is located within the autochthonous terrane of the Variscan Central Iberian Zone and is an example of the association between S-type granites and migmatites. The anatectic complex contacts to the north and south with low-grade metamorphic units through the Huebra and Juzbado–Penalva do Castelo shear zones, respectively. Integration of new U–Pb zircon and apatite age data allowed us to obtain Variscan crystallization ages, inherited zircon ages and unprecedented cooling rates for different facies of the FCR–LAC granites. The zircon crystallization ages mostly cluster around 313–317 Ma for the syn-tectonic granites, whereas the dated late-tectonic granite provided an age of 300 Ma. The cooling rates range from 13 to 35 °C Ma^{-1}, which implies fast exhumation (0.3–0.84 mm a^{-1}) and shallow emplacement (ca. 8 km deep), compatible with exhumation facilitated by large crustal-scale shear zones. Inherited zircon in the granites reveals melting of Cadomian metasediments (650–550 Ma), Upper Cambrian–Lower Ordovician (495–470 Ma) metaigneous rocks (Ollo de Sapo formation) and of minor older components, suggesting protolith affinity with the Northern Domain of the Central Iberian Zone.

5.1. INTRODUCTION

Development of collisional orogens implies low-pressure–high-temperature (LP–HT) metamorphism, crustal anatexis and generation of crustal-derived granitic magmas as late-stage features (e.g. Žák et al., 2011). The study of granitic magmatism is, of great importance to understand the evolution of orogenic belts, providing information regarding the interactions between magmatism and tectonics, as well as intracrustal heat and mass transfer processes.

The Variscan orogenic belt in Europe is a collisional orogen that developed during the complex collision of the Laurussia and Gondwana continents during the Devonian and Carboniferous periods (e.g. Kroner and Romer, 2013; Nance et al., 2010). Along the European Variscan Belt, the initial continental collision and related crustal thickening precede the formation of metamorphic core complexes characterized by exhumed mid-crustal migmatites, LP–HT metamorphism and large volumes of granitic magmas (Schulmann et al., 2008, 2002; Villaros et al., 2018; Žák et al., 2011).

Large volumes of granites can also be found in the Iberian Variscan Belt, particularly in the Central Iberian Zone (CIZ), (Azevedo and Valle Aguado, 2013; Dias da Silva et al., 2018; Dias et al., 1998; Ferreira et al., 1987; Valle Aguado et al., 2017; C. Villaseca et al., 1998), a zone which has been interpreted as a section of the Gondwana margin partially underlying a set of

allochthonous tectonic slices of continental and oceanic affinities (e.g. Arenas et al., 2016; Mateus et al., 2016; Ribeiro et al., 2007). In the CIZ, granitic plutons were emplaced after the first Variscan compressive event and Barrovian metamorphism, being usually interpreted as the result of syn-orogenic collapse (Dias da Silva et al., 2017; Escuder-Viruete et al., 1994; Valle Aguado et al., 2005). However, some of these complexes are associated with strike-slip shear zones (e.g. Costa et al., 2014; Pereira et al., 2017) raising an interesting and unsolved question concerning the role of the shear movements in the exhumation of anatectic complexes and, consequently, in the timing of the generation and emplacement of the associated Variscan granites during the intracontinental collision stages.

This study focuses on the granites within the Figueira de Castelo Rodrigo–Lumbrales Anatectic Complex (FCR–LAC), constrained by a major strike-slip shear zone: the Juzbado–Penalva do Castelo Shear Zone (JPCSZ; Iglesias and Ribeiro, 1981). The FCR–LAC has been the target of recent studies that partially constrained its evolution (Alves Ribeiro et al., 2017; Díez Fernández and Pereira, 2017, 2016; Pereira et al., 2017). However, for the complete understanding of this complex, it is still necessary to characterize/quantify the emplacement conditions of these anatectic granitic bodies, namely through the determination of crystallization ages and exhumation rates. Indeed, to date, and besides some past geochronological studies using K–Ar and Rb–Sr methods (Macedo, 1988; Ribeiro, 2001), only two studies presented U–Pb ages for granites of this complex (Díez Fernández and Pereira, 2017; Pereira et al., 2018) although 10 distinct intrusive facies have been described (Ribeiro, 2001).

The main objective of this work is to present new U–Pb zircon and apatite ages for distinct FCR–LAC granite facies with the purpose of, for the first time, constrain their crystallization ages and cooling rates, and, therefore, their emplacement conditions within the framework of the Variscan Orogeny. This innovative study aims to bring a better understanding for the tectono-metamorphic evolution of the internal zone of the Iberian Variscides, as well as for the role of intracontinental first-order shear zones in the exhumation of deep settled rocks in collisional orogens worldwide.

5.2. ANALYTICAL TECHNIQUES

All samples were prepared for the different types of analytical procedures at the Mineral Separation Lab of GeoFCUL—Department of Geology of the University of Lisbon. Zircon and apatite crystals were picked from a 63- to 250-μm fraction, after heavy liquid and electromagnetic separation.

Grains, mounted in epoxy resin mounts, were attached to metallic stubs with thin copper strips, and coated with a 1-nm pulverized gold film. Zircon and apatite grains were observed using a ZEISS EVO10MA scanning electron microscope (SEM) at the University of Portsmouth (UoP). For backscatter electron (BSE) imaging, an accelerating voltage of 20 kV and 700 pA beam current was applied to reveal internal structures in the analyzed grains.

U–Pb isotopic analyses were performed using an ASI RESOlution 193 nm ArF excimer laser coupled to the ANALYTIK JENA Plasma Quant Elite quadrupole ICP-MS at UoP. The detailed instrumental setup and ablation conditions can be found in Appendix B. For zircon U–Pb dating, a beam spot size of 20 μm (cores) and 11 μm (smaller grains and rims) was preferred. Beam energy densities used ranged from 2.1 to 2.5 J cm^{-2}, with a 2-Hz repetition rate. As for apatite, a beam spot size between 50 and 20 μm was used, with beam energy densities ranging from 2.8 to 3 J cm^{-2}, and a 3-Hz repetition rate. For additional information on the analytical conditions used for the LA-ICP-MS analyses, see Appendix B1.

Plešovice was used as a primary standard for zircon (337.13 ± 0.13 Ma; Sláma et al., 2007) whereas the Madagascar standard was used for apatite (473.5 ± 0.7 Ma; Thomson et al., 2012) (see Appendix B2 and B5, respectively). 91500 (1062.4 ± 0.4 Ma; Wiedenbeck et al. 1995), and GJ1 (608.5 ± 0.4 Ma; Jackson et al. 2004) were used as zircon secondary standards (Appendix B3 and B4, respectively), whereas for apatite were used McClure (523.51 ± 2.09 Ma; Schoene and Bowring, 2006) and Xuxa (unpublished, ca. 572 Ma, provided by courtesy of C. Lana, Federal University of Ouro Preto) (see Appendix B6 and B7, respectively). For all the above, reproducibility of the secondary standards was within 2%.

IOLITE 3.31 software package was used for data reduction. A sample-standard bracketing method was used to correct for both instrumental drift and elemental mass fractionation.

For zircon, Wetherill concordia and weighted mean $^{238}U/^{206}Pb$ ages were calculated using ISOPLOT/EX 4.1 (Ludwig, 2003). From the youngest zircon population data, only grains that were 95–105% concordant were used to determine crystallization ages.

For apatite, the isotopic data was processed using Vizual-Age_UcomPbine DRS and measured ^{207}Pb (Chew et al., 2014). This data reduction scheme allows for common-Pb (Pbcm) correction of the primary standard based on their known radiogenic and variable Pbcm compositions. This correction is then applied to the unknowns. Apatite Tera–Wasserburg concordia ages were determined using ISOPLOT/EX 4.1 (Ludwig, 2003).

Trace element analyses in zircon were performed using the same instrument setup as for U–Pb, and a standard-sample bracketing method to correct for instrumental drift. The following isotopes were analyzed: ^{29}Si, ^{31}P, ^{39}K, ^{40}Ca, ^{45}Sc, ^{49}Ti, ^{51}V, ^{52}Cr, ^{55}Mn, ^{85}Rb, ^{87}Sr, ^{89}Y, ^{90}Zr,

^{93}Nb, ^{95}Mo, ^{118}Sn, ^{121}Sb, ^{133}Cs, ^{137}Ba, ^{139}La, ^{140}Ce, ^{141}Pr, ^{146}Nd, ^{147}Sm, ^{153}Eu, ^{157}Gd, ^{159}Tb, ^{163}Dy, ^{165}Ho, ^{166}Er, ^{169}Tm, ^{172}Yb, ^{175}Lu, ^{177}Hf, ^{181}Ta, ^{182}W, ^{208}Pb, ^{209}Bi, ^{232}Th and ^{238}U.

A laser beam diameter of 40 μm for NIST612, 35 μm for secondary standards and 35–25 μm for unknowns was used, with beam energy densities ranging from 3.8 to 4.1 J cm^{-2}, with a 4-Hz repetition rate (Appendix B1). NIST612 was used as primary standard using concentrations by Jochum et al. (2011), whereas 91500 (Wiedenbeck et al., 1995) and GJ1 (Jackson et al., 2004) were used as secondary standards, as they are relatively homogenous in terms of trace element concentrations. Zr was used as an internal calibration standard, considering zircon stoichiometry (Zr = 43.1 wt%). Most analysed elements are within 10% and 5% accuracy relative to secondary standards published values, and ^{49}Ti is within 10% uncertainty of reported values (see Appendix B8), excluding uncertainties, with a detection limit of 3 ppm.

5.3. RESULTS

5.3.1. Zircon U–Pb ages

U–Pb zircon ages were obtained for five of the granite facies from the FCR–LAC defined by Ribeiro (2001) (Appendix C1): São Pedro-Vieiro (IIγ), Ribeira de Massueime-Galegos (IIIγ), Châs-Amargo (Vγ), Mêda-Escalhão (IXγ) and Sta. Comba-Algodres granite (Xγ).

Zircon external morphology has been widely used in petrogenetic studies, particularly those targeting granitoids (e.g. Barbarin, 1988; Belousova et al., 2006; Köksal et al., 2008; Pupin, 1980). Zircon morphology depends on the crystallization rate, fluid composition and on the temperature of the crystallization medium (Corfu et al., 2003). Pupin (1980) established a systematics for zircon using the relative development of the prismatic and pyramidal crystal forms, considering the development of prismatic faces mainly related with the temperature of crystallization and the pyramidal faces with chemical factors. These parameters inferred from a zircon population can be helpful to characterize the evolution of a magma system (Corfu et al., 2003). However, the morphology systematics proposed by Pupin (1980) has been questioned by several authors (e.g. Benisek and Finger, 1993; Vavra, 1993, 1990) which advocate that the zircon morphologies can only reflect the latest stages of growth.

Sometimes, it is possible to distinguish igneous and metamorphic zircon from its morphology. In general, euhedral, concentric oscillatory zoning and euhedral, prismatic external morphology are evidences for igneous zircons. Zircon from a high-grade metamorphic environment can exhibit patchwork zoning and multifaceted, equant, tabular external morphology (e.g. (Aleinikoff et al., 2006). However, at very high metamorphic grade, these morphological

distinctions related with the origin (igneous vs. metamorphic) are not so clear, especially under anatectic conditions (Aleinikoff et al., 2006). Th/U ratios has also been used to distinguish metamorphic (< 0.1) and magmatic (> 0.1) zircons (e.g. Rubatto and Gebauer, 2000; Williams et al., 1996), yet its use for such purpose is debatable (see Discussion).

Considering all these mentioned features, the selection of zircon grains for dating was made taking into account the maximum number of characteristics that was possible to determine/observe.

São Pedro-Vieiro granite (IIγ)

Zircon morphology of the São Pedro-Vieiro granite varies among elongated prismatic and oval shape (Figure 5.1a). Occasionally, zircon grains show the development of bipyramidal terminations (most of them 211), whereas others have one pyramid developed in one direction and the opposite edge is rounded. About the zircon prisms, most of them are 100. Regarding zircon internal morphology, oscillatory zoning is rare. All zircon crystals have narrow rims (2–18 μm), but most of them depicting an unzoned core and intermediate zones. At times, a few zircons appear fractured. The Th/U ratio ranges from 0.07 to 0.54.

From this granite, we analyzed 22 zircon grains for U–Pb. From 5 younger zircon cores (Appendix C1) yielding 300 ± 2.2 Ma (MSWD = 1.4) (Figure 5.2a), we determined the crystallization age of the IIγ granite, significantly younger than the K–Ar crystallization age (319 ± 6 Ma) obtained by Macedo (1988).

Recently, Díez Fernández and Pereira (2017) obtained a SHRIMP U–Pb zircon age of 307.8 ± 3.1 Ma (MSWD = 1.8) for the São Pedro-Vieiro granite, which is slightly older than our estimate and outside analytical uncertainty of our measurement.

Eleven zircon grains with concordant inherited cores yield dates ranging from Lower Devonian (400 Ma) to Paleoproterozoic (2000 Ma) (Appendix C2). From the inherited zircon cores, it was observed 4 younger overgrowths with Variscan age.

Ribeira de Massueime-Galegos granite (IIIγ)

In general, the Ribeira de Massueime-Galegos granite contains prismatic zircon, although a few crystals have acicular shape with oscillatory zoning and others have oval shapes with rounded terminations. When the oscillatory zoning is present, it is more visible in the thin zircon rims (5–18 μm) surrounding the unzoned cores and, quite rarely, the cores appear with convoluted zoning (Figure 5.1b). This feature is typical of zircon growing during high-temperature metamorphism (Corfu et al., 2003). The majority of the zircon grains have 211 pyramids and

100 prisms, and sometimes they appear fractured. The Th/U ratios are low, ranging from 0.01 to 0.06.

The ablation was done in 22 grains of the IIIγ granite. The young concordant dates (Appendix C1) (1 core and three rims) allowed to estimate the 314.1 ± 2.6 Ma (MSWD = 0.12) crystallization age for this granite (Figure 5.2b). Five old zircons provided Cambrian and Ediacaran ages around 485–600 Ma (Table C2).

Chas-Amargo granite (Vγ)

Zircon grains from the Chãs-Amargo granite have prismatic and oval morphology, sometimes with rounded terminations and narrow rims (4–18 μm) (Figure 5.1c). The zircon typology is heterogeneous, since the pyramids range between 211 and 101, and prisms between 110 and 100. The Th/U ratio varies between 0.005 and 0.24.

Thirty zircon grains were analyzed and it was determined a date of 316.2 ± 3.9 Ma (MSWD = 1.10) for the Vγ granite, using 5 younger zircons (Appendix C1) (4 cores and 1 rim), which is ascribed as its crystallization age (Figure 5.2c). From the 30 grains, 16 of them correspond to older concordant dates with ages from Lower Devonian (400 Ma) to Paleoproterozoic (2500 Ma) (Table C2).

Meda-Escalhao granite (IXγ)

The Mêda-Escalhão granite carries prismatic zircon grains, at times with planar or oval shape. Many crystals have the pyramids developed in one direction and occasionally, they appear fractured. In addition, they have thin rims and faint zoning in both cores and rims (3–26 μm) (Figure 5.1d). Most of the zircon grains exhibit 211 pyramids and 100 prisms. The Th/U ratio fluctuates between very low values of 0.004 and 0.13.

The U–Pb dating was carried out on 23 grains. From 4 younger zircon grains (Appendix C1) (3 cores and 1 rim) was determined a date of 317.4 ± 2.1 Ma (MSWD = 0.097) that corresponds to the crystallization age of the IXγ granite (Figure 5.2d).

Pereira et al. (2018) dated this granite facies (Mêda-Escalhão-Penedono massif) to the west of the FCR–LAC, estimating a LA-ICP-MS U–Pb zircon age of 318.7 ± 4.8 Ma (MSWD = 0.22) which is in agreement with the age obtained in this study, within error.

Five concordant old cores stand out, from the group of 23 grains, showing Cambrian and Cryogenian ages from 500 to 750 Ma (Table C2).

Sta. Comba-Algodres granite (Xγ)

Most of the zircon that compose the Sta. Comba-Algodres granite are prismatic and elongated, and a minority have acicular shape. The zircon rims (6–20 μm) are narrow and some of them have an incipient oscillatory zoning in the core (Figure 5.1e). A large proportion of the zircon have 101 pyramids and 100 prisms. The Th/U ratio exhibits a large range of values, from 0.02 to 7.1.

Thirty-three zircons were analyzed, resulting in 26 grains with younger dates. From the 26 younger dates, 20 of them defines a cluster of absolute dates between 307 and 320 Ma (Appendix C1)., similar within error between them, whose weighted mean average date is 312.9 ± 1.6 (MSWD = 1.6) (Figure 5.2e) which is considered the crystallization age of the Xγ granite. Three concordant older zircon grains provide Neoproterozoic dates from 600 to 750 Ma (Table C2).

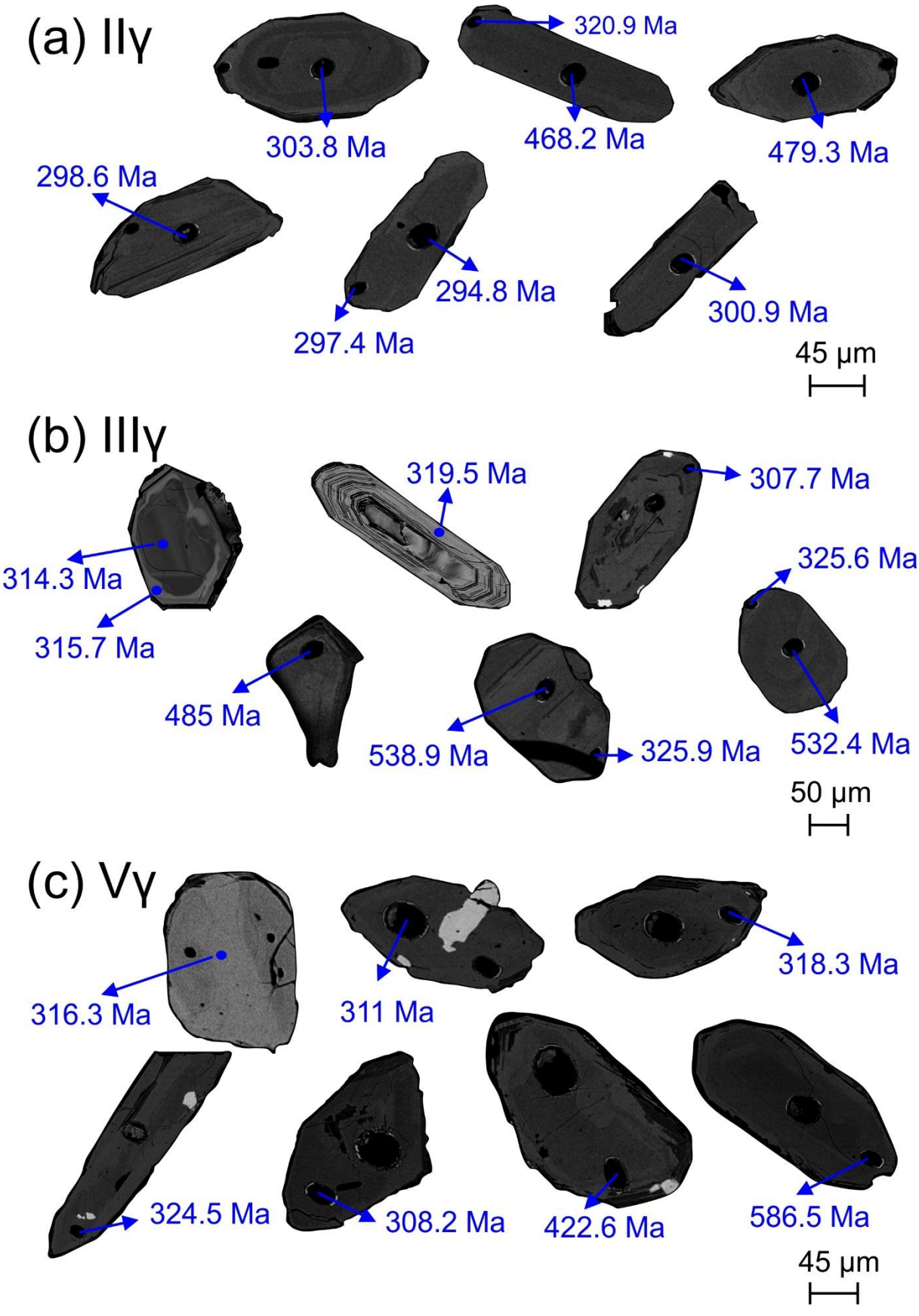
(a) IIγ
320.9 Ma
303.8 Ma
468.2 Ma
479.3 Ma
298.6 Ma
294.8 Ma
297.4 Ma
300.9 Ma
45 µm
(b) IIIγ
319.5 Ma
307.7 Ma
314.3 Ma
325.6 Ma
315.7 Ma
485 Ma
538.9 Ma
325.9 Ma
532.4 Ma
50 µm
(c) Vγ
316.3 Ma
311 Ma
318.3 Ma
324.5 Ma
308.2 Ma
422.6 Ma
586.5 Ma
45 µm

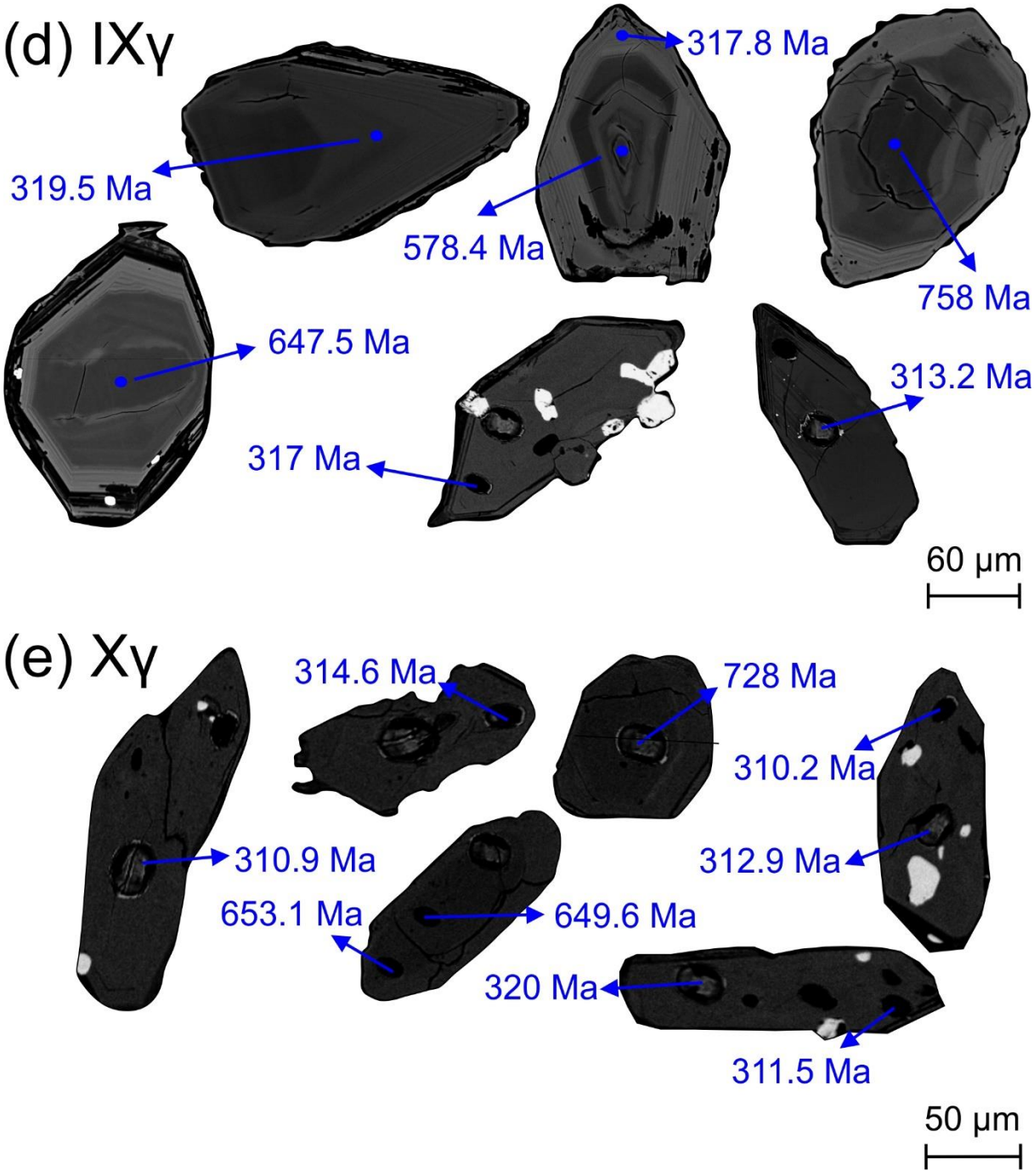

Figure 5.1 – Back-scattered electron images of representative zircon grains of the five studied granites: (a) São Pedro-Vieiro granite (IIγ); (b) Ribeira de Massueime-Galegos granite (IIIγ); (c) Chãs-Amargo granite (Vγ). (d) Mêda-Escalhão granite (IXγ); (e) Sta. Comba-Algodres granite (Xγ).

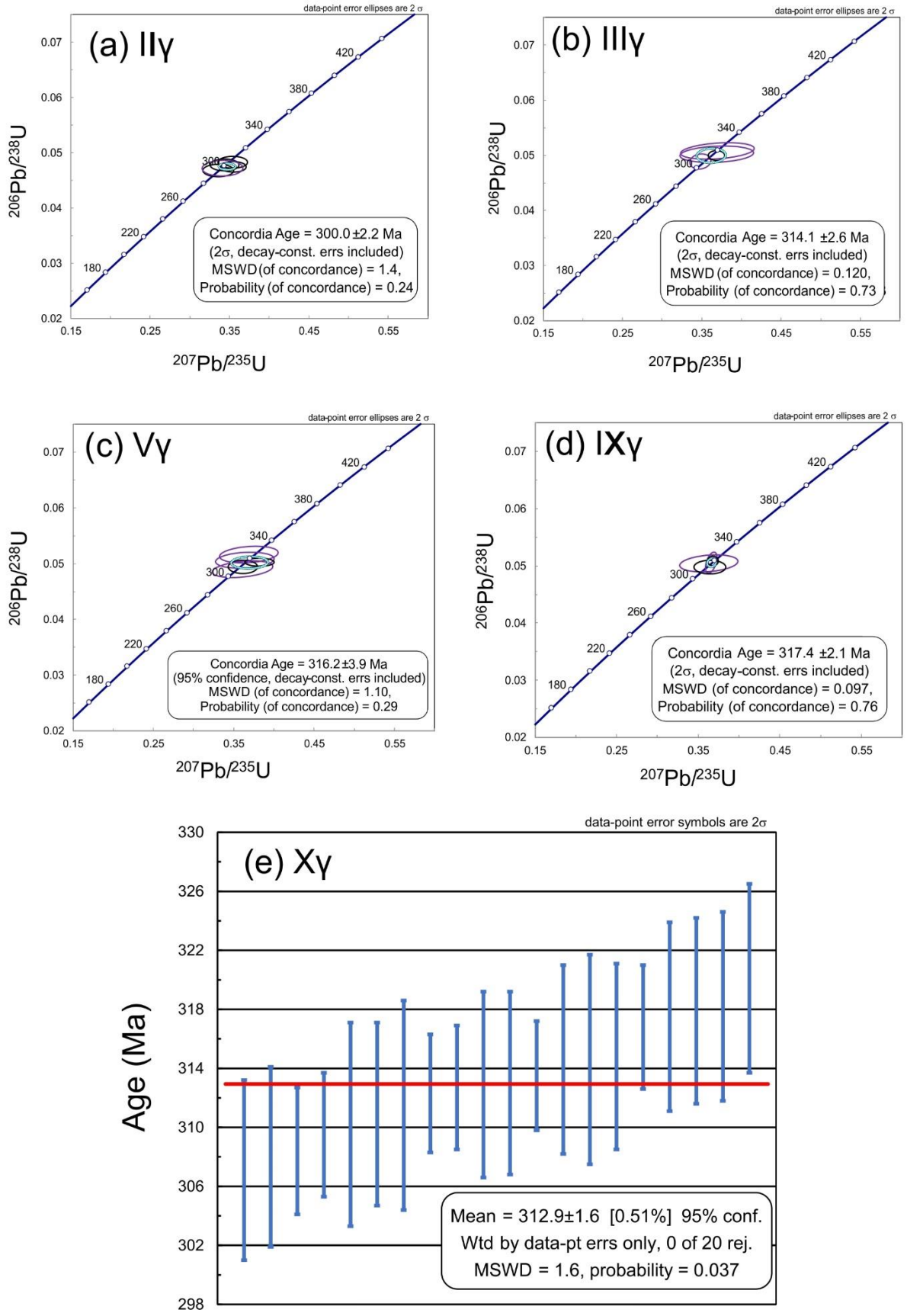

Figure 5.2 – Wetherill concordia diagrams showing the U–Pb crystallization ages for: (a) São Pedro-Vieiro granite (IIγ); (b) Ribeira de Massueime-Galegos granite (IIIγ); (c) Chãs-Amargo granite (Vγ); (d) Mêda-Escalhão granite (IXγ). € U–Pb crystallization ages of Sta. Comba-Algodres granite (Xγ) are represented by a weighted mean average diagram

5.3.2. Inherited zircon

A general overview of the inherited zircon grains found in the granites (total of 40 concordant ages) allowed to ascribe them to different age groups: 400–500 Ma, 500–650 Ma, 650–850 Ma and 2000–2500 Ma (Table C2). These age distributions help us constraining possible protoliths as the source of the FCR–LAC granites.

5.3.3. Apatite U‑Pb ages

In general, the apatite grains appear as elongated prisms, but occasionally show anhedral rounded shapes. Regarding the texture, the apatite grains do not show oscillatory zoning at backscattered electron imaging. However, the BSE imaging revealed several very small zircon inclusions (Figure 5.3). Apatite ages analyses (Table C3) are plotted in the Tera–Wasserburg (TW) diagrams due to their high and variable common Pb (Pbcm)/radiogenic Pb ratios, precluding further Pbcm corrections. The TW regression results in the determination of the initial Pbcm composition and cooling age.

Regarding the number of analyzed grains, around 25 apatite grains per granite were targeted, and apatite ages were estimated from ca. 22 grains. All these grains fall on an isochron in the TW diagram supporting the idea that they are cogenetic despite their rounded morphologies.

For the five granitic facies mentioned above, the following TW Concordia lower-intercept apatite ages were obtained: IIγ (301.4 ± 2.6 Ma; MSWD = 0.8), IIIγ (288.0 ± 14.0 Ma; MSWD = 3.3), Vγ (306.6 ± 8.5 Ma; MSWD = 3.9), IXγ (307.0 ± 10.0 Ma; MSWD = 3.6), and Xγ (302.6 ± 5.6 Ma; MSWD = 1.9) (Figure 5.4). The apatite ages reflect the timing at which the apatite closure temperature (450-550 ºC; Schoene and Bowring, 2007) was reached after their crystallization and are, therefore, younger than the equivalent magmatic zircon ages.

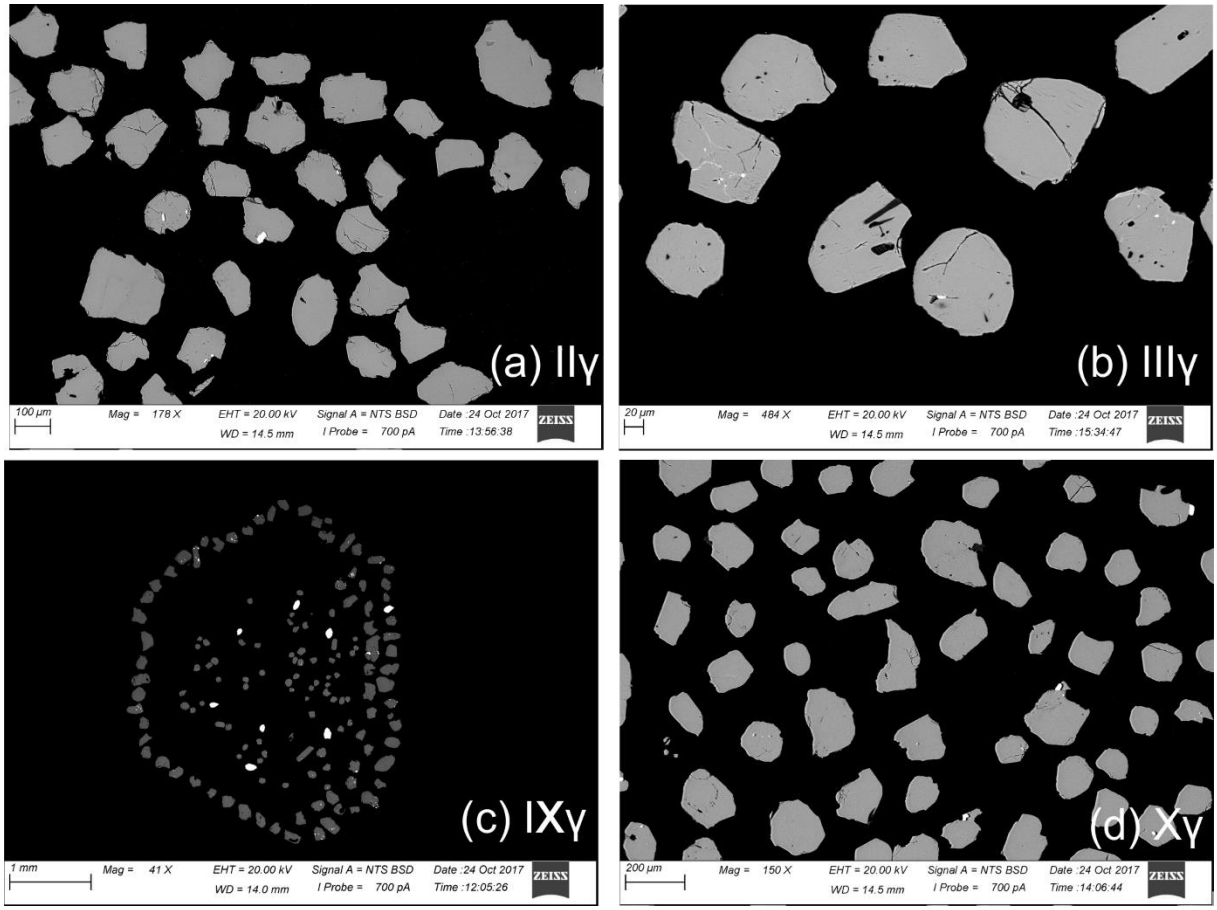

Figure 5.3 – Back-scattered electron images of representative apatite grains of four studied granites: (a) São Pedro-Vieiro granite (IIγ); (b) Ribeira de Massueime-Galegos granite (IIIγ): (c) Mêda-Escalhão granite (IXγ); (d) Sta. Comba-Algodres granite (Xγ).

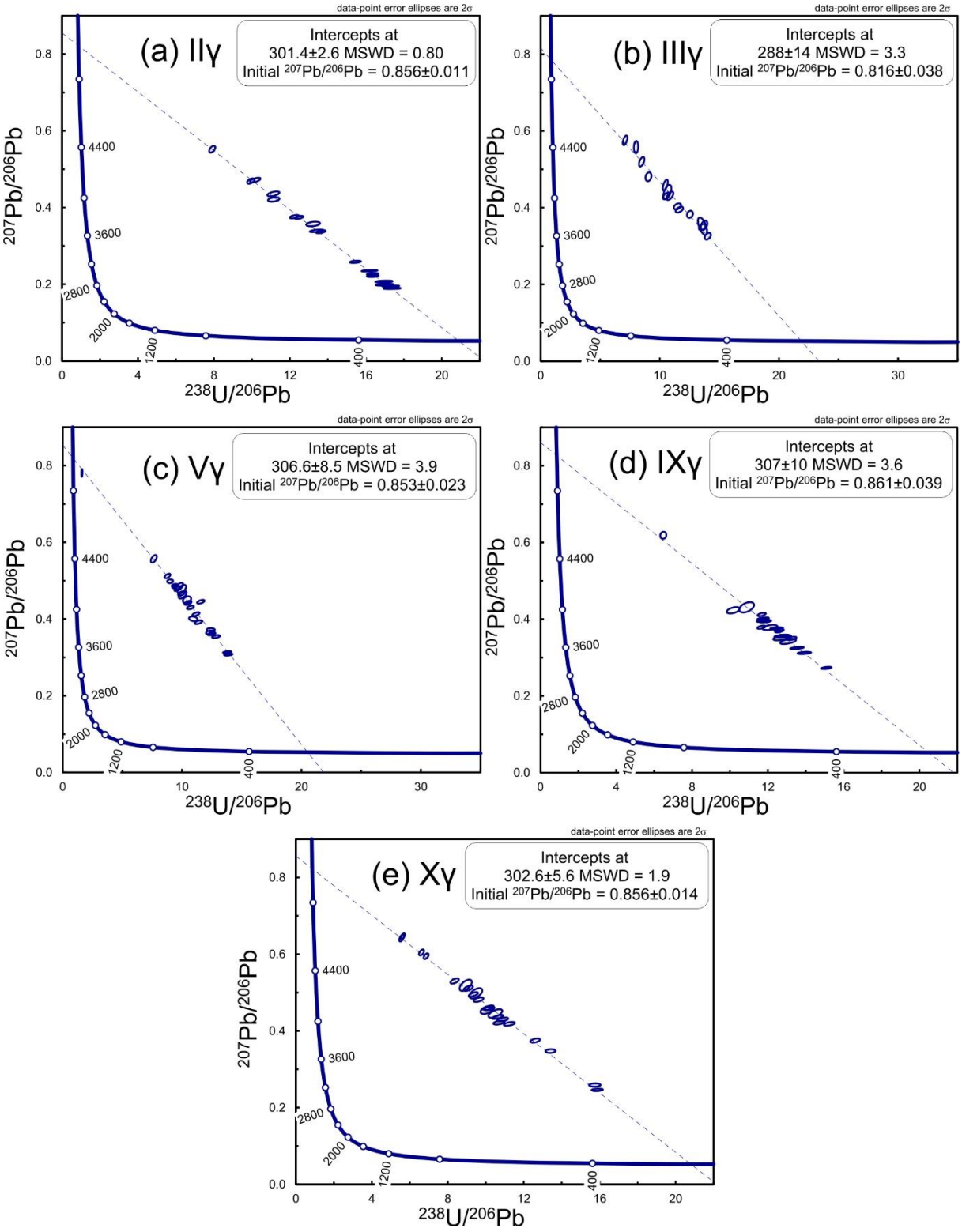

Figure 5.4 – Tera–Wasserburg U–Pb lower-intercept apatite ages for the five studied granites: (a) São Pedro-Vieiro granite (IIγ); (b) Ribeira de Massueime-Galegos granite (IIIγ); (c) Chãs-Amargo granite (Vγ); (d) Mêda-Escalhão granite (IXγ); (e) Sta. Comba-Algodres granite (Xγ).

5.4. DISCUSSION

5.4.1. Th/U zircon ratios in S-type granites

Th/U ratios have long been considered as an effective discriminator between metamorphic and magmatic zircon, with the value of 0.1 being a threshold below and above which, respectively, are placed those two types of zircons (e.g. Rubatto and Gebauer, 2000; Williams et al., 1996). However, it has been demonstrated that Th/U ratios can not be used as a rule of thumb given that the Th/U ratio of zircon largely depends on the coexistence with Th-rich minerals such as monazite and allanite (Möller et al., 2003; Schaltegger and Davies, 2017). For example, Rubatto (2017) showed that the occurrence of high-grade metamorphic rocks with zircons depicting Th/U > 0.1 is not rare, while Yakymchuk et al. (2018) referred a population of metamorphic zircons from Western Australia having a mean Th/U ratio of 0.4. On the other hand, Lopez-Sanchez et al. (2016) reported Th/U < 0.1 for zircon overgrowths of magmatic origin.

Considering all these facts, the reported Th/U ratios (Table 1) might be considered with caution. Indeed, due to the petrogenetic nature of these granites, with the melt being segregated from a HT metamorphic rock, it is expectable that magmatic zircon shows variable Th/U ratios. Under these circumstances, the determined zircon Th/U ratios can not be used as an independent discriminant factor for magmatic vs. metamorphic origin.

5.4.2. The timing of granites emplacement

The FCR–LAC granites have different facies allowing their subdivision in 10 distinct granitic bodies, referred as Iγ to Xγ, from oldest to young, based on the geometries of their contacts (Ribeiro, 2001).

In this study, we obtained U–Pb zircon ages for the five most representative granite facies, (IIγ, IIIγ, Vγ, IXγ and Xγ). Many of our ages are identical within error, despite ages spanning from 300.0 ± 2.2 Ma (IIγ) to 317 ± 2.1 Ma (IXγ). In the light of these new results, our data indicate that the FCR–LAC granite suite crystallized between 317 and 313 Ma with the final emplacement of IIγ at ca. 300 Ma, supported by its intrusive field relationships with respect to the anatectic complex (Figure 5.2).

It must be emphasized that the complexity of this granitic region can be higher than it can be inferred from the 10 mapped facies. Indeed, for the IIγ granite, besides the age here presented (300.0 ± 2.2 Ma), another age has been obtained, with similar number of zircons used to infer a concordia age, yielding 307.8 ± 3.1 Ma (Díez Fernández and Pereira, 2017). This suggests that the IIγ granite can comprise more than one late intrusive body, but reinforces it being a late

magmatic episode affecting this region. The crystallization age of the IIγ granite is substantially younger than the age obtained by Macedo (1988) of 319 ± 6 Ma using the K–Ar dating method. However, K–Ar ages are known to be prone to the effects of post-magmatic alteration processes leading commonly to younger ages by Ar loss (e.g. Baksi, 1994), but also to older ages as a consequence of preferential K mobility (e.g. Cerling et al., 1985). Indeed, these authors demonstrated that low-temperature alteration involving meteoric water can result in hydrogen exchange by K+ and Na+ without significant alteration of other elements, conditions under which Ar also appears to be less mobile than alkali ions. Also, Mata et al. (2015) noticed that dates determined by the K–Ar method elsewhere for doleritic rocks portraying evidences for alteration, resulted in older dates than those obtained by more robust methods.

The obtained age for IIγ granite confirms the diachronous deformation along this shear zone, progressing from east (Juzbado) to west (Penalva do Castelo), as previously suggested by Pereira et al. (2017). Indeed, in Juzbado, the eastern sector of the JPCSZ, the last shear event has been dated at 309 ± 2.5 Ma (40Ar–39Ar in white micas; Gutiérrez-Alonso et al., 2015). Later, Valle Aguado et al. (2017) showed that in the western sector deformation continued until ca. 299 Ma, which is within error of the date, we obtained for the D_3-affected IIγ granite (300.0 ± 2.2 Ma).

In the CIZ, significant granitic plutonism has been considered to occur during syn-, late- and post-D3 stage (e.g. Azevedo and Valle Aguado, 2013; Ferreira et al., 1987). Particularly, granites from this studied region have been classified as syn-D_3 which has been mainly developed between 310 and 320 Ma (e.g. Ribeiro, 2001; Azevedo and Valle Aguado, 2013). However, as mentioned before, IIγ granite (300.0 ± 2.2 Ma) was clearly deformed by D_3 allowing to consider it as late-D_3, while the other dated facies are syn-D_3.

5.4.3. Protoliths of the granites

The obtained data for inherited zircon data were compared with published detrital zircon ages from distinct domains of the Douro-Beiras Supergroup in the CIZ, namely the metasediments from the Northern and Southern domains (Orejana et al., 2015). Comparison with the kernel density estimate (KDE) plots for these domains (Figure 5.5) puts in evidence the similarities between metasediments of the Northern domain with our data, namely the existence of a main age group of the Lower Cambrian/Cryogenian, with minor Tonian and Paleoproterozoic contributions, and the absence of Mesoproterozoic ages.

Moreover, the second representative group of ages, 400–500 Ma (Upper Cambrian/Lower Devonian), seems to be related with the Ollo de Sapo formation that was emplaced in the Iberian

Massif between 495 and 470 Ma (García-Arias et al., 2018). These ages suggest that the Douro-Beiras Supergroup metasediments that melted to form these granites also included Ollo de Sapo magmatic rocks.

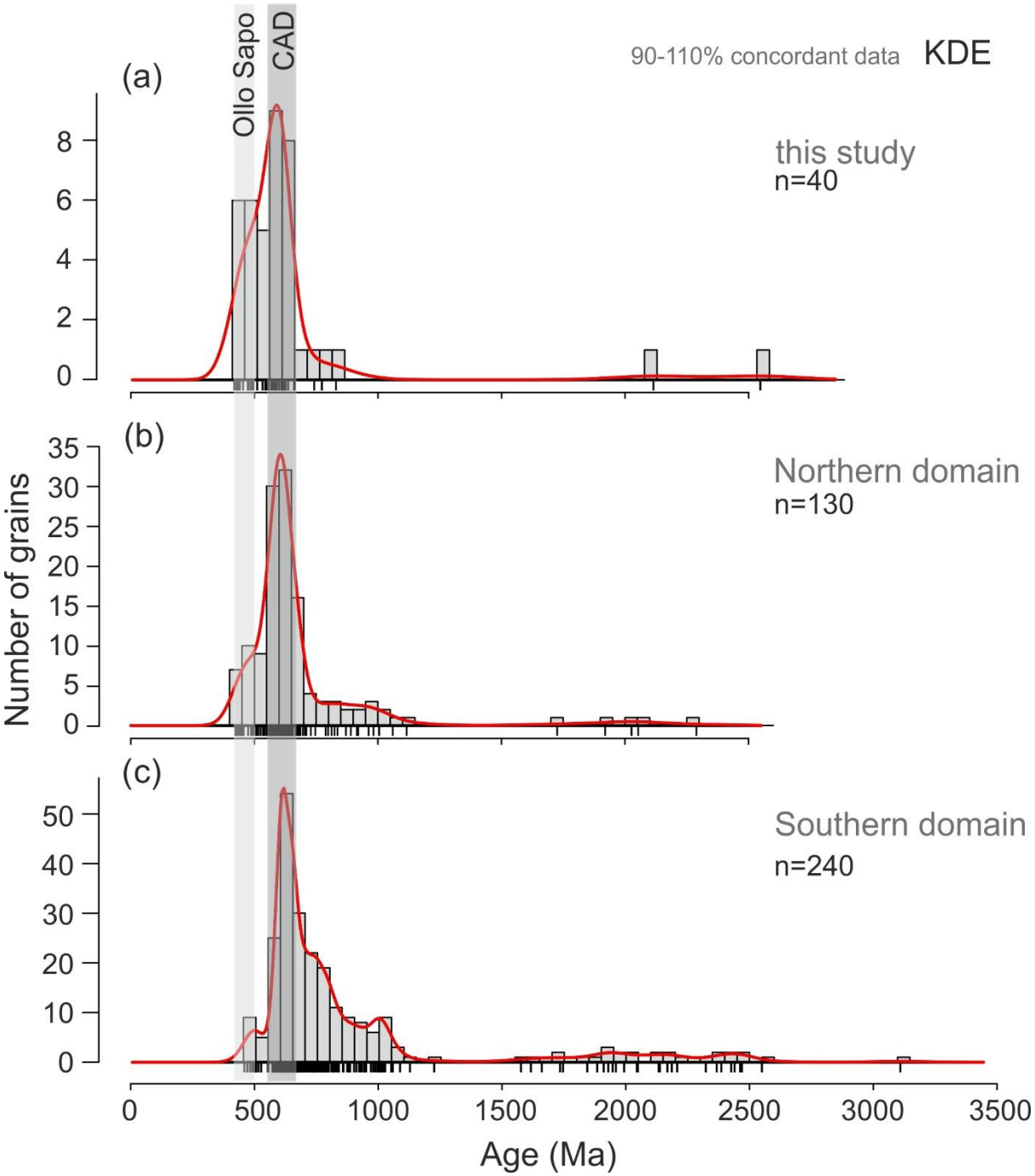

Figure 5.5 – Kernel density estimates (KDE) plots of inherited zircon ages for the studied granites (a) and also for the detrital zircons of the Northern (b) and Southern domains (c) of the CIZ (Orejana et al. 2015). The defined bin width is 50 Ma. The selected ages to perform the plots are $^{206}Pb/^{238}U$, when the age is < 1000 Ma, and $^{207}Pb/^{206}Pb$ for ages > 1000 Ma. The KDE plots were performed with the support of the Vermeesch (2018) program (IsoplotR).

5.4.4. Cooling and exhumation rates

In this work, we determined U–Pb ages for zircon and apatite occurring in the same rocks (see above), providing an opportunity to assess the cooling history of the granitic rocks where they crystallized. Indeed, closure temperatures (*T*c) for the system U–Pb are usually considered to be in excess of 900 °C for zircon (Cherniak and Watson, 2000), while for apatite *T*c of 450–550 °C has been usually considered (Schoene and Bowring, 2007). However, there have been reported apatite closure temperatures above 800 °C in doleritic rocks from the Armorican Massif (Pochon et al., 2016).

The concept of closure temperature was proposed by Dodson (1973) as referring to the temperature of a mineral at the time of its apparent ("freezing") age. It can be determined from:

$$E/RT_c = \ln [-AD_0RT_c^2/ \{a^2 (dT/dt) E\}] \quad (5.1)$$

where *E* is the activation energy for the diffusion process, *R* is the ideal gas constant, *T*c is the closure temperature, *A* is a numerical constant depending on the geometry of the grain (spherical or cylindrical), D_0 is the diffusion coefficient at infinitely high temperature, d*T*/d*t* is the cooling rate and *a* is an effective diffusion dimension (i.e., radius in the case of a sphere). This approach has implicit the role of the daughter element volume diffusion over time, which is function of temperature. Moreover, the *T*c is also dependent on the cooling rate. The *T*c parameter appears on both sides of equation, so the equation is solved through several iterations for a given value of cooling rate. This procedure allows to calculate a consistent set of closure temperatures and cooling rates from the ages of two mineral species. For these calculations, the zircon and apatite diffusion parameters compiled by Hodges et al. (2003) were used.

Ti-in-zircon and the zircon saturation (*T*Zircsat) geothermometers were determined in this study. The Ti-in-zircon geothermometer uses the Ti content in the zircon structure, which is dependent on temperature and independent of pressure, to estimate the magma temperature at the time of zircon crystallisation (Watson et al. 2006). The *T*Zircsat predicts the temperature at which zircon crystallisation begins in a cooling magma, and, on the other hand, the temperatures above which zircon dissolution should occur (Watson and Harrison, 1983).

In the case of zircon, we were faced with the problem that the experimental closure temperature (> 900 °C; Cherniak and Watson, 2000) is clearly above of those determined by Ti-in-zircon and *T*Zircsat geothermometers (Table 5.1), indicating that the studied zircon grains grew below their closure temperatures and, consequently, that diffusion processes did not occur after crystallization. Recently, Siégel et al. (2018) have shown that *T*Zircsat is a dynamic variable

that changes during magma crystallisation, and, thus, can not be used to constrain magmatic or partial melting temperatures. Consequently, we used the Ti-in-zircon geothermometer (Watson et al., 2006), which is considered as providing very reliable zircon crystallization temperatures, and therefore used as zircon closure temperatures. For the granite facies Vγ, IXγ and Xγ the use of this thermometer led to the following crystallization temperatures: Vγ = 825 ± 22 °C, IXγ = 836 ± 22 °C, and Xγ = 783 ± 31 °C (Table 5.1).

Table 5.1 – Zircon geothermometers applied to the Vγ, IXγ and Xγ granites.

Ti-in-zircon Thermometer						Zircon Saturation Thermometer			
Id	SiO_2 (wt. %)	Ti (ppm)	Error	T (ºC) Zircon	Error	Zr (ppm)	M	Zr.sat levels (ppm)	$T_{Zircsat}$ (ºC)
Vγ	71.39	24	1.8	825	22	116	1.11	81.9	779
IXγ	73.6	26.8	1.9	836	22	84	1.12	82.6	751
Xγ	70.97	17.3	2.8	783	31	287	1.22	89.6	854

The obtained temperatures are endorsed by data published by Pereira et al. (2017) pointing to metamorphic temperatures in excess of 800 °C at the onset of partial melting. These results are also consistent with extensive literature on the melting of pelitic rocks to form anatectic granitoids (e.g. Bento dos Santos et al., 2011; Clemens, 2003; Clemens and Stevens, 2016).

The next step was to obtain the apatite closure temperature for each granite facies through Dodson's equation, using *T*c = 446 °C as an initial experimental value, as proposed by Cherniak et al. (1991). This provided *T*c results between 483 and 465 °C (Table 5.2).

Combining the zircon and apatite *T*c with their respective ages, the cooling rates for the IIIγ, Vγ, IXγ and Xγ granite facies are of 13, 34, 35 and 28 °C Ma^{-1}, respectively (Table 5.2). It was not possible to infer the closure temperatures and respective cooling rates for the IIγ granite, because the apatite ages are slightly older than the zircon ages obtained for this sample, even considering their errors.

Table 5.2 – Zircon and apatite estimated closure temperatures for the granites in study and the respective cooling and exhumation rates.

Id	Zircon Age (Ma)	Apatite Age (Ma)	Δt (Ma)	Zircon T_c (ºC)	Apatite T_c (ºC)	Cooling Rate (ºC/Ma)	Exhumation Rate ($mm.a^{-1}$)
IIγ	300 ± 2.2	301 ± 2.6	-	-	-	-	-
IIIγ	314 ± 2.6	288 ± 14	26	814*	465	13 ± 16.5	0.3
Vγ	316 ± 3.9	306 ± 8.5	10	825	482	34 ± 4.1	0.8
IXγ	317 ± 2.1	307 ± 10	10	836	483	35 ± 3.1	0.8
Xγ	313 ± 1.9	302 ± 5.6	11	783	478	28 ± 39.5	0.7

*value estimated by the average of the other temperatures

Cooling rates of plutons are highly variable, with published values differing by more than two orders of magnitude (e.g. Chesley et al., 1993; Meert et al., 2001; Miyazaki and Santosh, 2005; Tsuchiya and Fujino, 2000). It depends essentially on the way heat is exchanged between the hot intrusive body and their surroundings. The heat transfer may be done by conduction or by fluid-assisted advection. Considering that thermal diffusivity is strongly dependent on temperature, with which correlates negatively, and the role of the latent heat of crystallization on lowering the cooling rate of a crystallizing melt (Nabelek et al., 2012; Whittington et al., 2009), the rates of conductive cooling are very low when compared with advective cooling.

Although it was not possible to infer the cooling rate for the IIγ granite, the closeness of the zircon and apatite crystallization ages points to an abrupt cooling, at least until the apatite *T*c. This suggests the localized intervention of significant fluid circulation during cooling within the JPCSZ. This hypothesis receives some support from the occurrence of abundant tourmaline in the diatexites and significant iron oxides enrichment in the metasedimentary rocks in contact with this granite facies.

The estimated granite cooling rates are similar for Vγ and IXγ, (34 ± 4.1 and 35 ± 3.1 °C Ma^{-1}) and lower for IIIγ and Xγ granite concerning their absolute value (13 ± 16.5 and 28 ± 39.5 °C Ma^{-1}). Nonetheless, these cooling rates are all identical within error (error determination in Appendix D). Comparing these cooling rates, particularly the Vγ and IXγ granites yielding small uncertainties, with high temperature metamorphic complexes (Bento dos Santos et al., 2010; 2014; Spear and Parrish, 1996), allows us to infer fast cooling conditions. In geodynamic settings where granitoid cooling is mainly driven by denudation, cooling rates are substantially lower, typically spanning from 0.5 to 5 °C Ma^{-1} (Ashwal et al., 1999; Bento dos Santos et al., 2010, 2014; Gallien et al., 2010; Munhá et al., 2005; Scibiorski et al., 2015). Cooling rates of the FCR–LAC granites are, therefore, compatible with rapid exhumation mechanisms and shallow crustal emplacement.

Gravity has been considered an important constrainer during the late stages of the collisional orogens, when the tectonic driving orogenic forces diminishes or ceases its influence (Jadamec et al., 2007). This leads to lateral release of potential gravitational energy characterizing the thickened crust, leading to orogenic collapse (Rey et al., 2001 and references therein). The pressure release associated with such collapse can be viewed as one of the triggering mechanisms for crustal partial melting. Yet, mantle to crust heat transfer and intra-crustal radioactive heating might also be considered as significant mechanisms behind crustal melting (Vanderhaeghe, 2009). Independent of the cause, partial melting triggers a significant strength/viscosity and density decrease, promoting the exhumation of migmatitic/granitic

complexes, which tend to form domes, emplaced at shallow crustal levels (Vanderhaeghe, 2009; Vanderhaeghe et al., 2018). This must be the case of the Tormes dome in the CIZ (Escuder-Viruete et al., 1994).

However, it is not yet clear how fast the exhumation caused by orogenic collapse can be (Scibiorski et al., 2015; Vanderhaeghe and Teyssier, 2001). Moreover, the interpretation of the fast cooling rates reported on this study can not be done without taking into account that the anatectic complex is delimitated by high-angle crustal-scale shear zones, which juxtapose side-by-side rocks with clearly distinct metamorphic grades, a structural architecture also evidenced by magnetotelluric imaging (see Fig. 7 in Alves Ribeiro et al. 2017). Granites and the associated high-grade metamorphic rocks preserve a low dipping non-horizontal transport lineation (6°–12°; Pereira et al. 2017), clearly indicative of a significant net vertical mass transfer when the 65–100 km lateral displacement is taken into account. Indeed, the associated migmatites of the FCR–LAC endured a significant tectonic exhumation, corresponding to a combined vertical displacement of 5–8 km (Pereira et al. 2017), which suggest that the granitic rocks within the complex must have endured the same tectonic uplift. Considering the upper Carboniferous geothermal gradient calculated by Pereira et al. (2017) for the FCR–LAC (42 °C km^{-1}), and taking into account the estimated closure temperatures and ages for zircon and apatite, the vertical exhumation of granitic rocks would have been, indeed, of ~ 8 km, thus reinforcing the idea of a common assisted tectonic exhumation for granites and migmatites inside the JPCSZ. Considering these ~ 8 km vertical exhumation required for the determined cooling rates, exhumation rates of 0.3–0.8 mm a^{-1} are obtained. Such exhumation rates are clearly faster than those inferred for erosional denudation of granitic plutons (0.16 mm a^{-1}; Yuguchi et al., 2017), but similar to granite exhumation rates in strike-slip shear zones (0.6–1 mm a^{-1}; Annen et al., 2006; Steenken et al., 2002; Zhang et al., 2004).

In conclusion, our unprecedented results for cooling and exhumation rates of the FCR–LAC granites clearly support the role of first-order shear zones in assisting the exhumation of mid-crustal rocks as has been described elsewhere (e.g. Bento dos Santos et al., 2010, 2014; Corsini and Rolland, 2009; Díaz-Azpiroz et al., 2014; Fernández et al., 2013; Pereira et al., 2017; Schulmann et al., 2008; Steenken et al., 2002), emphasizing the role of the JPCSZ in the emplacement of some Iberian collision-related Variscan granites. This mechanism should also be considered of utmost importance in intracrustal heat transfer, influencing the rheological behavior of the continental crust during and after collisional orogenesis.

5.5. CONCLUSIONS

The Variscan Orogeny dynamics was responsible for the emplacement of several plutono-metamorphic complexes in the Iberian Massif and other sectors of the European Variscan Belt. The Figueira de Castelo Rodrigo–Lumbrales Anatectic Complex (FCR–LAC) is an example of a plutono-metamorphic complex where the granite–migmatite association is delimited by two sinistral, east–west to ENE–WSW trending, first-order shear zones (Juzbado–Penalva do Castelo and Huebra shear zones).

New U–Pb zircon crystallization ages were determined for 5 different granite facies of this anatectic complex, yielding ages between 300 and 317 Ma, confirming that most of these granites formed during the syn-D_3 magmatic stage, with the exception of one late-tectonic granite facies which is clearly intrusive into the other facies and yet is affected by the late stages of Variscan shearing. Moreover, since these granites are genetically related with migmatites and both formed and exhumed together, these syn-D_3 crystallization ages (317 ± 2.1–313 ± 1.9 Ma) represent the maximum age (end of D_2 and beginning of D_3) and the duration of anatexis (*ca.* 5 Ma).

The inherited zircon population of these granites suggest that they are melting restites of units with Cadomian (650 to 550 Ma) and Upper Cambrian–Lower Ordovician (495 to 470 Ma) ages. In addition, these zircon age distributions reveal a protolith affinity with the Douro-Beiras Supergroup, as retrieved from the Spanish sector. It should also be noted a remarkable contribution of Upper Cambrian–Lower Ordovician ages, which point out to the contribution of metaigneous rocks of the Ollo de Sapo formation.

Combining the U–Pb zircon ages with the U–Pb apatite ages and their respective closure temperatures, it was possible, for the first time, to quantitatively constrain the emplacement conditions of the FCR–LAC granites. Zircon (317 ± 2.1–313 ± 1.9 Ma) and apatite (307 ± 10–288 ± 14 Ma) enable the calculation of cooling rates ranging from 13 to 35 °C Ma^{-1}. The closure temperatures of both geothermometers (zircon and apatite) allowed to estimate the emplacement of the studied granites at approximately 8 km of depth due to a fast exhumation mechanism. Such emplacement conditions are compatible with the transpressive shearing associated with the movement of the Juzbado–Penalva do Castelo shear zone, the most likely mechanism for the exhumation of the FCR–LAC (Pereira et al., 2017).

This novel application of zircon and apatite as petrochronometers, particularly in the CIZ where this approach was used for the first time, has proven to be useful in constraining the emplacement conditions (e.g., crystallization temperatures, cooling and exhumation rates) of

syn-tectonic, S-type granitoids. This new type of approach is, therefore, important to understand the behavior of the continental crust during orogenic processes.

CHAPTER 6. U-PB AGE CONSTRAINTS ON THE SOURCE, COOLING AND EXHUMATION OF A VARISCAN MIDDLE CRUST MIGMATITE COMPLEX FROM THE CENTRAL IBERIAN ZONE: INSIGHTS INTO THE VARISCAN METAMORPHIC EVOLUTION AND EDIACARAN PALEOGEOGRAPHIC IMPLICATIONS

J.A. Ferreira[1,2*]; I, Pereira[3,4]; T. Bento dos Santos [1,2]; J. Mata[1,2]

[1] Instituto Dom Luiz (IDL), Faculdade de Ciências, Universidade de Lisboa, Campo Grande, 1749-016, Lisboa, Portugal

[2] Departamento de Geologia, Faculdade de Ciências, Universidade de Lisboa, C6, Campo Grande, 1749-016 Lisboa, Portugal

[3] Université Clermont Auvergne, CNRS, IRD, OPGC, Laboratoire Magmas et Volcans, F-63000 Clermont-Ferrand, France

[4] School of Earth and Environmental Sciences, University of Portsmouth, Building Burnaby Rd Portsmouth P01 3QL, UK

Ferreira, J.A., Pereira, I., Bento dos Santos, T., Mata, J. *submitted*. U-Pb age constraints on the source, cooling and exhumation of a variscan middle crust migmatite complex from the Central Iberian Zone: insights into the variscan metamorphic evolution and Ediacaran paleogeographic implications. Precambrian Research

Abstract: The Figueira de Castelo Rodrigo – Lumbrales Anatectic Complex, a granite-migmatite complex located in the Iberian Variscan Belt delimited by two sinistral shear zones (Huebra and Juzbado-Penalva do Castelo shear zones), has been interpreted as a probable limit between the two Ediacaran-Cambrian basins that constitute the bulk of the Central Iberian Zone. We obtained thermochronological data on the anatectic complex in order to constrain the metamorphic events and constrain the relevance of the delimiting shear zones, as well as U-Pb detrital zircon signatures of both the anatectic and host rocks to assess detrital sources for the basins, thus constraining possible paleogeographic scenarios.

New U-Pb zircon and apatite ages for the migmatites allowed us to obtain a peak metamorphic age of the anatectic complex (316.8 ± 2.0 Ma), and to estimate their T-t evolution and exhumation conditions. Cooling rates ranged from 7 to 54 ºC/Ma, implying fast exhumation (0.2 to 1.3 $mm.a^{-1}$) and a vertical displacement of *ca.* 6 to 8 km, which is compatible with exhumation assisted by the two delimiting shear zones.

The U-Pb detrital zircon age distributions of the anatectic complex and the host Douro-Beiras Supergroup reveal an important Cadomian age component, and minor Neo-Mesoproterozoic to Archaean (up to 3.5 Ga) detrital components. The anatectic rocks in the complex exhibit an inherited zircon age distribution moderately similar to the Excomungada Formation of the Douro-Beiras Supergroup. The North and South domains of the Douro-Beiras Supergroup exhibit significantly distinct detrital zircon age populations, which are attributed to source variability from the late Neoproterozoic to the lower Cambrian, possibly implying a more restricted basin in the dependency of the inactive Cadomian arc. The zircon distribution ages of the Pinhão Formation are also compared to the Beiras greywackes and highlights contrasting sources and reinforces the existence of a physical barrier that inhibited older detrital components from reaching the Douro basin. Results, however, suggest that this physical barrier must be placed further south of the studied area.

Inherited zircon grains younger than 500 Ma retrieved from the anatectic rocks have been linked to the Ollo de Sapo (Lower Ordovician) magmatic intrusive rocks that melted alongside the metasedimentary units of DBSG during the Carboniferous, thus showing the existence of heterogeneous protoliths.

6.1. INTRODUCTION

Determining the timing of genesis and emplacement of granite-migmatite complexes is important to define the chronology of the higher temperature sections of the P-T-t paths

prevalent during orogenesis (e.g. Castiñeiras et al., 2008; Talavera et al., 2015; Yakymchuk, 2014). Additionally, zircon is known to survive anatexis, but to suffer only partial dissolution during the emplacement of granite magmas if the appropriate conditions are met (Bindeman and Melnik, 2016; Yakymchuk and Brown, 2014). Thus, comparison of inherited zircon populations offers an alternative way to access possible migmatite-granite links, as well as to identify metasedimentary protoliths and sources (e.g. Bea et al., 2007; Kitano et al., 2018).

The Variscan is seen as an example of a hot orogen during which the exhumation of mid-crustal rocks was common (e.g. Schulmann et al., 2008, 2002). In Europe, this orogen developed during the Middle-Upper Devonian to Late Carboniferous times as a consequence of the continental collision of Laurentia and Gondwana (e.g. Matte, 2001; Nance et al., 2012; Schulmann et al., 2014). This continental collision produced and exhumed high-grade mid-crustal metamorphic complexes, such as the Armorican Massif (St. Malo, France) (Milord et al., 2001), the Massif Central (France) (Ledru et al., 2001; Roger et al., 2015), the Bohemian Massif (Austria) (Vanderhaeghe, 2009) and several occurrences in Iberia (see below).

In the Iberian Massif, the southwestern branch of the European Variscan Belt, the Figueira de Castelo Rodrigo-Lumbrales Anatectic Complex (FCR-LAC) is an example of a granite-migmatite complex generated and exhumed during the Variscan Orogeny in the Central Iberian Zone (CIZ) (e.g. Díez Fernández and Pereira, 2016; Ferreira et al., 2019; Pereira et al., 2017). This anatectic complex has been studied by several authors recently (Díez Fernández and Pereira, 2017; Ferreira et al., 2019; Pereira et al., 2017, 2018) and has been shown as having an intricate evolution during the Variscan Orogeny, with its granitoids recording evidence for very fast cooling, which has been interpreted as connected to the movement of shear zones (the Huebra and Juzbado-Penalva shear zones) that delimit the anatectic complex (Ferreira et al., 2019). The idea that the entire anatectic complex was exhumed rapidly may be quite significant, because it is placed in the nearby region of the limit between the two major Neoproterozoic-Cambrian basins that constitute the most important sedimentary sequence of the CIZ, the Douro-Beiras Supergroup (DBSG). In fact, this anatectic complex and the surrounding shear zones were previously referred as possibly coincident with the physical boundary between the two basins, which, in this scenario, implies that the two delimiting shear zones would be the remnant of a pre-Variscan paleo-boundary (Iglesias and Ribeiro, 1981; Villaseca et al., 2014).

However, because stratigraphic correlations between Portuguese and Spanish metasedimentary units is still poorly developed, and structural studies (Dias da Silva, 2013; Silva, 2013) have been unable to solve this question, we aim at providing geochemical information capable of

contributing to this problematic in a two-fold way: a) by presenting new U-Pb zircon and apatite ages for the anatectic rocks of the FCR-LAC to constrain their migmatization and metamorphic peak ages, as well as the retrograde path ages and their cooling rates, thus defining their emplacement conditions within the framework of the Iberian Variscan Belt. This integrated geochronological study will provide a better understanding of the metamorphic evolution of this sector and of the real significance and relevance of the shear zones delimiting the anatectic complex during the exhumation path; and b) by presenting new U-Pb detrital zircon data from two units of the DBSG, one located north and the other south of the FCR-LAC. We explore this new data by comparing it to published detrital zircon data from potential stratigraphic equivalents in the Spanish sector and in the DBSG, and from the overlying Ordovician metasedimentary units. This approach allows the assessment of the evolution of the sedimentary sources during the Ediacaran – Cambrian – Ordovician, with implications on the paleogeographic and geodynamic evolution of the CIZ. We then provide a comparison between the detrital zircon populations of the DBSB with the inherited zircon ages retrieved from the anatectic complex lithologies (granites, metatexites and diatexites) in order to explore their genetic links, and better constrain their protoliths, providing further constraints on possible paleogeographic scenarios.

6.2. ANALYTICAL METHODS

We collected 8 samples of migmatites for U-Pb dating, 5 metatexites (JTJ-20, JTJ-25, JTJ-48B, JTJ-53, and JTJ-60A) 3 diatexites (JTJ-24A, JTJ-43, and JTJ-55), and 2 samples from the DBSG for detrital U-Pb zircon dating, one collected to the north of the FCR-LAC and the other to the south.

The mineral separation procedures were performed in the sample preparation laboratories of GeoFCUL – Departamento de Geologia, Universidade de Lisboa. Zircon and apatite crystals were picked from a 63 – 250 µm fraction, after heavy liquid and electromagnetic separation using the Frantz magnetic separator.

Further sample preparation took place at the University of Portsmouth for grain imaging, U-Pb dating and in-situ trace element analyses. Zircon and apatite grains were mounted in epoxy resin mounts, attached to metallic stubs with thin copper strips, and coated with a 1-nm pulverized gold film. The grains were observed using a ZEISS EVO10MA scanning electron microscope (SEM) at the University of Portsmouth (UoP). For backscatter electron (BSE) imaging, an accelerating voltage of 20 kV and 700 pA beam current was applied to reveal the

compositional zoning in the analyzed grains to identify inherited cores and rim overgrowths. Detrital zircon grains were imaged using a VPSE (CL) detector, using an accelerating voltage of 20 kV and 1 nA beam current to reveal internal structures.

U-Pb isotopic analyses were performed using an ASI RESOlution 193nm ArF excimer laser coupled to the ANALYTIK JENA Plasma Quant Elite quadrupole ICP-MS at UoP. For zircon U-Pb dating a beam spot size of 20 µm (cores) and 11 µm (smaller grains and rims) was preferred. Beam energy densities used ranged from 2.1 to 2.5 J cm−2, with a 2-Hz repetition rate. As for apatite, a beam spot size between 50 and 20 µm was used, with beam energy densities ranging from 2.8 to 3 J cm−2, and a 3-Hz repetition rate. For additional information on the analytical conditions used for the LA-ICP-MS analyses, see Appendix B1.

Plešovice was used as a primary standard for zircon from metatexites and diatexites. (337.13 ± 0.13 Ma; Sláma et al., 2007) whereas the Madagascar standard was used for apatite (473.5 ± 0.7 Ma; Thomson et al., 2012) (Appendix B2 and B5, respectively). 91500 (1062.4 ± 0.4 Ma; Wiedenbeck et al., 1995), and GJ1 (608.5 ± 0.4 Ma; Jackson et al., 2004) were used as zircon secondary standards (Appendix B3 and B4, respectively), whereas for apatite were used McClure (523.51 ± 2.09 Ma; Schoene and Bowring, 2006) and Xuxa (unpublished, ca. 572 Ma, provided by courtesy of C. Lana, Federal University of Ouro Preto) (Appendix B6 and B7). For all the above, reproducibility of the secondary standards was within 2%. For the detrital zircon analyses (DBSG), BB9 was used as primary standard (561 ± 2 Ma; Santos et al., 2017) (Appendix B9) while Plešovice, 91500 and GJ-1 as secondary standards with a reproducibility within 1%. (Appendix B10, B11 and B12, respectively)

IOLITE 3.31 software package was used for data reduction. A sample-standard bracketing method was used to correct for both instrumental drift and elemental mass fractionation. For zircon, Wetherill Concordia were calculated using ISOPLOT/EX 4.1 (Ludwig, 2003). From the youngest zircon population data, only grains that were 95-105% concordant were used to determine crystallization ages. For the detrital zircon statistical analysis were used ages within 90 – 110% of concordance, and <1000 Ma are used $^{206}Pb/^{238}U$ ages while >1000 Ma it is picked $^{207}Pb/^{206}Pb$ ages.

For apatite, the isotopic data was processed using VizualAge_UcomPbine DRS and measured ^{207}Pb (Chew et al., 2014). This data reduction scheme allows for common-Pb (Pbcm) correction of the primary standard based on their known radiogenic and variable Pbcm compositions. This correction is then applied to the unknowns. Apatite Tera-Wasserburg Concordia ages were determined using ISOPLOT/EX 4.1 (Ludwig 2003).

Trace element analyses in zircon were performed using the same instrument setup as for U–Pb, and a standard-sample bracketing method to correct for instrumental drift. The following isotopes were analysed: ^{29}Si, ^{31}P, ^{39}K, ^{40}Ca, ^{45}Sc, ^{49}Ti, ^{51}V, ^{52}Cr, ^{55}Mn, ^{85}Rb, ^{87}Sr, ^{89}Y, ^{90}Zr, ^{93}Nb, ^{95}Mo, ^{118}Sn, ^{121}Sb, ^{133}Cs, ^{137}Ba, ^{139}La, ^{140}Ce, ^{141}Pr, ^{146}Nd, ^{147}Sm, ^{153}Eu, ^{157}Gd, ^{159}Tb, ^{163}Dy, ^{165}Ho, ^{166}Er, ^{169}Tm, ^{172}Yb, ^{175}Lu, ^{177}Hf, ^{181}Ta, ^{182}W, ^{208}Pb, ^{209}Bi, ^{232}Th and ^{238}U.

A laser beam diameter of 40 μm for NIST612, 35 μm for secondary standards and 35–25 μm for unknowns was used, with beam energy densities ranging from 3.8 to 4.1 J cm−2, with a 4-Hz repetition rate. NIST612 was used as primary standard using concentrations by Jochum et al., (2011), whereas 91500 (Wiedenbeck et al., 1995) and GJ1 (Jackson et al., 2004) were used as secondary standards, as they are relatively homogenous in terms of trace element concentrations. Zr was used as an internal calibration standard, considering zircon stoichiometry (Zr = 43.1 wt%). Most analysed elements are within 10% and 5% accuracy relative to secondary standards published values, and ^{49}Ti is within 10% uncertainty of reported values, excluding uncertainties, with a detection limit of 3 ppm (Appendix B8).

6.3. RESULTS

6.3.1. Migmatites zircon U-Pb ages

Metatexites

Zircon grains of three samples of metatexite (JTJ-20, JTJ-25 and JTJ-60A) were analysed but only one sample provided metamorphic zircon that grew during Variscan times (JTJ-25; Appendix E1). In general, the analysed zircon population of the JTJ-25 sample exhibit a subhedral and elongated zircon morphology with {211} pyramids and {110} prisms (Figure 6.1a).

Twenty-four spots were analysed in the JTJ-25 sample using 13 zircon grains. The youngest concordant dates (12 cores and 1 rim) allowed to determine 314.8 ± 1.3 Ma (MSWD = 1.6) as the migmatization age (Figure 6.2a). Inherited ages were not obtained in this sample, yet the other two samples have 103 older cores with ages ranging from 445 (Upper Ordovician) to 3253 Ma (Mesoarchean/Paleoarchean).

Diatexites

JTJ-24A

The JTJ-24A zircon population is composed of 49 analysed grains. In general, younger zircon grains have subhedral and elongated shape. Few grains also reveal broad zoning. Morphologically, most of the grains occur with {101} pyramids and {100} prisms (Figure 6.1b). This sample yields a concordant age of 343.7 ± 2.5 Ma (MSWD = 0.84; n = 3; Appendix E1) (Figure 6.2b). Twenty-two older cores provided an age range between 524 Ma (Cambrian – Stage 2) and 2097 Ma (Mesoarchean).

JTJ-43

Fourteen zircon grains were ablated in this sample. Generally, the zircon population exhibit a subhedral morphology, with some grains elongated and others more oval, rarely with fine rims (7 – 14 µm) or fainting zoning. Additionally, the majority of the grains show {101} pyramids and {100} prisms (Figure 6.1c). The youngest zircon population is 328.8 ± 3.4 Ma (MSWD = 0.19; n = 3; Appendix E1) (Figure 6.2c). The inherited ages (7 cores) range from 579 Ma (Ediacaran) to 2643 Ma (Neoarchean).

JTJ-55

From the zircon population of this sample 42 grains were analysed. They display a subhedral, elongated and bipyramidal ({101} pyramids and {100} prisms) morphology (Figure 6.1d). Moreover, most of the grains exhibit faint oscillatory zoning and the rims thickness are between 15 and 31 µm. From 7 concordant young dates (3 cores and 4 rims; Appendix E1) was obtained the crystallization age of 318.8 ± 2.6 Ma (MSWD = 0.27) for this diatexite sample (Figure 6.2d). Eleven inherited concordant dates were determined with ages varying from 455 Ma (Upper Ordovician) to 2152 Ma (Paleoproterozoic).

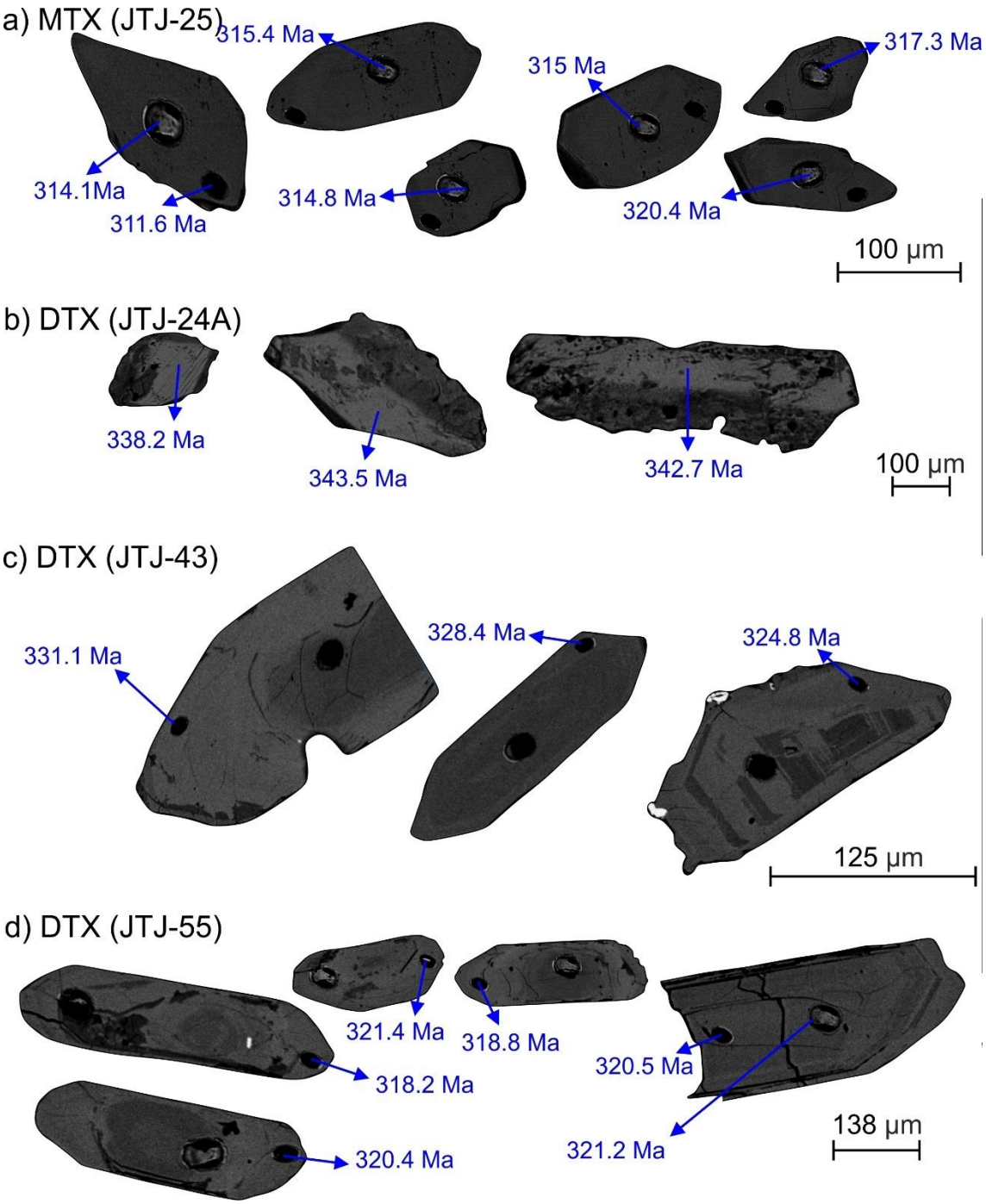

Figure 6.1 – Back-scattered electron images of representative zircon grains for the dated metatexite (MTX) and diatexites (DTX), showing the location of the analysed spots.

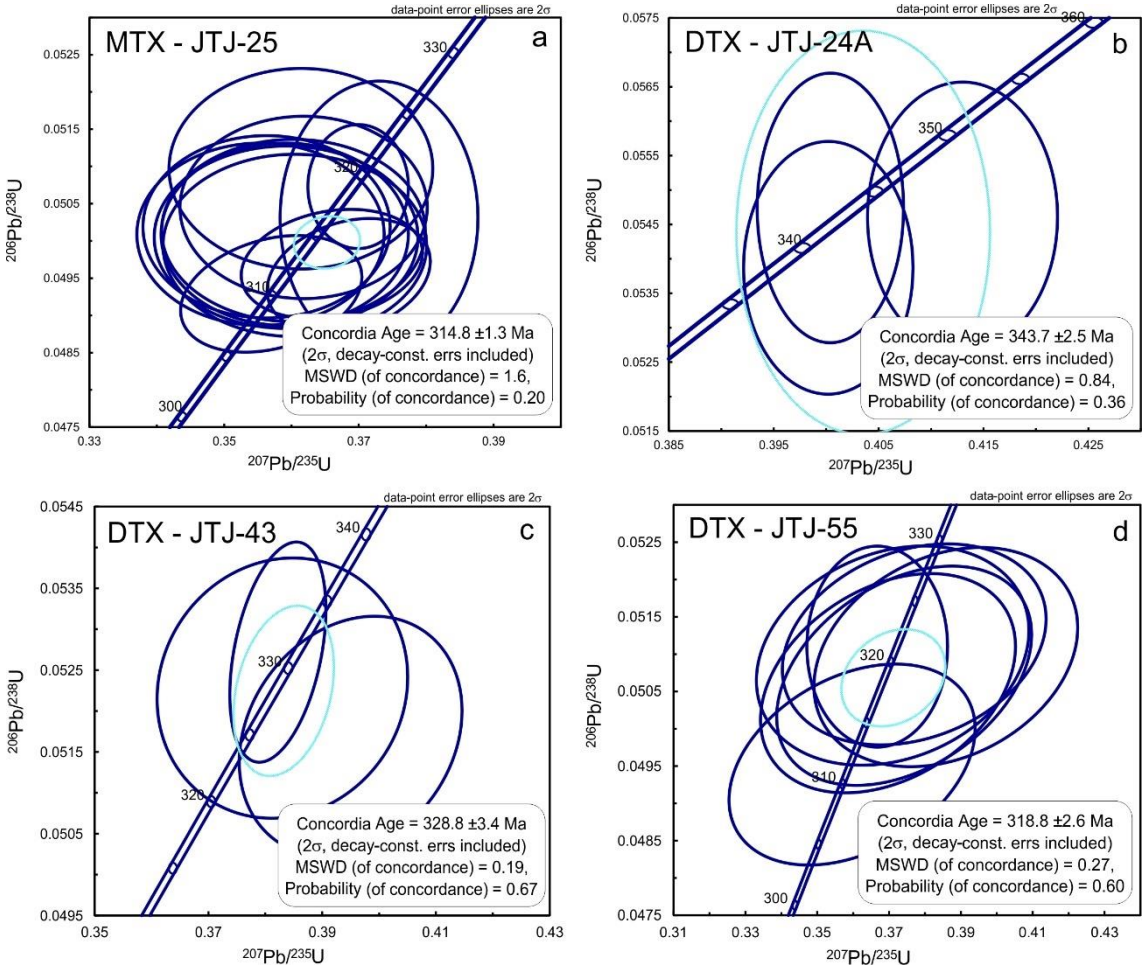

Figure 6.2 – Wetherill Concordia diagrams showing the U-Pb migmatization ages for the metatexite (MTX) and diatexites (DTX).

6.3.2. Ti-in-zircon geothermometer

We have applied the Ti-in zircon geothermometer to determine the metamorphic crystallization temperatures for the migmatites (Siégel et al., 2018; Watson et al., 2006; Table 6.1). These temperatures also represent the zircon closure temperatures since the diffusivity activity of this mineral reduces/stops with its crystallization. Thus, the Ti-in zircon thermometer temperatures are used to determine the migmatites cooling rates (see 6.4.2 section).

Table 6.1 – Ti-in-zircon thermometer for metatexite (MTX) and diatexites (DTX)

Ti-in-zircon thermometer				
Id	Ti (ppm)	stdev	T (ºC) Zircon	Uncertainty (ºC)
MTX	23.82	7.6	790	43
DTX (JTJ-24A)	8.00	3.3	716	48
DTX (JTJ-55)	36.40	2.2	869	21

Zircon growth/closure temperatures obtained for the migmatites are the following: metatexite = 790 ± 43 ºC; and diatexites = 716 ± 48 ºC (JTJ-24A) and 869 ± 21 ºC (JTJ-55) (Table 6.1). We were not able to analyse the trace element contents for the zircon population of one sample (JTJ-43), so its T_c is considered as the average of the T_c of the other two diatexite samples (JTJ-43 = 793 ± 14 ºC).

6.3.3. Inherited zircon ages in migmatites

A significant amount of inherited zircon ages was found in the FCR-LAC migmatites (Appendix E3). Considering the existent genetic link between all these rocks (Ferreira et al., under review), we have combined data into metatexite and diatexite groups. By doing so, metatexites zircon population includes 103 grains of inherited cores distributed by the following age groups: 450 – 500 Ma (n = 5); 500 – 650 Ma (n = 76); 650 – 1000 Ma (n = 18) and 2000 – 3500 Ma (n = 4). A lower number of inherited zircon grains were retrieved from diatexites (n=40), that are grouped as follows: 450 – 500 Ma (n = 6); 500 – 650 Ma (n = 22); 650 – 850 Ma (n = 3); 2000 – 2500 Ma (n = 3).

6.3.4. Migmatites apatite U-Pb ages

Apatites from metatexites, produced three suitable U-Pb dates for populations ranging from 8 to 25 grains. These grains have a mixed morphology that varies from prismatic subhedral to rounded anhedral shapes. Occasionally, the grains reveal zircon inclusions. For the diatexites (three samples), the apatite dates were determined using between 19 and 25 grains. As observed in the apatites from metatexites, many of the grains show a rounded anhedral shape and some prismatic subhedral morphology.

Apatite dates are plotted in the Tera–Wasserburg (TW) regression diagrams because they yield high and variable common Pb (Pb_{cm})/radiogenic Pb ratios (Appendix E2). The TW regression allows to determine the initial Pb_{cm} composition and apatite growth age. All the analysed grains per sample fall on an isochron in the TW diagram supporting their cogenetic nature.

TW Concordia lower-intercept apatite ages from metatexites yield: JTJ-20 (313 ± 11 Ma; MSWD = 0.75; Figure 6.3a), JTJ-25 (309.3 ± 3.2 Ma; MSWD = 0.49; Figure 6.3b), and JTJ-48B (309.6 ± 8.3 Ma; MSWD = 0.56; Figure 6.3c). The lower-intercept apatite ages of the diatexites are: JTJ-24A (303.7 ± 2.8 Ma; MSWD = 1.15; Figure 6.3d), JTJ-43 (314.3 ± 7.2 Ma; MSWD = 0.84; Figure 6.3e), and JTJ-55 (301.5 ± 8.2 Ma; MSWD = 1.04; Figure 6.3f). The apatite ages are younger than the zircon counterparts, when they exist, given that these ages

reflect the timing at which the apatite closure temperature (450-550 ºC; Schoene and Bowring, 2007) was reached after the metamorphic peak at T ≥ ca. 716 ºC (given from zircon ages; Table 6.1).

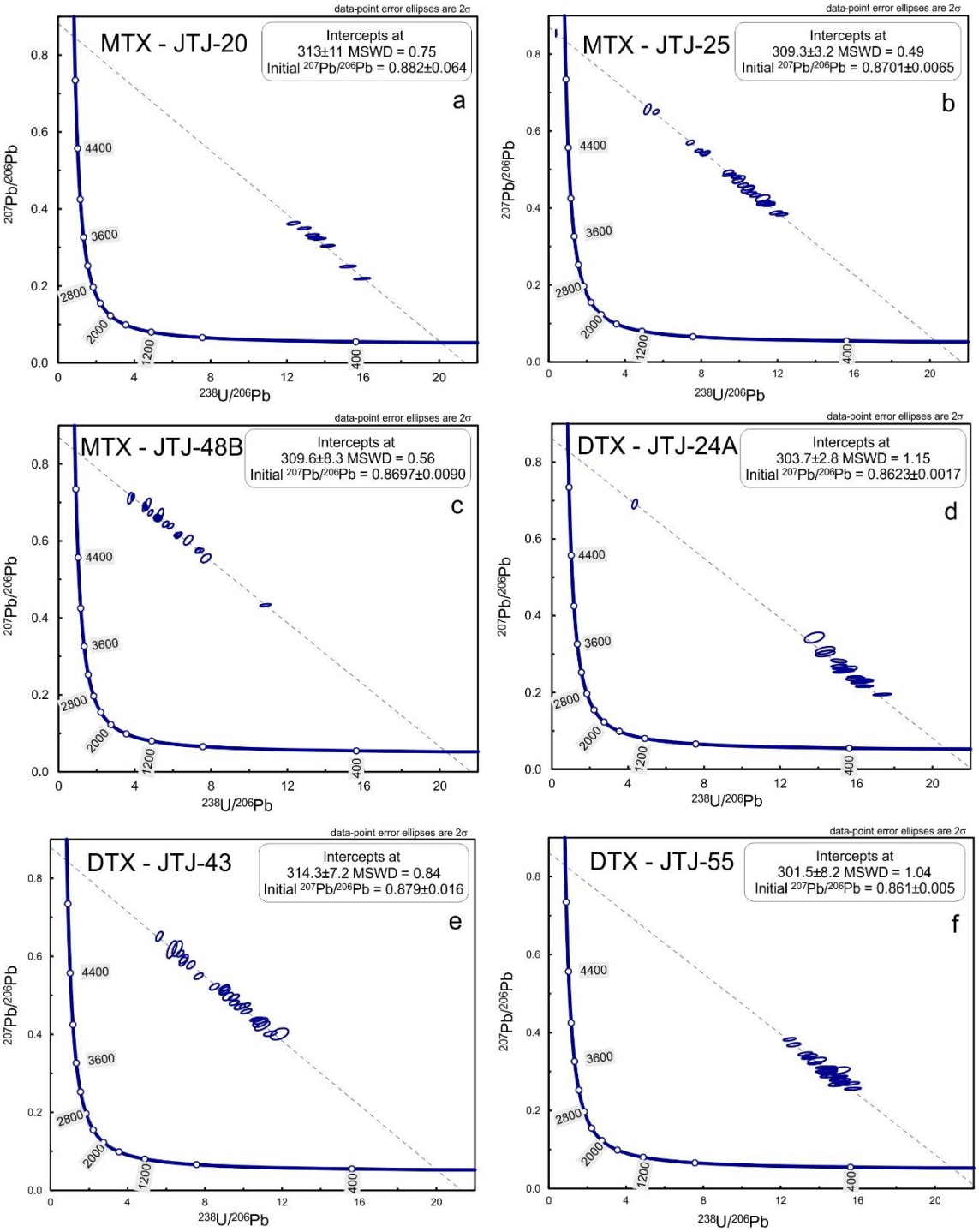

Figure 6.3 – Tera-Wasserburg U-Pb lower-intercept apatite ages for the metatexites (MTX) and diatexites (DTX).

6.3.5. Douro-Beiras Supergroup detrital zircon ages

The DBSG detrital zircons were analysed using one sample collected at the north (DBSG N – Pinhão Formation) and another one at the south (DBSG S – Excomungada Formation) of the anatectic complex (Appendix E4; Figure 6.4).

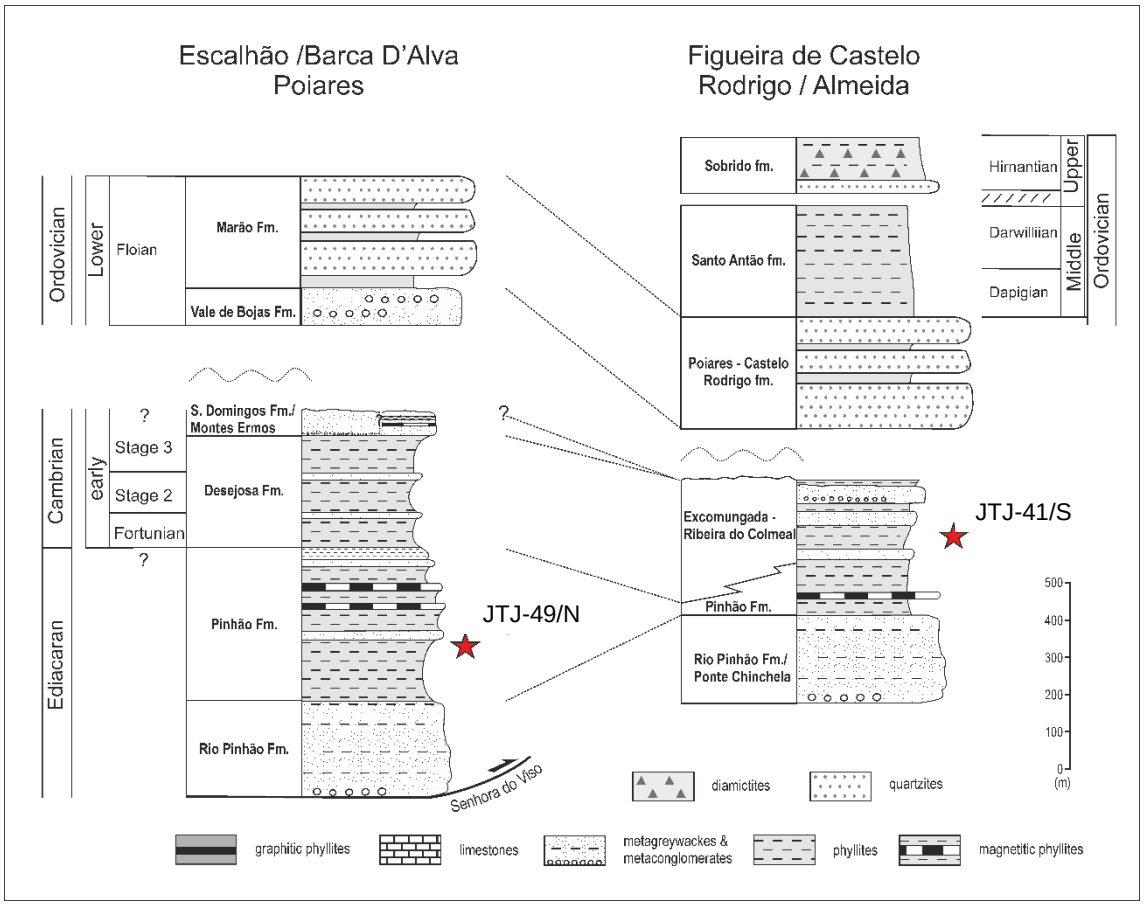

Figure 6.4 – Stratigraphic column with the position of the Douro-Beiras Supergroup samples analysed in this study (Dias et al., 2013; Sá et al., 2005; Silva, 2013).

Most of the grains of the Pinhão Formation are prismatic, euhedral to subhedral, bipyramidal and ranging between stubby and elongated shape. A minority of the grains have a rounded shape. Texturally, most of the grains exhibit a broad zoning and, occasionally, oscillatory zoning or weak/no zoning (Figure. 6.5a). This sample supplied 98 concordant ages (90 – 110% of concordance).

The U-Pb detrital zircon of the Pinhão Formation are dominated by Neoproterozoic ages (550-700 Ma; 65%), followed by zircon dates of the Paleoproterozoic ages (1814 – 2276 Ma; 10%), Neoproterozoic/Mesoproterozoic transition (930 – 1034 Ma; 8%), Mesoproterozoic ages (1212 – 1435 Ma; 2%), and minor Archean ages (2587 – 3209 Ma; 2%). The maximum depositional age ranges from 522.5 ± 9.3 Ma (youngest detrital zircon; Cambrian – Stage 2) to 573 ± 4.3 Ma (average age of the youngest cluster: 562 – 579 Ma; n = 6; upper Ediacaran).

In general, grains from the Excomungada Formation show prismatic and bipyramidal habit, euhedral to subhedral shape, and stubby and elongated crystals (a few of them are rounded). The grains also exhibit a wide range of internal structures: broad zoning, sector zoning, oscillatory zoning, and faint/no zoning (Figure. 6.5b). We were able to retrieve 117 U-Pb concordant zircon grains from the Excomungada Formation sample (90 – 110% of concordance).

The Excomungada Formation reveals a predominant U-Pb detrital zircon population of Cambrian/Neoproterozoic age (500-650 Ma; 84%) with minor Neoproterozoic/Mesoproterozoic transition ages (947 – 1007 Ma; 3%), Paleoproterozoic ages (2005 – 2041 Ma; 3%) and Archean ages (2548-3450 Ma; 3%). The maximum depositional age ranges from 506 ± 13 Ma (youngest detrital zircon; Cambrian – Wuliuan) to 523 ± 6.2 (average age of the youngest cluster: 515 – 529 n = 3; Cambrian – Stage 2).

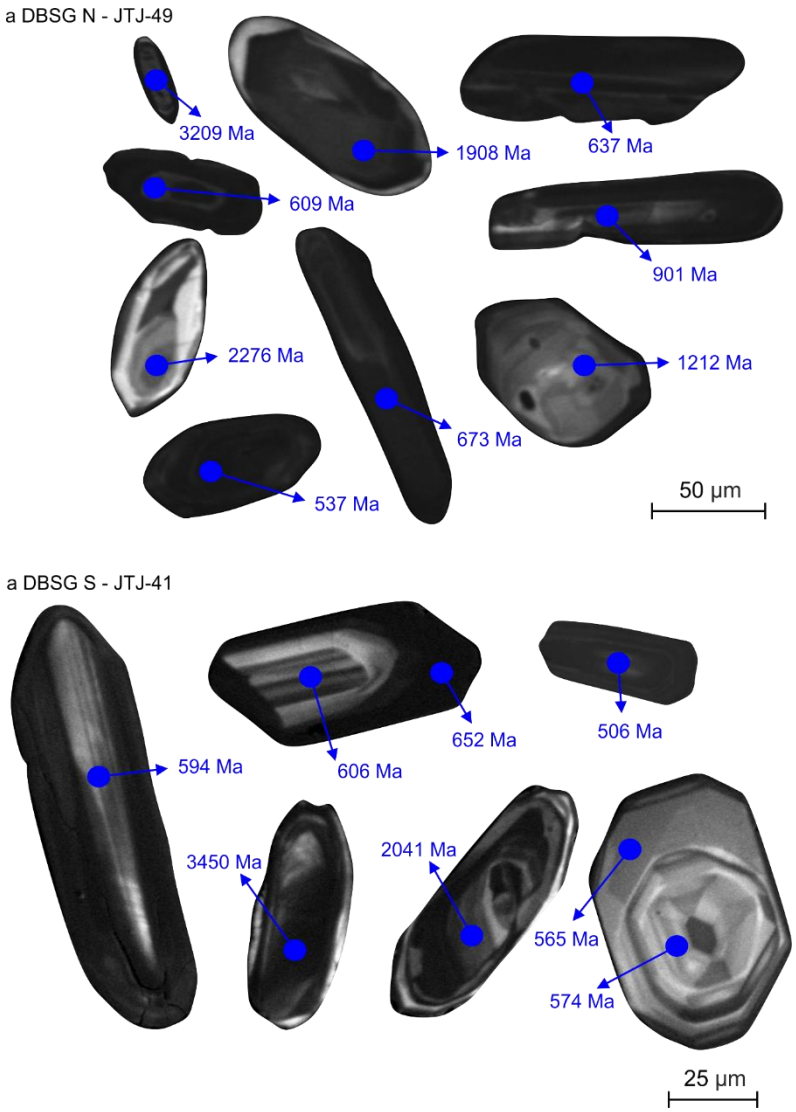

Figure 6.5 – Back-scattered electron images of representative zircon grains for the dated DBSG N – Pinhão Formation and DBSG S – Excomungada Formation.

6.4. DISCUSSION

6.4.1. Migmatization age

For the Serra da Freita migmatites (CIZ), Acciaioli et al. (2005) dated biotites and muscovites using the Ar-Ar method and constrained the metamorphic event to an age of 333.5 ± 4.4 Ma. Therefore, this age has been constraining the D_2 migmatization, while the granites installation is contemporaneous to the D_3 Variscan phase (Azevedo and Valle Aguado, 2013; Díez Fernández et al., 2012; Escuder-Viruete et al., 1998, 1994).

However, the zircon U-Pb ages retrieved from the FCR-LAC migmatites (metatexites and diatexites) in this study point to a more recent migmatization age and to a different temporal relation between migmatites and granites. The FCR-LAC metatexite exhibits a peak metamorphic age of 314.8 ± 1.3 Ma. Based on geochemical composition Ferreira et al. (*in revision*) divided diatexites in two groups, (type-1 and type-2; see section 7.3.1). Diatexites type-2 result from fluid-present melting reactions while diatexites type-1 were produced by fluid-absent melting reactions, which were mostly responsible for the genesis of granite plutons in the region. Taking into account that these authors considered that the fluid-present reactions occurred earlier and at lower temperatures than the fluid-absent reactions, the ages of the different type of migmatites should depict the temperature-time (T-t) relation characterizing the prograde metamorphic path. This is, in fact, observed with ages around 343.7 ± 2.5 Ma obtained for diatexite type-2 and 328.8 ± 3.4 Ma for a diatexite type-1, culminating in the metamorphic peak at 318.8 ± 2.6 Ma (diatexite type-1; Figure 6.2b to 6.2d). Therefore, there is a consistency between the partial melting reactions inferred by Ferreira et al. (*in revision*) and the ages obtained for the diatexites in this study.

The average age inferred from metatexites and diatexites for the metamorphic peak conditions is 316.8 ± 2.0 Ma. These data clearly point to a metamorphic peak synchronous with D_3 considering the deformation age intervals defined by Dallmeyer et al. (1997). This is at odds with the proposal by other authors (see above) but agrees with more recent results of the studies performed by Martínez Catalán et al. (2014) and Alcock et al. (2015), which consider that the migmatization age interval in the CIZ is 335 – 311 Ma, and 330 – 300 Ma, respectively. More importantly, these results emphasize that the metamorphic climax here inferred for the FCR-LAC (316.8 ± 2.0 Ma) is synchronous with the syntectonic granites crystallization/emplacement during the D_3 Variscan phase (313 ± 1.9 to 317 ± 2.1 Ma; Ferreira et al., 2019), indicating a short time period between melt generation and granite emplacement. Similar results and observations were obtained by Valle Aguado et al. (2005) for the Viseu batholiths within the CIZ. Additionally, Valverde-Vaquero et al. (2006) dated the HT-LP metamorphism in the Lumbrales Antiform (Salamanca) with ages between 316 and 314 Ma, contemporaneously with the D_3 plutonism, and in good agreement with the ages we report in this paper.

6.4.2. Cooling and exhumation rates

Accessory minerals are currently being used for countless studies in order to obtain significant petrological, geochemical and geochronological data, as well as critical information on the evolution of the crust, the mantle and the Earth itself (Cavosie et al., 2019; Pereira et al., 2020; Rubatto, 2017). In fact, combining the U-Pb metamorphic ages obtained from the zircons of the anatectic units, a mineral phase characterized by Pb closure temperatures in excess of 900 °C (Cherniak and Watson, 2001), with the U-Pb results obtained for apatites, whose closure temperatures are just under 500 °C (Cherniak et al., 1991), it was possible to determine the timing of both the metamorphic peak and of the retrograde conditions, by constraining the cooling and exhumation rates of this anatectic complex.

Dodson (1973) defined the closure temperature (T_c) as the temperature of a mineral at the time of its apparent ("freezing") age, which is calculated using the following equation:

$$E/RT_c = \ln [-AD_0RT_c^2/ \{a^2 (dT/dt) E\}], (6.1)$$

where E is the activation energy for the diffusion process, R is the ideal gas constant, T_c is the closure temperature, A is a numerical constant depending on the geometry of the grain (spherical or cylindrical), D_0 is the diffusion coefficient at infinitely high temperature, dT/dt is the cooling rate and a is an effective diffusion dimension (i.e. radius in the case of a sphere). In this study, closure temperatures are calculated using zircon and apatite diffusivity parameters compiled from Hodges et al. (2003). For more details about the estimation of closure temperatures we refer the reader to Maeda et al. (2011) and Ferreira et al. (2019).

Apatite closure temperatures (452 ºC – 492 ºC; Table 2) were iteratively calculated using Dodson's equation, while zircon closure temperatures correspond to the Ti-in-zircon temperatures (716 ºC – 869 ºC; Table1). Taking into account these temperatures and the ages above presented the obtained cooling rates for migmatites (7 to 54 ºC/Ma) encompass the range of values obtained for the associated S-type granites (13 – 35 ºC/Ma; Ferreira et al., 2019). These are high cooling rates in comparison to other high-temperature metamorphic complexes elsewhere (e.g. Ribeira Fold Belt (SE Brazil) – Bento dos Santos et al., 2010, 2015, 2014; Albany-Fraser Orogen (Western Australia) – Scibiorski et al., 2015; High Himalayan Crystallines (Sikkim, India) – Sorcar et al., 2014; Valhalla Complex (British Columbia, Canada) – Spear and Parrish, 1996). Yet, these cooling rates are within the upper range for Phanerozoic collisional orogens (5 to 50 ºC/Ma; Dunlap, 2000; Willigers et al., 2002).

Considering the upper Carboniferous geothermal gradient of 42 ºC.km^{-1} (Pereira et al., 2017) and the difference between zircon and apatite closure temperatures, we estimate a vertical displacement of 6 to 9 km. This vertical displacement and emplacement at shallower levels of the crust (host rocks are preserved in the biotite zone; *ca.* 400 ± 50 °C) is similar with the modelled displacement calculated for the FCR-LAC due to simple-shear dominated transpression of the JPCSZ (Pereira et al., 2017). By combining zircon and apatite ages and assuming 6 to 9 km of vertical displacement to reach apatite closure temperatures and emplacement depth we determine exhumation rates between 0.2 and 1.3 mm a^{-1}. Such rates are clearly higher than erosional rates (< 0.03 mm.a^{-1}; Matmon et al., 2003) and are typical of tectonically-assisted exhumation mechanisms (channel flow – 1 mm.a^{-1} – Annen et al., 2006 and Zhang et al., 2004; detachment fault – 0.2 to 6 mm.a^{-1} – Buscher et al., 2013 and Singleton et al., 2014; strike-slip fault – 0.4 to 6 mm.a^{-1} – Steenken et al., 2002).

As concluded to the granite exhumation in the Ferreira et al. (2019) study, the anatectic complex exhumation was tectonically-assisted where the Huebra and the Juzbado-Penalva do Castelo shear zones had an important role.

Table 6.2 – Zircon and apatite estimated closure temperatures and the respective cooling and exhumation rates, for granites (IIγ to Xγ) (Ferreira et al. 2019), diatexites (DTX) and metatexite (MTX).

Id	Zircon Age (Ma)	Apatite Age (Ma)	Zircon T_c (ºC)	Apatite T_c (ºC)	Cooling Rate (ºC/Ma)	Exhumation Rate (mm.a^{-1})
IIγ	300 ± 2.2	301 ± 2.6	-	-	-	-
IIIγ	314 ± 2.6	288 ± 14	814*	465	13 ± 16.5	0.3
Vγ	316 ± 3.9	306 ± 8.5	825	482	34 ± 4.1	0.8
IXγ	317 ± 2.1	307 ± 10	836	483	35 ± 3.1	0.8
Xγ	313 ± 1.9	302 ± 5.6	783	478	28 ± 39.5	0.7
DTX	319 ± 2.6	302 ± 8.2	869	475	23 ± 27	0.5
DTX	329 ± 3.4	314 ± 7.2	793*	474	22 ± 42	0.6
DTX	344 ± 2.5	304 ± 2.8	716	452	7 ± 2	0.2
MTX	315 ± 1.3	309 ± 3.2	790	492	54 ± 170	1.3

*value estimated by the average of the other temperatures for the same type of rocks.

6.4.3. Inherited and detrital zircon: comparison and source constraints

For the FCR-LAC migmatites the most dominant zircon age population (*ca.* 70%) is constrained between 500 and 650 Ma (Cambrian – Cryogenian) (Figure 6.10). This is in accordance with published zircon data for the spatially associated S-type granites (Ferreira et al., 2019), thus reinforcing the genetic link between these rocks proposed by these authors.

More complex is the definition of putative metasedimentary sources from inherited migmatite zircons. The first approach to compare detrital zircon data sets and, thus, define similarities/dissimilarities between them can be made using the Kernel Density Estimation (KDE) and the Cumulative Distribution Function (CDF), which reveal the age distribution of each data set. This approach is essentially qualitative/visual, so a quantitative/statistical method is needed to give further robustness to a study.

In searching a statistic test to evaluate the similarity between data set, Saylor and Sundell (2016) concluded that the cross-correlation of PDPs (Probability Density Plots) is the best method since it fulfils all the criteria of sample similarity assessment. The cross-correlation of PDPs provide a coefficient (R^2) resultant of the determination of a cross-plot of PDPs. The cross-plot evaluate the presence or absence of age peaks and the changes in the relative magnitude or shape of the peaks. The R^2 value of the cross-plot is equal to 1 for samples with identical age spectra, i.e. identical age peaks, peak shapes, and peak magnitudes; the R^2 coefficient is close to 0 for those samples that share no age peaks; for R^2 between 0 and 1, samples share some peaks, or have peaks of different magnitudes or shapes, with a higher R^2 value for samples that are more similar. This method is here applied using a MATLAB-based application, DZstats (2.3 version), created by Saylor and Sundell (2016).

Detrital zircon age distribution: Douro-Beiras Supergroup, Spanish lateral equivalents and Lower Ordovician Quartzites comparison

Stratigraphic correlations between the Portuguese and Spanish sectors are not very well constrained. In part, this reflects the scarcity of preserved fossils, which has inhibited cross-correlations between different units. Moreover, correlations between the Douro and Beiras Groups of the DBSG are tenuous and deposition ages have rarely been obtained. In this section, we tentatively compare units which are most probably stratigraphic lateral equivalents from the different sectors. Our aim is to explore these correlations using the maximum depositional ages (MDA), the Kernel Density Estimate (KDE) and the Cumulative Distribution Function (CDF) of detrital zircon from this study and published data, thus improving the current framework.

Firstly, we compare the metasedimentary formations (Pinhão and Excomungada Fms.) in contact with the anatectic complex, respectively to the North (DBSG N) and to the South (DBSG S) with their equivalent sequences in the Spanish sector, through detrital age distributions and MDA. The Pinhão Formation (DBSG N) can be envisaged as equivalent to

the Monterrubio Formation – Lower Series. Yet the Pinhão unit yields a slightly older MDA (572.8 ± 4.3 Ma) than the Monterrubio Fm. (MDA = 555 ± 14 Ma; Fernández-Suárez et al., 2014). Because these units were formed in the dependency of an active arc (Linnemann et al., 2008), their MDA are a good estimate of true deposition age implying that the Monterrubio Formation is at least partially younger than the Pinhão Formation. The KDE of the Pinhão Formation and the Monterrubio Formation – Lower Series (Figure 6.6) show the same age peaks between 900 and 1000 Ma, but the cluster around the 800 Ma age peak is only evident in the Lower Series, corresponding to a pronounced trough in the Pinhão Formation. Both units share the absence of Mesoproterozoic ages. The CDF of both sequences are broadly similar but reveal a variable distribution between the 800 and 1000 Ma interval (Figure 6.6). Quantitatively, the cross-correlation (R^2) between the Pinhão Formation and the Lower Series is 0.84 (Table 6.3).

The Excomungada Formation (DBSG S) with a MDA = 522.9 ± 6.2 Ma has been correlated with the Tamames Sandstone (MDA = 553 ± 4 Ma; Fernández-Suárez et al., 2014) and to the Desejosa Formation in the Douro Group (MDA = 516 ± 25 – 537 ± 22 Ma; Teixeira et al., 2013). Variation in the MDA might be due to sampling at different stratigraphic levels within these units, but implies that the Excomungada and the Desejosa Fms. are as young as the Tamames Sandstone. This is in good agreement with trace fossils retrieved from the Desejosa Fm. and the Tamames Sandstone (Dias da Silva et al., 2014; Liñan et al., 2015).

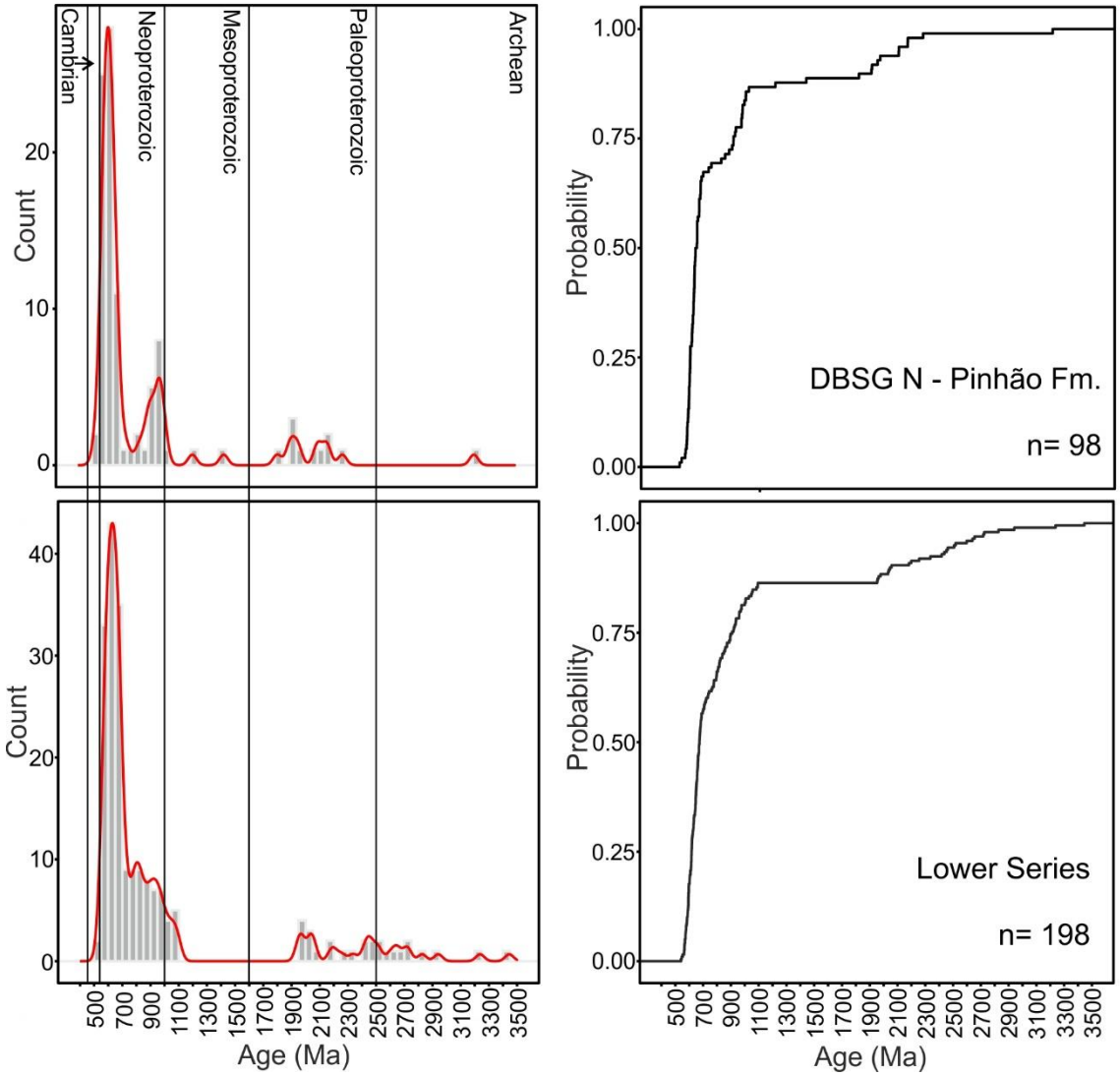

Figure 6.6 – Kernel Density Estimate (left) and Cumulative Distribution Function (right) plots for detrital zircon ages of the Pinhão Formation and the Lower Series (Monterrubio Formation; Fernández-Suárez et al., 2014) The KDE and CDF plots were performed with the support of the detzrcr package (Andersen et al., 2018).

The Tamames Sandstones yields a very high proportion of Cadomian age zircon grains, similarly to the Excomungada Fm. However, the Tamames Sandstone yields a higher proportion of *ca.* 800 Ma zircon grains and in the 900-1000 Ma age interval than the Excomungada Formation (Figure 6.7). The absence of Mesoproterozoic ages is only observed in the Excomungada Formation, implying that its source lacked such ages. The CDF patterns of these formations is broadly-similar with the main difference constrained in the 700-1100 Ma age interval (Figure 6.7). Their cross-correlation coefficient shows high similarity (R^2 = 0.95; Table 6.3), despite the difference mentioned above. These reflect a small variation in the source of these units, with slightly older basement exposed in the Tamames Sandstone basin catchment area (Figure 6.7).

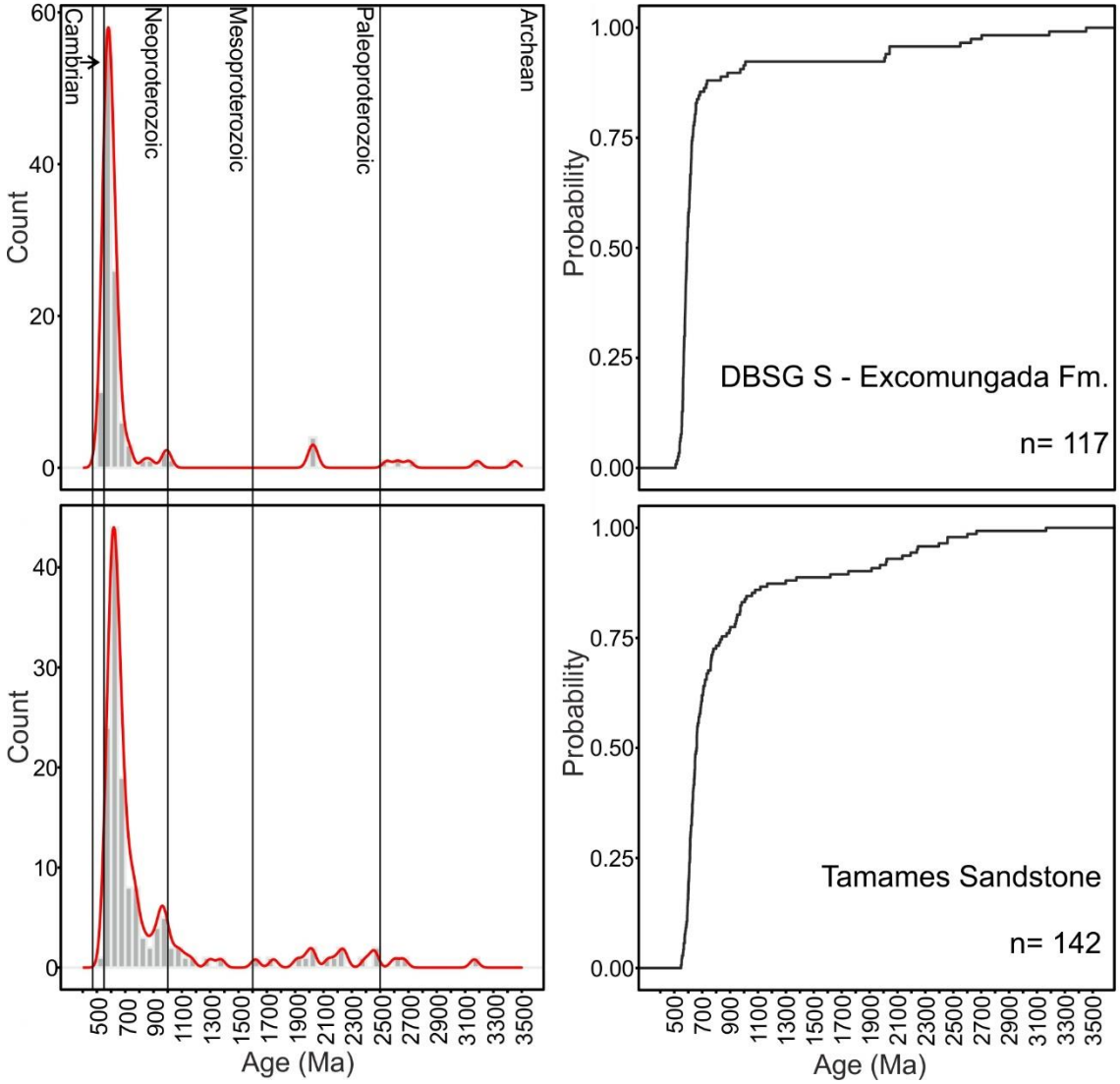

Figure 6.7 – Kernel Density Estimate (left) and Cumulative Distribution Function (right) plots for detrital zircon ages of the Excomungada Formation and the Tamames Sandstone (Fernández-Suárez et al., 2014) The KDE and CDF plots were performed with the support of the detzrcr package (Andersen et al., 2018).

As mentioned, the stratigraphic correlations between the Douro and Beiras Groups are generally weak. Given the similar MDA ages of the Pinhão Formation (572.8 ± 4.3 Ma) and the Beiras Group greywackes (PNC-1: 560.3 ± 6.6 Ma; PNC-2: 578.5 ± 4.3 Ma; Pereira et al., 2012a), we provide a more thorough comparison between these samples. The most important age peak in the three samples still correspond to the interval between 500 and 700 Ma, but arguably the age peak in the Pinhão Formation is younger and narrower in comparison to the equivalent units of the Beiras Group. PNC-2 sample stands out due to the double peak at 600 and 800 Ma, with the latter absent in the Pinhão Fm. Oppositely, the 1000 Ma age peak in the Pinhão Formation and the PNC-1 sample are not represented in PNC-2 (Figure 6.8). The presence of Paleoproterozoic and Neoarchean peak ages is more widespread in the Beiras Group Greywackes than in the

Pinhão Formation, implying partial derivation of an older basement to the Beiras basin. The CDF for the Beiras Group Greywackes and the Douro Group units reveal dissimilar patterns between the two DBSG groups (Figure 6.8). The cross-correlation coefficients support this dissimilarity: Pinhão Formation/PNC-1 (R^2 = 0.19) and Pinhão Formation/PNC-2 (R^2 = 0.22; Table 6.3). This is suggestive of a significantly different source. The Beiras basin detrital components were derived from active and dismantled Cadomian arc(s), with minor contributions from older basement of Paleoproterozoic and Neoarchean ages variably reworked during the Rodinia assembly. Unlikely, the Pinhão Formation reflects a potentially more restricted source involving the active arc and a Paleoproterozoic source probably reworked at 1000 Ma.

Table 6.3 – Cross-correlation coefficients of PDPs for Douro-Beiras Supergroup North and South domains (DBSG N – Pinhão Formation and DBSG S – Excomungada Formation, respectively); Lower Series (Monterrubio Formation); Tamames Sandstones (Fernández-Suárez et al., 2014); Beiras Group Greywackes (PNC-1 and PNC-2; Pereira et al., 2012a) and Armorican Quartzites (Armorican Qtz: PNC-4; Pereira et al., 2012a; LAZ-26 and LAZ-05; Shaw et al., 2014)

						Beiras Group		Armorican Qtz		
		DBSG N n=98	**DBSG S n=117**	**Lower Series n=198**	**Tamames Unit n=142**	**PNC-1 n=110**	**PNC-2 n=102**	**PNC-4 n=50**	**LAZ-26 n=141**	**LAZ-05 n=134**
	DBSG N	1								
	DBSG S	0.95	1							
	Lower Series	0.84	0.83	1						
	Tamames Unit	0.93	0.95	0.89	1					
Beiras Group	**PNC-1**	0.19	0.19	0.47	0.35	1				
	PNC-2	0.22	0.23	0.58	0.30	0.60	1			
Armorican Qtz	**PNC-4**	0.61	0.69	0.63	0.66	0.25	0.27	1		
	LAZ-26	0.90	0.92	0.92	0.97	0.40	0.40	0.71	1	
	LAZ-05	0.30	0.36	0.28	0.33	0.13	0.09	0.83	0.38	1

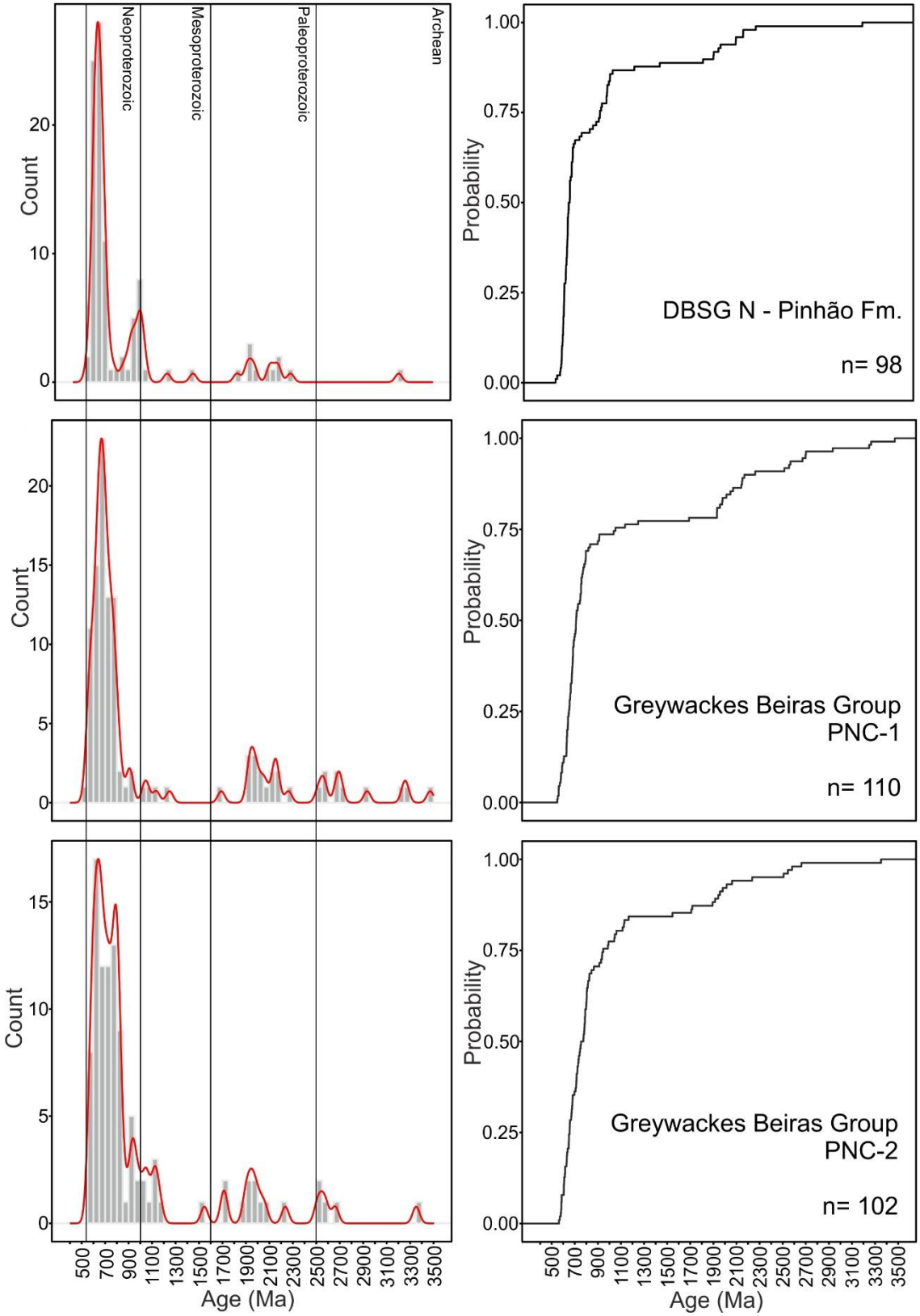

Figure 6.8 – Kernel Density Estimate (left) and Cumulative Distribution Function (right) plots for detrital zircon ages of the Pinhão Formation and the Beiras Group greywackes (PNC-1 and PNC-2; Pereira et al., 2012a). The KDE and CDF plots were performed with the support of the detzrcr package (Andersen et al., 2018).

From the Pinhão to the Excomungada Formation there is a decrease of an older component, namely the age peak constrained between the 900-1100 Ma age interval, as well as a decrease in the Paleoproterozoic aged zircon grains (as observed in the Desejosa Fm. – 3.0 to 5.8% – Teixeira et al., 2013). This could suggest a closer proximity to the arc during the lower Cambrian or a barrier that prevents older detrital components from reaching the basin where the Excomungada Formation was being deposited.

To assess the evolution of the sources from the Ediacaran/Cambrian to the Ordovician, we also compare the Pinhão and Excomungada Formations with the overlying sedimentary sequence of the Lower Ordovician Armorican Quartzite, which has been interpreted as being deposited in a passive margin setting during the opening of the Rheic Ocean (e.g. Nance et al., 2012).

In general terms, the KDEs of the Armorican Quartzite are broadly quite similar to that of the Pinhão Formation. In all three Ordovician units, there are detrital zircon with 800 Ma and also the 900-1000 Ma age interval (Figure 6.9). Unlike the Excomungada Formation, the Armorican Quartzites exhibit older detrital zircon of Paleoproterozoic and late Archean ages (Figure 6.9). The CDF age distribution of the Armorican Quartzite (LAZ-26 sample) is very similar to the Pinhão Formation CDF (Figure 6.9), and it is clear that all units except the Excomungada Formation yield a significantly older inherited component (Figure 6.9). The cross-correlation coefficients give high similarity for the following group of samples: Pinhão Formation/Armorican Quartzite LAZ-26 (R^2 = 0.90); Pinhão Formation/Armorican Quartzite PNC-4 (R^2 = 0.61; Table 6.3); Excomungada Formation/Armorican Quartzite LAZ-26 (R^2 = 0.92); Excomungada Formation/Armorican Quartzite PNC-4 (R^2 = 0.69). All these observations indicate that the underlying DBSG – Douro Group and the Armorican Quartzite, although deposited at different times, shared the same detrital sources or a common paleogeography (Shaw et al., 2014). Pereira et al. (2012a) identified affinities among the Armorican Quartzites in SW Iberia and the Beiras Group greywackes. The authors suggested that the Armorican Quartzite detrital zircons derived from recycling of the Ediacaran greywackes of the Beiras Group, which is a very likely explanation, due to the strong correlation coefficients and CDFs between these units, despite the significantly distinct age and depositional setting. This assumption is also valid to the Douro Group samples analysed in this study.

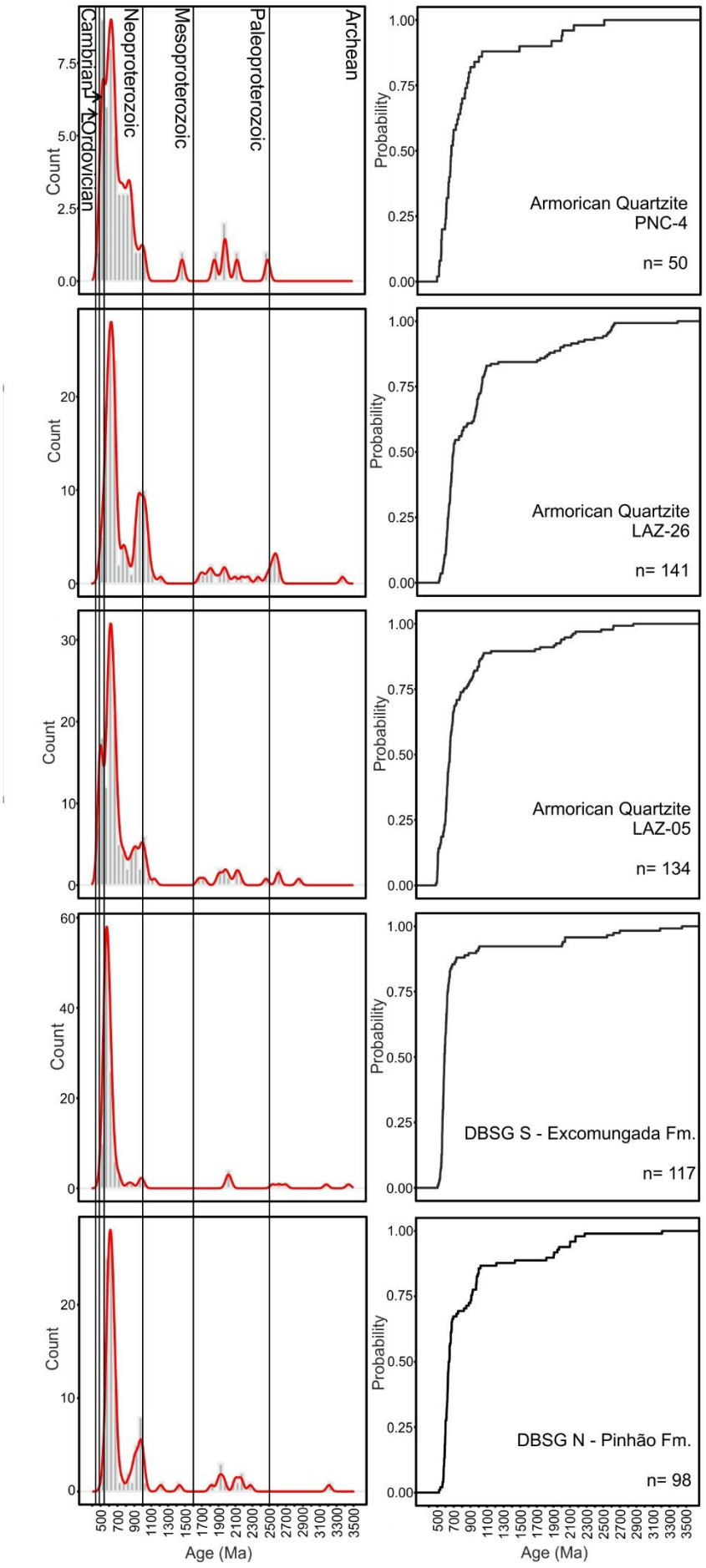

Figure 6.9 – Kernel Density Estimate (left) and Cumulative Distribution Function (right) plots for detrital zircon ages of the Pinhão and Excomungada Formations and the Armorican Quartzites (PNC-4 - Pereira et al., 2012a; LAZ-26 and LAZ-05 - Shaw et al., 2014). The KDE and CDF plots were performed with the support of the detzircr package (Andersen et al., 2018).

Inherited and detrital zircon age distribution: FCR-LAC, Ordovician, and Cambrian – Ediacaran comparison

Inherited zircon ages from migmatites have the potential to indicate the most probable source of these rocks. As previously referred, the detrital zircon age population of the FCR-LAC migmatites is dominantly (70%) composed of ages between 500 and 650 Ma (Cambrian – Cryogenian; Figure 6.10). The obtained range of inherited ages for the FCR-LAC migmatites is identical to that found in the detrital zircon age distribution of the siliciclastic Douro-Beiras Supergroup, which has been considered sourced on a North Gondwana Cadomian magmatic arc (Orejana et al., 2015; Pereira, 2015). The influence of the Cadomian arc in the DBSG sedimentation is also confirmed by the trace element composition of the DBSG and FCR-LAC metasediments whose La-Th-Sc and Th-Sc-Zr/10 ratios are compatible with a continental arc setting basin discrimination (see section 7.4.1; Ferreira et al., *in revision*).

Furthermore, migmatites reveal a statistically significant group of ages between 450 and 500 Ma (Upper Cambrian/Upper Ordovician; n = 11), which was also found in the associated anatectic granites (Ferreira et al., 2019; n = 9). These ages are commonly attributed to the Cambro-Ordovician Ollo de Sapo magmatic events (García-Arias et al., 2018). The youngest detrital zircon from the CIZ Ordovician quartzites (equivalent to the Marofa syncline quartzite; Meireles et al., 2006) yields 480 – 500 Ma (Pereira et al., 2012b; Shaw et al., 2014). Since these ages (480 – 450 Ma) are not represented within the siliciclastic units of the DBSG, thus cannot be related to deposition, we can interpret the presence of such age group in migmatites and granites as representing the melting, during Variscan times, of cryptic Ordovician magmatic rocks that previously had intruded the DBSG units at depth (as in Sánchez-García et al., 2019).

A comparison of the FCR-LAC detrital zircon data set with the Ordovician Quartzite (Pereira et al., 2012a; Shaw et al., 2014) and the Ediacaran-Cambrian formations is made in Figure 6.10 and 6.11. The Ediacaran-Cambrian formations include the DBSG data sets of this study, plus the Spanish lateral equivalent formations organized according to the data presented previously: Cambrian data set – Excomungada Fm. plus Tamames Sandstones (Fernández-Suárez et al., 2014); Ediacaran data set – Pinhão Fm. plus Lower Series (Monterrubio Fm.; Fernández-Suárez et al., 2014).

The KDEs (Figure 6.10) reveal similarities for diatexites and granites with the Ordovician data set, particularly for the Ordovician-Cambrian transition. In addition, the FCR-LAC rocks show similitude with the Cambrian data set (Figure 6.10 and 6.11).

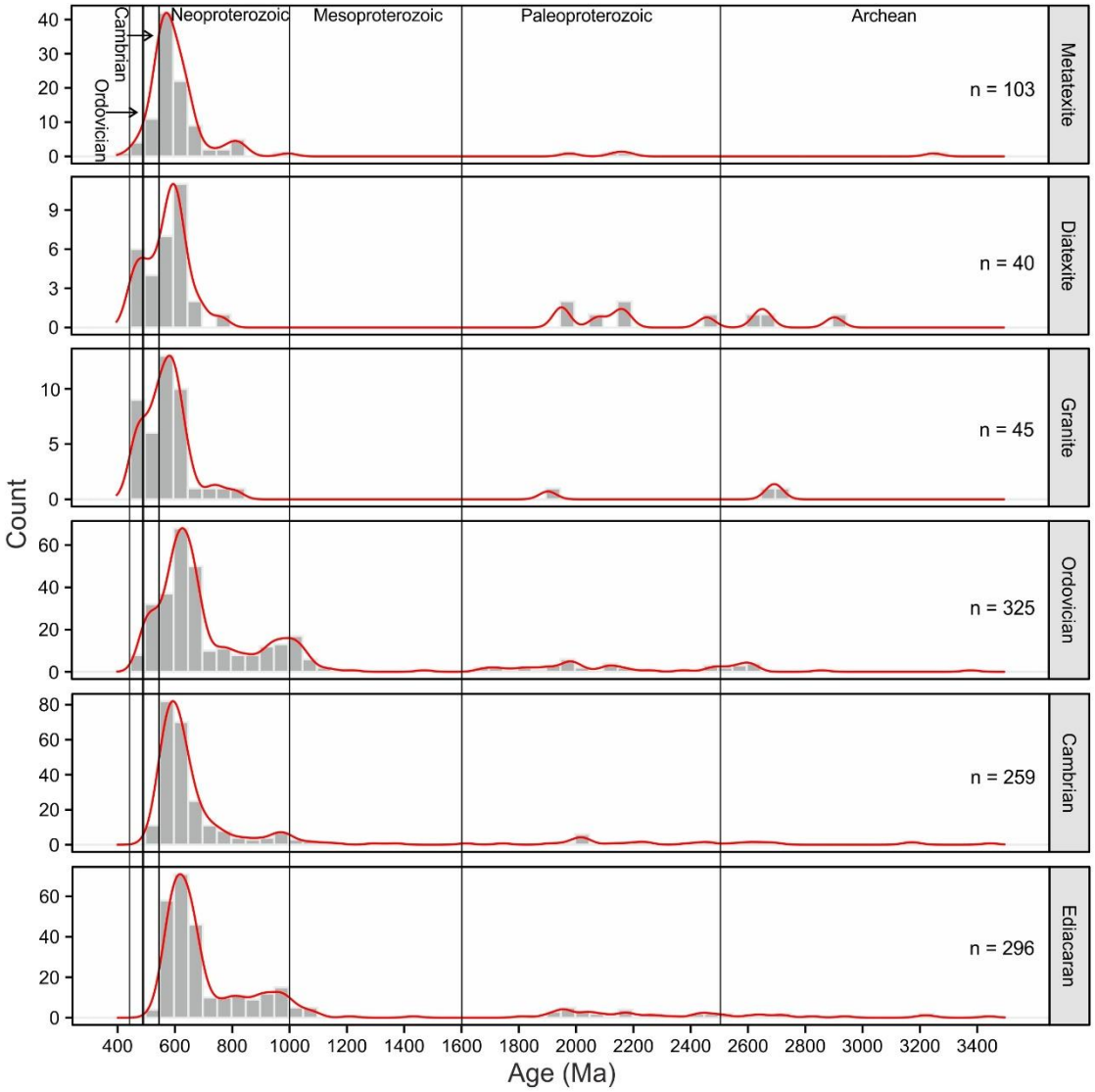

Figure 6.10 – KDE plots for the FCR-LAC, Ordovician (Pereira et al., 2012a; Shaw et al., 2014), Cambrian (Fernández-Suárez et al., 2014), and Ediacaran (Fernández-Suárez et al., 2014) data sets. The KDE plots were performed with the support of the detzrcr package (Andersen et al., 2018).

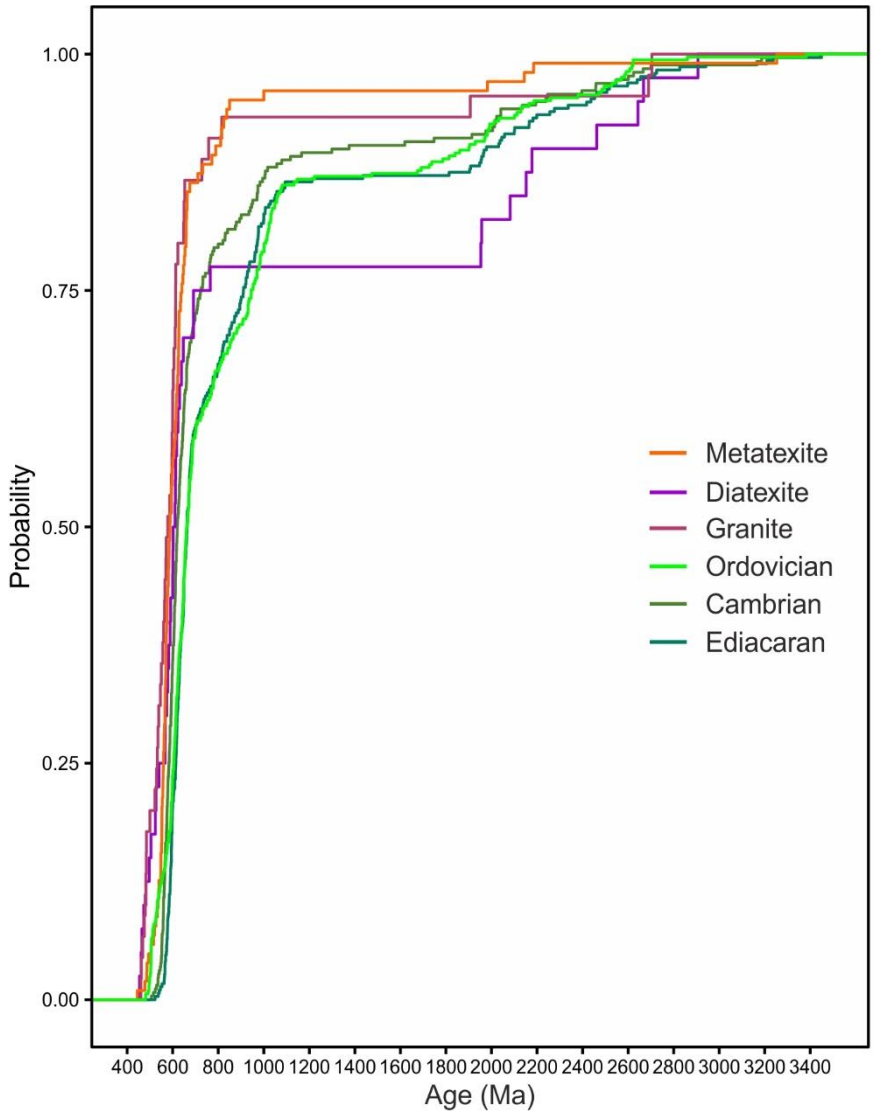

Figure 6.11 – CDF plot for the FCR-LAC, Ordovician (Pereira et al., 2012a; Shaw et al., 2014), Cambrian (Fernández-Suárez et al., 2014), and Ediacaran (Fernández-Suárez et al., 2014) data sets. The CDF plot was performed with the support of the detzrcr package (Andersen et al., 2018).

When the cross-correlation coefficient of PDPs are applied to the FCR-LAC, Ordovician, Cambrian and Ediacaran data sets (Table 6.4), a high similarity between the metatexites (the lower-grade rocks of the anatectic complex) and the Cambrian formations stands out (R^2 = 0.83). The diatexites and granites also reveal high similarity with the same formations, but with lower cross-correlation coefficients, 0.61 and 0.59, respectively. The metatexites detrital age distribution is too similar with Cambrian data set since metatexites have an inherited structure (paleosome bands) and geochemical composition inherited from the Cambrian unit (Metatexites εHf_{320} = -4.45 to -8.47; Excomungada Fm εHf_{320} = -7.16; see section 7.2.2; Ferreira et al., *in revision*). Concerning the diatexites and granites, the similarity is moderate

comparing with the Cambrian units because these rocks are formed at a higher temperature than the metatexites, so the source characteristics were obliterated. The metatexites and diatexites also exhibit a moderate similitude with Ediacaran units, 0.54 and 0.48, respectively. Regarding the Ordovician units, only the diatexites reveal some resemblance with these units showing a moderate cross-correlation coefficient (R^2 = 0.47), which is not surprising given the pelitic character of the FCR-LAC main source (i.e. DBSG).

Table 6.4 – Cross-correlation coefficients of PDPs for the FCR-LAC, Ordovician (Pereira et al., 2012a; Shaw et al., 2014), Cambrian (Fernández-Suárez et al., 2014), and Ediacaran (Fernández-Suárez et al., 2014) data sets.

	MTX (n=103)	**DTX (n=40)**	**Granites (n=45)**	**Ordovician (n=325)**	**Cambrian (n=259)**	**Ediacaran (n=296)**
MTX	1					
DTX	0.49	1				
Granites	0.58	0.67	1			
Ordovician	0.43	0.47	0.39	1		
Cambrian	0.83	0.61	0.59	0.63	1	
Ediacaran	0.54	0.48	0.35	0.79	0.77	1

The visual and the statistical comparison show that in general, the FCR-LAC rocks have a strong similarity with the Cambrian formations and a moderate one with Ediacaran units. Thus, the FCR-LAC is more akin with southern host unit, the Excomungada Fm. with Cambrian age.

6.4.4. Detrital zircon source and geodynamic implications

The results indicate that DBSG metasedimentary sequence is dominated by detrital zircons of Cambrian-Neoproterozoic ages (500-700 Ma) which highlights the importance of the Cadomian arc as a proximal source in the genesis of the Neoproterozoic to early Cambrian metasedimentary domains in study (Castiñeiras et al., 2008; Orejana et al., 2015; Pereira, 2015; Teixeira et al., 2017). The minor zircon populations found in the DBSG domains with transitional Neoproterozoic/Mesoproterozoic, Paleoproterozoic and Archean ages may have as a source distinct terranes of North Gondwana such as the Arabian-Nubian Shield, the Sahara Metacraton, or the West African Craton (such as in Orejana et al., 2015; Pereira, 2015; and references therein). The Tonian ages (≈ 800 Ma) found in the anatectic complex and its host rocks (Excomungada Formation) may have originated in the Arabian-Nubian Shield or the Sahara Metacraton. The ca. 1000 Ma age peak, more prominent in the Pinhão Formation, indicates a source area where there is basement rocks formed during the Rodinia assembly (1000-1100 Ma; Fernández-Suárez et al., 2014 and references therein).

It has been considered as established that the FCR-LAC host rocks (Pinhão and Excomungada Fms) belong to the Douro Group (Silva et al., 1989), which is consistent with the data presented in this study: similarities between the Excomungada Fm., the Desejosa Fm. (e.g. MDA) and its lateral equivalent unit in the Spanish sector, Tamames Sandstones (e.g. MDA and detrital zircon ages distribution).

The Pinhão and Excomungada Formations (R^2 = 0.19 to 0.23) detrital zircon signatures are distinct from the Beiras Group, confirming that these units belong to the Douro Group. This indicates that the physical barrier between the Douro and Beiras basin must be placed southern of the FCR-LAC and JPCSZ. This implies that the Huebra and Juzbado-Penalva do Castelo shear zones, although of major importance for the exhumation of the FCR-LAC rocks during the Variscan Orogeny, were not inherited Cadomian structures, as had been suggested or implied by Iglesias and Ribeiro (1981) and Villaseca et al. (2014).

The dominance of younger ages around 600 Ma and the 800-1000 Ma age interval of the Pinhão and Excomungada Fms reflect the proximity of the Douro Group basin with the juvenile Cadomian magmatic arc and sources from North Gondwana, respectively (e.g. Pereira, 2015; Villaseca et al., 2014). Sánchez-García et al. (2019; references therein) suggest that the Cadomian arc activity cessed at *ca.* 533 Ma, so, concerning the MDA of the Excomungada Fm. (522.9 ± 6.2 Ma), probably its deposition still occurred after the cessation of the arc activity accompanied by its denudation. Oppositely to the Beiras Group (Pereira et al., 2012a), the scarcity of older (Paleoproterozoic and Archean) detrital zircon ages in the Pinhão and Excomungada units corroborates the idea that the Douro Group basin was not a primary recipient of sediments from the Gondwana continent inland/cratonic areas.

The detrital age distribution resemblance of the Ordovician quartzites with the Pinhão Fm. and, partially, with the Excomungada Fm. indicates recycling of the Ediacaran-Cambrian units, as observed in other studies in the Iberian Massif (e.g. Fernández-Suárez et al., 2002; Pereira et al., 2012a). The recycling of the lower Douro Group units was probably caused by the formation of horst and grabens in the rift stages of the Rheic Ocean opening, leading to their denudation and sediment transport onto these basins.

6.5. CONCLUSIONS

The Figueira de Castelo Rodrigo-Lumbrales Anatectic Complex (FCR-LAC), bounded by two major shear zones, is an example of a migmatite-granite complex exhumed during the Variscan Orogeny in the Iberian Massif, whose timing and exhumation mechanism were still relatively

poorly constrained. In this study, we determined the age of migmatization (343.7 ± 2.5 – 314.8 ± 1.3 Ma) and considered and tested the existence of a paleogeographic boundary to the north and south of the FCR-LAC (Iglesias and Ribeiro, 1981; Villaseca et al., 2014), utilising and comparing the detrital zircon inputs from two Ediacaran/Cambrian sedimentary basins.

The new U-Pb zircon and apatite ages for the migmatites of the FCR-LAC allowed to temporally constraining the high temperature section of the metamorphic path (343.7 ± 2.5 – 314.8 ± 1.3 Ma) and, also, to obtain ages of cooling down to ca. 500 ºC (301.5 ± 8.2 – 314.3 ± 7.2 Ma). These ages allowed us to constrain the age of the metamorphic peak at 316.8 ± 2.0 Ma, which is coeval with the emplacement of the S-type granites (Ferreira et al., 2019). Thus, the anatexis event started during the D_2 Variscan phase and culminated during the D_3 Variscan phase, concomitantly with the emplacement of the S-type granites (Ferreira et al., 2019).

We infer fast cooling (7 – 54 ºC/Ma) and exhumation rates (0.2 and 1.3 mm a^{-1}), compatible with a tectonically-assisted mechanism for the exhumation of this anatectic complex by the two delimiting shear zones. These results agree with the cooling/exhumation conditions inferred from the cogenetic granites (Ferreira et al., 2019), implying that all the units of the anatectic complex (migmatites and granites) were exhumed together and quickly, which reinforces the relevance of the Juzbado-Penalva do Castelo and Huebra shear zones as key structures within the geodynamic evolution of the Variscan Orogeny in Iberia.

The detrital zircon age distributions of the FCR-LAC host rocks are in agreement with previous geochemical/isotopic data, putting in evidence that the Douro basin was in the dependency of the Cadomian continental magmatic arc, both during and after its activity ceased, thus representing a major sediment contributor to these basins. The detrital zircon ages from the Pinhão Fm (DBSG N) and their equivalent Beiras Group greywackes indicate strong source heterogeneity between them, the Douro having a lower proportion of older (Paleoproterozoic and Neoarchean) components. The Douro Group, represented by the Pinhão (DBSG N) and Excomungada Fm. (DBGS S), shows a younger Cadomian age peak (*ca.* 600 Ma) in comparison to the Beiras Group, whose spectra highlights a source from the protracted arc history (from 800 to 500 Ma). These differences might be envisaged as resulting from of a paleogeographic barrier which separated the Ediacaran/Cambrian Douro and Beiras basins, restricting the detrital component drained to the Douro basin. The Ordovician quartzite age spectra is statistically undistinguishable from the Pinhão Fm., which reinforces the interpretation of recycling of these Neoproterozoic-Cambrian units during the early Ordovician.

The DBSG detrital zircon and inherited zircon grains found in the anatectic rocks broadly reveal moderate similarities but are particularly stronger between the Excomungada Fm. (Cambrian) and the metatexites (more closely related to the FCR-LAC's protolith due to its lower metamorphic grade). This points to these metasedimentary units as the major components of the middle crust rocks that melted during the Carboniferous. Nonetheless, zircon ages younger than 500 Ma, absent in the lower grade metasedimentary units (including in the Ordovician Quartzite), are interpreted as representing the contribution of intrusive magmatic rocks from the Ordovician Ollo de Sapo Fm. (García-Arias et al., 2018) that must have intruded the middle crust. These results point to a heterogeneous middle crust (metasedimentary units with variable detrital input and igneous rocks) during the Variscan deformation events, resulting in the generation of melts with variable isotopic signatures.

CHAPTER 7. THE ROLE OF MELTING ON THE GEOCHEMICAL EVOLUTION AND ISOTOPIC VARIABILITY OF AN ANATECTIC COMPLEX IN THE IBERIAN VARISCIDES

Joana A. Ferreira[1,2*], João Mata[1,2], Telmo Bento dos Santos[1,2], Inês Pereira[3,4]

[1] Instituto Dom Luiz (IDL), Faculdade de Ciências, Universidade de Lisboa, Campo Grande, 1749-016, Lisboa, Portugal

[2] Departamento de Geologia, Faculdade de Ciências, Universidade de Lisboa, C6, Campo Grande, 1749-016 Lisboa, Portugal

[3] School of Earth and Environmental Sciences, University of Portsmouth, Building Burnaby Rd Portsmouth P01 3QL, UK

[4] Laboratoire Magmas et Volcans, Université Clermont Auvergne, 6 avenue Blaise Pascal, TSA 60026 – CS 60026, 63178 Aubiere Cedex, France

Ferreira, J.A., Mata, J., Bento dos Santos, T., Pereira, I. 2020. The role of melting on the geochemical evolution and isotopic variability of an anatectic complex in the Iberian Variscides. Lithos, 378-379. https://doi.org/10.1016/j.lithos.2020.105769

Abstract: The formation and evolution of migmatite-granite terranes usually involve a sum of complex petrological/geochemical processes leading its imprint on elemental and isotopic signatures. In this paper we assess the role of melting reactions on the genesis of the variscan Figueira de Castelo Rodrigo-Lumbrales Anatectic Complex (Central Iberian Zone – CIZ) which culminated in the generation of abundant S-type granites. It is demonstrated that no isotopic (Sr-Nd-Hf-Pb) disequilibrium occurred, yet variable contribution of the source minerals led to batches of melts characterized by distinct parent/daughter ratios, which explain the significant heterogeneity of present-day isotopic signatures. While Rb/Sr ratios and the Pb budget of the successively generated lithotypes were mainly controlled by major minerals such as muscovite, K-feldspar and plagioclase, the accessory phases were the main constrainers of Sm/Nd, Lu/Hf ratios and of U and Th contents. It is demonstrated the existence of two distinct diatexite groups produced by different reactions. Diatexites type-1 with high Rb composition and fractionated HREE are geochemically more akin with the S-type granites. They were produced via fluid-absent reactions during dehydration-melting of muscovite with production of peritectic K-feldspar, sillimanite and melt. The dehydration-melting of biotite was incipient. Diatexites type-2 require the participation of fluids during melting reactions, which consumes more plagioclase than muscovite. The estimated peak temperatures range between 760 and 890 ˚C which resulted in large volumes of melt being produced (in excess of 30%), contributing to the profusion of S-type granites within the CIZ. Isotopic data reveals the existence of two groups with distinct initial compositions, both composed by metatexites, diatexites and granites, which is explained by source heterogeneity. The main source of the anatectic complex is the Douro-Beiras Supergroup with minor contribution of the Ollo de Sapo magmatic rocks.

7.1. INTRODUCTION

Late-stage mountain building is typically characterized by low-pressure–high-temperature (LP–HT) metamorphism, crustal anatexis, and generation of granitic melts, common in the continental tectonic framework from the Archean to the Cenozoic (Whitney et al., 2004). Ascent of granitic magmas leaving a mafic residue leads to intracrustal differentiation, which explains the compositional distinction between lower and upper crust (Sawyer et al., 2011).

To produce large granitic bodies, through partial melting of a source rock, it is required the production of high proportions of melt during anatexis. This depends on protolith fertility, presence of fluids, and temperature-pressure conditions (Brown, 2013; Clemens, 2006). Metapelitic and metapsammitic rocks contain large amounts of hydrous mineral phases like muscovite and biotite (30% to 50%) which makes them fertile protoliths and potential sources

of peraluminous melts through metamorphic incongruent melting reactions (fluid-present or fluid-absent) involving these micas at 700 – 800 ºC (Brown, 2013; Sawyer et al., 2011). The fluid-absent melting of micas in metapelites and metagreywackes can yield up to 50 vol% of melt (Bento dos Santos et al., 2011; Brown, 2013; Clemens and Vielzeuf, 1987; Sawyer et al., 2011). For these reasons, migmatite-granite complexes have been the target of several studies in an attempt to explore links between high-grade metamorphism, partial melting processes, the origin of the associated granitic bodies and crustal differentiation (e.g. Bento dos Santos et al., 2011; Brown et al., 2016; Johannes et al., 2003; Sola et al., 2013).

In the Iberian Variscan Belt (the southwestern sector of the European Variscan orogen) and more precisely in the Central Iberian Zone (CIZ), several authors have stressed the association between some granites and migmatitic rocks (Areias et al., 2014; Carrington da Costa and Teixeira, 1957; Ferreira et al., 2014; Pereira et al., 2017; Ribeiro et al., 2011; Vanderhaeghe, 2009). The Figueira de Castelo Rodrigo-Lumbrales Anatectic Complex (FCR-LAC) is one of such anatectic complexes and has the particularity of showing a very clear spatial relationship between metatexites, diatexites and granites. This complex thus offers an opportunity to study the melting reactions linking metasedimentary units with migmatites (metatexites and diatexites) and granites. In a previous study, links between the FCR-LAC granites (Ferreira et al., 2019), and pre-Ordovician metasedimentary rocks has been suggested, based on the study of inherited zircons.

Radiogenic isotopes are widely applied to identify the source characteristics of magmatic rocks (e.g. basalts; White, 2010). Indeed, it is usually assumed that the isotopic composition of a magma is similar to that of the source rock, such hypothesis implies that no isotope fractionation occurs during melting and that almost the same happens with the parent (P)/daughter (D) element pairs. This is true if each of the source mineral phases is not a significant repository of any of the P or D elements for the isotopic systems considered, i.e. when the P and D elements are highly incompatible. However, in silica-rich magmatic systems, such as the case of S-type granites and the associated anatectic units, isotopic disequilibrium becomes more common. Indeed, a) temperature is sometimes insufficient to reach the closure temperature of some of the accessory phases, with which P and/or D elements are compatible with, resulting in significant residue/melt isotopic disequilibrium (up to > 20 εHf unites; Tang et al., 2014); and b) the sluggish chemical diffusivity compared with the time lapse necessary for melt extraction from the residue (Ayres and Harris, 1997; Farina and Stevens, 2011; Zeng et al., 2005; Tang et al., 2014; Wolf et al., 2019). This can lead to the perception that isotopic disequilibrium during anatexis is ubiquitous (e.g. Tommasini and Davies, 1997). However, in some cases, even for

situations specifically investigated for isotopic disequilibrium, no significant evidences were found (e.g. Wolf et al., 2019). In this perspective, the isotopic variability of an anatectic complex must also be addressed in the light of regional source heterogeneities, and on the role of melting reactions leading to distinct P/D pairs with the consequent development of distinct isotopic signatures due to variable rates of radiogenic ingrowth through time. For this, it is not yet consensual that isotopic disequilibrium necessarily takes place during anatexis.

It is expected that distinct isotope systems behave differently during anatexis, with some of them responding variably to diverse melting conditions (e.g. Wolf et al., 2019). This confers to multi-isotope studies the potential to investigate the hypothetical role of isotopic disequilibrium and source heterogeneity, as well as to better decipher the role of distinct melting reactions during the different stages of anatexis.

In this study, we use Sr, Nd, Hf and Pb isotope, elemental whole-rock compositions and trace-element zircon and apatite analyses from the FCR-LAC mainly to: 1) assess the melting reactions that led to the formation of its different lithotypes; 2) provide insights onto the causes of isotopic variability characterizing the anatectic complex; and 3) explore the geochemical link between the different stages of anatexis, from migmatites to granites, and also the potential metapelitic protoliths.

7.2. ANALYTICAL METHODS

7.2.1. Whole-rock geochemistry

Whole-rock geochemistry analyses of 55 samples, including granites, migmatites and phyllites from the Douro-Beiras Supergroup were conducted in the Activation Lab in Ontario, Canada using an Inductively Coupled Plasma-Mass Spectrometer (ICP-MS). Samples are mixed with a flux of lithium metaborate and lithium tetraborate and fused in an induction furnace. The molten melt is immediately poured into a solution of 5% nitric acid containing an internal standard and mixed continuously until completely dissolved. Samples were then diluted and analysed in a batch system using a reagent blank, certified reference materials (NIST 694, DNC-1, GBW-07113, LKSD-3, TDB-1, W-2a, SY-4, CTA-AC-1, BIR-1a, NCS DC86132, NCS DC70009, OREAS 100a, OREAS and 17%-diluted replicates. Three blanks and five reference materials (three before sample group and two after) are analysed per group of samples. Duplicates were analysed every 15 samples. Reproducibility is better than 3 relative-% for major element contents (i.e., SiO_2, TiO_2, Al_2O_3, Fe_2O_3, MnO, MgO, CaO, Na_2O, K_2O and P_2O_5), 7 relative-% for rare earth elements, 5 relative-% for elements like, Rb, Ba, U and Th.

Instrument is recalibrated every 40 samples Calibration was performed using USGS and CANMET certified reference materials with compositions similar to the studied rocks. A reference sample was measured after the analysis of every group of 10 samples to monitor instrumental drift. For further details see http://www.actlabs.com/ (package 4LITHO) (Appendix F).

7.2.2. Isotopic geochemistry

The isotopic analyses of Sr, Nd, Hf and Pb were performed in 13 samples, including 8 migmatites (5 metatexites and 3 diatexites), 5 granites and 2 metasedimentary units from the Douro-Beiras Supergroup at the Laboratoire G-Time (Geochemistry: Tracing by Isotopes, Minerals and Elements) of the Université Libre de Bruxelles (ULB, Belgium) using a Nu Plasma I Multi-Collector Inductively Coupled Mass Spectrometer (MC-ICP-MS) instrument.

For all the isotopic systems here analysed, the standards were systematically run between every two samples to monitor the instrumental mass bias during the analytical routine

Sr analyses were performed in dry plasma conditions with Cetac Aridus II desolvator. The raw data was normalized to $^{86}Sr/^{88}Sr = 0.1194$ and corrected for mass bias by standard sample bracketing using the lab in-house Sr standard solution (as in Mata et al., 2017). The in-house shelf Sr standard was calibrated and normalized to the certified value of NBS 987 Sr standard (0.710248) reported by Weis et al. (2006). During the analytical sessions, in-house standard solution was analysed in the beginning and in the end of the run after and before the NBS 987, respectively, and gave an average value of 0.708383 ± 0.000031 (2σ, $n = 40$).

Nd and Hf isotopes were analysed using dry plasma conditions in an Aridus II desolvating system resulting in $^{143}Nd/^{144}Nd = 0.511962 \pm 0.000058$ (2σ, $n = 7$) for the Rennes Nd standard, $^{176}Hf/^{177}Hf = 0.282162 \pm 0.000013$ (2σ, $n = 9$) for the JMC 475 Hf standard. The Nd and Hf isotopic measurements were internally normalized to $^{146}Nd/^{144}Nd = 0.7219$ and $^{179}Hf/^{177}Hf = 0.7325$, respectively. All Nd and Hf isotopic data are normalized to the reference values of 0.511961 and 0.282163, as published by Blichert-Toft et al. (1997) and Chauvel and Blichert-Toft (2001), respectively.

The Pb isotope analyses were performed in wet plasma conditions. ^{202}Hg is routinely monitored to correct for the potential isobaric interference of ^{204}Hg on ^{204}Pb. Mass discrimination was monitored using ln – ln plots and corrected by the external normalization and the standard sample bracketing method using the recommended values of Galer & Abouchami (1998) (e.g. $^{206}Pb/^{204}Pb = 16.9405 \pm 0.0015$, $^{207}Pb/^{204}Pb = 15.4963 \pm 0.0016$, $^{208}Pb/^{204}Pb = 36.7219 \pm 0.0044$). The repeated measurements of the NBS981 Pb standard gave the following values:

$^{206}Pb/^{204}Pb$ = 16.9406 ± 0.0018, $^{207}Pb/^{204}Pb$ = 15.4963 ± 0.0021 and $^{208}Pb/^{204}Pb$ = 36.7221 ± 0.0048 (2σ, n = 11) which is within the uncertainty of recommended values.

7.2.3. Zircon and Apatite trace elements

Zircon and apatite trace element analyses were performed for the anatectic units using an ASI RESOlution 193 nm ArF excimer laser coupled to the ANALYTIK JENA Plasma Quant Elite quadrupole ICP-MS at the University of Portsmouth (UoP).

In the case of zircon, the following isotopes were analysed: ^{29}Si, ^{31}P, ^{39}K, ^{40}Ca, ^{45}Sc, ^{49}Ti, ^{51}V, ^{52}Cr, ^{55}Mn, ^{85}Rb, ^{87}Sr, ^{89}Y, ^{90}Zr, ^{93}Nb, ^{95}Mo, ^{118}Sn, ^{121}Sb, ^{133}Cs, ^{137}Ba, ^{139}La, ^{140}Ce, ^{141}Pr, ^{146}Nd, ^{147}Sm, ^{153}Eu, ^{157}Gd, ^{159}Tb, ^{163}Dy, ^{165}Ho, ^{166}Er, ^{169}Tm, ^{172}Yb, ^{175}Lu, ^{177}Hf, ^{181}Ta, ^{182}W, ^{208}Pb, ^{209}Bi, ^{232}Th and ^{238}U. A laser beam diameter of 40 µm for NIST612, 35 µm for secondary standards and 35 - 25 µm for unknowns was used, with beam energy densities ranging from 3.8 and 4.1 J/cm^2, with a 4 Hz repetition rate. NIST612 was used as primary standard using concentrations by Jochum et al. (2011), whereas 91500 (Wiedenbeck et al., 1995) and GJ1 (Jackson et al., 2004) were used as secondary standards, as they are relatively homogenous in terms of trace element concentrations. Zr was used as an internal calibration standard, considering zircon stoichiometry (Zr = 43.1 wt%). Y, Hf, U, Th and most of the Rare Earth Elements (REE) are within 10% and 5% accuracy relative to secondary standards published values (Appendix B8). The detection limit of the Rare Earth Elements ranges between 0.01 and 0.11 ppm and for the remain elements (Hf, Y, U and Th) varies from 0.03 to 0.09 ppm. La and Pr have values below detection limit.

For apatite the analysed isotopes were: ^{29}Si, ^{87}Sr, ^{89}Y, ^{90}Zr, ^{93}Nb, ^{95}Mo, ^{137}Ba, ^{139}La, ^{140}Ce, ^{141}Pr, ^{146}Nd, ^{147}Sm, ^{153}Eu, ^{157}Gd, ^{159}Tb, ^{163}Dy, ^{165}Ho, ^{166}Er, ^{169}Tm, ^{172}Yb, ^{175}Lu, ^{181}Ta, ^{182}W, ^{208}Pb, ^{232}Th, ^{238}U and ^{85}Rb. A laser beam diameter of 40 µm was used for primary standard NIST610 (Jochum et al., 2011), while for the secondary reference materials and unknowns 30 µm ablation spots were preferred, with beam energy densities of ~3 J/cm^2, at a 3 Hz repetition rate. Durango was used as a secondary reference material, as it is well-characterised and relatively homogeneous (Chew et al., 2016). We also analysed the Madagascar reference material (Thomson et al., 2012) to compare with in-house measurements. Most analysed REE are within 10% and 1% accuracy relative to Durango values with exception of Lu that show an accuracy of 20% (Appendix B8). The REE detection limit is between 0.01 and 0.2 ppm, whereas Sr and Y are 4 ppm and 0.1 ppm, respectively.

7.3. RESULTS

7.3.1. Whole-rock elemental geochemistry

Whole-rock elemental compositions are presented in Appendix G1 where the studied samples are grouped according to their characteristics (i.e.: phyllites, metatexites, diatexites and granites).

Phyllites and metatexites are enriched in Al_2O_3, FeOt, MgO and TiO_2 in comparison to diatexites and granites, evidencing a negative correlation with silica (Figure 7.1). This reflects a larger abundance of refractory minerals (e.g. biotite and titanite) in the metasedimentary protoliths and in the metatexites paleosomes, representative of an incipient degree of partial melting. On the other hand, diatexites and granites commonly yield higher contents of SiO_2, Na_2O, K_2O and P_2O_5 as compared with metatexites , a difference consistent with higher degree of partial melting (e.g. Sawyer, 2008), and thus with the production of quartz-plagioclase-, K-feldspar- and apatite-rich melts.

As a whole, the lithologies that compose the anatectic complex have a high aluminosity (Al_2O_3 > 12 wt. %) all lithotypes being strongly peraluminous. Notice that is notorious the affinity of the phyllites and quartzphyllites with the metatexites (ASI = 1.2 – 3.3) for one side and between the more evolved diatexites and granites (ASI = 1.1 – 1.4).

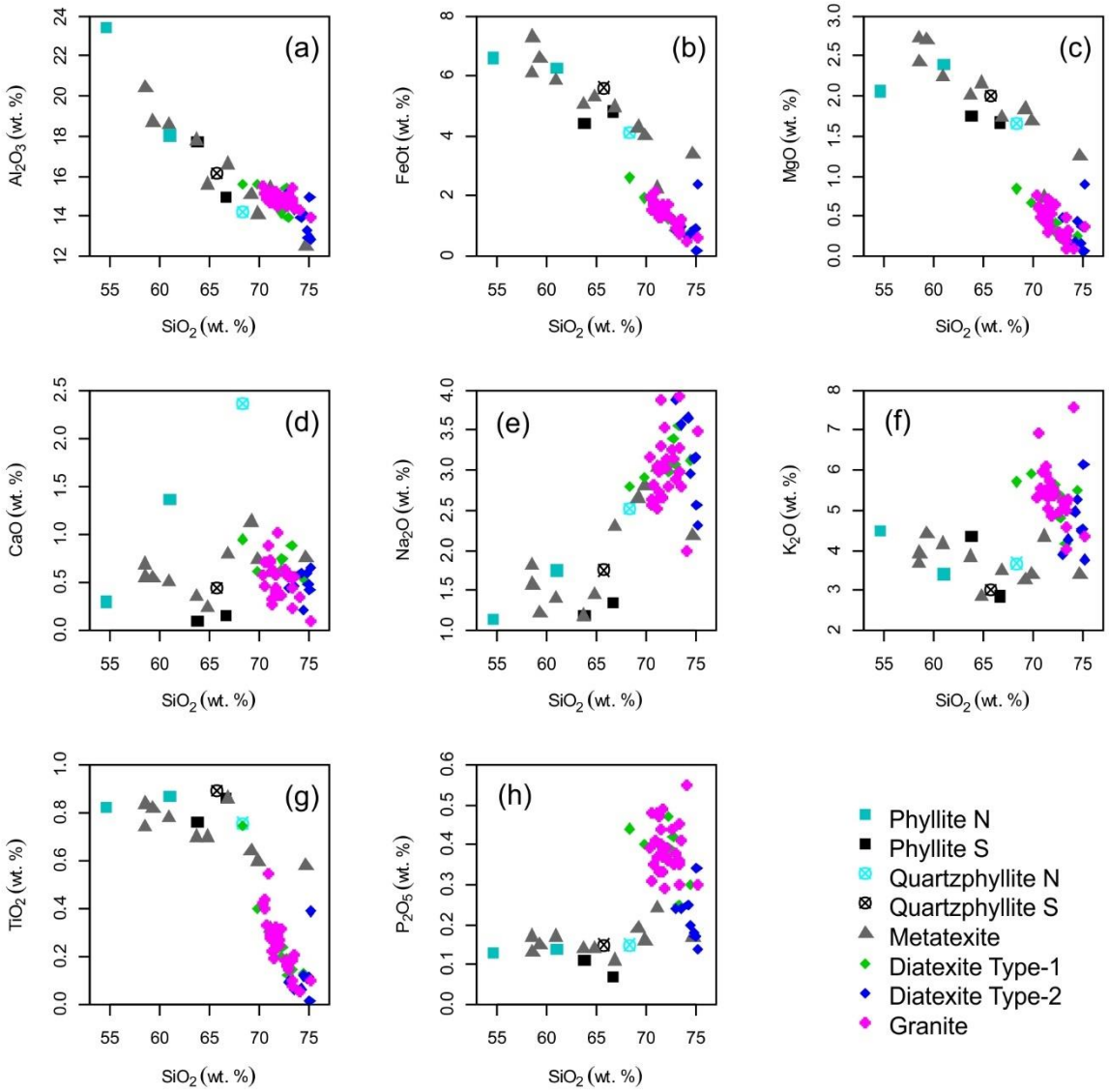

Figure 7.1 – Harker diagrams for major elements for the host rocks (phyllites and quartzphyllites) and FCR-LAC lithologies (metatexites, diatexites and granites).

The similitude of metatexites and phyllites revealed by major elements is also generally depicted by trace elements (Figure 7.2). Phyllites, quartzphyllites, and metatexites show significantly similar multi-element patterns with negative anomalies for Nb, K, Pb, Sr and Ti, and positive anomalies for U, Ta, La, Ce and Nd. Zr and Hf positive anomalies are only evident in the quartzphyllites (Figure 7.3a) their higher zircon contents expectable from their more psammitic characteristics. Diatexites and granites patterns overlap each other within error (Figure 7.3b), exhibiting a wider range in some elements, such as Th, REE and Zr-Hf. Both lithotypes show negative anomalies for Nb, Pb, Sr and Ti. Comparing the two multi-elements diagrams, there are some similarities among the metasediments/metatexites and diatexites/granites, with all the lithologies presenting negative anomalies for Nb, Pb, Sr and Ti.

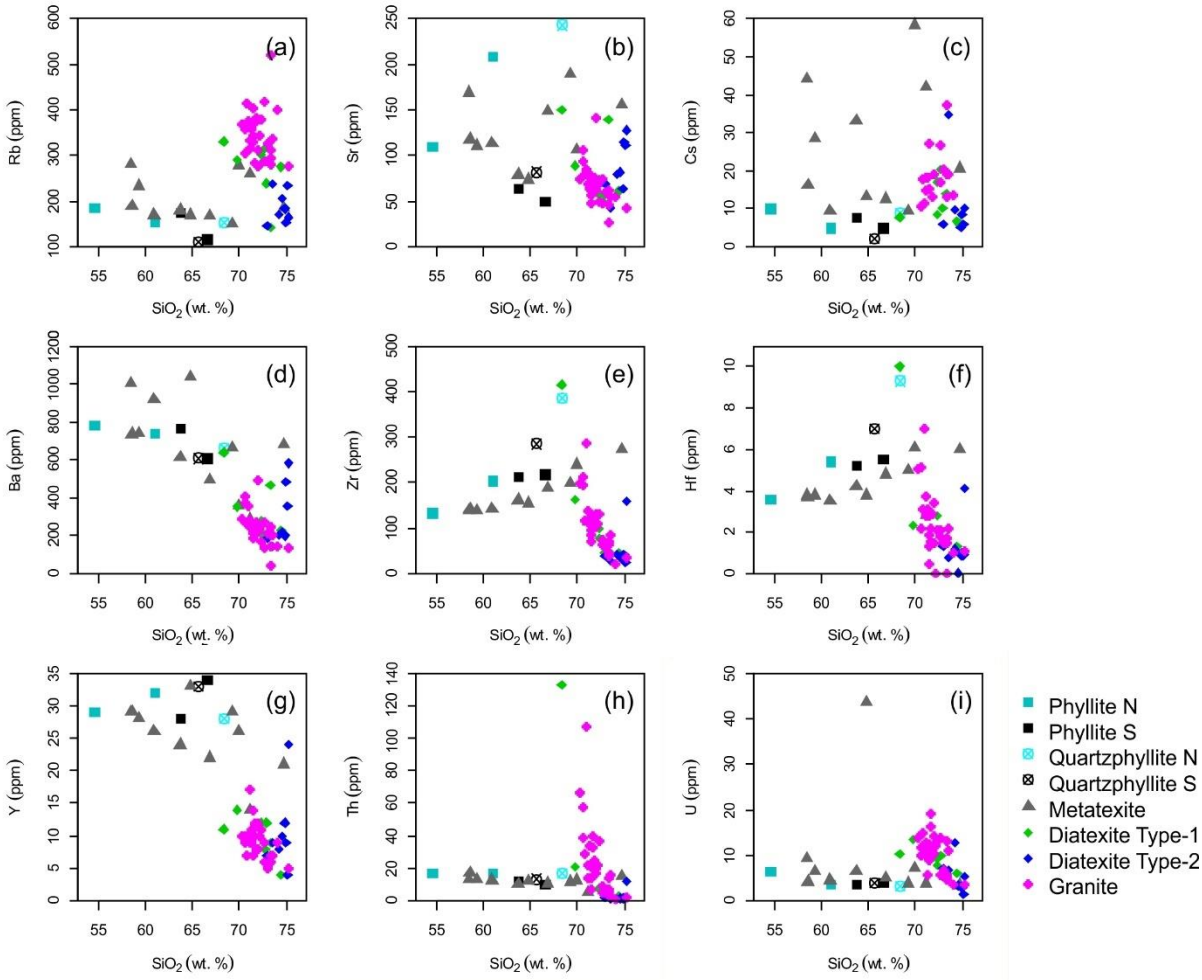

Figure 7.2 – Harker diagrams for trace elements for the host rocks (phyllites and quartzphyllites) and FCR-LAC lithologies (metatexites, diatexites and granites).

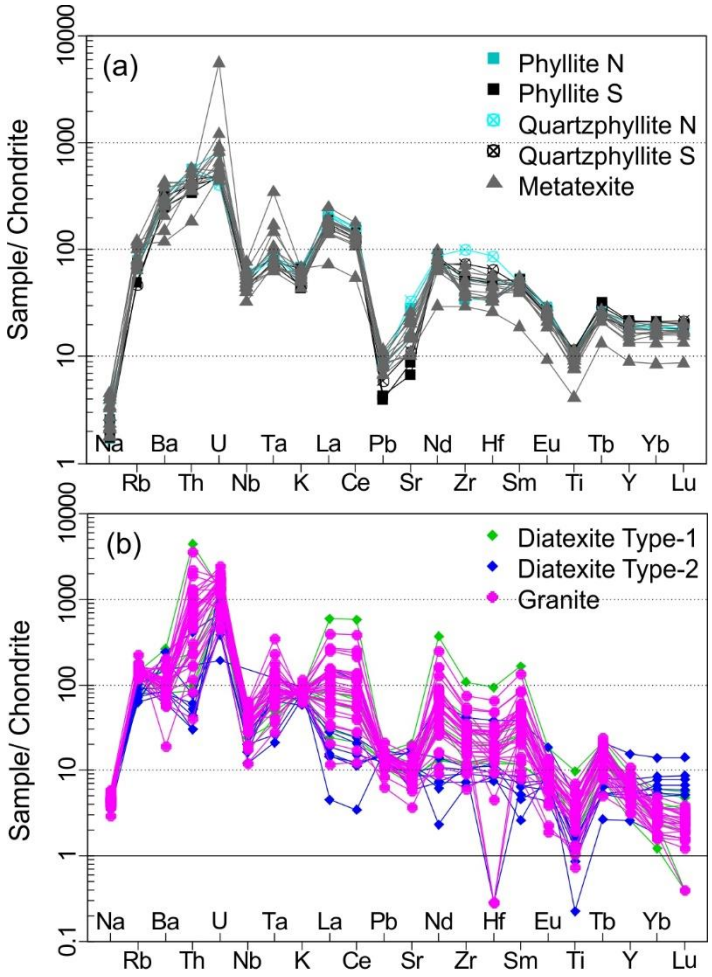

Figure 7.3 – a) Multi-element diagram for phyllites, quartzphyllites and metatexites; (b) Multi-element diagram for diatexites type-1, diatexites type-2 and granites. Chondrite normalization values after Palme and O'Neil (2003).

REE composition data are summarized in Appendix G1 and Figure 7.4. Phyllites, quartzphyllites and metatexites have an identical normalised patterns (Figure 7.4a) with all but one of the samples being encompassed on a small range of concentrations (e.g. La = 41 to 61 ppm; Yb = 2.2 to 3.5 ppm). The exception is one metatexite sample (JTJ-60A) which stands out of the group because of its lower REE concentrations (La = 18; Yb = 1.4) yet similar $(La/Yb)_N$ ratios (7.43 to 13.35). The Heavy Rare Earth Elements (HREE) are weakly fractionated (Dy/Yb_N = 1.07 – 1.35) and the Eu anomalies (Eu/Eu* = 0.5 – 0.7) are weakly pronounced.

Overall, both diatexites and granites (Figure 7.4b) present a wide range of REE concentrations (Σ = 8 – 777 ppm). Despite this significant range in the REE contents, the studied granites present similar normalised patterns for the different facies. At odds, diatexites show a wider variability translated, for example, in different degrees of HREE fractionation (Dy/Yb_N = 0.8 to 5) and Eu anomalies either negative (down to 0.2) or positive (up to 4). This high variability

of diatexites lead to its division in two groups (see Figure 7.2 and 7.4b), whose definition and meaning is the focus of one of the sections in the discussion.

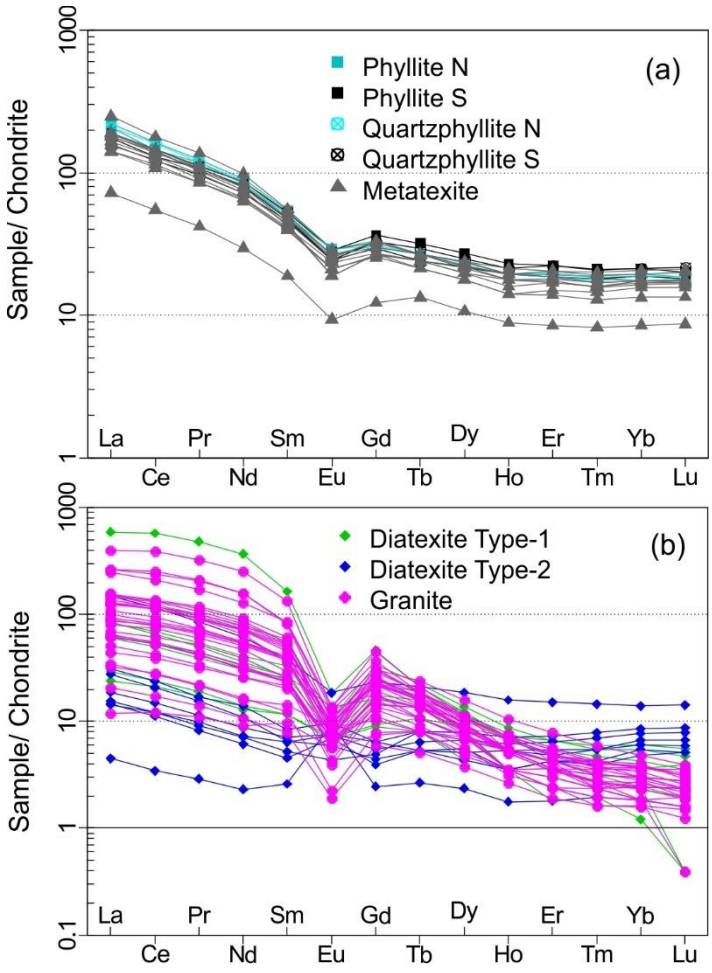

Figure 7.4 – (a) REE diagram for phyllites, quartzphyllites and metatexites; (b) REE diagram for diatexites type-1, diatexites type-2 and granites. Chondrite normalization values after Palme and O'Neil (2003).

7.3.2. Accessory minerals: trace element composition

Apatite

The trace element composition of the apatite grains from the FCR-LAC and the host rocks (phyllites) is remarkably distinct in Sr, Y, Th and REE compositions (Appendix G2). The highest Sr content in apatite is found in phyllites (317 – 1471 ppm), decreasing gradually in metatexites (113 – 487 ppm), diatexites (86 – 144 ppm) and granites (74 – 99 ppm). Thorium behaves similarly, being more enriched in apatite grains in the phyllites, and more depleted in the other units. On the other hand, Y contents in apatite are the lowest in phyllites (480 – 854 ppm), quite similar between metatexites (837 – 1973 ppm) and diatexites (847 – 2026 ppm) and show some spreading in granites (212 – 1546 ppm). The REE in apatite from different lithotypes show a marked enrichment in LREE compared to HREE (Figure 7.5a): phyllites (LREE = 2870

– 4503 ppm), metatexites (LREE = 1255 – 2008 ppm), diatexites (LREE = 1357 – 5108 ppm) and granites (LREE = 1229 – 3750 ppm). Apatite grains retrieved from the phyllite are more fractionated in the LREE than the apatites from the FCR-LAC rocks while the HREE fractionation is similar to the migmatites. Apatite grains from the migmatites show similar HREE and LREE fractionation. Apatites from granites exhibit higher REE fractionation compared to migmatites mainly influenced by the HREE fractionation. The IIγ granite has a REE fractionation higher than the remaining granite facies because of its LREE concentrations though its HREE fractionation is similar to the other granites. In general, the Eu anomalies are negative with exception of the late-tectonic granite (granite IIγ: 1.06) with no apparent anomaly.

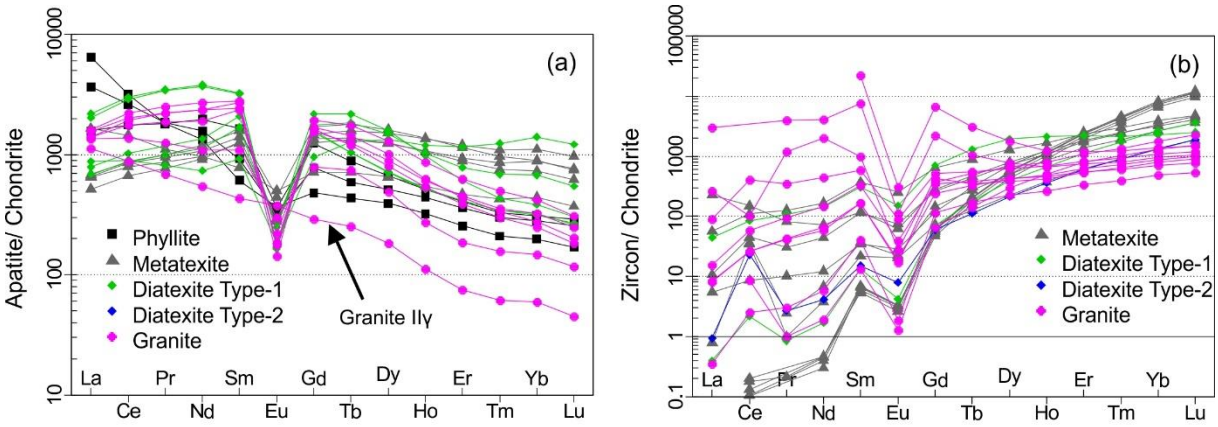

Figure 7.5 – (a) Apatite REE pattern for phyllites, quartzphyllites, metatexites, diatexites type-1, diatexites type-2 and granites; (b) Zircon REE pattern for metatexites, diatexites type-1, diatexites type-2 and granites. Chondrite normalization values after Palme and O'Neil (2003).

Zircon

Zircon grains control the budget of Hf, Y, U, Th and HREE contents from the migmatites and granites (Appendix G3). The Hf composition is similar between the metatexites (8180 – 14410 ppm), diatexites (11060 – 12750 ppm) and granites (10280 – 12670 ppm). Lu composition decreases in zircon grains from metatexites (48 – 309 ppm), to diatexites (48 – 91 ppm) and granites (14 – 58 ppm). We were only able to determine Y composition for half the measured points (11 out of 23). For the available measurements, metatexites yield 120 – 2074 ppm, diatexites 610 ppm, and granites range between 469 – 1199 ppm. U and Th contents are highly variable, with Th/U ratios in zircon from diatexites (0.06 – 0.11) and granites (0.11 – 5.88), being broadly higher than 0.1 (10 points of 12), while metatexites (0.003 – 0.845) yield ratios commonly lower than 0.1.

Zircon from the different units exhibit high and similar HREE concentrations (Figure 7.5b), in metatexites from 490 to 2430 ppm, in diatexites range from 488 to 1679 ppm, and in granites

from 261 to 2540 ppm. Eu anomalies are negative in zircon from the metatexites (0.16 – 0.52), diatexites (0.14 – 0.33) and granites (0.02 – 0.16). On the other hand, zircon from the different FCR-LAC rocks show Ce positive anomalies. Most of the zircon of the metatexitic samples have La below the detection limit, so to a better estimation of the REE fractionation is used the Ce/Yb_N parameter. REE fractionation values in zircon (Ce/Yb_N) retrieved from the metatexites (Ce/Yb_N = 0.00001 – 0.05) are not very fractionated, in comparison with zircon from granites (Ce/Yb_N = 0.01 – 0.4) and diatexites (Ce/Yb_N = 0.001 – 0.04) which yield higher Ce/Yb_N. However, the REE patterns (Figure 7.5b) reveal the opposite, the zircon from metatexites exhibit the most REE fractionated pattern. The Ce/Yb_N values are influenced by the LREE content, so give the idea that granites and diatexites have zircons with more fractionated REE. Overall, HREE from the zircon grains are more fractionated than the LREE, and HREE fractionation decreases from metatexites, to diatexites and granite zircon grains. This imparts variable Lu/Hf ratios in zircons from the different units, decreasing from metatexites (0.015), to diatexites (0.006) and granites (0.003).

7.3.3. Isotopic geochemistry

The radiogenic isotopes presented in this study were recalculated to 320 Ma, which corresponds to the migmatization age of the autochthonous domain of the CIZ (e.g. 318 – 325 Ma, Martínez Catalán et al., 2014; Ferreira et al., 2019) (Appendix G4). While in the previous section, granites were presented as a single lithological group, in this section they are presented as syn-tectonic granites and late-tectonic granites (Ferreira et al., 2019). Likewise, phyllites are presented as phyllite N and phyllite S, depending if they were collected to the North (N) or South (S) of the anatectic complex.

Sr-Nd isotopic compositions

All the studied migmatitic and granitic samples but two plot into the fourth quadrant (radiogenic Sr and less radiogenic Nd) of the $^{87}Sr/^{86}Sr_{320}$ vs. εNd_{320} diagram (Figure 7.6a), implying time-integrated evolutions characterized by enrichment of Rb and Nd relatively to the less incompatible Sr and Sm, respectively.

In general, migmatites and granites show $^{87}Sr/^{86}Sr_{320}$ (0.701 – 0.716) and εNd_{320} (-9 to -5), both ranges being compatible with the upper continental crust (Hart et al., 1999). Granites share similar εNd_{320} values (-6.03 to -8.89), but significantly different $^{87}Sr/^{86}Sr_{320}$ ratios (0.7022 to 0.7126). Overall, the metatexite compositions are similar to those of granites with $^{87}Sr/^{86}Sr_{320}$ values ranging between 0.7039 and 0.7124 and εNd_{320} ranging from -5.21 to -8.86.

Our samples are projected alongside data from other studies in the vicinity: Douro-Beiras Supergroup (Douro Group – Teixeira, 2008; Beiras Group – Tassinari et al., 1996; South CIZ – Villaseca et al., 2014), Aguiar da Beira granitoids (biotite granodiorite-granite and muscovite-biotite leucogranite; Costa et al., 2014), and Ollo de Sapo gneisses (Montero et al., 2017) (Figure 7.6b). The Aguiar da Beira granitoids were chosen because of its proximity with the FCR-LAC and their syn-tectonic character. The phyllite N ($^{87}Sr/^{86}Sr_{320}$ = 0.715284; εNd_{320} = -10.07) and phyllite S ($^{87}Sr/^{86}Sr_{320}$ = 0.708869; εNd_{320} = 3.28) show striking differences with phyllite N plotting in the field defined for Douro Group sector. Besides the difference between the phyllite N and the phyllite S for the εNd_{320}, the phyllite S is also completely different of the FCR-LAC Nd composition. Most granites and metatexites have a composition similar with the Aguiar da Beira muscovite-biotite leucogranite. Two samples of diatexite and one sample of metatexite have similarities with the Ollo de Sapo gneisses.

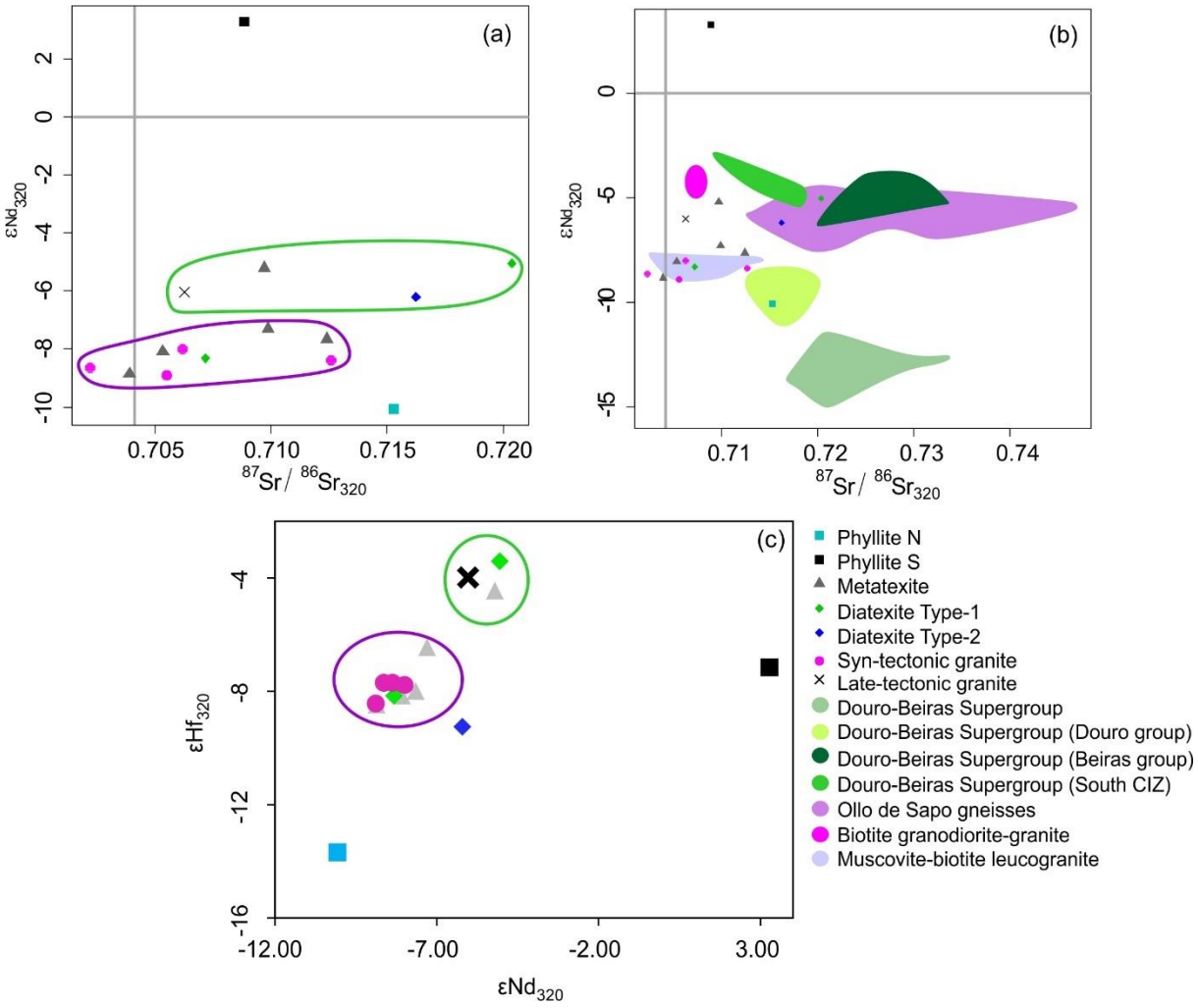

Figure 7.6 – (a) $^{87}Sr/^{86}Sr_{320}$ *versus* εNd_{320} diagram for the host rocks (phyllites) and FCR-LAC lithologies (metatexites, diatexites and granites); (b) $^{87}Sr/^{86}Sr_{320}$ *versus* εNd_{320} diagram for the host rocks (phyllites), FCR-LAC lithologies (metatexites, diatexites and granites) and comparison with other geological domains of the CIZ (references in the section 5.3); (c) εNd_{320} *versus* εHf_{320} diagram for the host rocks (phyllites) and FCR-LAC lithologies (metatexites, diatexites and granites).

Nd-Hf isotopic compositions

The anatectic units show enriched Hf isotopic compositions that result in εHf_{320} ranging from -3.42 to -9.25. Granites have similar, but more restricted εHf_{320} compositions (-7.70 to -8.43), except granite IIγ (εHf_{320} = -3.99). Hf isotopic compositions of the metasedimentary units show discrepant compositions (phyllites N with εHf_{320} = -13.68 and phyllite S with εHf_{320} = -7.16). The εNd_{320} *vs.* εHf_{320} diagram shows an overall positive correlation defined by the granites, metatexites and some of the diatexites (Figure 7.6c).

The phyllite N and S yield two-stage Nd model ages (TDM_2) of 1.83 and 779 Ma, respectively. The Nd TDM_2 for the lithologies of the complex are: metatexites (1.45 to 1.73 Ga), diatexites (1.43 to 1.69 Ga) and granites (1.51 to 1.73 Ga). The Hf TDM_2 ages are older with the following values: phyllite N (2.16 Ga), phyllite S (1.75 Ga), metatexites (1.57 to 1.83 Ga), diatexites (1.51

to 1.88 Ga) and granites (1.54 to 1.83 Ga). These Nd and Hf model ages are similar for most of the anatectic complex lithologies (granites, diatexites, and metatexites). The Nd TDM_2 for the phyllite S is different and younger than the remain analysed lithologies, and also significantly different from its Hf TDM_2.

Despite some isotopic variability, two tight clusters are noticeable in the εNd_{320} *vs.* εHf_{320} diagram, each including granites, metatexites and diatexites.

Pb-Pb isotopic composition

Pb isotopic ratios retrieved from phyllites become clustered onto one group with the remaining lithologies when recalculated to 320 Ma, the opposite to what was shown for the Sr, Nd, and Hf isotopic systems in sections 5.3.1 and 5.3.2. The $^{206}Pb/^{204}Pb_{320}$ and $^{207}Pb/^{204}Pb_{320}$ isotopic ratios tend to homogeneize for all the lithologies, with exception of one metatexite that represents an outlier. This limited variation in Pb isotopic composition is expressed with $^{206}Pb/^{204}Pb_{320}$ = 17.24 to 18.27 and $^{207}Pb/^{204}Pb_{320}$ = 15.61 to 15.67 (Figure 7.7a). In comparison, the $^{208}Pb/^{204}Pb_{320}$ (36.67 to 39.39) (Figure 7.7b) isotopic ratio is slightly more variable.

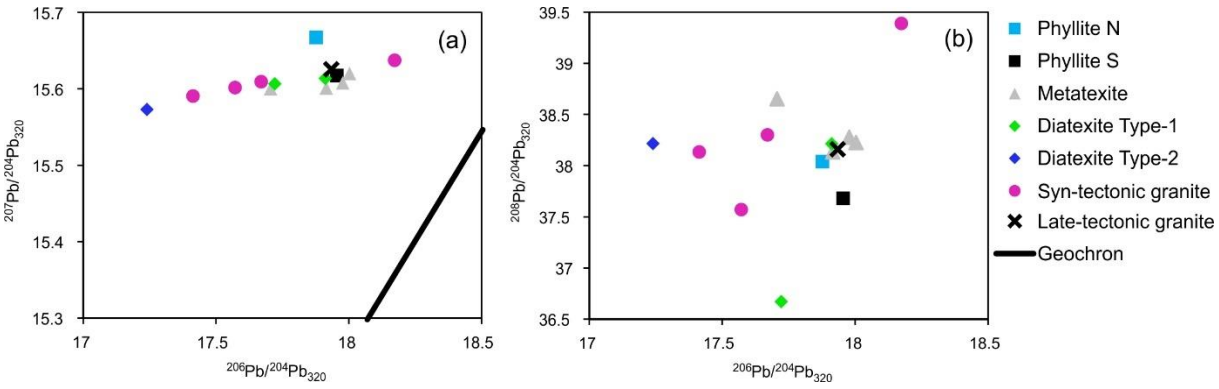

Figure 7.7 – (a) $^{206}Pb/^{204}Pb_{320}$ *versus* $^{207}Pb/^{204}Pb_{320}$ for the host rocks (phyllites) and FCR-LAC lithologies (metatexites, diatexites and granites); (b) $^{206}Pb/^{204}Pb_{320}$ *versus* $^{208}Pb/^{204}Pb_{320}$ for the host rocks (phyllites) and FCR-LAC lithologies (metatexites, diatexites and granites).

7.4. DISCUSSION

7.4.1. Systematics and tectonic setting

The intimate field association of granites, migmatites and metasediments in the FCR-LAC suggests a link between those lithotypes which is endorsed by the granite plotting close to ternary minimums in the Ab-Or-Q ternary diagram (Tuttle and Bowen, 1958) pointing to the S-type character of the studied granites. This is supported by their peraluminous character (ASI >

1.1) (Figure 7.8a) and by their positioning in the A-B granite classification diagram of Villaseca et al. (1998) (Figure 7.8b). Low CaO (0.2 – 1 wt.%), Na_2O (in general < 3.2 wt.%), K_2O compositions (≈ 5 wt.%) and $^{87}Sr/^{86}Sr_{320}$ ratios up to 0.7124 are also typical of S-type granites (Chappell and White, 1974). $^{87}Sr/^{86}Sr_{320}$ ratios are somewhat variable (0.7039 – 0.7124), reflecting some fluctuation between granite facies. This variability, typical of S-type granites (Chappell and White, 2001), can be a consequence of heterogeneous protoliths, or reflect isotopic disequilibrium (see below). Nevertheless, the εNd_{320} *vs.* εHf_{320} plot (Figure 7.6c), where the studied samples form two tight clusters put in evidence the cogenetic association amongst granites and migmatites (diatexites and metatexites), which reinforces their characterisation as S-type granites.

The abundant presence of perthites indicates the hypersolvus character of these granites compatible with relatively low H_2O pressure, which is also suggested by the positioning between the ternary minimum defined at 0.1 and 0.2 GPa in the Ab-Or-Q ternary diagram (Figure 7.8c).

The FCR-LAC granites are characterized by high Rb contents (> 276 ppm) but low Y concentrations (< 17 ppm) and Y+Nb (< 29) and Ta+Yb (< 5) which confers them characteristics typical of syn-collisional tectonic settings (Figure 7.8d; see Pearce et al., 1984). A similar signature is shown by diatexites Type-1. On the other hand the elemental characteristics of the metasediments are compatible, using the discriminant diagrams of Bhatia and Crook (1986) with their deposition in a continental arc setting (Figure 7.8e). Metatexites also fall in the continental arc setting field which emphasize its compositional similarity with the metasediments.

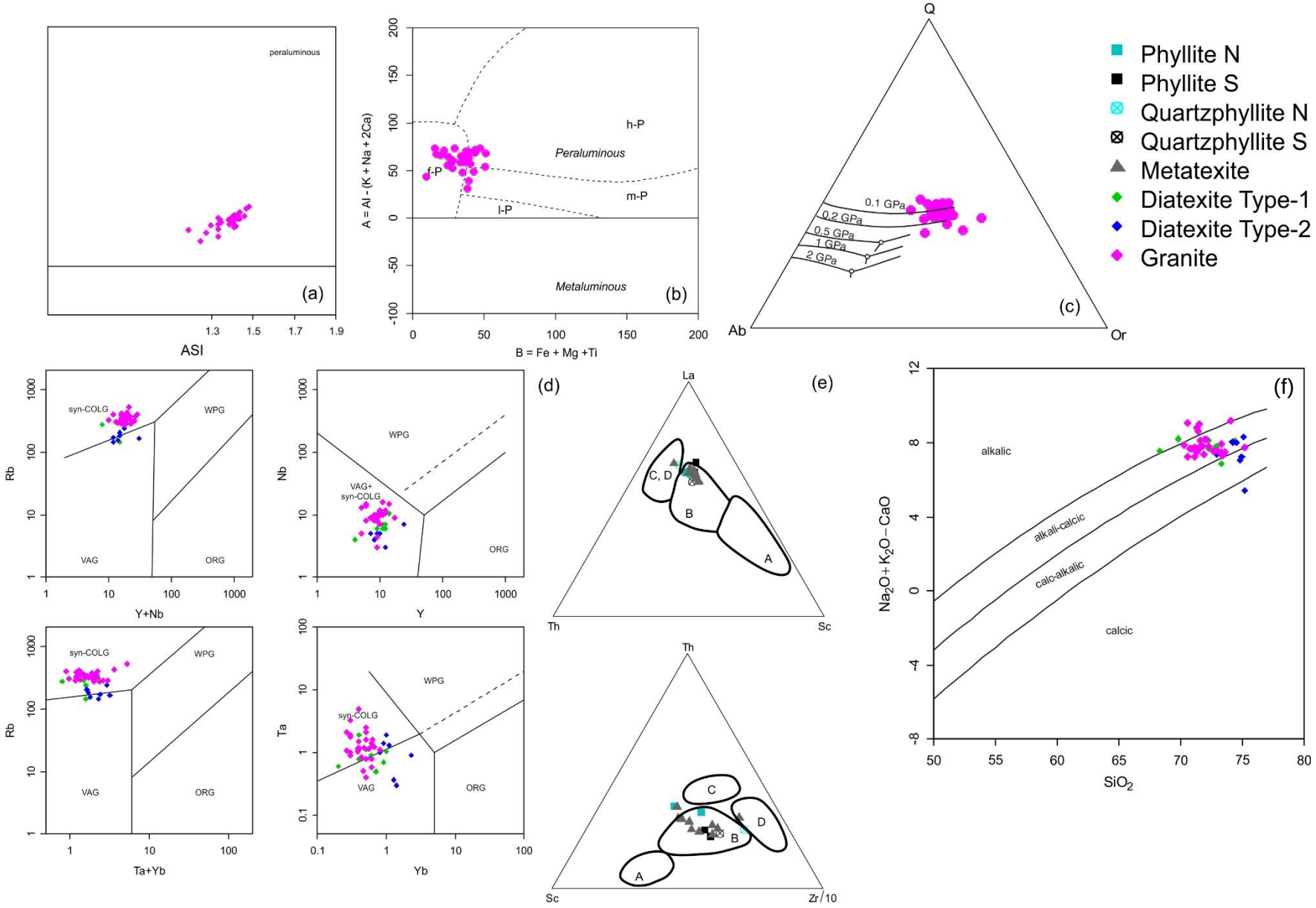

Figure 7.8 – (a) Aluminium Saturation Index (ASI) classification for granitic rocks proposed by (Frost et al., 2001); (b) A-B granite classification diagram of Villaseca et al. (1998); (c) Ab-Or-Q ternary diagram (Tuttle and Bowen, 1958) for the FCR-LAC granites; (d) Tectonic discrimination diagrams using trace elements (Pearce et al., 1984) for the FCR-LAC diatexites and granites: ORG – ocean ridge granites, VAG – volcanic arc granites, WPG – within plate granites, and syn-COLG – syn-collisional granites; (e) Tectonic setting discrimination of sedimentary basins, based on trace elements composition, after Bhatia and Crook (1986): A – Oceanic island arc, B – Continental island arc, C – Active continental margin, D – Passive margins; (f) Na2O+K2O-CaO (wt. %) versus SiO2 (wt. %) classification diagram (Frost et al., 2001) showing the ranges between alkalic and calcic composition for the FCR-LAC diatexites and granites.

7.4.2. The diatexite-granite link

In an anatectic complex, diatexites are regarded as the result of melting processes which by melt aggregation, migration, and emplacement give rise to granitic intrusive bodies (Milord et al., 2001). As mentioned before, diatexites in the FCR-LAC are characterized by a significant compositional variability, which can provide clues on the genetic links with granites.

The SiO_2 concentrations were used to geochemically separate distinct types of diatexites: type-1 (68 – 74 wt. %) and type-2 (74 – 75 wt. %), which can be also separated by other major elements (Figure 7.1) which, using the Frost et al. (2001) geochemical classification, allow to assign to diatexites type-1 and granites a alkali-calcic to alkalic signature, while diatexites type-2 range between the alkali-calcic and calc-alkalic (Figure 7.8f). Granites are generally less silica-enriched than diatexites type-2 rendering difficult the establishment of a genetic link between this type of diatexites and the outcropping granitic rocks.

Regarding trace element compositions, the diatexite type-2 group stands out by their lower Rb (145 – 238 ppm) (Figure 7.2a) and higher Yb and Lu concentrations (Figure 7.3b), and flat Tb to Yb patterns (Tb/Yb_N = 0.8 – 1.5) (Figure 7.4b), at odds with the observed for the other diatexites and granites where $(Tb/Yb)_N > 2.64$. In addition, diatexites type-1 exhibit fractionated HREE (Dy/Yb_N = 2 - 5) and Eu negative anomalies (0.2 – 0.7). By contrast, diatexites type-2 reveal unfractionated HREE (Dy/Yb_N = 0.8 - 1) and Eu slightly negative to pronounced positive anomalies (0.6 – 4). Comparing both types of diatexites with granites, it is notorious the similarity between granites and diatexites type-1.

Concerning the isotopic composition, the diatexites do not exhibit relevant disparities between them in the Sr, Nd and Pb systems. However, the Hf isotopic signatures are clearly distinct with εHf_{320} of the diatexite type-2 being less radiogenic than the diatexite type-1 and, significantly, also than granites, up to 6 units (Appendix G4). This reinforce the existence of two types of diatexites and the existence of a genetic link between diatexites type-1 and granites, which is not immediately apparent when diatexites type 2 are considered.

The distinction between two types of diatexites (diatexite type-1 and diatexite type-2) is clear in the FCR-LAC, as well as a notorious affinity between granites and diatexite type-1. Diatexites are related to these granites by melt-residuum separation. This mechanism can also be accounted for the geochemical variability between these different diatexite types, giving rise to melt-rich and residuum-rich diatexites (e.g. Milord et al., 2001; Sawyer, 1998). The role of melting reactions in this variability is potentially significant and is discussed in the following section.

7.4.3. Melting reactions

Partial melting generation of migmatite-granite complexes is the culmination of high-grade metamorphism. This is a sequential process where the production and accumulation of melt increases with time. As prograde reactions take place, melting of the protolith lead to the formation of metatexitic and diatexitic migmatites, culminating with a granitic melt at higher melt fractions (Brown, 2013). Melting reactions can take place at different temperatures, pressures and water proportions. Schematically, pelitic and greywacke protoliths begin to melt at about 650-700 ºC in the presence of an aqueous fluid (fluid-present reactions), producing ~ 7 – 12 vol.% of melt (Brown, 2013; Milord et al., 2001; Vielzeuf and Holloway, 1988). When the temperature increases to ca. 800-1000 ºC during the prograde metamorphic path, partial melting can occur in the absence of an external fluid giving place to a series of fluid-absent reactions, by dehydration of hydrous minerals such as micas and amphiboles, which progressively increase melt production up to 70 modal percent melt (Brown, 2013; Bucher and Grapes, 2011).

Field observations combined with major element geochemistry of FCR-LAC units show that the most probable protolith of the study area is of sedimentary origin (see sections 2 and 6.1). Moreover, the major elements geochemistry, in particular the CaO/Na_2O ratio reinforces the idea that FCR-LAC granites are derived from pelitic melts ($CaO/Na_2O < 0.3$; Jung and Pfänder, 2007) (Figure 7.9a). Based on the trace-element modelling (Rb, Ba, Sr; Inger and Harris, 1993) and also in the mineral assemblages of the FCR-LAC rocks (Chapter 4) we can infer that melting of the pelitic source were mainly controlled by three distinct reactions throughout the progressive increase of melt production.

Petrographic observations indicate that the metatexite paleosomes, which we consider as a residue after melting, is characterized by a lower plagioclase/muscovite modal proportion than the phyllites from where they are considered to be derived. This suggests the operation of the following fluid induced reaction (Patiño Douce and Harris, 1998):

$$9\ \text{muscovite} + 15\ \text{plagioclase} + 7\ \text{quartz} + x\ H_2O \rightarrow 31\ \text{melt} \quad (7.1)$$

The increase of Rb/Sr ratios from phyllite, metatexite to diatexite/granite combined with higher Sr and Ba from metatexites in comparison with diatexite/granite (Figure 7.9b) seems to support that early partial melting resulted from such congruent fluid-present reaction (7.1), consuming plagioclase in greater proportions than muscovite (see also Dou et al., 2019; Gao et al., 2017; Martini et al., 2019).

As temperature increases during prograde metamorphism, partial melting reactions take place in the absence of fluids. It is then required the consumption of hydrous minerals such as micas by fluid-absent reactions. A significant increase of Rb/Sr ratios and decrease of Sr and Ba is observed for granites and some diatexites (Figure 7.9b and 7.9c), suggesting dehydration-melting involving the significant consumption of muscovite and producing peritectic minerals such as K-feldspar and sillimanite (7.2) (Patiño Douce and Harris, 1998; see also Gao et al., 2017; Inger and Harris, 1993; Yang et al., 2019):

25 muscovite + 7 plagioclase + 8 quartz → 5 K-feldspar + 5 sillimanite + 25 melt (7.2)

The mineral assemblage in the diatexites type-1 and granites supports the existence of such reaction. Absence of primary muscovite indicates that muscovite was consumed during these melting reactions, and the appearance of K-feldspar and sillimanite in these rocks provides evidence for fluid-absent melting conditions. The reaction (7.2) also explains the low CaO/Na_2O ratios found in granites, because plagioclase will be less dissolved into the melt in this muscovite dehydration-melting reaction when compared to the fluid-present reaction (Dou et al., 2019; Gao et al., 2017).

After fluid absent reactions involving the consumption of muscovite, it is commonly described the dehydration-melting of biotite as a response to the temperature increase along the metamorphic path. There is some petrographic evidence stemming from migmatites for the breakdown of biotite, such as the occurrence of biotite crystals with corroded borders. However, reactions involving the melting consumption of biotite are accompanied by the peritectic production of garnet (> 0.4 GPa) or cordierite (< 0.4 GPa) (Spear et al., 1999; Bento dos Santos et al., 2011). Such minerals were not detected in the studied migmatites, therefore only incipient melting of biotite occurred. According to experimental results of Le Breton and Thompson (1988), the melt absent reaction consuming biotite, such as:

biotite + plagioclase + sillimanite + quartz → garnet/cordierite + K-feldspar + melt (7.3)

would occur at 760 - 850 ºC at 10 kbar, or somewhat less at lower pressure.

We demonstrated before the existence of two geochemically distinct types of diatexites (see section 7.3.1) and that diatexites type-1 were derived from fluid absent reactions (7.2) associated with dehydration-melting of muscovite. In general, diatexites type-2 exhibit positive Eu anomalies and low Ba and Rb/Sr contents (Figure 7.9c) compared to the remaining granites

and diatexites type-1. This implies that peritectic K-feldspar was not formed or only crystallized in small proportions (Dou et al., 2019; Gao et al., 2017), and, instead, another process must have operated. Fluid-fluxed melting of muscovite (7.1) is a more likely mechanism to generate melts that give origin to diatexites type-2. The melt productivity of such reaction is dependent on the amount of fluid present in the rock. The lower abundance of diatexites type-2 and the lack of granites with compositions compatible with this type of diatexites suggest that the amount of melt generated by that fluid-present reaction and also the amount of fluid in the source rock was small.

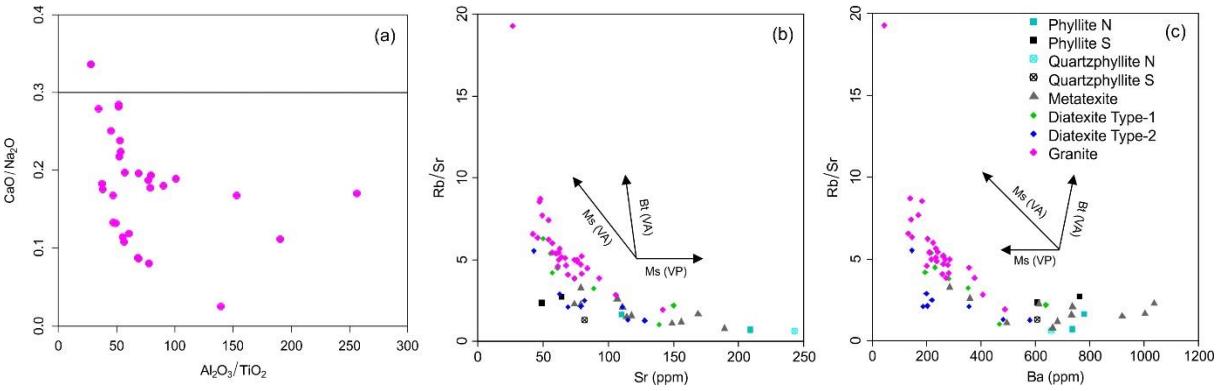

Figure 7.9 – (a) CaO/Na2O versus Al2O3/TiO2 (wt. %) distinguish between pelite-derived melts (CaO/Na2O < 0.3) and melts derived from greywackes or igneous sources (Jung and Pfänder, 2007) for FCR-LAC granites; (b) Rb/Sr versus Sr (ppm) and (c) Rb/Sr versus Ba (ppm) for the host rocks (phyllites) and FCR-LAC lithologies (metatexites, diatexites and granites). The vectors represent the evolution of partial melting reactions (Inger and Harris, 1993): Mu(VP) – vapour-present muscovite melting; Mu(VA) – vapour-absent muscovite melting; Bi(VA) – vapour-absent biotite melting.

Peak metamorphic temperatures can be estimated using the melt-generation temperatures for inherited zircon-rich rocks. Using zircon saturation temperatures (T_{Zr}; Miller et al., 2003; Watson and Harrison, 1983) the estimated melt temperatures for the FCR-LAC ranged from 651 to 891 ºC (Ferreira et al., 2019), which is concordant with the temperature range expected for the partial melting reactions that operated in this anatectic complex. At this temperature range, at least ~10 to 60% volume of melt is produced by the described partial melting reactions (Vielzeuf and Holloway, 1988), thus allowing melt extraction given that the critical melt percentage for melt migration (20 to 35% volume) is surpassed (e.g. Clemens and Vielzeuf 1987; Bento dos Santos et al., 2011). Additionally, this range of estimated melt temperatures are consistent with the minimum metamorphic peak temperature previously calculated from mineral equilibria for the FCR-LAC (T = 761 ± 50 ºC; Pereira et al., 2017).

7.4.4. The role of accessory minerals

Accessory minerals have an important role controlling the trace elements and isotope compositions of migmatites and granites (e.g. Ayres and Harris, 1997; Bea, 1996a, 1996b; Bea

et al., 1994; Zeng et al., 2005). Apatite and zircon are the main accessory minerals that occur in the FCR-LAC rocks and their trace element compositions are described in section 7.3.2.

The results demonstrate that apatite is the main carrier of LREE and Y in the FCR-LAC (Table 2) and exhibits a flat REE pattern (more evident for LREE; Figure 7.5a) typical of peraluminous rocks (Bea, 1996a). The moderate LREE and P_2O_5 covariation observed in the whole-rock geochemistry (Figure 7.10a) confirms the control that apatite has in the variation of these elements.

Conversely, the HREE composition of the anatectic rocks is exclusively influenced by zircon (Appendix G3). This influence is also confirmed by the covariation between HREE and Zr/Hf from the whole-rock geochemistry (Figure 7.10b-d). Granites show depletion in the HREE in comparison to metatexites, which can be tracked to the role of zircon. Indeed, Lu is preferentially retained in restitic zircon grains during partial melting, resulting in a constant decrease of the Lu concentration in subsequent crystallised zircons. This resulted in lower Lu/Hf ratios in granites in comparison with metatexites.

Inherited zircon grains are quite common in all these granites, surviving to zircon dissolution. For an average Zr bulk-rock composition of 150 ppm, an estimated maximum melting temperatures of 850 ˚C and considering a 1:1 proportion of metapelite and greywacke protolith, only about 15% of zircon is expected to dissolve into the melt (Yakymchuk et al., 2017). Thus, very little zircon must have dissolved during partial melting.

Apatite grains found in the metasedimentary units are highly enriched in LREE, and Th which is a typical feature of magmatic apatite (Henrichs et al., 2018). These must then represent relict magmatic grains in these detritic units, that were recrystallised during greenschist facies metamorphism. This can explain the relative depletion of LREE in metatexitic apatite, typical of metamorphic apatite (Henrichs et al., 2018). As LREE-rich relict apatite melted, the whole-rock ∑LREE increased, resulting in more enriched compositions in apatite grains from diatexites and granites. The availability of LREE due to apatite melting is also depicted in zircon from both diatexites and granites.

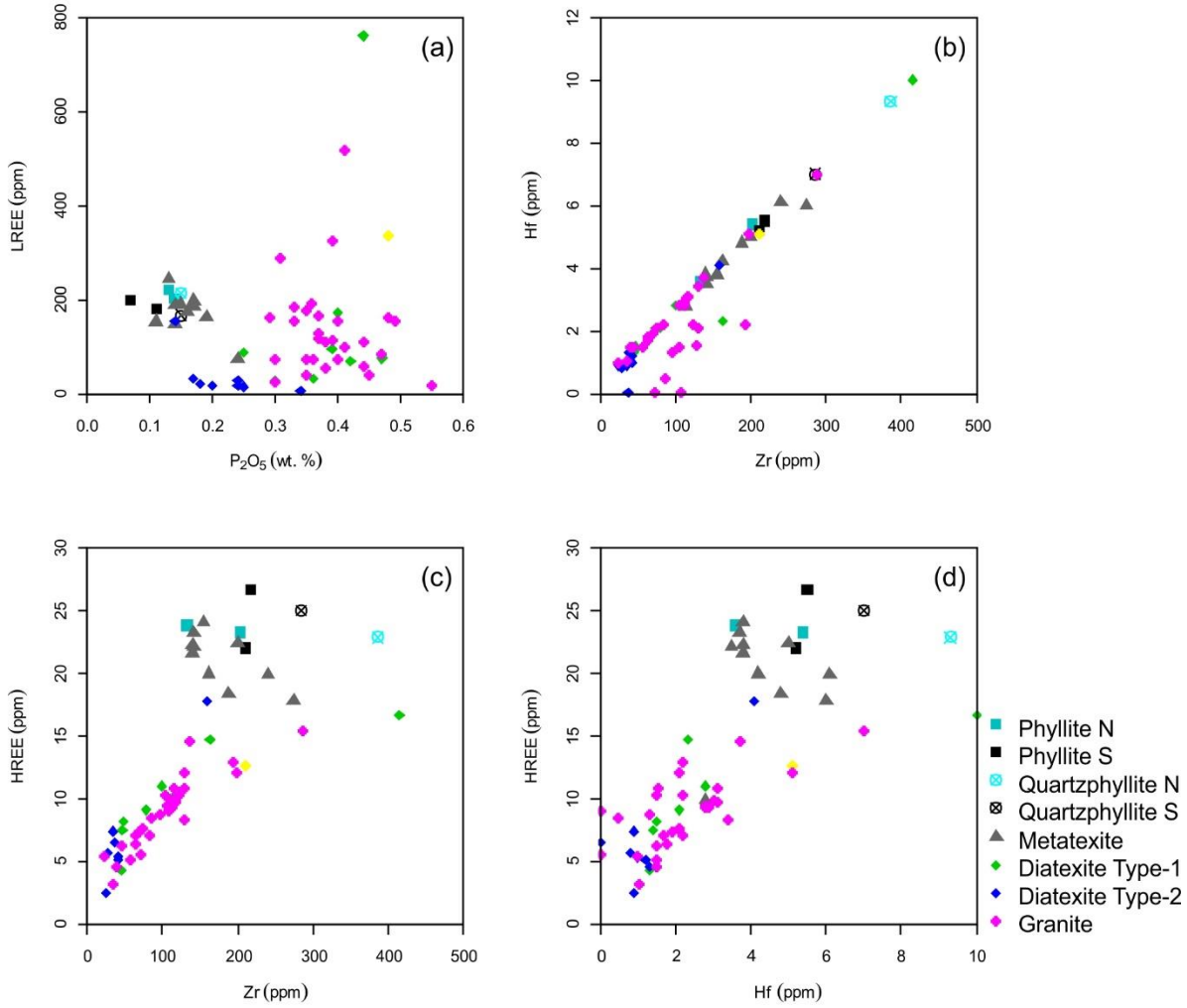

Figure 7.10 – Apatite and zircon role during the partial melting process in the FCR-LAC: (a) P_2O_5 versus LREE (ppm); (b) Zr versus Hf (ppm); (c) Zr versus HREE (ppm); (d) Hf versus HREE (ppm).

7.4.5. Isotope Variability

The εHf_{320} vs. εNd_{320} diagram (Figure 7.6c) reveals that the studied rocks form two tight clusters, each of them comprising metatexites, diatexites and granites. Sm, Nd, Lu and Hf, the parent and daughter elements of the Nd and Hf isotopic systems, are all characterized by high field strengths, which confer them a significant degree of immobility during meteoric and metamorphic processes. Considering this, such clusters clearly suggest the existence of two somewhat distinct sources for the FCR-LAC anatectic complex, in agreement with the significant isotopic variability of the DBSG phyllites (Teixeira, 2008). Additionally, the fact that each of the clusters comprise metatexites, diatexites and granites suggests that during partial melting no significant isotopic disequilibrium occurred, like those caused by the incomplete melt of zircon and the consequent variable release of zircon unradiogenic ^{177}Hf and non-zircon Hf upon melting (the zircon effect; Tang et al., 2014). Considering the very long

half-life of ^{176}Lu (37.1 Ga) and ^{147}Sm (106 Ga), the lack of evidence for isotopic disequilibrium point to a short time that protolith minerals had before melting to develop distinct isotope signatures. Alternatively, their isotopic compositions were homogenised during high-grade metamorphism preceding anatexis (Wolf et al., 2019).

It should be noticed that a significant difference is observed when εNd_0 and εHf_0 (Figure 7.11a) are compared with the initial values for the same systems (ε_{320}). Indeed, the present-day vales (ε_0) show a distinct behaviour of the isotope systems in consideration, with a significantly larger variation for the εHf_{320} values. This allow us to propose that a significant fractionation between Hf and Nd isotope systems occurred during melting and that it was caused by distinct behaviour of their parent/daughter pairs. As shown before, the melting process involved essentially micas and plagioclase, phases with no capability to significantly fractionate Sm from Nd and Lu from Hf, thus suggesting the role of an accessory phase.

Apatite, for which $D^{Sm/Nd} \approx 0.3$ and and $D^{Lu/Hf} \approx 70$ in peraluminous systems (Bea et al., 1994), is a good candidate. However, granites tend to present similar εNd_0, or slightly lower than those characterizing the associated metatexites, but significantly lower εHf_0. Thereof, the decoupling of Lu and Hf can not be the result of apatite during melting reactions, which, being characterized by very high Lu/Hf ratios, would induce, at odds with the observed, an increase with time of $^{176}Hf/^{177}Hf$ by radiogenic ingrowth of ^{176}Hf.

The observed decoupling of Hf and Nd isotopic systems can be achieved by the involvement of zircon. Zirconium and hafnium are usually considered as two geochemically coherent elements, which explains the very high D_{Hf} characterizing zircon. The consequent very low Lu/Hf ratios characterizing zircon will allow, that by incomplete melting of zircon, the melt Lu/Hf be distinct of that of the whole source rock, and that granite rocks would evolve with time to lower $^{176}Hf/^{177}Hf$ ratios than the less evolved metatexites. Moreover, distinct rates of zircon solubility will contribute to the production of melt batches characterized by significantly different Lu/Hf ratios. This would be facilitated by incomplete zircon dissolution, a process which has been demonstrated to frequently occur in peraluminous granitic magmas where zircon saturation occurs at relatively low Zr concentrations (~78 ppm; Harrison and Watson, 1983; Hogan and Sinha, 1991; Tang et al., 2014) and, also, by the fact that zircon is preferentially located inside biotite which can protect it from dissolution (Bea, 1996).

Each of the FCR-LAC metatexite/diatexite/granites groups defined on the εHf_{320} vs. εNd_{320} diagram (Figure 7.6c) display a significant present-day $^{87}Sr/^{86}Sr$ range at almost constant εNd (Figure 7.11b). This suggests that Sr isotope signatures evolved under distinct $^{87}Rb/^{86}Sr$ allowing the radiogenic ingrowth of ^{87}Sr at different rates. At odds with the Nd and Hf systems,

which are mainly controlled by the solubility of accessory phases, for the Rb/Sr system the melt composition is constrained by major mineral phases involved in melting reactions (Tang et al., 2014; Wolf et al., 2019). It should be noticed that an increase of $(^{87}Sr/^{86}Sr)_0$ from metatexites to diatexites and then to granites is observed (Figure 7.11b), indicating an increase of $^{87}Rb/^{86}Sr$ in the melts progressively generated at higher temperatures and with higher input of Rb from the melting of Rb-bearing micas. Indeed, if we take into account the melting reactions inferred for the FCR-LAC (see 7.4.3) there is first a significant and increasing contribution of muscovite to the melt (reactions 7.1 and 7.2) and later the dehydration melting of biotite (reaction 7.3), a mineral usually characterized by significantly higher Rb/Sr than coexisting muscovite (e.g. Neiva et al., 2002).

The range in Sr isotopes is observed even when considered the initial values $(^{87}Sr/^{86}Sr)_{320}$ (Figure 7.6a). There are several ways to explain variation on the initial Sr isotopic composition: isotopic disequilibrium, hydrothermal alteration and/or assimilation fractional crystallization (AFC), and source heterogeneity.

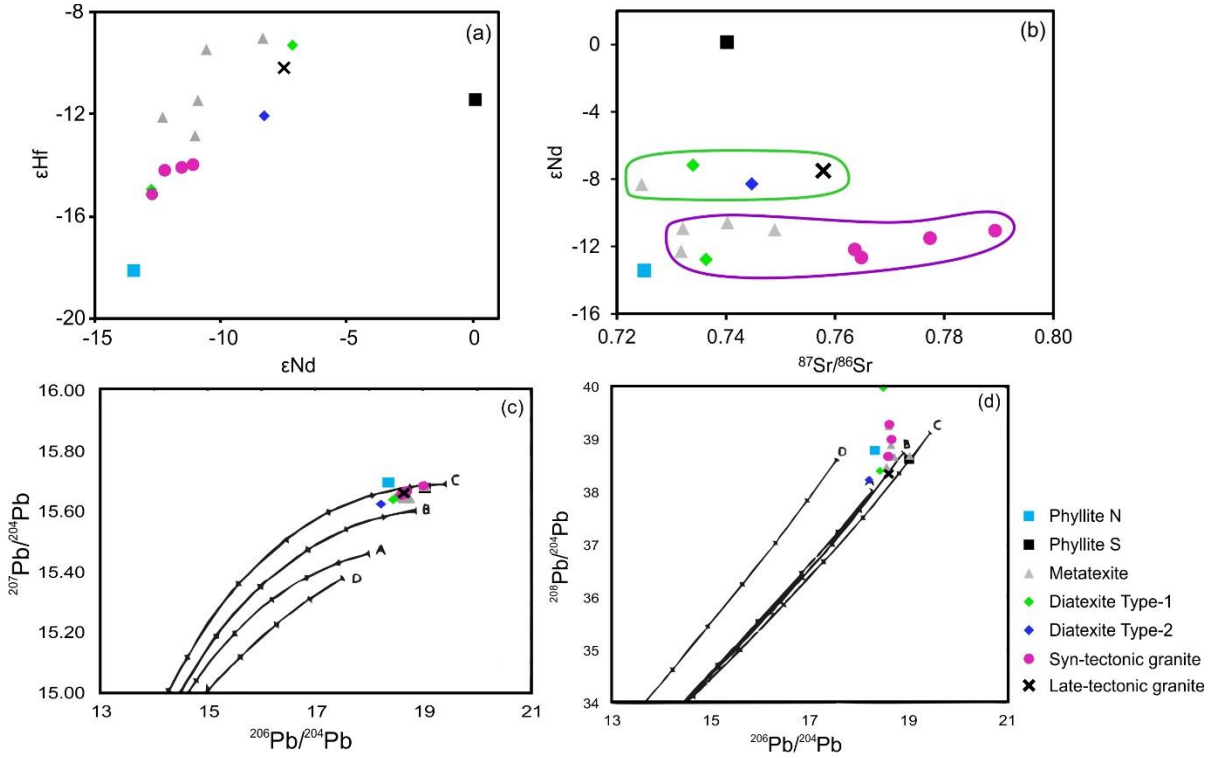

Figure 7.11 – (a) εNd versus εHf diagram for the host rocks (phyllites) and FCR-LAC lithologies (metatexites, diatexites and granites); (b) 87Sr/86Sr versus εNd diagram for the host rocks (phyllites) and FCR-LAC lithologies (metatexites, diatexites and granites); (b) and (c) Plumbotectonic model after Zartman and Doe (1981) applied to the host rocks (phyllites) and FCR-LAC lithologies (metatexites, diatexites and granites): A – mantle; B – orogene; C – upper crust; D – lower crust.

Isotopic disequilibrium taking place during the melting stages involving various minerals characterized by significantly distinct $^{87}Rb/^{86}Sr$ (plagioclase, muscovite, biotite) is a plausible mechanism in these settings (crustal anatexis). However, these isotopic signatures had to be

developed previously to melting to account for variable mineral $^{87}Sr/^{86}Sr$ during radiogenic ingrowth (Farina and Stevens, 2011; Zeng et al., 2005b). Yet, at odds with the commonly observed in situations of isotopic disequilibrium (e.g. Wolf et al., 2019), no systematic isotopic variation is observed when considered the different lithotypes (metatexites, diatexites, and granites), but only a significant overlapping of the $(^{87}Sr/^{86}Sr)_{320}$ characterizing metatexites and granites. In this perspective, the $(^{87}Sr/^{86}Sr)_{320}$ variability could likely just be the result of open-system processes, such as hydrothermal alteration and/or assimilation fractional crystallization (AFC). A hydrothermal overprint on these units would result in a lack of correlation between mobile and high field strength immobile elements, such as LILE and Ti, respectively (e.g. Huang et al., 2019). This is not supported by our data, which show a clearly linear correlation between K, Sr, Ba *vs.* TiO_2 (Figure 7.12a-c). Therefore, the interpretation of the $^{87}Sr/^{86}Sr_{320}$ variability as a result of post-magmatic overprint is not plausible.

AFC is not a very probable process in constraining the chemical variability of S-type granitic systems. Indeed, as suggested by Castro (2014), the small difference in density between melt and minerals precociously crystallised, as well as the high viscosity of high silica melts, lead to consider as probably small and inefficient the role of fractional crystallization on granitic magmas. In addition, it has been considered, based on thermodynamics, that granitic melts have a limited capability of assimilation of crustal rocks, which is more evident for relatively low-temperature S-type magmas like those in this study (e.g. Glazner, 2007). In agreement, no positive correlation is observed for the studied rocks between La/Sm and Th/Sc (Figure 7.12d), both ratios being expected to increase during AFC processes (Huang et al., 2019).

Given the lack of evidences for Sr isotopic disequilibrium and for the occurrence of hydrothermal alteration, the large variability of the $^{87}Sr/^{86}Sr_{320}$ could be envisaged as a consequence of source heterogeneity in agreement with geochemical studies of the DBSG phyllites which have shown a much larger heterogeneity of the Sr isotope ratios than the observed for $^{143}Nd/^{144}Nd$ (Teixeira, 2008).

On the $^{207}Pb/^{204}Pb$ vs $^{206}Pb/^{204}Pb$ diagram (Figure 7.11c), the studied rocks define a linear array close to the evolution line modelled for the upper continental crust by Zartman and Doe (1981). However, a significantly larger dispersion is observed in the $^{208}Pb/^{204}Pb$ vs. $^{206}Pb/^{204}Pb$ (Figure 7.11d and Figure 7.7b) suggesting a decoupling of ^{206}Pb and ^{207}Pb, the final products of decay chains initiated on ^{238}U and ^{235}U respectively, from ^{208}Pb the final radiogenic product of ^{232}Th. In granitic systems, the elemental Pb budget of whole-rocks is mainly controlled by K-feldspar, while accessory phases are the main repositories of U and Th (e.g. Bea, 1996), having thus the ability to strongly influence the lead isotope composition through the contribution of radiogenic

lead (Hogan and Sinha, 1991; Wolf et al., 2019). The controlling role of such accessory minerals on the isotopic composition of melts strongly depend on the solubility of such phases on the progressively generated melts (e.g. Hogan and Sinha, 1991). Taking this into account, the decoupling of uranogenic lead from thorogenic lead (Figure 7.7b) may reflect the variable modal proportions of these phases in the source materials and also the variable contribution to melts of U-rich (e.g.: zircon, apatite and monazite) and Th-rich (e.g.: monazite and apatite) minerals.

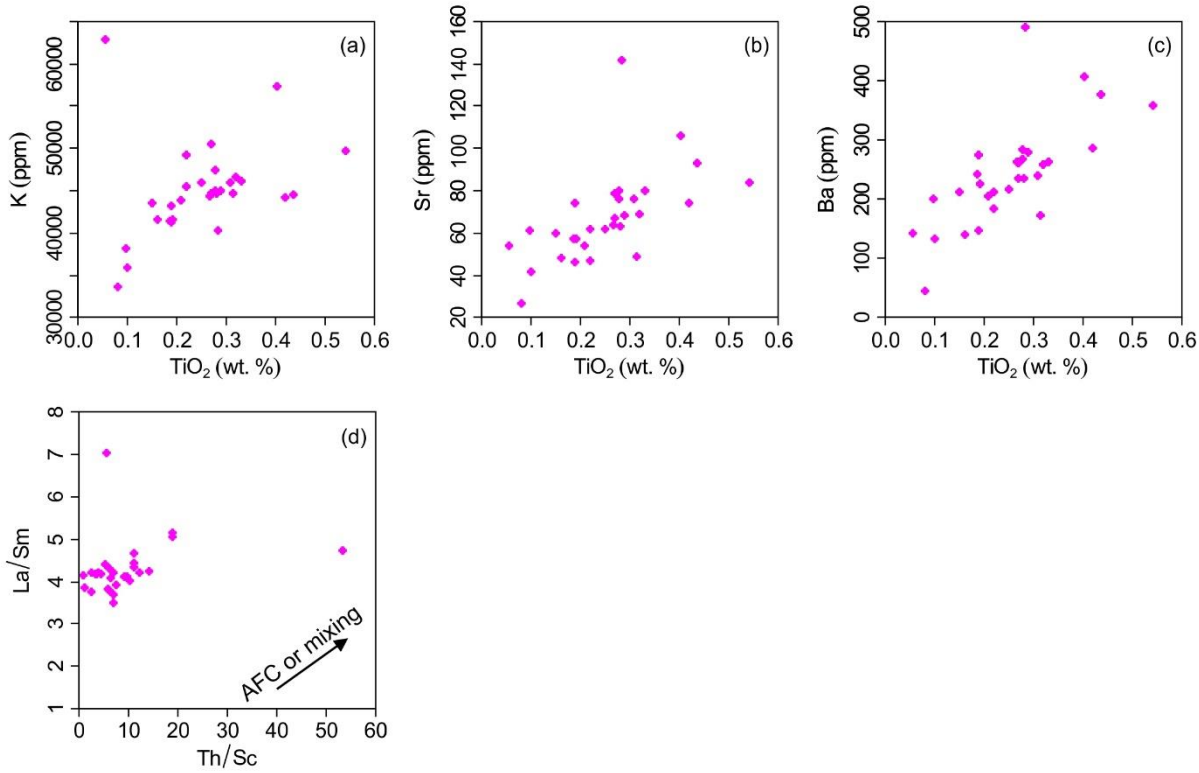

Figure 7.12 – Covariation between LILE (K, Sr and Ba) and HFSE (TiO_2), (a), (b) and (c), respectively; (d) AFC assessment – La/Sm versus Th/Sc (ppm).

7.4.6. Source rocks: some considerations

Based on the whole-rock geochemistry (e.g. Harker diagrams; Figure 7.1 and 7.2), we can distinguish the geochemical evolution due to partial melting and the progressive residuum-melt separation, where the metapelitic rocks (phyllites) are depicted in the origin of the metatexite-diatexite-granite sequence. This relationship is in clear agreement with field-based observations.

Despite the isotopic differences/variability between the phyllite N (Douro Group; Fig. 9b; Teixeira, 2008) and phyllite S, and even among the anatectic complex lithologies (e.g. clustering; Figure 7.6c), the Sr, Nd, and Hf isotopic compositions show a clear affinity between

these rocks. This is more evident in the phyllite N with Sr and Nd signatures within the range of the FCR-LAC units (Figure 7.6a and Appendix G4), than for phyllite S, where only Hf initial composition is within analytical uncertainty of the remaining anatectic units (Figure 7.6c and Appendix G4). TDM_2 provenance ages of the metasedimentary protoliths of the anatectic complex broadly agree with the phyllite units TDM_2 ages (Appendix G4), which reinforces the Douro-Beiras Supergroup as representing the most probable protolith.

While it is quite contentious to draw further links and attribute a definite source to this anatectic complex (either the Douro Group - phyllite N - or Beiras Group - phyllite S) due to the current small sample size, from the data here presented it seems reasonable to propose a stronger affinity with the Douro Group, sampled to the N. However, we cannot fully discard a source affinity with the Beiras Group (Tassinari et al., 1996) or even a minor contribution of the Ollo de Sapo magmatic rocks (Montero et al., 2017), particularly when the Nd initial isotopic compositions are taken into account (Figure 7.6b). This is the case of the IIγ late-tectonic granite, which exhibits distinct isotopic compositions when compared to the other syn-tectonic granites (Figure 7.6a and 7.6c). This is in good agreement with evidence for a distinct petrogenesis, given by its younger crystallization age (Ferreira et al., 2019).

The Nd and Hf isotopic variability between the phyllites from the northern (εNd_{320} = -10.07) and southern (εNd_{320} = 3.28) domains are striking. Similar variabilities in the CIZ have also been reported by Villaseca et al. (2014). This suggests source heterogeneities within both domains, with variable detrital inputs (more and less evolved crustal sources), which influenced the isotopic composition of the FCR-LAC. Further work is needed to clearly demonstrate: a) a systematic isotopic variability between the metasedimentary units to the North and South of the FCR-LAC; b) the affinity of the anatectic complex with the Douro Group. This will further elucidate the nature of the boundary between these two basins during the Precambrian/Cambrian, such as a major paleogeographic boundary as proposed by Villaseca et al. (2014) and Iglesias and Ribeiro (1981).

7.5. CONCLUSIONS

This study was conducted in order to assess the links between the distinct lithologies of the variscan Figueira de Castelo Rodrigo – Lumbrales Anatectic Complex (FCR-LAC) of the Central Iberian Zone (CIZ). The main conclusions are summarized below:

1) Based on whole-rock elemental and isotopic geochemistry a genetic link was established between metatexites, diatexites and granites, which are, thus,

representatives of the different stages of anatectic complex evolution, leading to the genesis of the S-type granites.

2) In this study, we were able to demonstrate the existence of two geochemically distinct diatexite groups, (type-1 and type-2) generated at different stages of the partial melting process. Diatexites type-1 with high Rb concentration and fractionated HREE are geochemically similar to the S-type granites of the region, while none of the outcropping granites seems to be linked to diatexites type-2.
3) Based on the mineral assemblage and whole-rock geochemistry we demonstrated that diatexites type-1 and granites were produced via fluid-absent reactions during dehydration-melting of muscovite and production of peritectic K-feldspar and sillimanite plus melt. On the contrary, Rb-poor, unfractionated HREE diatexites type-2 required the participation of fluids during melting reactions, which consumes more plagioclase than muscovite. The relatively scarcity of this group in comparison with Rb-rich diatexites (type-1) attest for a lack of interstitial or fluxed fluids within the metasedimentary units during peak metamorphism. Based on the evidence of incipient biotite melting and zircon saturation temperatures the estimated peak temperatures range between 760 and 890 ˚C. These conditions result in large volumes of melt being produced (in excess of 30%) which explains the profusion of S-type granites within the CIZ.
4) There are no signs of significant isotopic disequilibrium during melting. This means that the source minerals were in isotopic equilibrium at the onset of the melting process, either reflecting that they were formed shortly before melting, or, alternatively, that isotopic homogenization during the high-grade metamorphism preceded the melting process. However, the distinct contributions of mineral phases to the melt produced batches of melt with distinct parent/daughters' ratios, explaining the present-day significant isotopic heterogeneity.
5) Rb/Sr ratios and the Pb budget of the successively generated lithotypes were mainly controlled by major minerals like muscovite, K-feldspar and plagioclase. The accessory phases were the main constrainers of Sm/Nd, Lu/Hf ratios and of U and Th contents.
6) Two distinct groups, both comprising metatexites, diatexites and granites, were identified when comparing the initial isotopic ratios, testifying for the existence of a certain degree of source heterogeneity. This is consistent with the differences in the

initial Hf and Nd isotopic compositions between late-tectonic granite-migmatite cluster and the syn-tectonic granite-migmatite cluster.

7) The genetic links with probable protoliths of the anatectic complex were also explored showing that the Douro-Beiras Supergroup are related to the anatectic complex lithotypes, with possible minor contribution of the Ollo de Sapo magmatic rocks.

CHAPTER 8. FINAL REMARKS, CONCLUSIONS AND FUTURE RESEARCH

8.1. FINAL REMARKS

The main goal of this PhD project was contribute to an increased knowledge concerning the interdependence between migmatization, granitogenesis, deformation and exhumation of the anatectic complexes generated at deep crustal levels, during an orogeny. For these the Figueira de Castelo Rodrigo – Lumbrales Anatectic Complex was used as a case study, thus allowing a better understanding of the crustal heat and mass transfer processes in the axial zone of the Iberian sector of the Variscan orogen.

The research to the accomplishment of the thesis goals required a multi-method approach, including petrographic characterization, LA-ICP-MS U-Pb geochronology, whole-rock major and trace element geochemistry, whole-rock Sr-Nd-Hf-Pb geochemistry, accessory trace element composition (i.e. apatite and zircon) of the FCR-LAC lithologies and their host rocks.

The petrographic analysis allowed to characterize the mineralogical assemblage and textures of the FCR-LAC lithologies and metasedimentary host rocks. The U-Pb dating of zircon and apatite from the FCR-LAC lithologies constrained the ages of migmatization and granite emplacement for the studied area and, together with Ti-in-zircon geothermometry, it was obtained thermochronological results which defined the exhumation conditions of the anatectic complex through cooling and exhumation conditions. In addition, U-Pb detrital zircon age signatures from the FCR-LAC and their hosting metasedimentary were compared for source assessment purposes. The new U-Pb detrital zircon ages of the metasedimentary units were also compared to published detrital zircon data from potential stratigraphic equivalents in the Spanish sector and in the Beiras Group, and from the overlying Ordovician metasedimentary units. These allowed the evaluation of the evolution of the sediment sources during the Ediacaran – Cambrian – Ordovician, with implications on the geodynamic evolution of the CIZ.

The geochemical data is an important tool regarding petrogenetic evaluation. The elemental and isotopic results together with the petrographic characterization allowed to assess the melting reactions that led to the formation of FCR-LAC lithotypes; provided insights onto the causes of isotopic variability characterizing the anatectic complex; confirmed the geochemical link between the different stages of anatexis, from migmatites to granites; and allowed the assessment of the potential metapelitic protoliths together with the U-Pb detrital zircon data.

The main conclusions of this study are organized in this section accordingly with the key topics/methods of the PhD project.

8.2. CONCLUSIONS

The main conclusions of this study are organized in this section accordingly with the key topics/methods of the PhD project.

8.2.1. Migmatization and granite emplacement ages: constraints on exhumation

New U–Pb zircon crystallization ages were determined for 5 different granite facies of the FCR-LAC (IIγ, IIIγ, Vγ, IXγ and Xγ), yielding ages between 300 ± 2.2 (IIγ) and 317 ± 2.1 Ma (IXγ), confirming that most of these granites formed during the syn-D_3 magmatic stage, with the exception of one late-tectonic granite facies (IIγ), which is clearly intrusive into the other facies, yet is affected by the late stages of Variscan shearing by the JPCSZ. Additionally, the new U-Pb zircon ages for the migmatites of the FCR-LAC allowed to estimate the migmatization age, temporally constraining the high temperature section of the metamorphic path (343.7 ± 2.5 – 314.8 ± 1.3 Ma). The metatexite exhibits a peak metamorphic age of 314.8 ± 1.3 Ma, while for the diatexites this age is 318.8 ± 2.6 Ma. These ages constrain the age of the metamorphic peak at 316.8 ± 2.0 Ma for the anatectic complex, which is coeval with the emplacement of the S-type granites (313–317 Ma). Thus, the migmatization/peak metamorphic ages suggest that the anatexis event started during the D_2 Variscan phase and culminated during the D_3 Variscan phase, concomitantly with the emplacement of the S-type granites. The obtained U-Pb apatite ages indicate that the FCR-LAC cooled down to *ca.* 500 ºC between 301.4 ± 2.6 Ma and 314.3 ± 7.2 Ma.

Combining the U–Pb zircon and apatite ages with their respective closure temperatures, it was possible, for the first time, to quantitatively constrain the cooling/exhumation conditions of the FCR–LAC. The cooling rates for the anatectic complex lithologies range from 7 to 54 ºC/Ma and the exhumation between 0.2 and 1.3 mm a^{-1}. Considering the cooling rates (13 – 54 ºC) from the granites and the migmatites that represent the peak metamorphic are estimated an average cooling rate of 31 ºC/Ma. The metatexite is the FCR-LAC lithology with faster cooling rate (54 ºC/Ma) which is logical since the metatexites are the group of rocks that directly contacts with the "cold" host rocks. These rates imply fast cooling and exhumation rates compatible with a tectonically-assisted mechanism for the exhumation of this anatectic complex, with the movement of the Huebra and Juzbado-Penalva do Castelo shear zones playing an important role on the crustal mass transfer. The closure temperatures of both geothermometers (zircon and apatite) combined with the geothermal gradient defined by Pereira et al. 2017 allowed to estimate 6 to 9 km of vertical displacement for the anatectic complex.

8.2.2. Source constraints

In general, the FCR-LAC and DBSG detrital zircon comparison reveal moderate similarities, but these are particularly stronger between the Excomungada Fm. (Cambrian) and the metatexites which are closely related to the FCR-LAC's protolith due to its lower metamorphic grade. Yet, zircon ages younger than 500 Ma, absent in the DBSG are interpreted as representing the contribution of intrusive magmatic rocks from the Ordovician Ollo de Sapo Fm. (García-Arias et al., 2018) that must have intruded the middle crust. These conclusions point to a heterogeneous middle crust composed by metasedimentary units with variable input of detrital and igneous rocks during the Variscan deformation events. This heterogeneity of the middle crust influences the isotopic composition variability observed in the FCR-LAC rocks.

The detrital zircon age distributions of the DBSG units (Pinhão and Excomungada Fms.) put in evidence that the Douro basin sediments were mainly sourced in a Cadomian continental magmatic arc, during and after its activity.

The Pinhão and Excomungada formations were compared with the lateral equivalent Spanish units and with the Beiras Group following the maximum depositional age similarity criteria. The detrital zircon age signatures from the Pinhão Fm and their equivalent Beiras Group greywackes indicate significantly distinct sources, with the Douro unit showing lower proportion of Paleoproterozoic and Neoarchean components. The Pinhão and Excomungada Fms. (Douro Group) shows a younger Cadomian age peak (*ca.* 600 Ma) in comparison to the Beiras Group, whose spectra highlights a source from the protracted arc history (from 800 to 500 Ma). These differences between the Douro and Beiras Groups might be envisaged as a result of a paleogeographic barrier which separated them, restricting the detrital component drained to the Douro basin. The Ordovician quartzite age spectra is statistically undistinguishable from the Pinhão Fm., which reinforces the interpretation of recycling of these Neoproterozoic-Cambrian units during the early Ordovician.

8.2.3. Geochemistry and Petrogenesis

The whole-rock elemental and isotopic geochemistry confirms the genetic link between the FCR-LAC lithologies (metatexites, diatexites and granites), already suggested by field data, which are, thus, representatives of the different stages of anatectic complex evolution culminating with the genesis of the S-type granites.

The geochemical characterization of anatectic rocks demonstrate the existence of two distinct diatexite groups, (type-1 and type-2) generated at different stages of the partial melting process. Diatexites type-1 with high Rb concentration and fractionated HREE are geochemically akin to

the S-type granites of the region, while diatexites type-2 are SiO_2 enriched, low Rb concentration and unfractionated HREE.

Combining the mineral assemblage and whole-rock geochemistry, it was demonstrated that the diatexites type-1 and granites were produced via fluid-absent reactions during dehydration-melting of muscovite and production of peritectic K-feldspar and sillimanite plus melt. Oppositely, diatexites type-2 required the participation of fluids during melting reactions, which consumes more plagioclase than muscovite. Considering that the fluid-present reactions occurred earlier and at lower temperatures than the fluid-absent reactions, the ages of the different type of migmatites should depict the temperature-time (T-t) relationship characterizing the prograde metamorphic path. This is, in fact, observed with ages around 343.7 ± 2.5 Ma obtained for diatexite type-2 and 328.8 ± 3.4 Ma for a diatexite type-1, culminating in the metamorphic peak at 318.8 ± 2.6 Ma (diatexite type-1).

Based on the evidence of incipient biotite melting and zircon saturation temperatures, the estimated peak temperatures range between 760 and 890 ºC, similar to the Ti-in-zircon temperatures of the determined peak metamorphic ages (790 ºC and 869 ºC). These conditions resulted in significant percentages of melting (> 30%) with the consequent large volumes of melt being produced which explains the profusion of S-type granites within the CIZ.

At odds with has been proposed for other anatectic complexes elsewhere, the isotopic variability observed on the FCR-LAC lithologies it is not explained by isotopic disequilibrium during melting. It is here proposed that the distinct contributions of mineral phases to the melt through the different melting reactions produced batches of melt with distinct elemental parent/daughters' ratios, which explain the present-day significant isotopic heterogeneity. The Rb/Sr ratios and the Pb budget of the successively generated lithotypes were mainly controlled by major minerals like muscovite, K-feldspar and plagioclase while the accessory phases (i.e. apatite and zircon) were the main constrainers of Sm/Nd, Lu/Hf ratios and of U and Th contents. Two distinct groups, both comprising metatexites, diatexites and granites, were identified when comparing the initial isotopic ratios, particularly for the Nd and Hf isotopic systems, supporting the existence of a certain degree of source heterogeneity.

The genetic links with probable protoliths of the anatectic complex were also explored showing that the Douro-Beiras Supergroup is most probably the source rock of the anatectic complex, with possible minor and variable contribution of the Ollo de Sapo magmatic rocks, which cause the observed whole-rock isotopic variability, a percept also endorsed by the obtained U-Pb detrital zircon ages results.

8.3. FUTURE RESEARCH

This PhD thesis is an important contribution for the knowledge of the studied region, as well as for the study of the anatectic complexes evolution during the Variscan Orogeny, by the novelty of the geochronological and geochemical data and the applied research methodologies (e.g. thermochronology). However, in the future it will be fundamental to proceed to a more refined geothermobarometric study, further constrain the thermochronological path at lower temperatures and acquire more U-Pb detrital zircon ages from the Douro-Beiras Supergroup units that host the anatectic complex.

The geothermobarometric study implies the calculation of pseudosections which are phase diagrams that show the fields of stability of different equilibrium mineral assemblages, for a specific bulk-rock composition. Concerning thermochronology, this thesis already contemplates a study at high temperatures (> 500 ºC). However, for a better constrain of the T-t path it is necessary to perform a thermochronological study at lower temperatures applying methods such as apatite fission track and zircon U-Th/He. The acquisition of more U-Pb detrital zircon ages from the Douro-Beiras Supergroup units will allow an improved study on the evolution of the Douro basin, as well as a better definition of the paleogeographic scenarios during the Ediacaran-Cambrian ages.

Furthermore, it is also important to understand if the interpretations modelled in this work are also verified in other anatectic complexes of the CIZ, such as the Porto-Viseu Metamorphic Belt which occurs in physical continuity with the Figueira de Castelo Rodrigo-Lumbrales Anatectic Complex.

I hope that I could have a future in scientific research that allow me to contribute to the fill up the gaps still existent in the understanding of crustal evolution in the axial sector of the Iberian Variscan Belt.

REFERENCES

Ábalos, B.V., 1992. Cinemática y mecanismos en regimen de transpresion. Evoluvión estructural y metamorficca de la zona de cizalla dúctil de BadajozCórdoba.

Acciaioli, M.H., Santos, J.F., Munhá, J., 2005. Ar-Ar dates for two different stages of the Variscan D3 recorded in metapelites of Serra da Freita. Geophys Res Abs 7, 10076.

Alcock, J.E., Martínez, J.R., Rubio, F.J., Díez, A., Díez, R., Gómez, J., Arenas, R., Dias, Í., González, E., 2015. Tectonophysics 2-D thermal modeling of HT – LP metamorphism in NW and Central Iberia : Implications for Variscan magmatism , rheology of the lithosphere and orogenic evolution. Tectonophysics 657, 21–37. https://doi.org/10.1016/j.tecto.2015.05.022

Aleinikoff, J.N., Schenck, W.S., Plank, M.O., Srogi, L.A., Fanning, C.M., Kamo, S.L., Bosbyshell, H., 2006. Deciphering igneous and metamorphic events in high-grade rocks of the Wilmington complex, Delaware: Morphology, cathodoluminescence and backscattered electron zoning, and SHRIMP U-Pb geochronology of zircon and monazite. Bull. Geol. Soc. Am. 118, 39–64. https://doi.org/10.1130/B25659.1

Alves Ribeiro, J., Monteiro-Santos, F.A., Pereira, M.F., Díez Fernández, R., Dias da Silva, Í., Nascimento, C., Silva, J.B., 2017. Magnetotelluric imaging of the lithosphere across the Variscan Orogen (Iberian autochthonous domain, NW Iberia). Tectonics. https://doi.org/10.1002/2017TC004593

Amaro, P., Pereira, A.R., Pereira, M., Teixeira, M., Bento dos Santos, T., Mata, J., Ferreira, N., 2016. Estudo petrográfico, mineralógico e geotermobarométrico preliminar do Complexo Anatéctico da Serra da Estrela, in: VI Congresso Jovens Investigadores Em Geociências, LEG 2016. Estremoz, pp. 71–75.

Andersen, T., Kristoffersen, M., Elburg, M.A., 2018. Visualizing, interpreting and comparing detrital zircon age and Hf isotope data in basin analysis – a graphical approach. Basin Res. 30, 132–147. https://doi.org/10.1111/bre.12245

Annen, C., Scaillet, B., Sparks, R.S.J., 2006. Thermal Constraints on the Emplacement Rate of a Large Intrusive Complex: The Manaslu Leucogranite, Nepal Himalaya. J. Petrol. 47, 71–95.

Areias, M., Ribeiro, M.A., Santos, J.F., Dória, A., 2014. LP-HT anatectic processes and lithological heterogeneity in the Mindelo Migmatite Complex (NW Portugal). Estud. Geológicos 70, 1–20. https://doi.org/10.3989/egeol.41730.323

Arenas, R., Sánchez Martínez, S., Díez Fernández, R., Gerdes, A., Abati, J., Fernández-Suárez,

J., Andonaegui, P., González Cuadra, P., López Carmona, A., Albert, R., Fuenlabrada, J.M., Rubio Pascual, F.J., 2016. Allochthonous terranes involved in the Variscan suture of NW Iberia: A review of their origin and tectonothermal evolution. Earth-Science Rev. 161, 140–178. https://doi.org/10.1016/J.EARSCIREV.2016.08.010

Ashwal, L.D., D. Tucker, R., K. Zinner, E., 1999. Slow cooling of deep crustal granulites and Pb-loss in zircon. Geochim. Cosmochim. Acta 63, 2839–2851. https://doi.org/10.1016/S0016-7037(99)00166-0

Ayres, M., Harris, N., 1997. REE fractionation and Nd-isotope disequilibrium during crustal anatexis: constraints from Himalayan leucogranites. Chem. Geol. 139, 249–269. https://doi.org/10.1016/S0009-2541(97)00038-7

Azevedo, M.R., Valle Aguado, B., 2013. Origem e instalação de Granitóides Variscos na Zona Centro-Ibérica, in: Dias, R., Araújo, A.,Terrinha, P., Kullberg, J.C. (Ed.), Geologia de Portugal. Volume I – Geologia Pré-Mesozóica de Portugal. pp. 377–401.

Azevedo, M.R., Valle Aguado, B., Nolan, J., Estela Martins, M., Medina, J., 2005. Origin and emplacement of syn-orogenic Variscan granitoids in Iberia the Beiras massif. J. Virtual Explor. 19. https://doi.org/10.3809/jvirtex.2005.00115

Baksi, A.K., 1994. Geochronological studies on whole-rock basalts, Deccan Traps, India: evaluation of the timing of volcanism relative to the K-T boundary. Earth Planet. Sci. Lett. 121, 43–56. https://doi.org/10.1016/0012-821X(94)90030-2

Barbarin, B., 1988. Use of zircon typology for the study of some granites from the Massif Central, France. Rend. Soc. Ital. di Miner. e Petrol. 43, 463–476.

Barbero, L., 1995. Granulite-facies metamorphism in the Anatectic Complex of Toledo, Spain: late Hercynian tectonic evolution by crustal extension. J. Geol. Soc. London. 152, 365–382. https://doi.org/10.1144/gsjgs.152.2.0365

Barbero, L., Villaseca, C., 2000. Eclogite facies relics in metabasites from the Sierra de Guadarrama (Spanish Central System): P-T estimations and implications for the Hercynian evolution. Mineral. Mag. 64, 815–836. https://doi.org/DOI: 10.1180/002646100549814

Bea, F., 1996a. Residence of REE, Y, Th and U in granites and crustal protoliths; implications for the chemistry of crustal melts. J. Petrol. 37, 521–552. https://doi.org/10.1093/petrology/37.3.521

Bea, F., 1996b. Controls on the trace element composition of crustal melts. Trans. R. Soc. Edinb. Earth Sci. 87, 33–41. https://doi.org/10.1017/S0263593300006453

Bea, F., Montero, P., González-Lodeiro, F., Talavera, C., 2007. Zircon inheritance reveals

exceptionally fast crustal magma generation processes in Central Iberia during the Cambro-Ordovician. J. Petrol. 48, 2327–2339. https://doi.org/10.1093/petrology/egm061

Bea, F., Pereira, M.D., Stroh, A., 1994. Mineral/leucosome trace-element partitioning in a peraluminous migmatite (a laser ablation-ICP-MS study). Chem. Geol. 117, 291–312. https://doi.org/10.1016/0009-2541(94)90133-3

Belousova, E.A., Griffin, W.L., O'Reilly, S.Y., 2006. Zircon crystal morphology, trace element signatures and Hf isotope composition as a tool for oetrogenetic modelling: Examples from Eastern Australian granitoids. J. Petrol. 47, 329–353. https://doi.org/10.1093/petrology/egi077

Benisek, A., Finger, F., 1993. Factors controlling the development of prism faces in granite zircons: a microprobe study. Contrib. to Mineral. Petrol. 114, 441–451.

Bento dos Santos, T., Munhá, J.M., Tassinari, C.C.G., Fonseca, P.E., Dias Neto, C., 2010a. Thermochronology of central Ribeira Fold Belt, SE Brazil: Petrological and geochronological evidence for long-term high temperature maintenance during Western Gondwana amalgamation. Precambrian Res. 180, 285–298. https://doi.org/10.1016/j.precamres.2010.05.002

Bento dos Santos, T., Ribeiro, M.L., Clavijo, E., Díez Montes, A., Solá, A.R., 2010b. Geothermobarometric estimates and P-T paths for migmatites from Farilhões Islands, Berlengas archipelago, W Portugal, in: VIII Congresso Nacional de Geologia. e-Terra, pp. 1–4.

Bento dos Santos, T., Rodrigues, J.F., Castro, P., Meireles, C., Ferreira, N., Ferreira, P., Ferreira, J.A., Pereira, I., Ribeiro, A., Pereira, E., Guimarães, F., n.d. Exhumation of an anatectic complex by channel flow and extrusion tectonics: structural and metamorphic evidence from the Porto – Viseu Metamorphic Belt, Central-Iberian Zone. Int. J. Earth Sci.

Bento dos Santos, T., Valverde-Vaquero, P., Ribeiro, M.L., Solá, A.R., González-Clavijo, E., Díez-Montes, A., Dias da Silva, Í., 2019. Metamorfic Evolution of the Farilhões Anatectic Complex (Berlengas Archipelago): Geodynamic Implications, in: Quesada, C., Oliveira, J.T. (Eds.), The Geology of Iberia: A Geodynamic Approach Volume 2: The Variscan Cycle. Springer, pp. 453–455. https://doi.org/https://doi.org/10.1007/978-3-030-10519-8

Bento dos Santos, T.M., Munhá, J.M., Tassinari, C.C.G., Fonseca, P.E., 2011a. The link between partial melting, granitization and granulite development in central Ribeira Fold Belt, SE Brazil: New evidence from elemental and Sr-Nd isotopic geochemistry. J. South Am. Earth Sci. 31, 262–278. https://doi.org/10.1016/j.jsames.2011.01.004

Bento dos Santos, T.M., Munhá, J.M., Tassinari, C.C.G., Fonseca, P.E., Neto, C.D., 2011b.

Metamorphic P-T evolution of granulites in the central Ribeira Fold Belt, SE Brazil. Geosci. J. 15, 27–51. https://doi.org/10.1007/s12303-011-0004-1

Bento dos Santos, T.M., Tassinari, C.C.G., Fonseca, P.E., 2015. Diachronic collision, slab break-off and long-term high thermal flux in the Brasiliano-Pan-African orogeny: Implications for the geodynamic evolution of the Mantiqueira Province. Precambrian Res. 260, 1–22. https://doi.org/10.1016/j.precamres.2014.12.018

Bento dos Santos, T.M., Tassinari, C.C.G., Fonseca, P.E., 2014. Garnet-biotite diffusion mechanisms in complex high-grade orogenic belts: Understanding and constraining petrological cooling rates in granulites from Ribeira Fold Belt (SE Brazil). J. South Am. Earth Sci. 56, 128–138. https://doi.org/10.1016/J.JSAMES.2014.09.003

Bertrand, A., Rosenberg, C., Rabaute, A., Herman, F., Fügenschuh, B., 2017. Exhumation mechanisms of the Tauern Window (Eastern Alps) inferred from apatite and zircon fission track thermochronology. Tectonics 36, 207–228. https://doi.org/10.1002/2016TC004133

Bhatia, M.R., Crook, K.A.W., 1986. Trace element characteristics of graywackes and tectonic setting discrimination of sedimentary basins. Contrib. to Mineral. Petrol. 92, 181–193. https://doi.org/10.1007/BF00375292

Bindeman, I.N., Melnik, O.E., 2016. Zircon Survival, Rebirth and Recycling during Crustal Melting, Magma Crystallization, and Mixing Based on Numerical Modelling. J. Petrol. 57, 437–460. https://doi.org/10.1093/petrology/egw013

Blichert-Toft, J., Albarède, F., 1997. The Lu-Hf isotope geochemistry of chondrites and the evolution of the mantle-crust system. Earth Planet. Sci. Lett. 148, 243–258. https://doi.org/https://doi.org/10.1016/S0012-821X(97)00040-X

Blichert-Toft, J., Chauvel, C., Albarède, F., 1997. Separation of Hf and Lu for high-precision isotope analysis of rock samples by magnetic sector-multiple collector ICP-MS, Contributions to Mineralogy and Petrology. https://doi.org/10.1007/s004100050278

Brown, C.R., Yakymchuk, C., Brown, M., Fanning, C.M., Korhonen, F.J., Piccoli, P.M., Siddoway, C.S., 2016. From source to sink: Petrogenesis of cretaceous anatectic granites from the Fosdick migmatite-granite complex, West Antarctica. J. Petrol. 57, 1241–1278. https://doi.org/10.1093/petrology/egw039

Brown, M., 2013. Granite: From genesis to emplacement. Bull. Geol. Soc. Am. 125, 1079–1113. https://doi.org/10.1130/B30877.1

Bucher, K., Grapes, R., 2011. Petrogenesis of Metamorphic Rocks 8th Edition, Journal of Chemical Information and Modeling. https://doi.org/10.1007/978-3-540-74169-5

Buscher, J.T., Hampel, A., Hetzel, R., Dunkl, I., Glotzbach, C., Struffert, A., Akal, C., Rätz,

M., 2013. Quantifying rates of detachment faulting and erosion in the central Menderes Massif (western Turkey) by thermochronology and cosmogenic 10Be. J. Geol. Soc. London. 170, 669–683. https://doi.org/10.1144/jgs2012-132

Capdevila, R., Floor, P., 1970. Les differents types de granites hercyniens et leur distribution dans le Nord-Ouest de l'Espagne. Bol. Geol. Min. 81, 215–225.

Carríngton da Costa, J., 1950. Notícia sobre uma carta geológica do Buçaco de Nery Delgado. Comunicações dos Serviçoes Geológicos de Portugal.

Carríngton da Costa, J., Teixeira, C., 1957. Carta Geológica de Portugal, na escala 1/50.000, Notícia Explicativa da Folha 9-C. Serviços Geológicos Port. 39 pp.

Carvalhosa, A., 1960. Carta Geológica de Portugal à escala 1:50 000, folha 15-D (Figueira de Castelo Rodrigo). Serviços Geológicos Port.

Castiñeiras, P., Villaseca, C., Barbero, L., Romera, M.C., 2008. SHRIMP U-Pb zircon dating of anatexis in high-grade migmatite complexes of Central Spain: Implications in the Hercynian evolution of Central Iberia. Int. J. Earth Sci. 97, 35–50. https://doi.org/10.1007/s00531-006-0167-6

Castro, A., 2014. The off-crust origin of granite batholiths. Geosci. Front. 5, 63–75. https://doi.org/10.1016/J.GSF.2013.06.006

Cavosie, A.J., Valley, J.W., Wilde, S.A., 2019. The Oldest Terrestrial Mineral Record, in: Earth's Oldest Rocks. pp. 255–278. https://doi.org/10.1016/b978-0-444-63901-1.00012-5

Cerling, T.E., Brown, F.H., Bowman, J.R., 1985. Low-temperature alteration of volcanic glass: Hydration, Na, K, 18O and Ar mobility. Chem. Geol. Isot. Geosci. Sect. 52, 281–293. https://doi.org/10.1016/0168-9622(85)90040-5

Chappell, B.W., White, A.J.R., 2001. Two contrasting granite types: 25 years later. Aust. J. Earth Sci. 48, 489–499.

Chappell, B.W., White, A.J.R., 1974. Two contrasting granite types. Pacific Geol. 8, 173–174.

Chauvel, C., Blichert-Toft, J., 2001. A hafnium isotope and trace element perspective on melting of the depleted mantle. Earth Planet. Sci. Lett. 190, 137–151. https://doi.org/10.1016/S0012-821X(01)00379-X

Cherniak, D.., Watson, E.., 2001. Pb diffusion in zircon. Chem. Geol. 172, 5–24. https://doi.org/10.1016/S0009-2541(00)00233-3

Cherniak, D.J., Lanford, W.A., Ryerson, F.J., 1991. Lead diffusion in apatite and zircon using ion implantation and Rutherford Backscattering techniques. Geochim. Cosmochim. Acta 55, 1663–1673. https://doi.org/10.1016/0016-7037(91)90137-T

Cherniak, D.J., Watson, E.B., 2000. Pb diffusion in zircon. Contrib. to Mineral. Petrol. 160,

383–390. https://doi.org/10.1007/s00410-009-0483-5

Chesley, J.T., Halliday, A.N., Snee, L.W., Mezger, K., Shepherd, T.J., Scrivener, R.C., 1993. Thermochronology of the Cornubian batholith in southwest England: Implications for pluton emplacement and protracted hydrothermal mineralization. Geochim. Cosmochim. Acta 57, 1817–1835. https://doi.org/10.1016/0016-7037(93)90115-D

Chew, D.M., Babechuk, M.G., Cogné, N., Mark, C., O'Sullivan, G.J., Henrichs, I.A., Doepke, D., McKenna, C.A., 2016. (LA,Q)-ICPMS trace-element analyses of Durango and McClure Mountain apatite and implications for making natural LA-ICPMS mineral standards. Chem. Geol. 435, 35–48. https://doi.org/10.1016/J.CHEMGEO.2016.03.028

Chew, D.M., Petrus, J.A., Kamber, B.S., 2014. U-Pb LA-ICPMS dating using accessory mineral standards with variable common Pb. Chem. Geol. 363. https://doi.org/10.1016/j.chemgeo.2013.11.006

Clemens, J., 2006. Melting of the continental crust: Fluid regimes, melting reactions, and source-rock fertility, Evolution and Differentiation of the Continental Crust.

Clemens, J.D., 2003. S-type granitic magmas - petrogenetic issues, models and evidence. Earth-Science Rev. 61, 1–18. https://doi.org/10.1016/S0012-8252(02)00107-1

Clemens, J.D., Stevens, G., 2016. Melt segregation and magma interactions during crustal melting: Breaking out of the matrix. Earth-Science Rev. 160, 333–349. https://doi.org/10.1016/j.earscirev.2016.07.012

Clemens, J.D., Vielzeuf, D., 1987. Constraints on melting and magma production in the crust. Earth Planet. Sci. Lett. 86, 287–306. https://doi.org/10.1016/0012-821X(87)90227-5

Coke, C., Pires, C.A.C., Sá, A.A., Ribeiro, A., 2000. O Vulcanismo na transição Câmbrico/Ordovícico na Zona Centro-Ibérica na região de Trás-os-Montes (NE Portugal) como elemento de referência estratigráfica. Rev. Lab. Xeol. Laxe 16 pp.

Corfu, F., Hanchar, J.M., Hoskin, P.W.O., Kinny, P.D., 2003. Atlas of zircon textures. Rev. Mineral. Geochemistry 53, 469–500. https://doi.org/10.2113/0530469

Corsini, M., Rolland, Y., 2009. Late evolution of the southern European Variscan belt: Exhumation of the lower crust in a context of oblique convergence. Comptes Rendus - Geosci. 341, 214–223. https://doi.org/10.1016/j.crte.2008.12.002

Costa, M.M., Neiva, A.M.R., Azevedo, M.R., Corfu, F., 2014. Distinct sources for syntectonic Variscan granitoids: Insights from the Aguiar da Beira region, Central Portugal. Lithos 196–197, 83–98. https://doi.org/10.1016/j.lithos.2014.02.023

Dallmeyer, R.D., Martínez Catalán, J.R., Arenas, R., Gil Ibarguchi, J.I., Gutiérrez Alonso, G., Farias, P., Bastida, F., Aller, J., 1997. Diachronous Variscan tectonothermal activity in the

NW Iberian Massif: Evidence from40Ar/39Ar dating of regional fabrics. Tectonophysics 277, 307–337. https://doi.org/10.1016/S0040-1951(97)00035-8

Damas, A., Azevedo, M., Valle Aguado, B., Gomes, M., 2016. Complexo Migmatítico de Bemposta (NE Portugal): Dados petrográficos, geoquímicos e isotópicos preliminares, in: XIII Congresso de Geoquímica Dos Países de Língua Portuguesa.

Davies, G.R., Tommasini, S., 2000. Isotopic disequilibrium during rapid crustal anatexis: Implications for petrogenetic studies of magmatic processes. Chem. Geol. 162, 169–191. https://doi.org/10.1016/S0009-2541(99)00123-0

Dias da Silva, I., 2013. Geología de las Zonas Centro Ibérica y Galicia – Trás-os-Montes en la parte oriental del Complejo de Morais, Portugal/España / Geology of the Central Iberian and Galicia – Trás-Os-Montes zones in the Eastern part of the Morais Complex, Portugal/Spain.

Dias da Silva, Í., Gómez-Barreiro, J., Martínez Catalán, J.R., Ayarza, P., Pohl, J., Martínez, E., 2017. Structural and microstructural analysis of the Retortillo Syncline (Variscan belt, Central Iberia). Implications for the Central Iberian Orocline. Tectonophysics 717, 99–115. https://doi.org/10.1016/j.tecto.2017.07.015

Dias da Silva, I., Jensen, S., Clavijo, E., 2014. Trace fossils from the Desejosa Formation (Schist and Greywacke Complex, Douro Group, NE Portugal): new Cambrian age constraints. Geol. Acta 12, 109–120. https://doi.org/10.1344/105.000002080

Dias da Silva, Í., Pereira, M.F., Silva, J.B., Gama, C., 2018. Time-space distribution of silicic plutonism in a gneiss dome of the Iberian Variscan Belt: The Évora Massif (Ossa-Morena Zone, Portugal). Tectonophysics 747–748, 298–317. https://doi.org/10.1016/j.tecto.2018.10.015

Dias, G., Leterrier, J., Mendes, A., Simões, P.P., Bertrand, J.M., 1998. U-Pb zircon and monazite geochronology of post-collisional Hercynian granitoids from the Central Iberian Zone (Northern Portugal). Lithos 45, 349–369. https://doi.org/10.1016/S0024-4937(98)00039-5

Dias, R., Ribeiro, A., Coke, C., Pereira, E., Rodrigues, J., Castro, P., Moreira, N., Rebelo, J., 2013. Evolução estrutual dos sectores setentrionais do Autóctone da Zona Centro-Ibérica, in: Dias, R., Araújo, A., Terrinha, P., Kullberg, J.C. (Eds.), Geologia de Portugal, Vol. 1. Escolar Editora, pp. 74–147.

Dias, R., Ribeiro, A., Romão, J., Coke, C., Moreira, N., 2016. A review of the arcuate structures in the Iberian Variscides; constraints and genetic models. Tectonophysics 681, 170–194. https://doi.org/10.1016/j.tecto.2016.04.011

Díaz-Azpiroz, M., Barcos, L., Balanyá, J.C., Fernández, C., Expósito, I., Czeck, D.M., 2014. Applying a general triclinic transpression model to highly partitioned brittle-ductile shear zones: A case study from the Torcal de Antequera massif, external Betics, southern Spain. J. Struct. Geol. 68, 316–336. https://doi.org/10.1016/J.JSG.2014.05.010

Díez Fernández, R., Martínez Catalán, J.R., Barreiro, J.G., Arenas, R., 2012. Extensional Flow during Gravitational Collapse: A Tool for Setting Plate Convergence (Padrón Migmatitic Dome, Variscan Belt, NW Iberia). J. Geol. 120, 83–103. https://doi.org/10.1086/662735

Díez Fernández, R., Pereira, M.F., 2017. Strike-slip shear zones of the Iberian Massif: Are they coeval? Lithosphere 9, 726–744. https://doi.org/10.1130/L648.1

Díez Fernández, R., Pereira, M.F., 2016. Extensional orogenic collapse captured by strike-slip tectonics: Constraints from structural geology and U[sbnd]Pb geochronology of the Pinhel shear zone (Variscan orogen, Iberian Massif). Tectonophysics 691, 290–310. https://doi.org/10.1016/j.tecto.2016.10.023

Dodson, M.H., 1973. Closure temperature in cooling geochronological and petrological systems. Contrib. to Mineral. Petrol. 40, 259–274. https://doi.org/10.1007/BF00373790

Dou, J., Siebel, W., He, J., Chen, F., 2019. Different melting conditions and petrogenesis of peraluminous granites in western Qinling, China, and tectonic implications. Lithos 336–337, 97–111. https://doi.org/10.1016/j.lithos.2019.04.003

Dunlap, W.J., 2000. Nature's diffusion experiment: The cooling-rate cooling-age correlation. Geology 28, 139–142. https://doi.org/10.1130/0091-7613(2000)28<139:NDETCC>2.0.CO;2

Escuder-Viruete, J., Arenas, R., Catalán, J.R.M., 1994. Tectonothermal evolution associated with Variscan crustal extension in the Tormes Gneiss Dome (NW Salamanca, Iberian Massif, Spain). Tectonophysics 238, 117–138. https://doi.org/10.1016/0040-1951(94)90052-3

Escuder-Viruete, J., Hernáiz Huerta, P.P., Valverde-Vaquero, P., Rodríguez Fernández, R., Dunning, G., 1998. Variscan syncollisional extension in the Iberian Massif: structural, metamorphic and geochronological evidence from the Somosierra sector of the Sierra de Guadarrama (Central Iberian Zone, Spain). Tectonophysics 290, 87–109. https://doi.org/10.1016/S0040-1951(98)00014-6

Escuder Viruete, J., Villar, P., Rodriguez Fernandez, L.R., Monteserin, V., Santisteban, J.I., 1995. Evolucion tectonotermica del area metamorfica del SO de Salamanca (Zona Centroiberica O de Espana). Bol. Geol. y Min. 106, 303–315.

Esteves, A.F., 2006. As rochas metamórficas da região de Viseu. University of Aveiro.

Farias, P., Gallastegui, G., González-Lodeiro, F., Marquínez, J., Martín Parra, L., Martínez Catalán, J., Pablo Maciá, J., Rodríguez Fernández, L., 1987. Aportaciones al conocimiento de la litoestratigrafía y estructura de Galicia Central. Memórias da Fac. Ciências, Univ. do Porto 1, 411–431.

Farina, F., Stevens, G., 2011. Lithos Source controlled 87 Sr / 86 Sr isotope variability in granitic magmas : The inevitable consequence of mineral-scale isotopic disequilibrium in the protolith. LITHOS 122, 189–200. https://doi.org/10.1016/j.lithos.2011.01.001

Fernández-Suárez, J., Gutiérrez-Alonso, G., Pastor-Galán, D., Hofmann, M., Murphy, J.B., Linnemann, U., 2014. The Ediacaran-Early Cambrian detrital zircon record of NW Iberia: Possible sources and paleogeographic constraints. Int. J. Earth Sci. 103, 1335–1357. https://doi.org/10.1007/s00531-013-0923-3

Fernández-Suárez, J., Gutiérrez Alonso, G., Jeffries, T.E., 2002. The importance of along-margin terrane transport in northern Gondwana: insights from detrital zircon parentage in Neoproterozoic rocks from Iberia and Brittany. Earth Planet. Sci. Lett. 204, 75–88. https://doi.org/https://doi.org/10.1016/S0012-821X(02)00963-9

Fernández, C., Czeck, D.M., Díaz-Azpiroz, M., 2013. Testing the model of oblique transpression with oblique extrusion in two natural cases: Steps and consequences. J. Struct. Geol. 54, 85–102. https://doi.org/10.1016/J.JSG.2013.07.001

Ferreira, J.A., Bento dos Santos, T., Pereira, I., Mata, J., 2019. Tectonically assisted exhumation and cooling of Variscan granites in an anatectic complex of the Central Iberian Zone , Portugal : constraints from LA - ICP - MS zircon and apatite U – Pb ages. Int. J. Earth Sci. https://doi.org/10.1007/s00531-019-01755-1

Ferreira, J.A., Mata, J., Bento dos Santos, T., Pereira, I., *in revision*. The role of melting on the geochemical evolution and isotopic variability of an anatectic complex in the Iberian Variscides. Lithos.

Ferreira, J.A., Ribeiro, M.A., Martins, H.C.B., 2014. The Pedregal granite (Portugal): petrographic and geochemical characterization of a peculiar granitoid. Estud. Geológicos 70, e019. https://doi.org/10.3989/egeol.41730.321

Ferreira, N., Iglésias, M., Noronha, F., Pereira, E., Ribeiro, A., Ribeiro, M.., 1987. Granitóides da zona Centro-Ibérica e seu enquadramento geodinâmico, in: Bea, F., Carnicero, A., Gonzalo, J.C., López-Plaza, M., Rodrígues Alonso, M.D. (Eds.), Geologia de Los Granitoids y Rocas Associadas Del Macizo Hespérico, Libro Homenagem a L.C.G. Figuerola. Editorial Rueda, Madrid, pp. 37–53.

Frost, B.R., Calvin, G.B., William, J.C., Arculus, R.J., Ellis, D.J., Frost, C.D., 2001. A

Geochemical Classification for Granitic Rocks. J. Petrol. 42, 2033–2048.

Galer, S.J.G., Abouchami, W., 1998. Practical application of lead triple spiking for correction of instrumental mass discrimination. Miner. Mag. A 62, 491–492.

Gallien, F., Mogessie, A., Bjerg, E., Delpino, S., Machuca, B., Thöni, M., Urs, K., 2010. Timing and rate of granulite facies metamorphism and cooling from multi-mineral chronology on migmatitic gneisses, Sierras de La Huerta and Valle Fértil, NW Argentina. Lithos 114, 229–252. https://doi.org/10.1016/j.lithos.2009.08.011

Gao, L.E., Zeng, L., Asimow, P.D., 2017. Contrasting geochemical signatures of fluid-absent versus fluid-fluxed melting of muscovite in metasedimentary sources: The Himalayan leucogranites. Geology 45. https://doi.org/10.1130/G38336.1

García-Arias, M., Díez-Montes, A., Villaseca, C., Blanco-Quintero, I.F., 2018. The Cambro-Ordovician Ollo de Sapo magmatism in the Iberian Massif and its Variscan evolution: A review. Earth-Science Rev. 176, 345–372. https://doi.org/10.1016/j.earscirev.2017.11.004

Griffin, W.L., Wang, X., Jackson, S.E., Pearson, N.J., O'Reilly, S.Y., Xu, X., Zhou, X., 2002. Zircon chemistry and magma mixing, SE China: In-situ analysis of Hf isotopes, Tonglu and Pingtan igneous complexes. Lithos 61, 237–269. https://doi.org/https://doi.org/10.1016/S0024-4937(02)00082-8

Gutiérrez-Alonso, G., Collins, A.S., Fernández-Suárez, J., Pastor-Galán, D., González-Clavijo, E., Jourdan, F., Weil, A.B., Johnston, S.T., 2015. Dating of lithospheric buckling: 40Ar/39Ar ages of syn-orocline strike-slip shear zones in northwestern Iberia. Tectonophysics 643, 44–54. https://doi.org/10.1016/j.tecto.2014.12.009

Gutiérrez-Alonso, G., Fernández-Suárez, J., Jeffries, T.E., Johnston, S.T., Pastor-Galán, D., Murphy, J.B., Franco, M.P., Gonzalo, J.C., 2011. Diachronous post-orogenic magmatism within a developing orocline in Iberia, European Variscides. Tectonics 30. https://doi.org/10.1029/2010TC002845

Hart, S.R., Blusztajn, J., Dick, H.J.B., Meyer, P.S., Muehlenbachs, K., 1999. The fingerprint of seawater circulation in a 500-meter section of ocean crust gabbros. Geochim. Cosmochim. Acta 63, 4059–4080. https://doi.org/10.1016/S0016-7037(99)00309-9.

Henrichs, I.A., O'Sullivan, G., Chew, D.M., Mark, C., Babechuk, M.G., McKenna, C., Emo, R., 2018. The trace element and U-Pb systematics of metamorphic apatite. Chem. Geol. 483, 218–238. https://doi.org/10.1016/j.chemgeo.2017.12.031

Hodges, K. V, Heinrich, D.H., Karl, K.T., 2003. Geochronology and Thermochronology in Orogenic Systems. Treatise on Geochemistry 3, 263–292. https://doi.org/http://dx.doi.org/10.1016/B0-08-043751-6/03024-3

Iglesias, M., Ribeiro, A., 1981. La zone de cisaillement ductile de Juzbado (Salamanca)-Penalva Do Castelo (Viseu): un linéament ancien réactivé pendant l'orogénese hercynienne? Comun. dos Serviços Geológicos Port. 67(1), 89–93.

Inger, S., Harris, N., 1993. Geochemical Constraints on Leukogranite Magmatism in the Langtang Valley, Nepal Himalaya. J. Petrol. 34, 345–368. https://doi.org/10.1093/petrology/34.2.345

Jackson, S.E., Pearson, N.J., Griffin, W.L., Belousova, E.A., 2004. The application of laser ablation-inductively coupled plasma-mass spectrometry to in situ U–Pb zircon geochronology. Chem. Geol. 211, 47–69.

Jacobsen, S.B., Wasserburg, G.J., 1980. Sm-Nd isotopic evolution of chondrites. Earth Planet. Sci. Lett. 50, 139–155. https://doi.org/https://doi.org/10.1016/0012-821X(80)90125-9

Jadamec, M.A., Turcotte, D.L., Howell, P., 2007. Analytic models for orogenic collapse. Tectonophysics 435, 1–12. https://doi.org/10.1016/j.tecto.2007.01.007

Jochum, K.P., Weis, U., Stoll, B., Kuzmin, D., Yang, Q., Raczek, I., Jacob, D.E., Stracke, A., Birbaum, K., Frick, D.A., 2011. Determination of reference values for NIST SRM 610–617 glasses following ISO guidelines. Geostand. Geoanalytical Res. 35, 397–429.

Johannes, W., Ehlers, C., Kriegsman, L.M., Mengel, K., 2003. The link between migmatites and S-type granites in the Turku area , southern Finland. Lithos 68, 69–90. https://doi.org/10.1016/S0024-4937(03)00032-X

Julivert, M., Fontboté, J.M., Ribeiro, A., Conde, L., 1972. Mapa tectónico de la Peninsula Ibérica y Baleares E: 1:1000000. Instituto Geológico y Minero de España, Madrid.

Jung, S., 2005. Isotopic equilibrium/disequilibrium in granites, metasedimentary rocks and migmatites (Damara orogen, Namibia) - A consequence of polymetamorphism and melting. Lithos 84, 168–184. https://doi.org/10.1016/j.lithos.2005.03.013

Jung, S., Pfänder, J.A., 2007. Source composition and melting temperatures of orogenic granitoids: constraints from CaO/Na2O, Al2O3/TiO2 and accessory mineral saturation thermometry. Eur. J. Mineral. 19, 859–870. https://doi.org/10.1127/0935-1221/2007/0019-1774

Kitano, I., Osanai, Y., Nakano, N., Adachi, T., Fitzsimons, I., 2018. Detrital zircon and igneous protolith ages of high-grade metamorphic rocks in the Highland and Wanni Complexes, Sri Lanka: Their geochronological correlation with southern India and East Antarctica. J. Asian Earth Sci. 156, 122–144. https://doi.org/10.1016/j.jseaes.2018.01.017

Köksal, S., Cemal Göncüoglu, M., Toksoy-Köksal, F., Möller, A., Kemnitz, H., 2008. Zircon typologies and internal structures as petrogenetic indicators in contrasting granitoid types

from central Anatolia, Turkey. Mineral. Petrol. 93, 185–211. https://doi.org/10.1007/s00710-007-0228-y

Kroner, U., Romer, R.L., 2013. Two plates — Many subduction zones : The Variscan orogeny reconsidered. Gondwana Res. 24, 298–329. https://doi.org/10.1016/j.gr.2013.03.001

Le Breton, N., Thompson, A., 1988. Fluid-absent (dehydration) melting of biotite in metapelites in the early stages of crustal anatexis. Contrib. to Mineral. Petrol. 99, 226–237. https://doi.org/10.1007/BF00371463

Ledru, P., Courrioux, G., Dallain, C., Lardeaux, J.M., Montel, J.M., Vanderhaeghe, O., Vitel, G., 2001. The Velay dome (French Massif Central): Melt generation and granite emplacement during orogenic evolution. Tectonophysics 342, 207–237. https://doi.org/10.1016/S0040-1951(01)00165-2

Liew, T., Hofmann, A., 1988. Precambrian crustal components, plutonic associations, plate environment of the Hercynian Fold Belt of central Europe: Indications from a Nd and Sr isotopic study. Contrib. to Mineral. Petrol. 98, 129–138. https://doi.org/10.1007/BF00402106

Liñan, E., Gámez Vintaned, J., Gozalo, R., 2015. The middle lower Cambrian (Ovetian) Lunagraulos n. gen. from Spain and the oldest trilobite records. Geol. Mag. 'FirstView Artic. 6, 1–14. https://doi.org/10.1017/S0016756815000084

Linnemann, U., Pereira, M.F., Jeffries, T.E., Drost, K., Gerdes, A., 2008. The Cadomian Orogeny and the opening of the Rheic Ocean: The diacrony of geotectonic processes constrained by LA-ICP-MS U-Pb zircon dating (Ossa-Morena and Saxo-Thuringian Zones, Iberian and Bohemian Massifs). Tectonophysics 461, 21–43. https://doi.org/10.1016/j.tecto.2008.05.002

Lopez-Sanchez, M.A., Aleinikoff, J.N., Marcos, A., Martínez, F.J., Llana-Fúnez, S., 2016. An example of low-Th/U zircon overgrowths of magmatic origin in a late orogenic Variscan intrusion: the San Ciprián massif (NW Spain). J. Geol. Soc. London. 173, 282–291. https://doi.org/10.1144/jgs2015-071

Lotze, F., 1945. Zur Gliederung der Varisziden der Iberischen Meseta. Geotekt Forsch 6, 78–92.

Ludwig, K.R., 2003. User's manual for Isoplot/Ex version 3.00, a geochronological toolkit for Microsoft Excel. Berkeley Geochronol. Cent. Spec. Publ. 72pp.

Lugmair, G.W., Marti, K., 1978. Lunar initial 143Nd/144Nd: Differential evolution of the lunar crust and mantle. Earth Planet. Sci. Lett. 39, 349–357. https://doi.org/https://doi.org/10.1016/0012-821X(78)90021-3

Macedo, C.C.R., 1988. Granitóides, Complexo Xisto-Grauváquico e Ordovícico na região entre Trancoso e Pinhel - geologia, petrologia, geocronologia. Universidade de Coimbra.

Maeda, J., Zeniya, R., Kuramoto, Y., Itaya, T., Kagami, H., 2011. A procedure for calculating a consistent set of closure temperatures and cooling rate using Dodson's formula. J. Geol. Soc. Japan 117, 99–103. https://doi.org/10.5575/geosoc.117.99

Martínez Catalán, J., Arenas, R., Diez Balda, M., 2004. Extensión y metamorfismo de baja pressión en el Manto de Mondoñedo., in: Vera, J. (Ed.), Geologia de España. SGE-IGME, Madrid, pp. 59–59.

Martínez Catalán, J.R., Rubio Pascual, F.J., Montes, A.D., Fernández, R.D., Barreiro, J.G., Dias Da Silva, Í., Clavijo, E.G., Ayarza, P., Alcock, J.E., 2014. The late Variscan HT/LP metamorphic event in NW and Central Iberia: relationships to crustal thickening, extension, orocline development and crustal evolution. Geol. Soc. London, Spec. Publ. 405, 225–247. https://doi.org/10.1144/SP405.1

Martini, A., Fátima, M. De, Weinberg, R.F., Betino, G., Toni, D., Nardi, L.V.S., 2019. From migmatite to magma - crustal melting and generation of granite in the Camboriú Complex , south Brazil. Lithos 340–341, 270–286. https://doi.org/10.1016/j.lithos.2019.05.017

Martins, L.M.O., Teixeira, R.J.S., Coke, C., Dias, R., Gomes, M.E.P., 2012. A importância da geocronologia U-Pb na determinação da proveniência de rochas metaconglomeráticas de Desejosa/Castanheiro do Sul e Valongo, Norte de Portugal., in: Livro de Actas – II Congresso Jovens Investigadores Em Geociências, LEG 2012,. Estremoz.

Mata, J., C.F., A., Martins, L., R, M., Madeira, J., Pimentel, N., Martins, S., Azevedo, M., Youbi, N., De Min, A., I.M., A., Bensalah, M., Terrinha, P., 2015. 40Ar/39Ar ages and petrogenesis of the West Iberian Margin onshore magmatism at the Jurassic-Cretaceous transition: Geodynamic implications and assessment of open-system processes involving saline materials. Lithos 236–237, 156–172.

Mata, J., Martins, S., Mattielli, N., Madeira, J., Faria, B., Ramalho, R.S., Silva, P., Moreira, M., Caldeira, R., Moreira, M., Rodrigues, J., Martins, L., 2017. The 2014–15 eruption and the short-term geochemical evolution of the Fogo volcano (Cape Verde): Evidence for small-scale mantle heterogeneity. Lithos 288–289, 91–107. https://doi.org/10.1016/J.LITHOS.2017.07.001

Mateus, A., Munhá, J., Ribeiro, A., Tassinari, C.C.G., Sato, K., Pereira, E., Santos, J.F., 2016. U–Pb SHRIMP zircon dating of high-grade rocks from the Upper Allochthonous Terrane of Bragança and Morais Massifs (NE Portugal); geodynamic consequences. Tectonophysics 675, 23–49. https://doi.org/10.1016/J.TECTO.2016.02.048

Matmon, A., Bierman, P.R., Larsen, J., Southworth, S., Pavich, M., Caffee, M., 2003. Temporally and spatially uniform rates of erosion in the southern Appalachian Great Smoky Mountains. Geology 31, 155–158. https://doi.org/10.1130/0091-7613(2003)031<0155:TASURO>2.0.CO;2

Matte, P., 2001. The Variscan collage and orogeny (480–290 Ma) and the tectonic definition of the Armorica microplate: a review - Matte - 2003 - Terra Nova - Wiley Online Library. Terra Nov. 13, 122–128.

Meert, J.G., Hall, C., Nédélec, A., Madison Razanatseheno, M.O., 2001. Cooling of a Late-Syn Orogenic Pluton: Evidence from Laser K-feldspar Modelling of the Carion Granite, Madagascar. Gondwana Res. 4, 541–550. https://doi.org/10.1016/S1342-937X(05)70353-1

Meireles, C., Pereira, E., Ferreira, N., Castro, P., 2006. O Ordovícico da Serra da Marofa: novos dados litoestratigráficos e estruturais., in: Mirão, J., Balbino, A. (Eds.), Livro de Actas, VII Congresso Nacional de Geologia. Pólo de Estremoz da Universidade de Évora., Évora, pp. 645–648.

Miller, C.F., McDowell, S.M., Mapes, R.W., 2003. Hot and cold granites: Implications of zircon saturation temperatures and preservation of inheritance. Geology 31, 529–532. https://doi.org/10.1130/0091-7613(2003)031<0529:HACGIO>2.0.CO;2

Milord, I., Sawyer, E.W., Brown, M., 2001. Formation of diatexite migmatite and granite magma during anatexis of semi-pelitic metasedimentary rocks: An example from St. Malo, France. J. Petrol. 42, 487–505. https://doi.org/10.1093/petrology/42.3.487

Miyazaki, T., Santosh, M., 2005. Cooling history of the Puttetti alkali syenite pluton, southern India. Gondwana Res. 8, 567–574. https://doi.org/10.1016/S1342-937X(05)71156-4

Moita, P., Santos, J.F., Pereira, M.F., 2009. Layered granitoids: Interaction between continental crust recycling processes and mantle-derived magmatism. Examples from the ??vora Massif (Ossa-Morena Zone, southwest Iberia, Portugal). Lithos 111, 125–141. https://doi.org/10.1016/j.lithos.2009.02.009

Möller, A., O'Brien, P.J., Kennedy, A., Kröner, A., 2003. The use and abuse of Th-U ratios in the interpretation of zircon, in: Geophysical Research Abstracts, European Geosciences Union. p. 12113.

Montero, P., Talavera, C., Bea, F., 2017. Geochemical, isotopic, and zircon (U-Pb, O, Hf isotopes) evidence for the magmatic sources of the volcano-plutonic Ollo de Sapo Formation, Central Iberia. Geol. Acta 15, 245–260. https://doi.org/10.1344/GeologicaActa2017.15.4.1

Munhá, J.M.U., Cordani, U.G., Tassinari, C.G., Palácios, T., 2005. Petrologia e Termocronologia de Gnaisses Migmatíticos da Faixa de Dobramentos Araçuaí (Espirito Santo, Brasil). Rev. Bras. Geociências 35, 123–134.

Nabelek, P.I., Hofmeister, A.M., Whittington, A.G., 2012. The influence of temperature-dependent thermal diffusivity on the conductive cooling rates of plutons and temperature-time paths in contact aureoles. Earth Planet. Sci. Lett. 317–318, 157–164. https://doi.org/10.1016/j.epsl.2011.11.009

Nance, R.D., Gutiérrez-Alonso, G., Keppie, J.D., Linnemann, U., Murphy, J.B., Quesada, C., Strachan, R.A., Woodcock, N.H., 2012. A brief history of the Rheic Ocean. Geosci. Front. 3, 125–135. https://doi.org/10.1016/j.gsf.2011.11.008

Nance, R.D., Gutiérrez-Alonso, G., Keppie, J.D., Linnemann, U., Murphy, J.B., Quesada, C., Strachan, R.A., Woodcock, N.H., 2010. Evolution of the Rheic Ocean. Gondwana Res. 17, 194–222. https://doi.org/10.1016/j.gr.2009.08.001

Noronha, F., Ramos, J.M.F., Rebelo, J.A., Ribeiro, A., Ribeiro, M.L., 1979. Essai de corrélation des phases de déformation hercynienne dans le Nord- Ouest Péninsulaire. Bol. da Soc. Geológica Port. 21, 227–237.

Oen, I.S., 1958. The Geology, petrology and ore deposits of the Viseu region (Northern Portugal). Comun. dos Serviços Geológicos Port. 41.

Oliveira, J., Pereira, E., Piçarra, J., Young, T., Romano, M., 1992. O Paleozóico Inferior de Portugal: síntese da estratigrafia e da evolução paleogeográfica., in: Gutiérrez Marco, J.C., Saavedra, J., Rábano, I. (Eds.), Paleozóico Inferior de Ibero-América. Universidad de Extremadura, Badajoz, pp. 359–375.

Orejana, D., Merino Martínez, E., Villaseca, C., Andersen, T., 2015. Ediacaran–Cambrian paleogeography and geodynamic setting of the Central Iberian Zone: Constraints from coupled U–Pb–Hf isotopes of detrital zircons. Precambrian Res. 261, 234–251. https://doi.org/10.1016/J.PRECAMRES.2015.02.009

Palme, H., O'Neil, H.S.C., 2003. Cosmochemical estimatess of mantle composition. mantle core 2, 1–38. https://doi.org/10.1016/B978-0-08-095975-7.00201-1

Patiño Douce, A.E., Harris, N., 1998. Experimental Constraints on Himalayan Anatexis. J. Petrol. 39, 689–710. https://doi.org/10.1093/petroj/39.4.689

Pearce, J.A., Harris, N.B.W., Tindle, A.G., 1984. Trace Element Discrimination Diagrams for the Tectonic Interpretation of Granitic Rocks. J. Petrol. 25, 956–983. https://doi.org/10.1093/petrology/25.4.956

Pereira, I., Dias, R., Bento dos Santos, T., Mata, J., 2017. Exhumation of a migmatite complex

along a transpressive shear zone: Inferences from the Variscan Juzbado-Penalva do Castelo Shear Zone (Central Iberian Zone). J. Geol. Soc. London. 174, 1004–1018. https://doi.org/10.1144/jgs2016-159

Pereira, I., Dias, R., Bento dos Santos, T., Mata, J., 2014. Juzbado-Penalva do Castelo shear zone in the Figueira de Castelo Rodrigo sector: Implications for the exhumation of high grade metamorphic rocks. Comun. Geol. 101, 289–292.

Pereira, I., Storey, C.D., Strachan, R.A., Bento dos Santos, T., Darling, J.R., 2020. Detrital rutile ages can deduce the tectonic setting of sedimentary basins. Earth Planet. Sci. Lett. 537, 116193. https://doi.org/10.1016/j.epsl.2020.116193

Pereira, M.F., 2015. Potential sources of Ediacaran strata of Iberia: A review. Geodin. Acta 27, 1–14. https://doi.org/10.1080/09853111.2014.957505

Pereira, M.F., Díez Fernández, R., Gama, C., Hofmann, M., Gärtner, A., Linnemann, U., 2018. S-type granite generation and emplacement during a regional switch from extensional to contractional deformation (Central Iberian Zone, Iberian autochthonous domain, Variscan Orogeny). Int. J. Earth Sci. 107, 251–267. https://doi.org/10.1007/s00531-017-1488-3

Pereira, M.F., Linnemann, U., Hofmann, M., Chichorro, M., Sol??, A.R., Medina, J., Silva, J.B., 2012a. The provenance of Late Ediacaran and Early Ordovician siliciclastic rocks in the Southwest Central Iberian Zone: Constraints from detrital zircon data on northern Gondwana margin evolution during the late Neoproterozoic. Precambrian Res. 192–195, 166–189. https://doi.org/10.1016/j.precamres.2011.10.019

Pereira, M.F., Linnemann, U., Hofmann, M., Chichorro, M., Solá, A.R., Medina, J., Silva, J.B., 2012b. The provenance of Late Ediacaran and Early Ordovician siliciclastic rocks in the Southwest Central Iberian Zone: Constraints from detrital zircon data on northern Gondwana margin evolution during the late Neoproterozoic. Precambrian Res. 192–195, 166–189. https://doi.org/10.1016/j.precamres.2011.10.019

Pérez-Cáceres, I., Martínez Poyatos, D., Simancas, J.F., Azor, A., 2017. Testing the Avalonian affinity of the South Portuguese Zone and the Neoproterozoic evolution of SW Iberia through detrital zircon populations. Gondwana Res. 42, 177–192. https://doi.org/https://doi.org/10.1016/j.gr.2016.10.010

Perini, G., Cesare, B., Gömez-Pugnaire, M.T., Ghezzi, L., Tommasini, S., 2009. Armouring effect on Sr-Nd isotopes during disequilibrium crustal melting: the case study of frozen migmatites from El Hoyazo and Mazarrón, SE Spain. Eur. J. Mineral. 21, 117–131. https://doi.org/10.1127/0935-1221/2009/0021-1882

Pochon, A., Poujol, M., Gloaguen, E., Branquet, Y., Cagnard, F., Gumiaux, C., Gapais, D.,

2016. U-Pb LA-ICP-MS dating of apatite in mafic rocks: Evidence for a major magmatic event at the Devonian-Carboniferous boundary in the Armorican Massif (France), American Mineralogist. https://doi.org/10.2138/am-2016-5736

Pupin, J.P., 1980. Zircon and granite petrology. Contrib. to Mineral. Petrol. 73, 207–220. https://doi.org/10.1007/BF00381441

Rebelo, J.A., Romano, M., 1986. A contribution to the lithostratigraphy and palaeontology of the Lower Palaeozoic rocks of the Moncorvo Region, Northeast Portugal. Comun. dos Serviços Geológicos Port. 72, 45–57.

Rey, P., Vanderhaeghe, O., Teyssier, C., 2001. Gravitational collapse of the continental crust: Definition, regimes and modes. Tectonophysics 342, 435–449. https://doi.org/10.1016/S0040-1951(01)00174-3

Ribeiro, A., 2013. Evolução geodinâmica de Portugal; os ciclos ante-mesozóicos., in: Dias, R., Araújo, A., Terrinha, P., Kullberg, J.C. (Ed.), Geologia de Portugal. Volume I – Geologia Pré-Mesozóica de Portugal. Escolar Editora, pp. 15–57.

Ribeiro, A., Munhá, J., Dias, R., Mateus, A., Pereira, E., Ribeiro, L., Fonseca, P., Araújo, A., Oliveira, T., Romão, J., Chaminé, H., Coke, C., Pedro, J., 2007. Geodynamic evolution of the SW Europe Variscides. Tectonics 26. https://doi.org/10.1029/2006TC002058

Ribeiro, A., Pereira, E., Dias, R., 1990. Structure of the Northwest of the Iberian Peninsula, in: Dallmeyer, R.D., Garcia, M. (Eds.), Pre-Mesozoic Geology of Iberia. Springer-Verlag, Berlin, pp. 220–236.

Ribeiro, M.A., Sant'Ovaia, H., Dória, A., 2011. Litologias gnaisso-migmatíticas da faixa Lavadores-Madalena: possível significado das paragéneses com hercinite. Simpósio Model. Sist. Geológicos 343–351.

Ribeiro, M.L., 2001. Carta geológica simplificada do Parque Arqueológico do vale do Côa: Escala 1:80.000: Notícia explicativa.

Ribeiro, M.L., 1978. Algumas observações sobre o metamorfismo na região de Tourém (N de Portugal). Serviços Geológicos Port. 151–169.

Ribeiro, M. L., Castro, A., Almeida, A., Menéndez, L.G., Jesus, A., Lains, J.A., Lopes, J.C., Martins, H.C.B., Mata, J., Mateus, A., Moita, P., Neiva, A.M.R., Ribeiro, M.A., Santos, J.F., Solá, A.R., 2019. Variscan Magmatism, in: Quesada, C., Oliveira, J.T. (Eds.), The Geology of Iberia: A Geodynamic Approach: Volume 2: The Variscan Cycle. Springer, pp. 497–526. https://doi.org/10.1007/978-3-030-10519-8_13

Ribeiro, M L, Reche, J., López-Carmona, A., Aguilar, C., dos Santos, T., Chichorro, M., da Silva, Í., Díez-Montes, A., González-Clavijo, E., Gutiérrez-Alonso, G., Leal, N., Liesa,

M., Martínez, F.J., Mateus, A., Mendes, M.H., Moita, P., Pedro, J., Quesada, C, Santos, J.F., Solá, A.R., Valverde-Vaquero, P., 2019. Variscan Metamorphism, in: Quesada, Cecilio, Oliveira, J.T. (Eds.), The Geology of Iberia: A Geodynamic Approach: Volume 2: The Variscan Cycle. Springer International Publishing, Cham, pp. 431–495. https://doi.org/10.1007/978-3-030-10519-8_12

Rodrigues, J.F., Bento dos Santos, T., Castro, P., Meireles, C., Ferreira, P., Ribeiro, A., Pereira, E., Ferreira, N., 2013. Deformação não-coaxial na Faixa Metamórfica Porto-Viseu Détachement extensional ou par thrustunderthrust contracional, in: 9ª Conferência Anual Do GGET/SGP. Estremoz, pp. 131–134.

Roger, F., Teyssier, C., Respaut, J.P., Rey, P.F., Jolivet, M., Whitney, D.L., Paquette, J.L., Brunel, M., 2015. Timing of formation and exhumation of the montagne noire double dome, french massif central. Tectonophysics 640. https://doi.org/10.1016/j.tecto.2014.12.002

Romão, J., Dunning, G., Marcos, A., Dias, R., Ribeiro, A., 2010. O lacólito granítico de Mação-Penhascoso: idade e as suas implicações (SW da Zona Centro-Ibérica)., in: Livro de Resumos Do VIII Congresso Nacional Geologia. Universidade do Minho, Braga, pp. IX–5.

Romão, J.M.C., 1991. Litostratigrafia e estrutura do Complexo Xisto-Grauváquico (Grupo das Beiras) entre a serra do Moradal e o rio Erges. Rel. Inéd. Serv. Geol. Port. 150pp.

Rubatto, D., 2017. Zircon: The Metamorphic Mineral. Rev. Mineral. Geochemistry 83, 261–295. https://doi.org/10.2138/rmg.2017.83.9

Rubatto, D., Gebauer, D., 2000. Use of cathodoluminescence for U-Pb zircon dating by ion microprobe: some examples from the Western Alps, in: Cathodoluminescence in Geosciences. Springer, pp. 373–400.

Rubio Pascual, F.J., Arenas, R., Martínez Catalán, J.R., Rodríguez Fernández, L.R., Wijbrans, J.R., 2013. Thickening and exhumation of the Variscan roots in the Iberian Central System: Tectonothermal processes and 40Ar/39Ar ages. Tectonophysics 587, 207–221. https://doi.org/https://doi.org/10.1016/j.tecto.2012.10.005

Sá, A.A., Meireles, C., Coke, C., Gutiérrez-Marco, J.C., 2005. Unidades litoestratigráficas do Ordovícico da região de Trás-os-Montes (Zona Centro Ibérica). Comun. Geológicas 92, 31–74.

Sánchez-García, T., Chichorro, M., Solá, A.R., Álvaro, J.J., Díez-Montes, A., Bellido, F., Ribeiro, M.L., Quesada, C., Lopes, J.C., Dias da Silva, Í., González-Clavijo, E., Gómez Barreiro, J., López-Carmona, A., 2019. The Cambrian-Early Ordovician Rift Stage in the

Gondwanan Units of the Iberian Massif. https://doi.org/10.1007/978-3-030-10519-8_2

Sawyer, E.W., 2008. Atlas of Migmatites. NRC Research Press and Mineralogical Association of Canada. https://doi.org/doi:10.1139/9780660197876

Sawyer, E.W., 1998. Formation and Evolution of Granite Magmas During Crustal Reworking: the Significance of Diatexites. J. Petrol. 39, 1147–1167. https://doi.org/10.1093/petroj/39.6.1147

Sawyer, E.W., Cesare, B., Brown, M., 2011. When the continental crust melts. Elements 7, 229–234. https://doi.org/10.2113/gselements.7.4.229

Saylor, J.E., Sundell, K.E., 2016. Quantifying comparison of large detrital geochronology data sets. Geosphere 12, 203–220. https://doi.org/10.1130/GES01237.1

Schaltegger, U., Davies, J.H.F.L., 2017. Petrochronology of Zircon and Baddeleyite in Igneous Rocks: Reconstructing Magmatic Processes at High Temporal Resolution, in: Reviews in Mineralogy and Geochemistry. pp. 297–328. https://doi.org/10.2138/rmg.2017.83.10

Schermerhorn, L.J.G., 1956. Igneous, metamorphic and ore geology of the Castro Daire-São Pedro do Sul-Satão region (Northern Portugal). Comun. dos Serviços Geológicos Port. 37, 1–24.

Schoene, B., Bowring, S.A., 2007. Determining accurate temperature-time paths from U-Pb thermochronology: An example from the Kaapvaal craton, southern Africa. Geochim. Cosmochim. Acta 71, 165–185. https://doi.org/10.1016/j.gca.2006.08.029

Schoene, B., Bowring, S.A., 2006. U-Pb systematics of the McClure Mountain syenite: Thermochronological constraints on the age of the40Ar/39Ar standard MMhb. Contrib. to Mineral. Petrol. 151, 615–630. https://doi.org/10.1007/s00410-006-0077-4

Schulmann, K., Catalán, J.R.M., Lardeaux, J.M., Janoušek, V., Oggiano, G., 2014. The Variscan orogeny: Extent, timescale and the formation of the European crust. Geol. Soc. Spec. Publ. 405, 1–6. https://doi.org/10.1144/SP405.15

Schulmann, K., Lexa, O., Štípská, P., Racek, M., Tajčmanová, L., Konopásek, J., Edel, J.B., Peschler, A., Lehmann, J., 2008. Vertical extrusion and horizontal channel flow of orogenic lower crust: Key exhumation mechanisms in large hot orogens? J. Metamorph. Geol. 26, 273–297. https://doi.org/10.1111/j.1525-1314.2007.00755.x

Schulmann, K., Schaltegger, U., Jezek, J., Thompson, A.B., Edel, J.B., 2002. Rapid burial and exhumation during orogeny: Thickening and synconvergent exhumation of thermally weakened and thinned crust (Variscan Orogen in Western Europe). Am. J. Sci. 302, 856–879. https://doi.org/10.2475/ajs.302.10.856

Scibiorski, E., Tohver, E., Jourdan, F., 2015. Rapid cooling and exhumation in the western part

of the Mesoproterozoic Albany-Fraser Orogen, Western Australia. Precambrian Res. 265, 232–248. https://doi.org/10.1016/j.precamres.2015.02.005

Shaw, J., Gutiérrez-Alonso, G., Johnston, S.T., Pastor Galán, D., 2014. Provenance variability along the Early Ordovician north Gondwana margin: Paleogeographic and tectonic implications of U-Pb detrital zircon ages from the Armorican Quartzite of the Iberian Variscan belt. Bull. Geol. Soc. Am. 126, 702–719. https://doi.org/10.1130/B30935.1

Siégel, C., Bryan, S.E., Allen, C.M., Gust, D.A., 2018. Use and abuse of zircon-based thermometers: A critical review and a recommended approach to identify antecrystic zircons. Earth-Science Rev. https://doi.org/10.1016/j.earscirev.2017.08.011

Silva, A.. F., Rebelo, J.A.., Ribeiro, M.L., 1989. Carta Geológica de Portugal na escala 1/50.000. Notícia Explicativa da Folha 11-C (Torre de Moncorvo). Serviços Geológicos de Portugal, Lisboa.

Silva, A.. F., Romão, J.M.C., Sequeira, A.. J.D., Oliveira, J.T., 1995. A sucessão litostratigráfica anté-ordovícica na Zona Centro-Ibérica (ZCI), em Portugal: Ensaio de interpretação com base nos dados actuais, in: XIII Reunión de Geologia Del Oeste Peninsular, RGOP/PICG. Salamanca, pp. 71–72.

Silva, A., Ribeiro, M.L., 2000. Carta Geológica Simplificada do Parque Arqueológico do Vale do Côa. Vila Nova de Foz Côa.

Silva, A., Ribeiro, M.L., 1994. Carta Geológica de Portugal na Escala 1:50 000 e Notícia Explicativa da Folha 15-B (Freixo de Espada à Cinta). Instituto Geológico e Mineiro, Lisboa.

Silva, A., Ribeiro, M.L., 1991. Carta Geológica de Portugal na Escala 1:50 000 e Notícia Explicativa da Folha 15-A (Vila Nova de Foz Côa). Serviços Geológicos de Portugal, Lisboa.

Silva, A.F., 2013. A Litostratigrafia e Estrutura do Supergrupo Dúrico-Beirão (Complexo Xisto-Grauváquico), em Portugal, e sua correlação com as correspondentes sucessões em Espanha. Bol. Minas 48, 97–142.

Silva, A.F., 2005. Litostratigrafia e Estrutura do Supergrupo Dúrico-Beirão (Complexo Xisto-Grauváquico). Rel. Inéd. Inst. Nac. Eng. Tec. Inov. (INETI) / Lab. Nac. Energ. Geol. (LNEG), Lisboa.

Silva, A.F., Ribeiro, A., 1985. Thrust tectonics of sardic age in the Alto Douro region (Northeastern Portugal). Comun. dos Serviços Geológicos Port. 71, 151–157.

Silva, A.F., Romão, J.M.C., Sequeira, A.J.D., Ribeiro, M.L., 1988. Geotransversal no Grupo das Beiras (Complexo Xisto-Grauváquico) entre os sinclinórios de Mação e Penha Garcia

(Centro-Leste de Portugal), in: Resumo de Comunicação/Painel Apresentado à X Reunião de Geologia Do Oeste Peninsular. Bragança.

Simancas, J.F., 2019. Variscan Cycle BT - The Geology of Iberia: A Geodynamic Approach: Volume 2: The Variscan Cycle, in: Quesada, C., Oliveira, J.T. (Eds.), . Springer International Publishing, Cham, pp. 1–25. https://doi.org/10.1007/978-3-030-10519-8_1

Singleton, J.S., Stockli, D.F., Gans, P.B., Prior, M.G., 2014. Timing, rate, and magnitude of slip on the Buckskin-Rawhide detachment fault, west central Arizona. Tectonics 33, 1596–1615. https://doi.org/10.1002/2013TC003517

Sláma, J., Kosler, J., Crowley, J.L., Gerdes, A., Hanchar, J., Horstwood, M., Morris, G.A., Nasdala, L., Norberg, N., Schaltegger, U., others, 2007. Plesovice zircon-A new natural standard for U-Pb and Hf isotopic microanalysis. Geochim. Cosmochim. Acta 71, A947--A947.

Söderlund, U., Patchett, P.J., Vervoort, J., Isachsen, C., 2004. The 176Lu decay constant determined by Lu-Hf and U-Pb isotope systematics of Precambrian mafic intrusions. Earth Planet. Sci. Lett. 219, 311–324. https://doi.org/10.1016/S0012-821X(04)00012-3

Sola, A.M., Becchio, R.A., Pimentel, M.M., 2013. Petrogenesis of migmatites and leucogranites from Sierra de Molinos , Salta , Northwest Argentina : A petrologic and geochemical study Lithos Petrogenesis of migmatites and leucogranites from Sierra de Molinos , Salta , Northwest Argentina : A petrologic . LITHOS 177, 470–491. https://doi.org/10.1016/j.lithos.2013.07.025

Solar, G.S., Brown, M., 2001. Petrogenesis of Migmatites in Maine, USA: Possible Source of Peraluminous Leucogranite in Plutons? J. Petrol. 42, 789–823. https://doi.org/10.1093/petrology/42.4.789

Sorcar, N., Hoppe, U., Dasgupta, S., Chakraborty, S., 2014. High-temperature cooling histories of migmatites from the High Himalayan Crystallines in Sikkim, India: rapid cooling unrelated to exhumation? Contrib. to Mineral. Petrol. 167. https://doi.org/10.1007/s00410-013-0957-3

Sousa, B., 1982. Litostratigrafia e estrutura do «Complexo Xisto-Grauváquico ante-ordovícico» - Grupo do Douro, Mem. Not. Lab. Min. Geol. Universidade de Coimbra.

Sousa, M.B., 1989. O Complexo Xisto-Grauváquico da Marofa (Figueira de Castelo Rodrigo-Portugal Central). Mem. Not. , Publ. Mus. Lab. Min. Geol. Univ. Coimbra 108, 1–10.

Sousa, M.B., 1984. Considerações sobre a estratigrafia do Complexo Xisto-Grauváquico (CXG) e sua relação com o Paleozóico inferior. Cuad. Geol. Ibérica 9, 9–36.

Sousa, M.B., Sequeira, A.J.D., 1993. O limite Precâmbrico – Câmbrico na Zona Centro Ibérica,

em Portugal. XII Reun. Geol. do Oeste Penins. I, 17–28.

Spear, F.S., Kohn, M.J., Cheney, J.T., 1999. P - T paths from anatectic pelites. Contrib. to Mineral. Petrol. 134, 17–32. https://doi.org/10.1007/s004100050466

Spear, F.S., Parrish, R.R., 1996. Petrology and cooling rates of the Valhalla Complex, British Columbia, Canada. Jour. Pet. 37, 733–765.

Steenken, A., Siegesmund, S., Heinrichs, T., Fügenschuh, B., 2002. Cooling and exhumation of the Rieserferner Pluton (Eastern Alps, Italy/Austria). Int. J. Earth Sci. 91, 799–817. https://doi.org/10.1007/s00531-002-0260-4

Steiger, R.H., Jäger, E., 1977. Subcommission on geochronology: Convention on the use of decay constants in geo- and cosmochronology. Earth Planet. Sci. Lett. 36, 359–362. https://doi.org/https://doi.org/10.1016/0012-821X(77)90060-7

Talavera, C., Martínez Poyatos, D., González Lodeiro, F., 2015. SHRIMP U–Pb geochronological constraints on the timing of the intra-Alcudian (Cadomian) angular unconformity in the Central Iberian Zone (Iberian Massif, Spain). Int. J. Earth Sci. 104, 1739–1757. https://doi.org/10.1007/s00531-015-1171-5

Tassinari, C.C.G., Medina, J., Pinto, M.S., 1996. Rb-Sr and Sm-Nd geochronology and isotope geochemistry of central Iberian metasedimentary rocks (Portugal). Geol. en Mijnb. 75, 69–79.

Teixeira, C., 1955. Notas sobre a Geologia de Portugal: o Complexo Xisto-Grauváquico ante-Ordoviciano. Empresa Literária Fluminense, Lisboa.

Teixeira, R., Coke, C., Gomes, M.H., Dias, R., 2013. U-Pb geochronology of detrital zircons from metasedimentary rocks from Formation of Desejosa, Serra do Marão, Portugal, in: Mineralogical Magazine. p. 2318. https://doi.org/10.1180/minmag.2013.077.5.20

Teixeira, R.J.S., 2008. Mineralogia, petrologia e geoquímica dos granitos e seus encraves da região de Carrazeda de Ansiães. Universidade de Trás-os-Montes e Alto Douro.

Teixeira, R.J.S., Neiva, A.M.R., Silva, P.B., Gomes, M.E.P., Andersen, T., Ramos, J.M.F., 2017. Combined U-Pb geochronology and Lu-Hf isotope systematics by LAM-ICPMS of zircons from granites and metasedimentary rocks of Carrazeda de Ansiães and Sabugal areas , Portugal , to co ... Lithos Combined U – Pb geochronology and Lu – Hf isotope systematics. LITHOS 125, 321–334. https://doi.org/10.1016/j.lithos.2011.02.015

Thomson, S.N., Gehrels, G.E., Ruiz, J., Buchwaldt, R., 2012. Routine low-damage apatite U-Pb dating using laser ablation-multicollector- ICPMS. Geochemistry, Geophys. Geosystems 13. https://doi.org/10.1029/2011GC003928

Tommasini, S., Davies, G.R., 1997. Isotope disequilibrium during anatexis: a case study of

contact melting, Sierra Nevada, California. Earth Planet. Sci. Lett. 148, 273–285.

Tsuchiya, N., Fujino, K., 2000. Evaluation of cooling history of the Quarternary Takidani Pluton using thermoluminescence technique. Proc. World Geotherm. Congr. 2000 3939–3944.

Tuttle, O.F., Bowen, N.L., 1958. Origin of granite in the light of experimental studies in the system NaAlSi3O8-KAlSi3O8-SiO2-H2O, Geological Society of America Memoir.

Valle Aguado, B., Azevedo, M.R., Nolan, J., Medina, J., Costa, M.M., Corfu, F., Martínez Catalán, J.R., 2017. Granite emplacement at the termination of a major Variscan transcurrent shear zone: The late collisional Viseu batholith. J. Struct. Geol. 98, 15–37. https://doi.org/10.1016/j.jsg.2017.04.002

Valle Aguado, B., Azevedo, M.R., Schaltegger, U., Martínez Catalán, J.R., Nolan, J., 2005. U-Pb zircon and monazite geochronology of Variscan magmatism related to syn-convergence extension in Central Northern Portugal. Lithos 82, 169–184. https://doi.org/10.1016/j.lithos.2004.12.012

Valverde-Vaquero, P., Dí-ez Balda, M.A., Dí-ez Montes, A., Dörr, W., Escuder-Viruete, J., González-Clavijo, E., Maluski, H., Rodrí-guez-Fernández, L.R., Rubio, F., Villar, P., 2006. Timing of Variscan metamorphism and the Central Iberian paradox. Geophys. Res. Abstr. Eur. Geosci. Union 8, 1.

Valverde-Vaquero, P., Díez Balda, M.A., Díez Montes, A., Dörr, W., Escuder Viruete, J., González-Clavijo, E., Maluski, H., Rodríguez-Fernández, L.R., Rubio, F., Villar, P., 2007. The “hot orogen”: two separate Variscan low-pressure metamorphic events in the Central Iberian Zone. Mech. Variscan Orogeny a Mod. view Orog. Res. Géologie la Fr. 2, 1–168.

Vanderhaeghe, O., 2009. Migmatites, granites and orogeny: Flow modes of partially-molten rocks and magmas associated with melt/solid segregation in orogenic belts. Tectonophysics 477, 119–134. https://doi.org/10.1016/j.tecto.2009.06.021

Vanderhaeghe, O., Kruckenberg, S., Gerbault, M., Martin, L., Duchêne, S., Deloule, E., 2018. Crustal-scale convection and diapiric upwelling of a partially molten orogenic root (Naxos dome, Greece). Tectonophysics 746, 459–469. https://doi.org/10.1016/j.tecto.2018.03.007

Vanderhaeghe, O., Teyssier, C., 2001. Crustal-scale rheological transitions during late-orogenic collapse. Tectonophysics 335, 211–228. https://doi.org/10.1016/S0040-1951(01)00053-1

Vavra, G., 1993. A guide to quantitative morphology of accessory zircon. Chem. Geol. 110, 15–28. https://doi.org/10.1016/0009-2541(93)90245-E

Vavra, G., 1990. On the kinematics of zircon growth and its petrogenetic significance: a cathodoluminescence study. Contrib. to Mineral. Petrol. 106, 90–99.

https://doi.org/10.1007/BF00306410

Vermeesch, P., 2018. Geoscience Frontiers IsoplotR : A free and open toolbox for geochronology. Geosci. Front. 9, 1479–1493. https://doi.org/10.1016/j.gsf.2018.04.001

Vernon, R.H., Clarke, G.L., 2008. Principles of metamorphic petrology. Cambridge University Press.

Vervoort, J.D., Blichert-Toft, J., 1999. Evolution of the depleted mantle: Hafnium isotope evidence from juvenile rocks through time. \gca 63, 533–556. https://doi.org/10.1016/S0016-7037(98)00274-9

Vielzeuf, D., Holloway, J., 1988. Experimental determination of the fluid-absent melting relations in the pelitic system. Contrib. to Mineral. Petrol. 98, 257–276. https://doi.org/10.1007/BF00375178

Villar Alonso, P., Fernández Ruiz, J., Bellido, F., Carrasco, R.., Rodriguez Fernández, L.., 2000. Memoria del mapa geológico de España 1:50000, Lumbrales (Hoja 475). Série magna, 1ªed, 2ªsérie,. Madrid.

Villaros, A., Laurent, O., Couzinié, S., Moyen, J.-F., Mintrone, M., 2018. Plutons and domes: the consequences of anatectic magma extraction—example from the southeastern French Massif Central. Int. J. Earth Sci. 0, 0. https://doi.org/10.1007/s00531-018-1630-x

Villaros, A., Stevens, G., Moyen, J.F., Buick, I.S., 2009. The trace element compositions of S-type granites: Evidence for disequilibrium melting and accessory phase entrainment in the source. Contrib. to Mineral. Petrol. 158, 543–561. https://doi.org/10.1007/s00410-009-0396-3

Villaseca, Carlos, Barbero, L., Herreros, V., 1998. A re-examination of the typology of peraluminous granite types in intracontinental orogenic belts. Trans. R. Soc. Edinb. Earth Sci. 89, 113–119. https://doi.org/DOI: 10.1017/S0263593300007045

Villaseca, C., Barbero, L., Rogers, G., 1998. Crustal origin of Hercynian peraluminous granitic batholiths of central Spain: petrological, geochemical and isotopic (Sr, Nd) constraints. Lithos 43, 55–79. https://doi.org/10.1016/S0024-4937(98)00002-4

Villaseca, C., Merino, E., Oyarzun, R., Orejana, D., P?rez-Soba, C., Chicharro, E., 2014. Contrasting chemical and isotopic signatures from Neoproterozoic metasedimentary rocks in the Central Iberian Zone (Spain) of pre-Variscan Europe: Implications for terrane analysis and Early Ordovician magmatic belts. Precambrian Res. 245, 131–145. https://doi.org/10.1016/j.precamres.2014.02.006

Watson, E.B., Harrison, T.M., 1983. Zircon saturation revisited: temperature and composition effects in a variety of crustal magma types. Earth Planet. Sci. Lett. 64, 295–304.

https://doi.org/10.1016/0012-821X(83)90211-X

Watson, E.B., Wark, D.A., Thomas, J.B., 2006. Crystallization thermometers for zircon and rutile. Contrib. to Mineral. Petrol. 151, 413–433. https://doi.org/10.1007/s00410-006-0068-5

Weis, D., Kieffer, B., Maerschalk, C., Barling, J., de Jong, J., Williams, G.A., Hanano, D., Pretorius, W., Mattielli, N., Scoates, J.S., 2006. High-precision isotopic characterization of USGS reference materials by TIMS and MC-ICP-MS. Geochemistry, Geophys. Geosystems 7.

White, W., 2010. Oceanic Island Basalts and Mantle Plumes: The Geochemical Perspective. Annu. Rev. Earth Planet. Sci 38, 133–160. https://doi.org/10.1146/annurev-earth-040809-152450

Whitney, D.L., Teyssier, C., Vanderhaeghe, O., 2004. Gneiss domes and crustal flow. Spec. Pap. 380 Gneiss Domes Orogeny 15–33. https://doi.org/10.1130/0-8137-2380-9.15

Whittington, A.G., Hofmeister, A.M., Nabelek, P.I., 2009. Temperature-dependent thermal diffusivity of the Earth's crust and implications for magmatism. Nature 458, 319–321. https://doi.org/10.1038/nature07818

Wiedenbeck, M., Allé, P., Corfu, F., Griffin, W.L., Meier, M., Oberli, F., Quadt, A. VON, Roddick, J.C., Spiegel, W., 1995. Three Natural Zircon Standards for U-Th-Pb, Lu-Hf, Trace Element and Ree Analyses. Geostand. Newsl. 19, 1–23. https://doi.org/10.1111/j.1751-908X.1995.tb00147.x

Williams, I.S., Buick, I.S., Cartwright, I., 1996. An extended episode of early Mesoproterozoic metamorphic fluid flow in the Reynolds Range, central Australia. J. Metamorph. Geol. 14, 29–47. https://doi.org/10.1111/j.1525-1314.1996.00029.x

Willigers, B.J.A., van Gool, J.A.M., Wijbrans, J.R., Krogstad, E.J., Mezger, K., 2002. Posttectonic Cooling of the Nagssugtoqidian Orogen and a Comparison of Contrasting Cooling Histories in Precambrian and Phanerozoic Orogens. J. Geol. 110, 503–517. https://doi.org/10.1086/341595

Wolf, M., Romer, R.L., Glodny, J., 2019. Isotope disequilibrium during partial melting of metasedimentary rocks. Geochim. Cosmochim. Acta 257, 163–183. https://doi.org/10.1016/j.gca.2019.05.008

Yakymchuk, C., Brown, M., 2014. Behaviour of zircon and monazite during crustal melting. J. Geol. Soc. London. 171. https://doi.org/10.1144/jgs2013-115

Yakymchuk, C., Clark, C., White, R.W., 2017. Phase Relations, Reaction Sequences and Petrochronology. Rev. Mineral. Geochemistry 83, 13–53.

https://doi.org/10.2138/rmg.2017.83.2

Yakymchuk, C., Kirkland, C.L., Clark, C., 2018. Th/U ratios in metamorphic zircon. J. Metamorph. Geol. 36, 715–737. https://doi.org/10.1111/jmg.12307

Yakymchuk, C.J.A., 2014. Anatexis and Crustal Differentiation: Insights From the Fosdick Migmatite–Granite Complex, West Antarctica. University of Maryland. https://doi.org/https://doi.org/10.13016/M2501K

Yang, L., Liu, X.-C., Wang, J.-M., Wu, F.-Y., 2019. Is Himalayan leucogranite a product by in situ partial melting of the Greater Himalayan Crystalline? A comparative study of leucosome and leucogranite from Nyalam, southern Tibet. Lithos 342–343, 542–556.

Yuguchi, T., Sueoka, S., Iwano, H., Danhara, T., Ishibashi, M., Sasao, E., Nishiyama, T., 2017. Spatial distribution of the apatite fission-track ages in the Toki granite, central Japan: Exhumation rate of a Cretaceous pluton emplaced in the East Asian continental margin. Isl. Arc 26, 1–4. https://doi.org/10.1111/iar.12219

Žák, J., Verner, K., Finger, F., Faryad, S.W., Chlupácová, M., Veselovskỳ, F., 2011. The generation of voluminous S-type granites in the Moldanubian unit, Bohemian Massif, by rapid isothermal exhumation of the metapelitic middle crust. Lithos 121, 25–40. https://doi.org/10.1016/j.lithos.2010.10.002

Zartman, R.E., Doe, B.R., 1981. Plumbotectonics - the model. Tectonophysics 75, 135–162.

Zeng, L., Asimow, P.D., Saleeby, J.B., 2005. Coupling of anatectic reactions and dissolution of accessory phases and the Sr and Nd isotope systematics of anatectic melts from a metasedimentary source. Geochim. Cosmochim. Acta 69, 3671–3682. https://doi.org/10.1016/J.GCA.2005.02.035

Zhang, C., Holtz, F., Koepke, J., Berndt, J., Ma, C., 2014. Decompressional anatexis in the migmatite core complex of northern Dabie orogen, eastern China: Petrological evidence and Ti-in-quartz thermobarometry. Lithos 202–203, 227–236. https://doi.org/10.1016/j.lithos.2014.05.024

Zhang, H., Harris, N., Parrish, R., Kelley, S., Zhang, L., Rogers, N., Argles, T., King, J., 2004. Causes and consequences of protracted melting of the mid-crust exposed in the North Himalayan antiform. Earth Planet. Sci. Lett. 228, 195–212. https://doi.org/10.1016/J.EPSL.2004.09.031

APPENDIX A – Sample List

Sample	Lithology	Latitude	Longitude	Whole-rock geochemistry	Isotope geochemistry	Apatite trace element composition	Zircon trace element composition	U-Pb geochronology
JTJ-1a	Phyllite	41.014	-7.038					
JTJ-1b	Phyllite	41.014	-7.038					
JTJ-2	Phyllite	41.018	-7.042	X	X	X		X
JTJ-5	Metatexite	40.999	-7.063					
JTJ-6	Phyllite	40.998	-7.069	X				
JTJ-7	Metatexite	40.997	-7.074					
JTJ-8	Metatexite	40.992	-7.057	X		X		X
JTJ-9	Granite IXγ	40.984	-7.056	X				
JTJ-10	Granite IXγ	40.973	-7.052	X		X		X
JTJ-11	Granite Vγ	40.955	-7.024	X				
JTJ-12	Granite Vγ	40.944	-7.014	X	X	X	X	X
JTJ-13	Granite IIIγ	40.917	-7.011	X		X		X
JTJ-14	Quartzite	40.878	-6.967					
JTJ-15	Quartzphyllite	40.872	-6.977	X				
JTJ-16	Quartzite	40.864	-6.991					
JTJ-17	Slate	40.828	-6.951	X				
JTJ-18	Phyllite	40.855	-6.984	X				
JTJ-19	Phyllite	40.848	-7.002	X	X			X
JTJ-20	Metatexite	40.889	-7.032	X	X	X	X	X
JTJ-21A	Quartzphyllite	40.869	-7.054					
JTJ-21B	Quartzite	40.869	-7.054					

JTJ-22A	Diatexite	40.872	-7.058	X				
JTJ-22B	Metatexite	40.872	-7.058	X				
JTJ-22C	Diatexite	40.872	-7.058					
JTJ-23A	Diatexite	40.874	-7.061	X				
JTJ-23B	Metatexite-Diatexite transition	40.874	-7.061					
JTJ-24A	Diatexite	40.882	-7.066	X	X	X	X	X
JTJ-24B	Metatexite	40.882	-7.066	X				
JTJ-24C	Leucosome/Nebulite	40.882	-7.066					
JTJ-24D	Nebulite	40.882	-7.066	X				
JTJ-25	Metatexite	40.882	-7.083	X	X	X	X	X
JTJ-26	Diatexite	40.884	-7.08	X				
JTJ-27	Diatexite	40.9	-7.064	X				
JTJ-28A	Diatexite	40.901	-7.063	X				
JTJ-28B	Metatexite-Nebulite transition	40.901	-7.063					
JTJ-29	Metatexite	40.884	-7.027					
JTJ-30	Diatexite	40.893	-7.073	X				
JTJ-31A	Granite Xγ	40.897	-7.082	X				
JTJ-31B	Metatexite	40.897	-7.082					
JTJ-31C	Diatexite	40.897	-7.082	X				
JTJ-31D	Doleritic vein	40.897	-7.082					
JTJ-31E	Metatexite-Diatexite transition	40.897	-7.082					

JTJ-32	Granite Xγ	40.905	-7.091	X				
JTJ-33	Granite Xγ	40.906	-7.107					
JTJ-34	Granite Xγ	40.911	-7.11	X	X	X	X	X
JTJ-35	Granite VIIIγ	40.911	-7.121	X	X	X		X
JTJ-36	Granite IIγ	40.853	-7.132	X	X	X		X
JTJ-37	Metatexite	40.858	-7.144	X				
JTJ-38	Diatexite	40.868	-7.16					
JTJ-39	Metatexite-Diatexite transition	40.871	-7.162					
JTJ-40	Granite Xγ	40.884	-7.178	X				
JTJ-41a	Quartzphyllites with quartz-bearing intercalations	40.85	-6.838					
JTJ-41b	Quartzphyllites	40.85	-6.838	X				X
JTJ-42	Quartzite	40.878	-6.878					
JTJ-43	Diatexite	40.887	-6.888	X	X	X		X
JTJ-44	Granite IXγ	40.904	-6.898	X				
JTJ-45	Granite IXγ	40.923	-6.91	X	X		X	X
JTJ-46	Granite IXγ	40.941	-6.92					
JTJ-47	Granite IXγ	40.964	-6.934	X				
JTJ-48A	Diatexite	40.987	-6.927	X				
JTJ-48B	Metatexite	40.987	-6.927	X	X			X
JTJ-48C	Leucosome	40.987	-6.927	X				
JTJ-49	Quartzphyllite	40.992	-6.937	X				X

JTJ-50	Granite IXγ	40.941	-6.931	X				
JTJ-51	Diatexite	40.902	-6.96	X				
JTJ-52	Diatexite	40.894	-7.033	X				
JTJ-53	Metatexite	40.965	-7.086	X	X	X		X
JTJ-54A	Leucosome	40.971	-7.088	X				
JTJ-54B	Metatexite	40.971	-7.088	X				
JTJ-54C	Pegmatite	40.971	-7.088					
JTJ-55	Diatexite	40.846	-7.178	X	X	X	X	X
JTJ-56A	Metatexite	40.846	-7.182	X				
JTJ-56B	Diatexite	40.846	-7.182	X				
JTJ-57	Metatexite	40.84	-7.191					
JTJ-58	Granite Iγ	40.791	-7.192	X				
JTJ-59	Granite IVγ	40.8	-7.182	X				
JTJ-60A	Metatexite	40.832	-7.189	X	X	X		X
JTJ-60B	Diatexite	40.832	-7.189	X				
JTJ-61	Granite IXγ	40.45	-7.19					
JTJ-62	Granite IXγ	40.45	-7.19	X				

APPENDIX B – LA-ICP-MS analytical details

Appendix B1: Instrumental setup, ablation parameters and conditions for zircon and apatite U-Pb and zircon trace element analysis

Laser ablation system	**U-Pb**		**Traces**
	Zircon	Apatite	Zircon
Laser system	ASI RESOlution ArF excimer		
Ablation cell	S155 Laurin Technic		
Laser wavelength (nm)	193		
Pulse width (ns)	5-7		
Laser beam diameter (µm)	11 - 25	20 - 50	35 – 25
Fluence (measured) (J/cm^2)	2.1 – 2.5	2.8 - 3	3.8 – 4.1
Energy distribution	Flat, homogenised		
Repetition rate (Hz)	2	3	4
Carrier gas (l/min)	a mix of He (0.3) and pure N (0.003)		

ICP Parameters	
ICPMS	ANALYTIK JENA Plasma Quant Elite
RF Power (KW)	1.3
Gas flow (l/min)	
Plasma Flow	10
Auxiliary Flow	1.65
Nebulizer Flow	0.88-0.89
Sampling Depth (mm)	7 to 8
Acquisition parameters	
Scanning mode	Peak hoping
Acquisition mode	Time resolved
Analysis time	1 pulse cleaning, 10 s delay, 20 s blank, 30 s ablation, 5 s wash-out
Dwell times (ms)	
^{202}Hg, ^{204}Hg+Pb, ^{208}Pb, ^{232}Th, ^{235}U, ^{238}U	10
^{206}Pb	20
^{207}Pb	30
Traces*	10

Oxides (^{232}Th^{16}O/^{232}Th)	0.1	0.1-0.2
Fractionation (^{238}U/^{232}Th)	97-100	98
^{204}Hg+Pb Bkg (cps)	400-550	
Tuning NIST612 (^{238}U kcps)	920-1000	400 (balanced)

* see text for all the analysed isotopes

Appendix B2: U-Pb ages and ratios of the zircon primary standard (Plesovice)

Zircon primary standard				Common-lead uncorrected ratios					Final Ages (Ma)						
Id	U (ppm)	Th (ppm)	Th/U	$^{207}Pb/^{235}U$	±2σ	$^{206}Pb/^{238}U$	±2σ	Rho	$^{207}Pb/^{235}U$	±2σ	$^{206}Pb/^{238}U$	±2σ	$^{207}Pb/^{206}Pb$	±2σ	Con-cord-ance (%)
Z_Plesovice_1	776	84	0.11	0.400	0.017	0.0536	0.0007	0.15	340	12	336	4	324	84	99
Z_Plesovice_2	765	81	0.11	0.392	0.017	0.05384	0.00078	0.22	335	13	338	5	306	86	101
Z_Plesovice_3	763	81	0.11	0.392	0.017	0.05383	0.00078	0.22	335	13	338	5	305	86	101
Z_Plesovice_4	773	82	0.11	0.386	0.017	0.05373	0.00072	0.31	331	12	337	4	278	83	102
Z_Plesovice_5	735	76	0.10	0.411	0.018	0.05374	0.00078	0.25	349	13	337	5	334	86	97
Z_Plesovice_6	734	76	0.10	0.410	0.018	0.05372	0.00078	0.25	349	13	337	5	330	88	97
Z_Plesovice_7	785	83	0.11	0.387	0.017	0.05345	0.00072	0.06	331	12	336	4	291	85	101
Z_Plesovice_8	779	83	0.11	0.387	0.017	0.05356	0.00072	0.19	331	12	336	4	313	85	102
Z_Plesovice_9	732	74	0.10	0.386	0.017	0.05327	0.00068	0.15	331	12	335	4	307	85	101
Z_Plesovice_10	785	84	0.11	0.396	0.017	0.0543	0.0007	0.20	338	12	341	4	311	84	101
Z_Plesovice_11	722	74	0.10	0.381	0.019	0.05329	0.00085	0.15	328	14	335	5	284	96	102
Z_Plesovice_12	798	86	0.11	0.400	0.017	0.05370	0.00074	0.19	341	12	337	5	344	83	99
Z_Plesovice_13	742	76	0.10	0.389	0.017	0.05394	0.00073	0.19	332	13	339	4	268	87	102
Z_Plesovice_14	758	78	0.10	0.399	0.017	0.05380	0.00074	0.30	340	12	338	5	339	80	99
Z_Plesovice_15	755	78	0.10	0.397	0.018	0.05348	0.00067	0.19	338	13	336	4	302	86	99
Z_Plesovice_1	756	78	0.10	0.395	0.011	0.05402	0.00077	0.23	338	8	339	5	302	50	100
Z_Plesovice_2	752	77	0.10	0.394	0.011	0.05335	0.00077	0.33	337	8	335	5	324	52	99
Z_Plesovice_3	758	79	0.10	0.387	0.011	0.05338	0.00081	0.20	331	8	335	5	286	56	101
Z_Plesovice_4	759	78	0.10	0.402	0.011	0.05415	0.00081	0.13	342	8	340	5	341	55	99
Z_Plesovice_5	741	76	0.10	0.392	0.013	0.05405	0.00084	0.26	334	9	339	5	283	62	101
Z_Plesovice_6	874	97	0.11	0.398	0.012	0.05354	0.00082	0.23	339	8	336	5	339	54	99
Z_Plesovice_7	696	69	0.10	0.386	0.012	0.05329	0.00083	0.17	330	9	335	5	286	61	101
Z_Plesovice_8	769	81	0.11	0.393	0.012	0.05339	0.00078	0.21	336	9	335	5	315	57	100
Z_Plesovice_9	736	70	0.09	0.396	0.013	0.05370	0.00078	0.23	338	9	337	5	312	60	100

Z_Plesovice_10	772	88	0.11	0.392	0.011	0.05404	0.00078	0.21	335	8	339	5	287	53	101
Z_Plesovice_11	777	88	0.11	0.401	0.011	0.05349	0.00075	0.12	342	8	336	5	362	55	98
Z_Plesovice_12	743	75	0.10	0.392	0.013	0.05394	0.00078	0.29	334	9	339	5	279	60	101
Z_Plesovice_13	736	76	0.10	0.388	0.012	0.05315	0.00081	0.20	332	9	334	5	301	60	101
Z_Plesovice_14	769	79	0.10	0.396	0.012	0.05407	0.00086	0.24	338	9	339	5	309	58	101
Z_Plesovice_1	777	82	0.11	0.3934	0.0091	0.05379	0.00076	0.26	336	7	338	5	304	47	101
Z_Plesovice_2	747	77	0.10	0.3927	0.0084	0.05358	0.00078	0.21	336	6	336	5	318	44	100
Z_Plesovice_3	727	74	0.10	0.3928	0.0097	0.05355	0.00077	0.19	335	7	336	5	311	51	100
Z_Plesovice_4	778	81	0.10	0.398	0.008	0.05384	0.00076	0.22	340	6	338	5	335	42	99
Z_Plesovice_5	781	79	0.10	0.3938	0.0089	0.05364	0.00077	0.16	337	6	337	5	327	47	100
Z_Plesovice_6	760	78	0.10	0.3913	0.0089	0.05360	0.00078	0.18	335	7	337	5	313	48	101
Z_Plesovice_7	671	72	0.11	0.3949	0.0088	0.05374	0.00076	0.18	338	6	337	5	308	47	100
Z_Plesovice_8	839	84	0.10	0.3905	0.0085	0.05365	0.00078	0.26	334	6	337	5	288	44	101
Z_Plesovice_9	791	81	0.10	0.399	0.008	0.05369	0.00076	0.25	341	6	337	5	343	41	99
Z_Plesovice_10	771	80	0.10	0.392	0.009	0.05373	0.00077	0.12	336	7	337	5	305	49	101
Z_Plesovice_11	668	68	0.10	0.39	0.01	0.05351	0.00083	0.16	334	8	336	5	308	55	100
Z_Plesovice_12	832	94	0.11	0.3957	0.0088	0.05378	0.00075	0.25	338	7	338	5	316	46	100
Z_Plesovice_13	701	71	0.10	0.3923	0.0098	0.05355	0.00079	0.29	335	7	336	5	305	50	100
Z_Plesovice_14	770	80	0.10	0.3950	0.0092	0.05395	0.00077	0.20	337	7	339	5	305	49	101
Z_Plesovice_15	788	82	0.10	0.3941	0.0085	0.05350	0.00075	0.21	337	6	336	5	322	45	100
Z_Plesovice_1	755	78	0.10	0.3940	0.0079	0.0536	0.0012	0.21	336	6	337	7	358	74	100
Z_Plesovice_2	752	77	0.10	0.3941	0.0082	0.0543	0.0012	0.20	337	6	341	7	279	75	101
Z_Plesovice_3	755	78	0.10	0.3944	0.0083	0.0538	0.0012	0.21	338	6	338	7	294	75	100
Z_Plesovice_4	757	78	0.10	0.3961	0.0087	0.0533	0.0012	0.22	338	6	335	7	314	77	99
Z_Plesovice_5	752	78	0.10	0.3889	0.0085	0.0534	0.0012	0.29	333	6	335	7	273	76	101
Z_Plesovice_6	756	78	0.10	0.3969	0.0081	0.0533	0.0012	0.32	339	6	335	8	353	74	99
Z_Plesovice_7	755	78	0.10	0.3938	0.0077	0.0539	0.0012	0.24	336	6	338	7	317	74	101
Z_Plesovice_8	755	78	0.10	0.3929	0.0088	0.0536	0.0012	0.26	336	6	337	7	309	75	100
Z_Plesovice_9	756	78	0.10	0.3946	0.0079	0.0532	0.0012	0.30	338	6	334	7	350	72	99

Z_Plesovice_10	755	78	0.10	0.3946	0.0081	0.0541	0.0012	0.32	338	6	340	7	302	74	101
Z_Plesovice_11	753	78	0.10	0.3930	0.0073	0.0537	0.0012	0.44	336	5	337	7	307	70	100
Z_Plesovice_12	761	79	0.10	0.3939	0.0077	0.0541	0.0012	0.32	337	6	340	7	311	74	101
Z_Plesovice_13	752	77	0.10	0.3944	0.0085	0.0538	0.0012	0.25	337	6	338	7	337	76	100
Z_Plesovice_14	753	78	0.10	0.3950	0.0078	0.0527	0.0012	0.28	337	6	331	7	386	75	98
Z_Plesovice_15	778	84	0.11	0.3934	0.0075	0.0542	0.0012	0.24	336	5	340	7	291	74	101
Z_Plesovice_16	743	75	0.10	0.3939	0.0096	0.0535	0.0012	0.35	336	7	336	7	297	78	100
Z_Plesovice_1	886	91	0.10	0.414	0.042	0.0540	0.0013	0.04	349	31	339	8	343	190	97
Z_Plesovice_2	772	81	0.11	0.398	0.042	0.0540	0.0013	0.14	336	31	339	8	242	190	101
Z_Plesovice_3	689	69	0.10	0.394	0.042	0.0538	0.0013	0.09	334	31	338	8	220	190	101
Z_Plesovice_4	747	77	0.10	0.390	0.042	0.0532	0.0013	0.12	330	31	334	8	230	190	101
Z_Plesovice_5	729	75	0.10	0.382	0.041	0.0536	0.0013	0.13	324	30	337	8	190	190	104
Z_Plesovice_6	813	84	0.10	0.388	0.041	0.0535	0.0013	0.21	330	30	336	8	250	190	102
Z_Plesovice_7	758	79	0.10	0.384	0.042	0.0540	0.0014	0.22	328	32	339	8	220	190	103
Z_Plesovice_8	732	76	0.10	0.37	0.04	0.0532	0.0013	0.01	314	30	334	8	170	190	106
Z_Plesovice_9	795	85	0.11	0.403	0.044	0.0536	0.0014	0.04	342	32	336	8	330	190	98
Z_Plesovice_10	783	82	0.10	0.402	0.042	0.0539	0.0013	0.05	339	30	338	8	311	190	100
Z_Plesovice_11	671	70	0.10	0.378	0.041	0.0534	0.0014	0.09	324	31	336	9	200	190	104
Z_Plesovice_12	843	98	0.12	0.420	0.044	0.0543	0.0014	0.12	352	32	341	8	385	190	97
Z_Plesovice_13	897	96	0.11	0.403	0.042	0.0536	0.0013	0.16	342	31	337	8	325	190	98
Z_Plesovice_14	657	66	0.10	0.368	0.041	0.0539	0.0014	0.09	314	30	338	8	90	190	108
Z_Plesovice_15	792	82	0.10	0.397	0.041	0.0537	0.0014	0.29	337	30	337	8	284	190	100
Z_Plesovice_16	805	82	0.10	0.38	0.04	0.0540	0.0013	0.23	318	30	339	8	143	190	107
Z_Plesovice_17	800	81	0.10	0.39	0.04	0.0528	0.0012	0.04	331	30	332	8	262	190	100
Z_Plesovice_18	755	78	0.10	0.389	0.041	0.0539	0.0013	0.01	331	29	338	8	210	190	102
Z_Plesovice_19	758	77	0.10	0.38	0.04	0.0530	0.0013	0.01	322	30	333	8	193	190	103
Z_Plesovice_20	752	80	0.11	0.448	0.047	0.0550	0.0013	0.21	372	32	345	8	464	190	93
Z_Plesovice_21	733	75	0.10	0.396	0.042	0.0535	0.0013	0.11	335	30	336	8	260	190	100
Z_Plesovice_1	762	80	0.11	0.391	0.017	0.0538	0.0017	0.06	332	13	338	10	205	93	102

Z_Plesovice_2	755	79	0.10	0.403	0.017	0.0535	0.0017	0.07	340	12	336	10	300	90	99
Z_Plesovice_3	728	75	0.10	0.395	0.018	0.0539	0.0017	0.01	334	13	338	10	238	95	101
Z_Plesovice_4	752	77	0.10	0.393	0.019	0.0536	0.0016	0.15	332	14	337	10	270	99	101
Z_Plesovice_5	710	71	0.10	0.393	0.019	0.0536	0.0017	0.11	332	14	336	10	310	100	101
Z_Plesovice_6	779	80	0.10	0.385	0.017	0.0537	0.0016	0.05	328	13	337	10	234	98	103
Z_Plesovice_7	764	79	0.10	0.394	0.018	0.0537	0.0017	0.25	335	13	337	10	268	95	101
Z_Plesovice_8	771	80	0.10	0.392	0.017	0.0533	0.0016	0.14	332	12	335	10	242	88	101
Z_Plesovice_9	733	76	0.10	0.395	0.017	0.0544	0.0017	0.21	336	12	342	10	238	89	102
Z_Plesovice_10	795	84	0.11	0.396	0.016	0.0535	0.0017	0.12	337	12	337	10	326	87	100
Z_Plesovice_11	732	74	0.10	0.386	0.018	0.0533	0.0017	0.10	328	13	335	10	254	96	102
Z_Plesovice_12	739	77	0.10	0.405	0.018	0.0540	0.0016	0.10	341	13	339	10	289	98	99
Z_Plesovice_13	731	76	0.10	0.387	0.018	0.0535	0.0016	0.18	328	13	336	10	218	94	102
Z_Plesovice_14	760	79	0.10	0.392	0.017	0.0538	0.0016	0.16	332	13	338	10	236	91	102
Z_Plesovice_15	754	78	0.10	0.404	0.019	0.0534	0.0016	0.08	340	14	335	10	311	98	99
Z_Plesovice_16	770	80	0.10	0.394	0.016	0.0538	0.0017	0.10	337	12	338	10	294	91	100
Z_Plesovice_1	718	74	0.10	0.417	0.018	0.0539	0.0011	0.25	353	13	338	7	443	100	96
Z_Plesovice_2	715	73	0.10	0.397	0.018	0.0542	0.0011	0.31	339	13	340	7	319	100	100
Z_Plesovice_3	753	78	0.10	0.384	0.018	0.0532	0.0011	0.22	329	13	334	7	275	100	102
Z_Plesovice_4	777	81	0.10	0.383	0.017	0.0535	0.0011	0.26	328	13	336	7	260	100	102
Z_Plesovice_5	773	81	0.10	0.386	0.017	0.0540	0.0011	0.24	331	13	339	7	250	100	102
Z_Plesovice_6	742	76	0.10	0.389	0.017	0.0536	0.0011	0.28	333	13	337	7	293	100	101
Z_Plesovice_7	778	81	0.10	0.396	0.018	0.0537	0.0011	0.24	339	13	337	7	327	100	100
Z_Plesovice_8	737	75	0.10	0.392	0.018	0.0535	0.0011	0.17	336	13	336	7	316	100	100
Z_Plesovice_9	777	81	0.10	0.401	0.018	0.0542	0.0011	0.09	341	13	340	7	323	100	100
Z_Plesovice_10	739	75	0.10	0.387	0.017	0.0529	0.0011	0.21	331	13	332	7	303	100	100
Z_Plesovice_11	738	75	0.10	0.392	0.018	0.0536	0.0011	0.23	335	13	336	7	295	98	100
Z_Plesovice_12	746	76	0.10	0.397	0.018	0.0543	0.0011	0.19	340	13	341	7	295	100	100
Z_Plesovice_13	765	79	0.10	0.406	0.019	0.0534	0.0011	0.28	345	13	335	7	376	100	97
Z_Plesovice_14	767	78	0.10	0.395	0.018	0.0540	0.0011	0.28	337	13	339	7	297	100	100

Z_Plesovice_15	737	74	0.10	0.390	0.017	0.0536	0.0011	0.13	334	13	337	7	305	100	101
Z_Plesovice_16	785	93	0.12	0.413	0.019	0.0531	0.0011	0.19	350	13	334	7	460	100	95
Z_Plesovice_17	768	78	0.10	0.387	0.018	0.0538	0.0011	0.25	331	13	338	7	280	100	102
Z_Plesovice_18	734	73	0.10	0.394	0.018	0.0542	0.0011	0.15	336	13	340	7	291	100	101
Z_Plesovice_19	780	79	0.10	0.386	0.018	0.0534	0.0011	0.22	330	13	335	7	283	100	102
Z_Plesovice_20	749	76	0.10	0.391	0.018	0.0538	0.0011	0.19	334	13	338	7	294	100	101
Z_Plesovice_21	758	78	0.10	0.393	0.017	0.0538	0.0011	0.14	336	13	338	7	302	100	101
Z_Plesovice_22	746	76	0.10	0.400	0.018	0.0535	0.0011	0.18	340	13	336	7	345	100	99
Z_Plesovice_1	779	81	0.10	0.394	0.014	0.05422	0.00087	0.26	337	10	340	5	301	70	101
Z_Plesovice_2	733	75	0.10	0.391	0.014	0.0538	0.0009	0.17	335	10	337	6	295	73	101
Z_Plesovice_3	746	76	0.10	0.394	0.014	0.05358	0.00088	0.22	336	10	336	5	307	71	100
Z_Plesovice_4	803	85	0.11	0.392	0.014	0.05337	0.00086	0.31	335	10	335	5	319	68	100
Z_Plesovice_5	765	79	0.10	0.397	0.014	0.0540	0.0009	0.18	340	10	339	6	320	70	100
Z_Plesovice_6	738	77	0.10	0.410	0.014	0.05358	0.00088	0.26	348	10	336	5	413	69	97
Z_Plesovice_7	761	78	0.10	0.388	0.014	0.05325	0.00089	0.21	332	10	334	5	301	72	101
Z_Plesovice_8	737	77	0.10	0.386	0.014	0.05281	0.00087	0.27	331	10	332	5	306	70	100
Z_Plesovice_9	758	79	0.10	0.387	0.014	0.0539	0.0009	0.16	331	10	338	6	275	70	102
Z_Plesovice_10	724	75	0.10	0.394	0.014	0.0540	0.0009	0.23	337	10	339	6	310	70	101
Z_Plesovice_11	786	83	0.11	0.399	0.014	0.05411	0.00088	0.28	340	10	340	5	330	67	100
Z_Plesovice_12	748	77	0.10	0.388	0.014	0.05362	0.00091	0.26	332	10	337	6	288	70	101
Z_Plesovice_13	774	78	0.10	0.394	0.014	0.05367	0.00086	0.31	336	10	337	5	316	67	100
Z_Plesovice_14	771	78	0.10	0.393	0.014	0.05387	0.00087	0.16	335	10	338	5	295	71	101
Z_Plesovice_15	768	79	0.10	0.391	0.014	0.05304	0.00087	0.37	334	10	333	5	320	68	100
Z_Plesovice_16	764	80	0.10	0.407	0.014	0.05393	0.00088	0.33	346	10	339	5	376	69	98
Z_Plesovice_17	720	74	0.10	0.396	0.014	0.05377	0.00086	0.23	339	10	338	5	324	72	100
Z_Plesovice_18	777	81	0.10	0.394	0.014	0.05409	0.00089	0.21	337	10	340	5	303	72	101
Z_Plesovice_19	758	78	0.10	0.389	0.014	0.05322	0.00087	0.24	333	10	334	5	297	72	100
Z_Plesovice_20	773	80	0.10	0.394	0.014	0.05389	0.00088	0.31	337	10	338	5	307	69	100
Z_Plesovice_1	750	78	0.10	0.391	0.015	0.05383	0.00075	0.02	332	11	338	5	253	81	102

Z_Plesovice_3	760	79	0.10	0.398	0.015	0.05372	0.00077	0.06	337	11	337	5	294	83	100
Z_Plesovice_4	747	77	0.10	0.390	0.016	0.05346	0.00073	0.16	331	11	336	5	255	84	101
Z_Plesovice_5	755	78	0.10	0.394	0.015	0.05363	0.00076	0.18	334	11	337	5	279	81	101
Z_Plesovice_8	755	78	0.10	0.394	0.016	0.05364	0.00084	0.18	334	12	337	5	272	88	101
Z_Plesovice_11	755	78	0.10	0.394	0.014	0.0537	0.0008	0.17	334	10	337	5	281	77	101
Z_Plesovice_12	755	78	0.10	0.394	0.015	0.05374	0.00068	0.23	335	11	337	4	296	80	101
Z_Plesovice_14	754	78	0.10	0.393	0.016	0.05359	0.00078	0.13	335	12	337	5	284	87	100
Z_Plesovice_15	756	78	0.10	0.394	0.018	0.05371	0.00078	0.12	333	13	337	5	260	94	101
Z_Plesovice_2	763	79	0.10	0.398	0.015	0.05369	0.00077	0.07	337	11	337	5	296	83	100
Z_Plesovice_6	755	78	0.10	0.394	0.014	0.05375	0.00069	0.21	336	10	338	4	282	74	101
Z_Plesovice_7	755	78	0.10	0.394	0.014	0.05375	0.00069	0.21	336	10	338	4	282	74	101
Z_Plesovice_9	754	78	0.10	0.394	0.016	0.05365	0.00084	0.18	334	12	337	5	271	88	101
Z_Plesovice_10	755	78	0.10	0.394	0.014	0.0537	0.0008	0.17	334	10	337	5	281	77	101
Z_Plesovice_13	756	78	0.10	0.395	0.015	0.05370	0.00069	0.23	336	11	337	4	299	80	100
Z_Plesovice_16	754	78	0.10	0.394	0.018	0.05367	0.00078	0.12	333	13	337	5	256	94	101
Z_Plesovice_1	731	74	0.10	0.392	0.033	0.0530	0.0013	0.16	333	24	333	8	299	180	100
Z_Plesovice_2	767	79	0.10	0.374	0.032	0.0542	0.0013	0.10	320	23	340	8	167	180	106
Z_Plesovice_3	781	82	0.10	0.403	0.034	0.0539	0.0012	0.03	341	25	338	8	313	180	99
Z_Plesovice_4	755	79	0.10	0.398	0.034	0.0538	0.0013	0.12	338	24	338	8	312	180	100
Z_Plesovice_5	773	87	0.11	0.406	0.034	0.0536	0.0013	0.11	343	24	337	8	352	180	98
Z_Plesovice_6	755	77	0.10	0.406	0.034	0.0542	0.0013	0.22	343	24	340	8	322	180	99
Z_Plesovice_7	784	83	0.11	0.385	0.033	0.0533	0.0013	0.16	327	24	335	8	237	180	102
Z_Plesovice_8	710	71	0.10	0.393	0.034	0.0542	0.0013	0.15	334	25	340	8	247	180	102
Z_Plesovice_9	742	77	0.10	0.394	0.034	0.0540	0.0013	0.07	335	24	339	8	266	180	101
Z_Plesovice_10	756	78	0.10	0.386	0.032	0.0522	0.0012	0.09	330	24	328	8	295	180	99
Z_Plesovice_11	736	75	0.10	0.425	0.036	0.0537	0.0013	0.09	356	26	337	8	432	180	95
Z_Plesovice_12	759	78	0.10	0.377	0.032	0.0533	0.0013	0.07	322	24	335	8	218	180	104
Z_Plesovice_13	812	86	0.11	0.403	0.034	0.0544	0.0013	0.21	342	25	342	8	285	180	100
Z_Plesovice_14	716	72	0.10	0.377	0.033	0.0537	0.0013	0.11	322	24	337	8	176	180	105

Z_Plesovice_15	781	83	0.11	0.398	0.033	0.0537	0.0013	0.02	339	25	337	8	300	180	99
Z_Plesovice_1	752	78	0.10	0.386	0.016	0.0542	0.0013	0.07	328	12	340	8	183	93	104
Z_Plesovice_2	811	83	0.10	0.403	0.016	0.0533	0.0013	0.16	341	12	334	8	304	92	98
Z_Plesovice_3	738	76	0.10	0.394	0.015	0.0536	0.0013	0.06	334	11	336	8	288	90	101
Z_Plesovice_4	752	78	0.10	0.392	0.017	0.0537	0.0013	0.30	332	13	337	8	221	92	101
Z_Plesovice_5	753	77	0.10	0.396	0.016	0.0538	0.0013	0.27	335	12	338	8	297	89	101
Z_Plesovice_6	778	81	0.10	0.394	0.015	0.0536	0.0013	0.18	334	11	336	8	334	86	101
Z_Plesovice_7	792	84	0.11	0.395	0.016	0.0540	0.0013	0.08	335	12	339	8	314	95	101
Z_Plesovice_8	699	70	0.10	0.394	0.016	0.0533	0.0012	0.12	335	12	335	8	307	91	100
Z_Plesovice_9	820	85	0.10	0.392	0.016	0.0539	0.0013	0.20	334	12	338	8	233	87	101
Z_Plesovice_10	722	73	0.10	0.395	0.017	0.0537	0.0013	0.20	336	12	337	8	308	93	100
Z_Plesovice_11	770	86	0.11	0.395	0.016	0.0536	0.0013	0.09	336	12	337	8	363	90	100
Z_Plesovice_12	749	75	0.10	0.392	0.016	0.0537	0.0013	0.08	333	12	337	8	263	91	101
Z_Plesovice_13	752	77	0.10	0.396	0.016	0.0536	0.0013	0.04	335	12	336	8	266	93	100
Z_Plesovice_14	829	86	0.10	0.393	0.016	0.0540	0.0013	0.05	333	11	339	8	241	90	102
Z_Plesovice_15	698	70	0.10	0.395	0.017	0.0534	0.0013	0.11	335	13	335	8	287	97	100
Z_Plesovice_16	763	79	0.10	0.391	0.016	0.0533	0.0013	0.18	331	12	335	8	248	91	101
Z_Plesovice_17	827	88	0.11	0.397	0.017	0.0542	0.0013	0.25	337	13	340	8	246	94	101

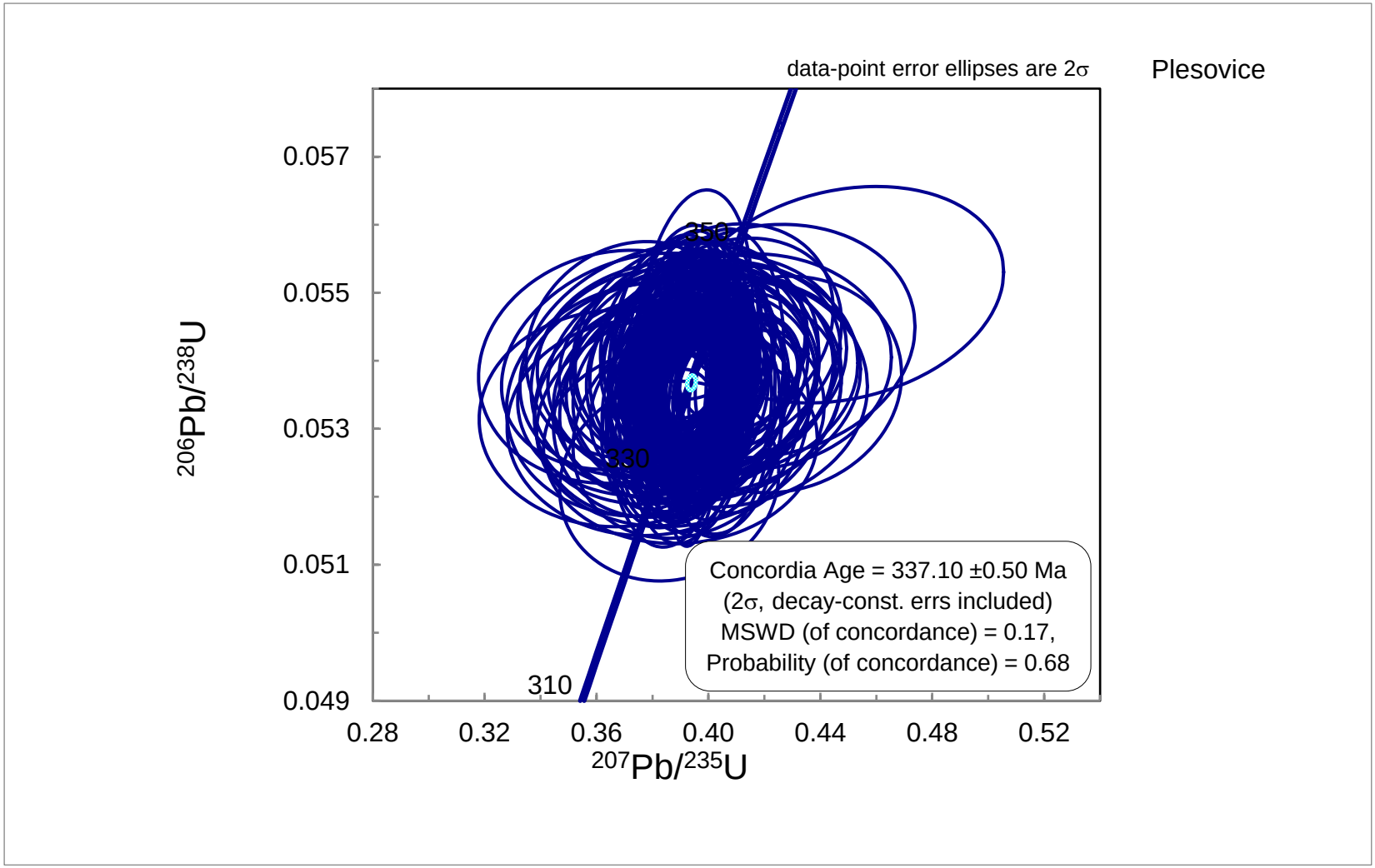
data-point error ellipses are 2σ
Plesovice
0.057
0.055
0.053
0.051
0.049
350
330
310
Concordia Age = 337.10 ±0.50 Ma
(2σ, decay-const. errs included)
MSWD (of concordance) = 0.17,
Probability (of concordance) = 0.68
0.28
0.32
0.36
0.40
0.44
0.48
0.52
206Pb/238U
207Pb/235U

Appendix B3: U-Pb ages and ratios of the zircon secondary standard (91500)

Zircon secondary standard				Common-lead uncorrected ratios					Final Ages (Ma)						
Id	U (ppm)	Th (ppm)	Th/U	$^{207}Pb/^{235}U$	±2σ	$^{206}Pb/^{238}U$	±2σ	Rho	$^{207}Pb/^{235}U$	±2σ	$^{206}Pb/^{238}U$	±2σ	$^{207}Pb/^{206}Pb$	±2σ	Concord-ance (%)
91500	117	51	0.44	1.804	0.087	0.1786	0.0028	0.17	1035	32	1060	16	922	92	102
91500	86	33	0.38	1.792	0.087	0.1791	0.0029	0.26	1041	32	1062	16	983	91	102
91500	85	31	0.37	1.790	0.083	0.1779	0.0029	0.07	1034	30	1055	16	1008	90	102
91500	96	39	0.40	1.833	0.088	0.1805	0.0027	0.19	1046	31	1069	15	1005	90	102
91500	111	47	0.43	1.782	0.085	0.1786	0.0027	0.27	1031	31	1059	15	977	89	103
91500	93	37	0.40	1.853	0.088	0.1794	0.0027	0.18	1057	31	1064	15	1017	88	101
91500	112	48	0.43	1.936	0.097	0.1803	0.0034	0.94	1065	25	1068	18	1019	75	100
91500	119	52	0.44	1.858	0.063	0.178	0.003	0.16	1061	23	1057	17	1042	66	100
91500	123	53	0.43	1.79	0.06	0.1786	0.0027	0.07	1036	23	1059	15	949	66	102
91500	106	49	0.46	1.913	0.066	0.180	0.003	0.09	1076	23	1064	16	1082	64	99
91500	109	49	0.45	1.894	0.077	0.1801	0.0029	0.03	1062	22	1067	16	1019	63	100
91500	117	51	0.44	1.842	0.065	0.1755	0.0031	0.32	1053	23	1041	17	1064	63	99
91500	117	51	0.44	1.892	0.063	0.1812	0.0029	0.28	1070	22	1073	16	1059	56	100
91500	87	31	0.35	1.82	0.05	0.176	0.003	0.28	1046	18	1045	17	1037	56	100
91500	87	34	0.39	1.826	0.055	0.177	0.003	0.16	1050	20	1053	16	1037	60	100
91500	92	38	0.42	1.836	0.055	0.1802	0.0029	0.25	1049	20	1069	16	1017	55	102
91500	85	31	0.37	1.857	0.052	0.181	0.003	0.28	1061	19	1071	16	1015	55	101
91500	85	30	0.35	1.839	0.048	0.1773	0.0031	0.14	1056	17	1053	17	1044	56	100
91500	88	36	0.41	1.808	0.052	0.179	0.003	0.16	1040	19	1058	16	988	61	102
91500	91	36	0.39	1.827	0.051	0.178	0.003	0.26	1048	19	1056	17	1003	55	101
91500	87	34	0.39	1.832	0.054	0.1763	0.0031	0.22	1050	20	1046	17	1040	61	100
91500	109	44	0.41	1.87	0.21	0.1784	0.0054	0.14	1037	75	1056	29	890	210	102
91500	113	48	0.42	1.84	0.21	0.178	0.005	0.20	1025	79	1054	27	880	220	103
91500	107	45	0.42	1.78	0.21	0.1783	0.0054	0.16	1005	77	1058	30	790	220	105
91500	105	44	0.42	1.8	0.2	0.1772	0.0054	0.16	1005	74	1052	29	840	210	105

91500	100	40	0.40	1.81	0.21	0.1810	0.0052	0.03	1009	80	1070	28	770	230	106
91500	89	35	0.40	1.84	0.21	0.1838	0.0058	0.19	1028	77	1085	31	810	220	106
91500	92	38	0.42	1.8	0.1	0.1760	0.0062	0.16	1000	40	1043	34	800	130	104
91500	90	35	0.39	1.78	0.11	0.1802	0.0067	0.24	1003	41	1068	37	820	130	106
91500	87	34	0.39	1.77	0.12	0.180	0.007	0.10	988	47	1066	38	760	150	108
91500	96	38	0.40	1.75	0.11	0.1749	0.0059	0.06	1002	43	1037	33	820	140	103
91500	89	35	0.40	1.88	0.11	0.1776	0.0062	0.10	1031	41	1054	34	890	130	102
91500	87	35	0.40	1.94	0.12	0.1828	0.0062	0.06	1058	42	1083	35	910	130	102
91500	76	30	0.39	1.87	0.09	0.1853	0.0042	0.12	1065	33	1095	23	989	100	103
91500	79	31	0.39	1.840	0.093	0.177	0.004	0.11	1054	32	1052	22	1026	110	100
91500	80	31	0.39	1.839	0.095	0.180	0.004	0.15	1052	33	1069	22	993	110	102
91500	79	30	0.38	1.816	0.092	0.178	0.004	0.23	1041	34	1057	21	979	110	102
91500	76	28	0.38	1.83	0.09	0.179	0.004	0.18	1050	32	1058	22	1015	110	101
91500	78	29	0.38	1.783	0.093	0.1786	0.0042	0.12	1034	33	1058	23	958	110	102
91500	93	38	0.41	1.908	0.096	0.1732	0.0035	0.16	1056	35	1028	19	1030	110	97
91500	79	30	0.38	1.808	0.093	0.1781	0.0039	0.13	1030	34	1055	21	910	110	102
91500	84	33	0.39	1.79	0.16	0.1773	0.0049	0.04	1018	61	1050	27	890	200	103
91500	78	30	0.38	1.78	0.17	0.1804	0.0054	0.12	1008	63	1067	29	810	210	106
91500	84	33	0.39	1.85	0.17	0.1790	0.0052	0.02	1037	63	1060	28	920	200	102
91500	78	30	0.39	1.95	0.19	0.1802	0.0052	0.12	1052	69	1066	28	930	210	101
91500	91	35	0.38	1.86	0.12	0.1768	0.0053	0.14	1037	42	1047	29	910	140	101
91500	85	33	0.39	1.667	0.091	0.1767	0.0052	0.17	980	36	1047	28	810	120	107
91500	79	30	0.38	1.74	0.12	0.1703	0.0054	0.13	988	45	1011	29	890	150	102
91500	73	26	0.36	1.83	0.12	0.1779	0.0054	0.14	1016	45	1053	29	830	140	104
91500	84	33	0.39	1.82	0.12	0.1758	0.0055	0.21	1016	46	1042	30	850	140	103

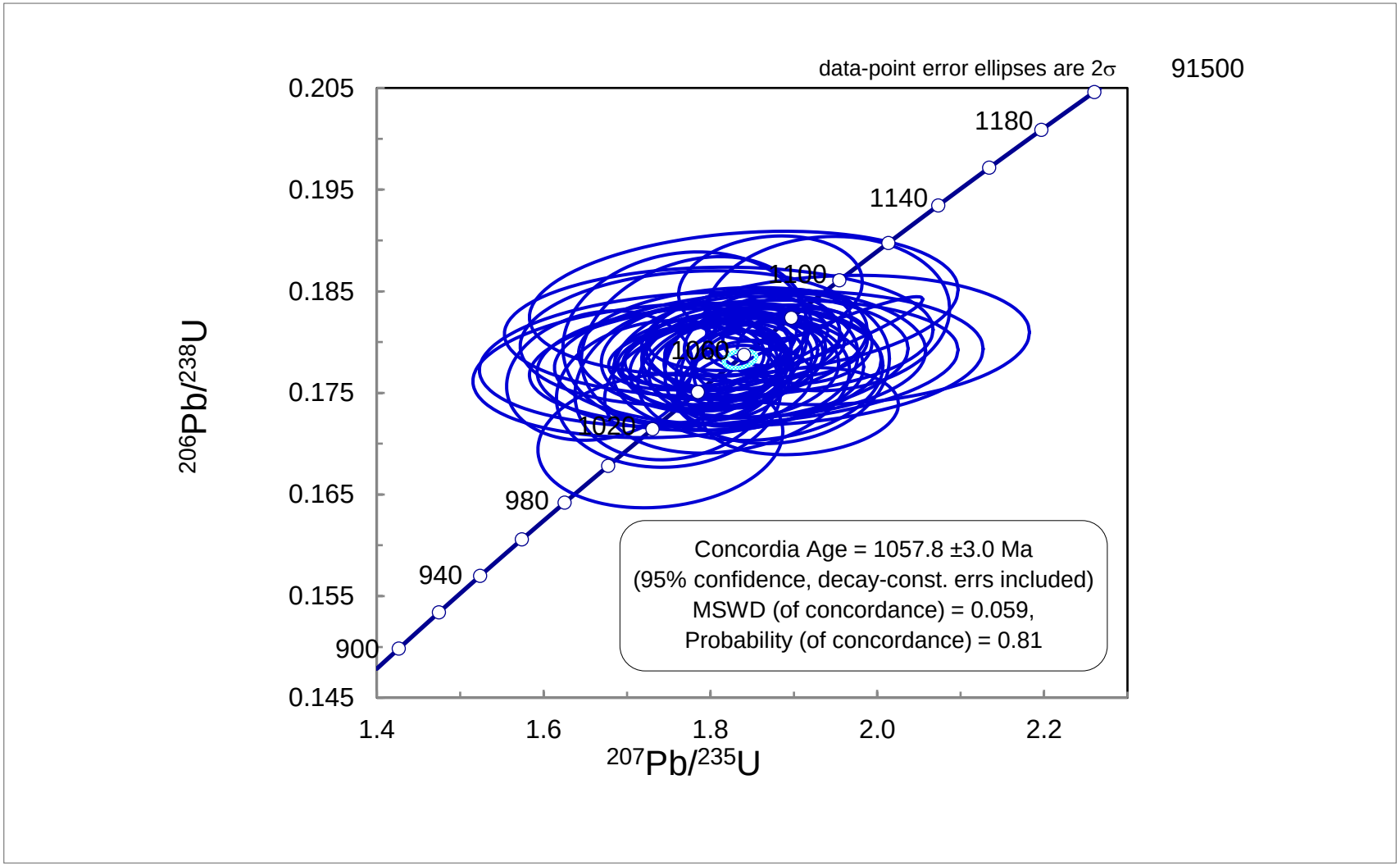
data-point error ellipses are 2σ
91500
0.205
0.195
0.185
0.175
0.165
0.155
0.145
1180
1140
1100
1060
1020
980
940
900
1.4
1.6
1.8
2.0
2.2
206Pb/238U
207Pb/235U
Concordia Age = 1057.8 ±3.0 Ma
(95% confidence, decay-const. errs included)
MSWD (of concordance) = 0.059,
Probability (of concordance) = 0.81

Appendix B4: U-Pb ages and ratios of the zircon secondary standard (GJ-1)

Zircon secondary standard				Common-lead uncorrected ratios					Final Ages (Ma)						
Id	U (ppm)	Th (ppm)	Th/U	$^{207}Pb/^{235}U$	±2σ	$^{206}Pb/^{238}U$	±2σ	Rho	$^{207}Pb/^{235}U$	±2σ	$^{206}Pb/^{238}U$	±2σ	$^{207}Pb/^{206}Pb$	±2σ	Concord-ance (%)
GJ1	412	14	0.03	0.792	0.034	0.0969	0.0012	0.10	590	19	596	7	552	86	101
GJ1	441	15	0.03	0.796	0.034	0.0984	0.0013	0.14	593	20	605	8	549	86	102
GJ1	469	17	0.04	0.788	0.034	0.0959	0.0013	0.29	587	19	590	8	558	84	101
GJ1	484	17	0.04	0.795	0.034	0.0955	0.0013	0.29	593	19	588	7	554	79	99
GJ1	469	16	0.04	0.789	0.033	0.0958	0.0014	0.26	589	19	590	8	501	80	100
GJ1	377	12	0.03	0.785	0.033	0.0958	0.0012	0.26	586	19	590	7	576	83	101
GJ1	385	12	0.03	0.787	0.033	0.0987	0.0013	0.06	588	19	607	8	537	83	103
GJ1	461	16	0.03	0.783	0.033	0.0969	0.0013	0.26	585	19	596	8	558	80	102
GJ1	448	16	0.04	0.782	0.033	0.0974	0.0012	0.15	586	19	599	7	541	83	102
GJ1	388	12	0.03	0.810	0.034	0.0981	0.0012	0.15	601	19	603	7	566	83	100
GJ1	374	12	0.03	0.815	0.034	0.0986	0.0012	0.26	603	19	606	7	584	77	101
GJ1	375	12	0.03	0.805	0.034	0.0975	0.0013	0.20	599	19	600	8	583	79	100
GJ1	376	12	0.03	0.820	0.034	0.0977	0.0013	0.24	606	19	601	8	596	79	99
GJ1	437	15	0.03	0.780	0.021	0.0969	0.0014	0.12	584	12	596	8	515	50	102
GJ1	495	18	0.04	0.800	0.022	0.0967	0.0014	0.24	595	12	595	8	571	50	100
GJ1	521	19	0.04	0.805	0.022	0.0972	0.0014	0.29	599	12	598	8	582	49	100
GJ1	521	18	0.03	0.807	0.022	0.0967	0.0014	0.16	599	13	595	8	588	53	99
GJ1	457	17	0.04	0.791	0.021	0.0952	0.0014	0.21	590	12	586	8	586	50	99
GJ1	373	12	0.03	0.796	0.019	0.0958	0.0014	0.30	593	11	590	8	591	46	99
GJ1	360	11	0.03	0.811	0.019	0.0977	0.0015	0.19	602	11	601	9	597	50	100
GJ1	374	12	0.03	0.791	0.017	0.0966	0.0014	0.37	591	10	594	8	570	40	101
GJ1	381	13	0.03	0.805	0.018	0.0972	0.0014	0.27	598	10	598	8	575	47	100
GJ1	356	10	0.03	0.793	0.017	0.0962	0.0014	0.07	591	10	592	8	571	46	100
GJ1	359	11	0.03	0.805	0.018	0.0968	0.0014	0.17	598	10	596	8	592	44	100
GJ1	369	12	0.03	0.784	0.017	0.0955	0.0013	0.25	587	10	588	8	573	43	100

GJ1	349	11	0.03	0.795	0.017	0.0967	0.0022	0.32	592	10	595	13	593	73	101
GJ1	357	12	0.03	0.781	0.017	0.0966	0.0021	0.23	584	10	594	13	543	76	102
GJ1	380	12	0.03	0.810	0.015	0.0963	0.0021	0.26	600	9	593	13	601	72	99
GJ1	419	14	0.03	0.805	0.016	0.0967	0.0021	0.22	599	9	595	12	569	74	99
GJ1	384	13	0.03	0.820	0.017	0.0973	0.0022	0.20	607	10	599	13	619	77	99
GJ1	374	12	0.03	0.797	0.016	0.0962	0.0021	0.29	594	9	592	12	593	73	100
GJ1	344	11	0.03	0.799	0.018	0.0959	0.0022	0.27	594	10	590	13	594	77	99
GJ1	349	11	0.03	0.784	0.015	0.0969	0.0022	0.26	586	9	596	13	548	74	102
GJ1	336	11	0.03	0.790	0.017	0.0976	0.0022	0.25	591	10	600	13	557	75	102
GJ1	454	15	0.03	0.818	0.084	0.0965	0.0023	0.13	600	47	594	14	558	190	99
GJ1	494	17	0.03	0.790	0.082	0.0961	0.0023	0.02	589	48	591	14	516	190	100
GJ1	489	17	0.03	0.814	0.085	0.0978	0.0025	0.16	595	49	601	15	549	200	101
GJ1	450	15	0.03	0.804	0.084	0.0951	0.0024	0.18	592	47	585	14	552	200	99
GJ1	422	14	0.03	0.807	0.085	0.0977	0.0024	0.24	590	48	601	14	472	200	102
GJ1	368	12	0.03	0.806	0.087	0.1001	0.0025	0.12	590	49	614	15	420	190	104
GJ1	365	12	0.03	0.849	0.035	0.098	0.003	0.08	614	20	600	18	577	95	98
GJ1	378	12	0.03	0.824	0.035	0.0995	0.0032	0.04	601	19	611	19	551	92	102
GJ1	368	12	0.03	0.811	0.034	0.0977	0.0031	0.06	600	19	601	18	540	94	100
GJ1	380	12	0.03	0.782	0.035	0.0962	0.0029	0.19	577	20	592	17	446	94	103
GJ1	360	12	0.03	0.835	0.037	0.097	0.003	0.13	606	21	597	18	561	98	98
GJ1	358	12	0.03	0.824	0.042	0.0966	0.0031	0.10	599	23	594	18	540	110	99
GJ1	337	11	0.03	0.790	0.036	0.097	0.002	0.09	589	20	595	12	555	110	101
GJ1	324	10	0.03	0.802	0.037	0.098	0.002	0.19	597	21	605	12	534	100	101
GJ1	338	11	0.03	0.798	0.037	0.0980	0.0021	0.27	593	21	602	12	549	98	102
GJ1	334	10	0.03	0.798	0.036	0.096	0.002	0.26	593	21	592	12	568	100	100
GJ1	325	10	0.03	0.783	0.036	0.098	0.002	0.18	584	21	605	12	499	100	104
GJ1	322	10	0.03	0.796	0.037	0.096	0.002	0.17	591	21	593	12	560	100	100
GJ1	319	10	0.03	0.81	0.03	0.0977	0.0016	0.30	600	17	601	9	569	72	100
GJ1	315	10	0.03	0.82	0.03	0.0970	0.0016	0.12	605	17	597	10	616	72	99

GJ1	310	10	0.03	0.786	0.029	0.0964	0.0016	0.18	587	16	593	9	536	71	101
GJ1	322	10	0.03	0.80	0.03	0.0969	0.0016	0.16	595	17	596	10	572	74	100
GJ1	308	9	0.03	0.812	0.031	0.0966	0.0016	0.19	601	17	594	10	598	75	99
GJ1	325	10	0.03	0.800	0.029	0.0969	0.0016	0.24	595	16	596	9	566	71	100
GJ1	381	12	0.03	0.818	0.033	0.0962	0.0015	0.04	600	18	592	9	570	84	99
GJ1	325	10	0.03	0.745	0.032	0.0953	0.0017	0.07	564	19	586	10	416	96	104
GJ1	352	11	0.03	0.790	0.066	0.0948	0.0023	0.08	585	38	583	14	548	180	100
GJ1	325	10	0.03	0.801	0.068	0.0976	0.0024	0.13	589	38	600	14	492	180	102
GJ1	357	11	0.03	0.825	0.072	0.0965	0.0024	0.20	602	40	594	14	573	190	99
GJ1	339	11	0.03	0.802	0.069	0.0964	0.0025	0.05	591	39	593	15	525	190	100
GJ1	396	13	0.03	0.818	0.036	0.0957	0.0024	0.18	599	20	589	14	573	99	98
GJ1	369	12	0.03	0.782	0.038	0.0969	0.0024	0.22	575	22	596	14	490	100	104
GJ1	366	12	0.03	0.749	0.033	0.0957	0.0024	0.10	561	19	589	14	468	100	105
GJ1	375	12	0.03	0.81	0.03	0.0968	0.0024	0.06	598	17	595	14	542	92	100
GJ1	390	13	0.03	0.766	0.033	0.0978	0.0025	0.06	568	19	601	15	388	99	106

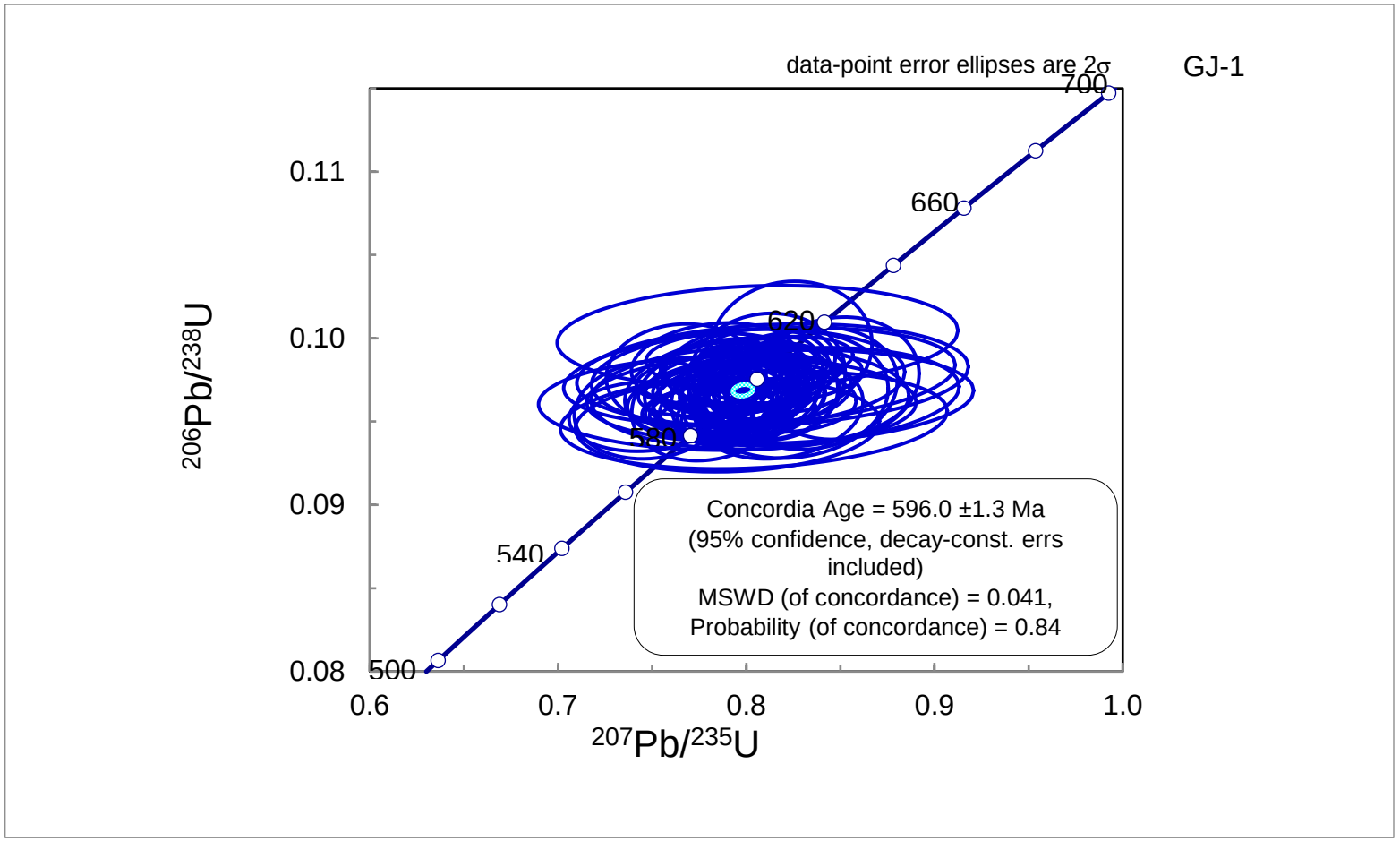
data-point error ellipses are 2σ
GJ-1
700
660
620
580
540
500
0.11
0.10
0.09
0.08
0.6
0.7
0.8
0.9
1.0
206Pb/238U
207Pb/235U
Concordia Age = 596.0 ±1.3 Ma
(95% confidence, decay-const. errs included)
MSWD (of concordance) = 0.041,
Probability (of concordance) = 0.84

Appendix B5: U-Pb ages and ratios of the apatite primary standard (Madagascar)

Apatite primary standard	207Pb-based DRS common-Pb correction										Final Ages (Ma)				
Id	$^{207}Pb/^{235}U$	±2σ	$^{206}Pb/^{238}U$	±2σ	Rho	$^{238}U/^{206}Pb$	±2σ	$^{207}Pb/^{206}Pb$	±2σ	Rho	$^{207}Pb/^{235}U$	±2σ	$^{206}Pb/^{238}U$	±2σ	Con-cordance (%)
A_MAD_JD_1	0.603	0.014	0.0764	0.0018	1.00	13.08901	0.30838	0.057196	0.0000000003	0.0305	478	9	475	11	99
A_MAD_JD_2	0.607	0.014	0.0770	0.0018	1.00	12.98533	0.303514	0.057196	0.0000000003	0.0755	482	9	478	11	99
A_MAD_JD_3	0.608	0.014	0.0771	0.0018	1.00	12.96849	0.302727	0.057196	0.0000000003	0.0418	482	9	479	11	99
A_MAD_JD_4	0.595	0.014	0.0754	0.0017	1.00	13.26436	0.299104	0.057196	0.0000000003	0.0329	473	9	469	10	99
A_MAD_JD_5	0.594	0.014	0.0754	0.0017	1.00	13.2714	0.299421	0.057196	0.0000000003	0.0118	473	9	468	10	99
A_MAD_JD_6	0.611	0.014	0.0775	0.0018	1.00	12.90656	0.299843	0.057196	0.0000000003	0.0554	484	9	481	11	99
A_MAD_JD_7	0.594	0.014	0.0753	0.0017	1.00	13.28021	0.299819	0.057196	0.0000000003	0.1115	473	9	468	10	99
A_MAD_JD_8	0.594	0.014	0.0754	0.0017	1.00	13.26964	0.299342	0.057196	0.0000000003	0.0687	474	9	468	10	99
A_MAD_JD_9	0.609	0.014	0.0772	0.0018	1.00	12.95337	0.302022	0.057196	0.0000000003	0.0072	482	9	479	11	99
A_MAD_JD_10	0.602	0.014	0.0763	0.0018	1.00	13.1096	0.309351	0.057196	0.0000000003	0.0089	478	9	474	11	99
A_MAD_JD_11	0.594	0.014	0.0753	0.0017	1.00	13.28198	0.299899	0.057196	0.0000000003	0.0160	473	9	468	10	99
A_MAD_JD_12	0.602	0.014	0.0764	0.0018	1.00	13.09415	0.308622	0.057196	0.0000000003	0.0535	478	9	474	11	99
A_MAD_JD_13	0.609	0.014	0.0772	0.0018	1.00	12.94834	0.301787	0.057196	0.0000000003	0.0080	483	9	480	11	99
A_MAD_JD_14	0.606	0.014	0.0769	0.0018	1.00	13.0107	0.3047	0.057196	0.0000000003	0.0997	481	9	477	11	99
A_MAD_JD_15	0.603	0.014	0.0765	0.0018	1.00	13.07531	0.307735	0.057196	0.0000000003	0.0010	479	9	475	11	99
A_MAD_JD_16	0.604	0.014	0.0766	0.0018	1.00	13.05313	0.306691	0.057196	0.0000000003	0.0262	480	9	476	11	99
A_MAD_JD_17	0.589	0.014	0.0747	0.0017	1.00	13.39585	0.305063	0.057196	0.0000000003	0.0388	470	9	464	10	99
A_MAD_JD_18	0.600	0.014	0.0761	0.0018	1.00	13.13543	0.310571	0.057196	0.0000000003	0.0192	477	9	473	11	99
A_MAD_JD_19	0.599	0.014	0.0759	0.0018	1.00	13.17176	0.312292	0.057196	0.0000000003	0.0117	476	9	472	11	99
A_MAD_JD_20	0.604	0.014	0.0765	0.0018	1.00	13.06506	0.307253	0.057196	0.0000000003	0.1002	479	9	475	11	99
A_MAD_JD_21	0.613	0.014	0.0777	0.0018	1.00	12.86339	0.29784	0.057196	0.0000000003	0.0114	485	9	483	11	99
A_MAD_JD_22	0.595	0.014	0.0755	0.0018	1.00	13.24679	0.315859	0.057196	0.0000000003	0.0548	474	9	469	11	99
A_MAD_JD_23	0.600	0.014	0.0761	0.0018	1.00	13.14233	0.310898	0.057196	0.0000000003	0.0952	478	9	473	11	99

A_MAD_JD_24	0.605	0.014	0.0768	0.0018	1.00	13.02592	0.305414	0.057196	0.0000000003	0.0079	480	9	477	11	99
A_MAD_JD_25	0.601	0.014	0.0762	0.0018	1.00	13.11819	0.309757	0.057196	0.0000000003	0.0276	478	9	474	11	99
A_MAD_JD_26	0.599	0.014	0.0760	0.0018	1.00	13.16656	0.312045	0.057196	0.0000000003	0.0142	477	9	472	11	99
A_MAD_JD_27	0.607	0.014	0.0770	0.0018	1.00	12.99545	0.303987	0.057196	0.0000000003	0.0378	481	9	478	11	99
A_MAD_JD_28	0.598	0.014	0.0759	0.0018	1.00	13.1787	0.312621	0.057196	0.0000000003	0.0501	476	9	471	11	99
A_MAD_JD_29	0.600	0.014	0.0760	0.0018	1.00	13.1527	0.311389	0.057196	0.0000000003	0.0422	477	9	472	11	99
A_MAD_JD_30	0.601	0.014	0.0762	0.0017	1.00	13.12508	0.292855	0.057196	0.0000000003	0.0022	477	9	473	10	99
A_MAD_JD_31	0.597	0.014	0.0757	0.0018	1.00	13.20306	0.313778	0.057196	0.0000000003	0.0595	475	9	471	11	99
A_MAD_JD_32	0.602	0.014	0.0764	0.0018	1.00	13.09072	0.30846	0.057196	0.0000000003	0.0233	478	9	474	11	99
A_MAD_JD_33	0.605	0.014	0.0767	0.0018	1.00	13.04291	0.306212	0.057196	0.0000000003	0.0751	480	9	476	11	99
A_MAD_JD_34	0.593	0.014	0.0752	0.0018	1.00	13.29257	0.318046	0.057196	0.0000000003	0.0206	473	9	468	11	99
A_MAD_JD_35	0.603	0.014	0.0765	0.0017	1.00	13.06848	0.290335	0.057196	0.0000000003	0.0086	479	9	475	10	99
A_MAD_JD_36	0.604	0.014	0.0765	0.0018	1.00	13.06506	0.307253	0.057196	0.0000000003	0.0163	479	9	475	11	99
A_MAD_JD_1	0.595	0.015	0.0755	0.0019	1.00	13.24503	0.333319	0.057196	0.0000000003	0.0098	474	9	469	11	99
A_MAD_JD_2	0.605	0.015	0.077	0.002	1.00	13.03781	0.339969	0.057196	0.0000000004	0.1717	480	10	477	12	99
A_MAD_JD_3	0.610	0.016	0.077	0.002	1.00	12.93661	0.334712	0.057196	0.0000000003	0.0309	483	10	480	12	99
A_MAD_JD_4	0.603	0.015	0.0765	0.0019	1.00	13.07702	0.324916	0.057196	0.0000000003	0.0671	479	9	475	11	99
A_MAD_JD_5	0.595	0.015	0.0754	0.0019	1.00	13.2626	0.334203	0.057196	0.0000000003	0.0344	473	10	469	12	99
A_MAD_JD_6	0.597	0.015	0.0757	0.0019	1.00	13.21004	0.33156	0.057196	0.0000000003	0.0702	475	10	470	12	99
A_MAD_JD_7	0.603	0.015	0.0765	0.0019	1.00	13.0736	0.324746	0.057196	0.0000000003	0.0468	480	10	475	12	99
A_MAD_JD_8	0.606	0.016	0.077	0.002	1.00	13.02083	0.339084	0.057196	0.0000000003	0.0625	480	10	477	12	99
A_MAD_JD_9	0.601	0.015	0.0762	0.0019	1.00	13.1268	0.327395	0.057196	0.0000000003	0.0169	477	10	473	12	99
A_MAD_JD_10	0.597	0.015	0.0757	0.0019	1.00	13.21004	0.33156	0.057196	0.0000000003	0.0465	475	10	470	12	99
A_MAD_JD_11	0.605	0.015	0.077	0.002	1.00	13.03781	0.339969	0.057196	0.0000000003	0.0001	480	10	476	12	99
A_MAD_JD_12	0.600	0.015	0.0761	0.0019	1.00	13.1406	0.328083	0.057196	0.0000000003	0.0087	477	10	473	12	99
A_MAD_JD_13	0.603	0.015	0.077	0.002	1.00	13.0719	0.341749	0.057196	0.0000000003	0.0046	479	10	475	12	99
A_MAD_JD_14	0.599	0.015	0.076	0.002	1.00	13.15789	0.34626	0.057196	0.0000000003	0.0295	477	10	472	12	99
A_MAD_JD_15	0.602	0.016	0.076	0.002	1.00	13.10616	0.343543	0.057196	0.0000000003	0.0163	478	10	474	12	99
A_MAD_JD_16	0.603	0.016	0.077	0.002	1.00	13.0719	0.341749	0.057196	0.0000000003	0.0380	479	10	476	12	99

A_MAD_JD_17	0.596	0.015	0.0755	0.0019	1.00	13.24153	0.333142	0.057196	0.0000000003	0.0854	474	10	469	11	99
A_MAD_JD_18	0.610	0.016	0.077	0.002	1.00	12.93661	0.334712	0.057196	0.0000000003	0.0254	483	10	480	12	99
A_MAD_JD_19	0.606	0.016	0.077	0.002	1.00	13.0039	0.338203	0.057196	0.0000000003	0.0242	481	10	477	12	99
A_MAD_JD_20	0.586	0.015	0.0743	0.0019	1.00	13.45895	0.344172	0.057196	0.0000000003	0.0156	468	10	462	11	99
A_MAD_JD_21	0.608	0.015	0.0771	0.0019	1.00	12.9668	0.319462	0.057196	0.0000000003	0.0386	482	10	479	12	99
A_MAD_JD_22	0.602	0.015	0.076	0.002	1.00	13.10616	0.343543	0.057196	0.0000000003	0.0616	478	10	474	12	99
A_MAD_JD_1	0.602	0.012	0.0764	0.0016	1.00	13.08901	0.274115	0.057196	0.0000000003	0.1639	478	8	474	9	99
A_MAD_JD_2	0.604	0.012	0.0766	0.0015	1.00	13.05483	0.255643	0.057196	0.0000000004	0.0292	479	8	475	9	99
A_MAD_JD_3	0.605	0.012	0.0768	0.0015	1.00	13.02083	0.254313	0.057196	0.0000000003	0.0683	480	8	477	9	99
A_MAD_JD_4	0.602	0.012	0.0763	0.0015	1.00	13.10616	0.257657	0.057196	0.0000000003	0.0652	478	8	474	9	99
A_MAD_JD_5	0.591	0.012	0.0749	0.0015	1.00	13.35113	0.267379	0.057196	0.0000000003	0.0038	471	8	466	9	99
A_MAD_JD_6	0.604	0.012	0.0765	0.0015	1.00	13.0719	0.256312	0.057196	0.0000000003	0.0623	479	8	475	9	99
A_MAD_JD_7	0.600	0.012	0.0761	0.0015	1.00	13.1406	0.259013	0.057196	0.0000000003	0.0762	477	7	473	9	99
A_MAD_JD_8	0.601	0.012	0.0762	0.0016	1.00	13.12336	0.275556	0.057196	0.0000000003	0.0888	477	8	473	9	99
A_MAD_JD_9	0.600	0.012	0.0761	0.0015	1.00	13.1406	0.259013	0.057196	0.0000000003	0.0369	476	8	472	9	99
A_MAD_JD_10	0.609	0.013	0.0772	0.0016	1.00	12.95337	0.268464	0.057196	0.0000000003	0.1051	483	8	479	10	99
A_MAD_JD_11	0.594	0.012	0.0753	0.0015	1.00	13.28021	0.264546	0.057196	0.0000000003	0.0157	472	8	468	9	99
A_MAD_JD_12	0.606	0.012	0.0769	0.0015	1.00	13.0039	0.253652	0.057196	0.0000000003	0.0419	481	8	477	9	99
A_MAD_JD_13	0.601	0.012	0.0762	0.0015	1.00	13.12336	0.258334	0.057196	0.0000000003	0.0509	478	8	473	9	99
A_MAD_JD_14	0.601	0.011	0.0762	0.0014	1.00	13.12164	0.241048	0.057196	0.0000000003	0.0872	477	7	473	9	99
A_MAD_JD_15	0.601	0.012	0.0762	0.0016	1.00	13.12336	0.275556	0.057196	0.0000000003	0.0897	477	8	473	9	99
A_MAD_JD_16	0.604	0.012	0.0766	0.0015	1.00	13.05483	0.255643	0.057196	0.0000000003	0.0133	479	7	476	9	99
A_MAD_JD_17	0.597	0.012	0.0757	0.0015	1.00	13.21004	0.261758	0.057196	0.0000000003	0.0793	475	8	471	9	99
A_MAD_JD_18	0.606	0.012	0.0768	0.0015	1.00	13.02083	0.254313	0.057196	0.0000000003	0.0261	480	8	477	9	99
A_MAD_JD_19	0.598	0.012	0.0758	0.0016	1.00	13.19261	0.278472	0.057196	0.0000000003	0.1215	475	8	471	9	99
A_MAD_JD_1	0.59	0.02	0.0753	0.0026	1.00	13.28021	0.458547	0.057196	0.0000000003	0.0746	472	13	468	16	99
A_MAD_JD_2	0.61	0.02	0.0771	0.0025	1.00	12.97017	0.420563	0.057196	0.0000000003	0.0867	481	12	478	15	99
A_MAD_JD_3	0.607	0.022	0.0769	0.0027	1.00	13.0039	0.456574	0.057196	0.0000000003	0.0402	479	14	477	16	100
A_MAD_JD_4	0.59	0.02	0.0751	0.0026	1.00	13.31558	0.460992	0.057196	0.0000000003	0.0999	470	13	466	15	99

A_MAD_JD_5	0.607	0.022	0.0770	0.0028	1.00	12.98701	0.472255	0.057196	0.0000000003	0.0015	479	14	478	17	100
A_MAD_JD_6	0.60	0.02	0.0758	0.0026	1.00	13.19261	0.452517	0.057196	0.0000000003	0.0415	474	13	471	15	99
A_MAD_JD_7	0.606	0.022	0.0769	0.0027	1.00	13.0039	0.456574	0.057196	0.0000000003	0.0468	480	14	477	16	99
A_MAD_JD_8	0.600	0.022	0.0760	0.0027	1.00	13.15789	0.467452	0.057196	0.0000000003	0.0481	474	14	472	16	100
A_MAD_JD_9	0.603	0.021	0.0765	0.0026	1.00	13.0719	0.444274	0.057196	0.0000000003	0.0211	477	13	475	16	100
A_MAD_JD_10	0.596	0.021	0.0755	0.0026	1.00	13.24503	0.45612	0.057196	0.0000000003	0.0385	473	13	470	16	99
A_MAD_JD_11	0.60	0.02	0.0762	0.0026	1.00	13.12336	0.447779	0.057196	0.0000000003	0.1194	475	13	473	16	99
A_MAD_JD_12	0.61	0.02	0.0769	0.0026	1.00	13.0039	0.439664	0.057196	0.0000000003	0.0384	479	13	477	15	100
A_MAD_JD_13	0.60	0.02	0.0762	0.0025	1.00	13.12336	0.430556	0.057196	0.0000000003	0.1161	476	12	473	15	99
A_MAD_JD_14	0.600	0.021	0.0760	0.0027	1.00	13.15789	0.467452	0.057196	0.0000000003	0.0437	474	13	472	16	100
A_MAD_JD_15	0.60	0.02	0.0765	0.0026	1.00	13.0719	0.444274	0.057196	0.0000000003	0.0311	478	13	475	16	99
A_MAD_JD_16	0.587	0.021	0.0745	0.0027	1.00	13.42282	0.486465	0.057196	0.0000000003	0.0633	469	14	464	17	99
A_MAD_JD_17	0.61	0.02	0.0773	0.0026	1.00	12.93661	0.435125	0.057196	0.0000000003	0.0320	481	13	479	15	100

Appendix B6: U-Pb ages and ratios of the apatite secondary standard (McClure)

Apatite secondary standard	Ratios (corrected for Standard common-Pb)										Final Ages (Ma)				
Id	$^{207}Pb/^{235}U$	±2σ	$^{206}Pb/^{238}U$	±2σ	Rho	$^{238}U/^{206}Pb$	±2σ	$^{207}Pb/^{206}Pb$	±2σ	Rho	$^{207}Pb/^{235}U$	±2σ	$^{206}Pb/^{238}U$	±2σ	Con-cord-ance (%)
MCCLURE	4.66	0.13	0.116	0.003	0.04	8.65	0.21	0.295	0.0066	0.54	1757	23	705	16	40
MCCLURE	4.20	0.11	0.112	0.003	0.15	8.96	0.22	0.274	0.0052	0.55	1673	21	682	16	41
MCCLURE	4.30	0.11	0.113	0.003	0.08	8.83	0.20	0.277	0.0044	0.55	1690	20	691	15	41
MCCLURE	3.71	0.13	0.107	0.003	0.14	9.31	0.24	0.251	0.0073	0.40	1568	28	657	16	42
MCCLURE	3.74	0.11	0.108	0.003	0.14	9.23	0.23	0.252	0.0061	0.48	1572	24	663	16	42
MCCLURE	2.04	0.06	0.093	0.002	0.27	10.74	0.24	0.159	0.0028	0.29	1126	18	574	13	51
MCCLURE	3.43	0.10	0.106	0.003	0.13	9.43	0.22	0.236	0.0054	0.40	1505	23	650	15	43
MCCLURE	3.13	0.08	0.103	0.002	0.15	9.68	0.22	0.221	0.0039	0.44	1438	20	634	14	44
MCCLURE	4.08	0.11	0.111	0.003	0.12	8.98	0.21	0.267	0.0047	0.48	1646	21	681	15	41
MCCLURE	5.19	0.14	0.119	0.003	0.11	8.42	0.21	0.318	0.0062	0.57	1847	23	723	17	39
MCCLURE	3.55	0.12	0.107	0.003	0.19	9.35	0.25	0.242	0.0068	0.44	1528	27	655	17	43
MCCLURE	3.17	0.11	0.104	0.003	0.13	9.63	0.26	0.222	0.0063	0.41	1439	27	637	16	44
MCCLURE	4.21	0.15	0.115	0.003	0.17	8.67	0.25	0.266	0.0079	0.44	1669	28	703	19	42
MCCLURE	2.87	0.10	0.101	0.003	0.05	9.90	0.26	0.209	0.0068	0.52	1368	26	620	16	45
MCCLURE	2.90	0.11	0.103	0.003	0.14	9.71	0.25	0.206	0.0064	0.34	1371	29	631	16	46
MCCLURE	3.67	0.24	0.104	0.004	0.14	9.58	0.39	0.263	0.0170	0.44	1528	55	639	25	42
MCCLURE	4.48	0.28	0.118	0.005	0.07	8.48	0.38	0.287	0.0190	0.48	1670	55	716	30	43
MCCLURE	3.65	0.22	0.108	0.004	0.18	9.29	0.37	0.254	0.0150	0.40	1505	51	657	25	44

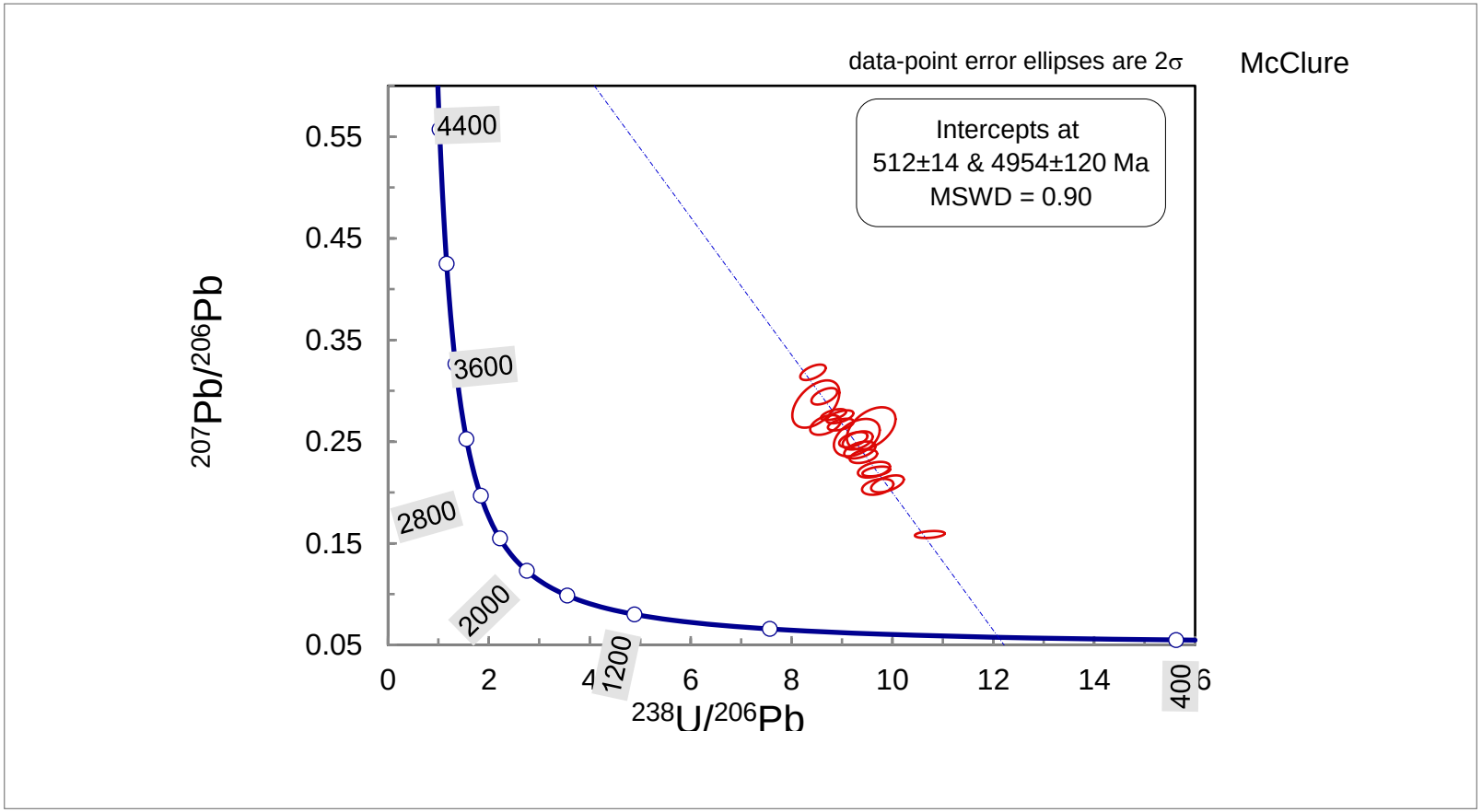
data-point error ellipses are 2σ
McClure
Intercepts at
512±14 & 4954±120 Ma
MSWD = 0.90
4400
3600
2800
2000
1200
400
0.55
0.45
0.35
0.25
0.15
0.05
0
2
4
6
8
10
12
14
16
207Pb/206Pb
238U/206Pb

Appendix B7: U-Pb ages and ratios of the apatite secondary standard (Xuxa)

Apatite secondary standard	Ratios (corrected for Standard common-Pb)										Final Ages (Ma)				
Id	$^{207}Pb/^{235}U$	±2σ	$^{206}Pb/^{238}U$	±2σ	Rho	$^{238}U/^{206}Pb$	±2σ	$^{207}Pb/^{206}Pb$	±2σ	Rho	$^{207}Pb/^{235}U$	±2σ	$^{206}Pb/^{238}U$	±2σ	Concord-ance (%)
XUXA	1.73	0.04	0.103	0.002	0.14	9.68	0.21	0.121	0.0014	0.42	1021	15	634	13	62
XUXA	1.90	0.04	0.107	0.002	0.22	9.35	0.20	0.129	0.0014	0.37	1080	15	655	13	61
XUXA	1.75	0.04	0.102	0.002	0.21	9.81	0.21	0.125	0.0014	0.37	1027	15	626	13	61
XUXA	1.94	0.05	0.106	0.002	0.28	9.47	0.21	0.133	0.0014	0.30	1094	15	647	13	59
XUXA	1.86	0.04	0.105	0.002	0.18	9.56	0.20	0.129	0.0014	0.37	1067	15	641	13	60
XUXA	1.65	0.04	0.103	0.002	0.07	9.72	0.21	0.116	0.0013	0.41	988	15	631	13	64
XUXA	1.76	0.04	0.104	0.002	0.20	9.65	0.21	0.123	0.0013	0.28	1028	15	635	13	62
XUXA	1.88	0.04	0.106	0.002	0.18	9.46	0.21	0.129	0.0015	0.33	1072	16	648	13	60
XUXA	1.81	0.04	0.103	0.002	0.25	9.73	0.21	0.128	0.0014	0.34	1047	15	631	13	60
XUXA	1.87	0.04	0.107	0.002	0.16	9.37	0.20	0.127	0.0012	0.38	1070	15	654	13	61
XUXA	1.66	0.04	0.102	0.002	0.33	9.77	0.21	0.118	0.0013	0.22	992	15	628	13	63
XUXA	1.88	0.04	0.105	0.002	0.19	9.55	0.20	0.130	0.0013	0.39	1074	15	642	13	60
XUXA	1.88	0.04	0.104	0.002	0.13	9.63	0.20	0.131	0.0015	0.33	1071	15	637	13	59
XUXA	1.77	0.04	0.103	0.002	0.17	9.67	0.21	0.125	0.0013	0.39	1035	15	634	13	61
XUXA	1.89	0.04	0.105	0.002	0.18	9.48	0.21	0.130	0.0013	0.35	1079	15	646	13	60
XUXA	1.71	0.04	0.102	0.002	0.24	9.76	0.21	0.121	0.0012	0.28	1010	15	629	13	62
XUXA	1.91	0.05	0.106	0.002	0.32	9.45	0.21	0.131	0.0015	0.22	1084	16	649	13	60
XUXA	1.72	0.04	0.105	0.002	0.28	9.56	0.20	0.119	0.0013	0.27	1014	15	641	13	63
XUXA	1.67	0.04	0.102	0.002	0.21	9.83	0.21	0.119	0.0013	0.29	998	14	624	13	63
XUXA	1.86	0.04	0.105	0.002	0.22	9.50	0.20	0.128	0.0014	0.34	1064	15	645	13	61
XUXA	1.78	0.04	0.103	0.002	0.19	9.69	0.21	0.125	0.0012	0.33	1036	15	633	13	61
XUXA	1.91	0.04	0.106	0.002	0.13	9.43	0.20	0.131	0.0013	0.41	1084	15	650	13	60
XUXA	1.81	0.04	0.104	0.002	0.13	9.62	0.20	0.126	0.0013	0.36	1046	15	637	13	61
XUXA	1.78	0.04	0.104	0.002	0.27	9.61	0.20	0.124	0.0013	0.30	1038	15	638	13	61
XUXA	1.52	0.04	0.100	0.002	0.19	10.01	0.21	0.110	0.0013	0.36	939	14	614	12	65

XUXA	1.66	0.04	0.102	0.002	0.21	9.84	0.21	0.118	0.0012	0.30	991	15	624	13	63
XUXA	1.71	0.04	0.102	0.002	0.20	9.80	0.21	0.122	0.0012	0.30	1013	15	626	13	62
XUXA	1.94	0.04	0.105	0.002	0.23	9.54	0.20	0.134	0.0011	0.31	1094	15	642	13	59
XUXA	1.69	0.04	0.102	0.002	0.27	9.77	0.21	0.120	0.0012	0.23	1006	14	628	13	62
XUXA	1.63	0.04	0.102	0.002	0.29	9.80	0.21	0.116	0.0013	0.24	982	15	627	13	64
XUXA	1.70	0.04	0.103	0.002	0.09	9.73	0.21	0.120	0.0013	0.41	1009	14	631	13	63
XUXA	1.88	0.04	0.105	0.002	0.24	9.50	0.20	0.130	0.0013	0.26	1073	15	645	13	60
XUXA	1.68	0.04	0.104	0.002	0.30	9.64	0.20	0.118	0.0011	0.29	1001	15	636	13	64
XUXA	1.79	0.04	0.104	0.002	0.16	9.60	0.20	0.125	0.0013	0.35	1040	15	639	13	61
XUXA	1.84	0.04	0.105	0.002	0.18	9.50	0.20	0.127	0.0013	0.31	1058	15	645	13	61
XUXA	1.81	0.04	0.105	0.002	0.16	9.52	0.20	0.125	0.0013	0.33	1048	15	644	13	61
XUXA	1.57	0.04	0.101	0.002	0.25	9.93	0.23	0.113	0.0015	0.35	955	16	619	14	65
XUXA	1.76	0.05	0.104	0.002	0.23	9.64	0.22	0.123	0.0017	0.27	1030	17	636	14	62
XUXA	1.78	0.05	0.104	0.002	0.24	9.66	0.22	0.125	0.0015	0.31	1038	16	635	14	61
XUXA	1.70	0.04	0.104	0.002	0.21	9.62	0.22	0.119	0.0015	0.34	1008	16	637	14	63
XUXA	1.63	0.04	0.102	0.002	0.14	9.82	0.22	0.116	0.0016	0.38	981	16	625	14	64
XUXA	1.80	0.05	0.104	0.002	0.36	9.59	0.22	0.125	0.0016	0.20	1043	17	640	14	61
XUXA	1.60	0.04	0.101	0.002	0.13	9.94	0.23	0.115	0.0017	0.37	968	16	618	13	64
XUXA	1.66	0.04	0.103	0.002	0.08	9.75	0.22	0.118	0.0019	0.35	993	16	629	14	63
XUXA	1.99	0.05	0.106	0.002	0.32	9.40	0.21	0.136	0.0018	0.17	1111	17	652	14	59
XUXA	1.61	0.04	0.101	0.002	0.13	9.91	0.23	0.116	0.0016	0.40	974	16	620	13	64
XUXA	1.82	0.05	0.105	0.002	0.15	9.50	0.22	0.125	0.0017	0.38	1050	16	645	14	61
XUXA	1.74	0.04	0.104	0.002	0.09	9.59	0.22	0.122	0.0017	0.44	1023	16	640	14	63
XUXA	1.85	0.05	0.105	0.002	0.28	9.50	0.22	0.128	0.0015	0.29	1064	16	645	14	61
XUXA	1.67	0.04	0.102	0.002	0.15	9.80	0.22	0.119	0.0015	0.38	995	16	626	14	63
XUXA	1.67	0.04	0.102	0.002	0.10	9.85	0.22	0.119	0.0019	0.40	993	16	624	14	63
XUXA	1.78	0.05	0.104	0.002	0.00	9.61	0.22	0.124	0.0019	0.51	1036	17	638	14	62
XUXA	1.78	0.05	0.103	0.002	0.26	9.70	0.23	0.126	0.0018	0.29	1039	17	632	14	61
XUXA	1.75	0.04	0.103	0.002	0.14	9.68	0.22	0.124	0.0016	0.36	1028	16	634	14	62

XUXA	1.71	0.04	0.103	0.002	0.13	9.69	0.23	0.121	0.0017	0.41	1012	16	633	14	63
XUXA	1.81	0.05	0.105	0.002	0.16	9.54	0.22	0.126	0.0018	0.29	1048	17	643	14	61
XUXA	1.78	0.05	0.104	0.002	0.14	9.64	0.22	0.124	0.0017	0.40	1035	16	636	14	62
XUXA	1.89	0.05	0.105	0.002	0.20	9.51	0.22	0.130	0.0019	0.32	1074	17	645	14	60
XUXA	1.92	0.04	0.105	0.002	0.12	9.50	0.14	0.132	0.0016	0.41	1088	12	645	9	59
XUXA	1.61	0.03	0.099	0.002	0.23	10.07	0.15	0.118	0.0016	0.26	973	12	610	9	63
XUXA	1.82	0.03	0.103	0.002	0.13	9.67	0.15	0.128	0.0017	0.41	1052	12	634	9	60
XUXA	1.98	0.04	0.106	0.002	0.12	9.39	0.14	0.135	0.0016	0.27	1106	12	652	10	59
XUXA	1.91	0.04	0.106	0.002	0.17	9.47	0.14	0.131	0.0017	0.37	1083	12	647	10	60
XUXA	1.78	0.06	0.104	0.003	0.10	9.66	0.26	0.126	0.0032	0.42	1036	22	635	16	61
XUXA	1.72	0.06	0.102	0.003	0.22	9.78	0.26	0.122	0.0027	0.31	1011	21	628	16	62
XUXA	1.72	0.06	0.102	0.003	0.12	9.83	0.26	0.123	0.0030	0.33	1010	22	624	16	62
XUXA	1.83	0.06	0.103	0.003	0.15	9.68	0.25	0.129	0.0025	0.37	1054	20	634	16	60
XUXA	1.74	0.06	0.102	0.003	0.15	9.83	0.25	0.125	0.0028	0.34	1019	21	625	15	61
XUXA	1.61	0.05	0.101	0.003	0.01	9.86	0.26	0.116	0.0028	0.47	972	20	622	16	64
XUXA	1.80	0.06	0.104	0.003	0.09	9.62	0.26	0.126	0.0031	0.40	1040	22	637	16	61
XUXA	1.86	0.06	0.102	0.003	0.12	9.83	0.26	0.133	0.0029	0.38	1060	21	625	16	59
XUXA	1.80	0.06	0.102	0.003	0.18	9.83	0.26	0.128	0.0030	0.34	1038	21	624	16	60
XUXA	1.72	0.06	0.103	0.003	0.13	9.75	0.27	0.122	0.0030	0.38	1011	21	630	16	62
XUXA	1.76	0.06	0.103	0.003	0.13	9.72	0.25	0.125	0.0030	0.35	1025	21	631	16	62
XUXA	1.77	0.06	0.104	0.003	0.17	9.66	0.26	0.124	0.0028	0.36	1028	21	635	16	62
XUXA	1.81	0.06	0.103	0.003	0.06	9.73	0.26	0.129	0.0032	0.41	1046	21	630	16	60
XUXA	1.68	0.05	0.101	0.003	0.16	9.95	0.26	0.121	0.0027	0.34	994	21	618	15	62
XUXA	1.75	0.06	0.103	0.003	0.06	9.72	0.25	0.124	0.0032	0.41	1020	22	631	16	62
XUXA	1.73	0.06	0.102	0.003	0.15	9.82	0.26	0.124	0.0030	0.33	1017	21	625	16	61

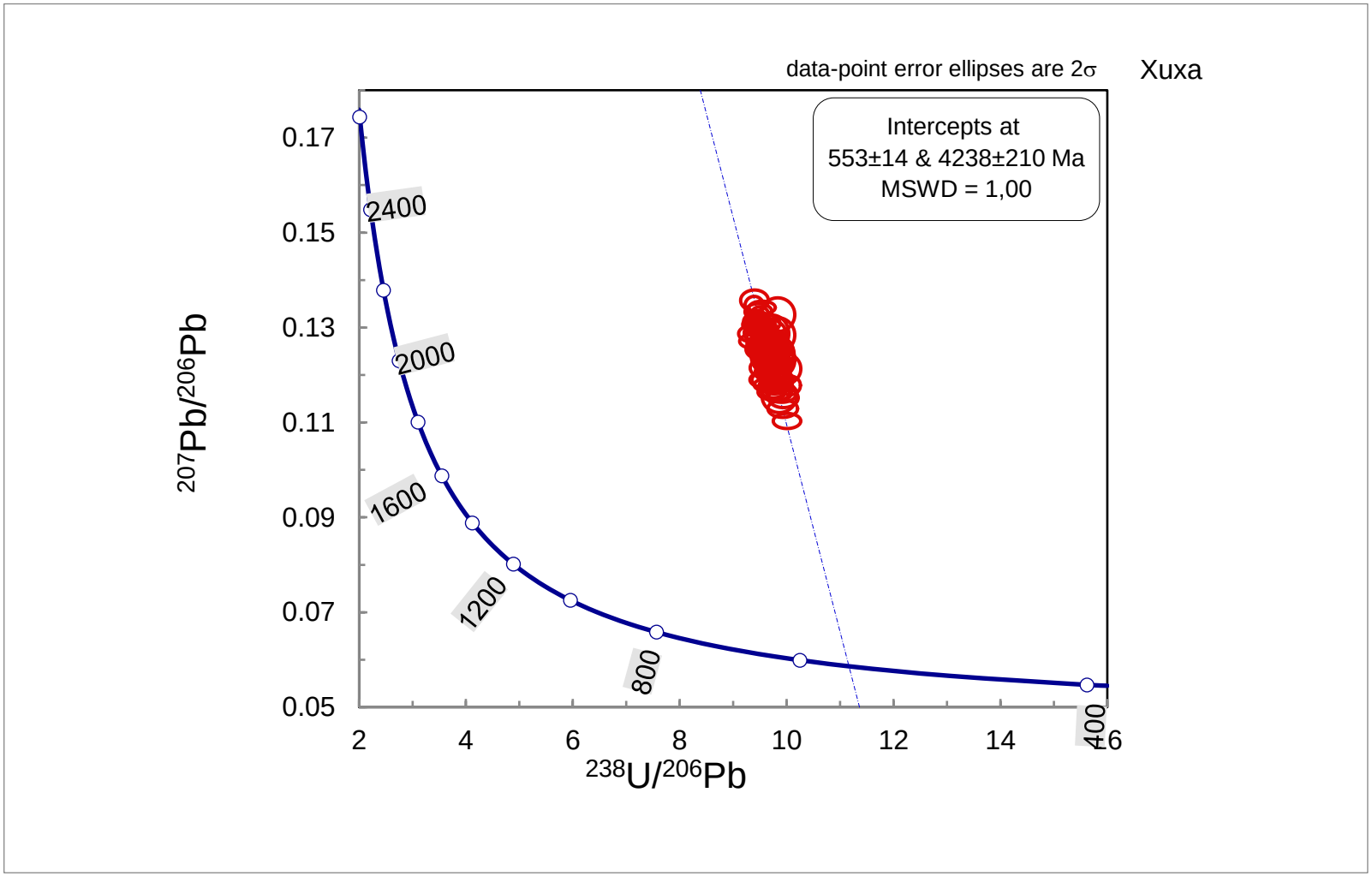
data-point error ellipses are 2σ
Xuxa
Intercepts at
553±14 & 4238±210 Ma
MSWD = 1,00
0.17
0.15
0.13
0.11
0.09
0.07
0.05
2400
2000
1600
1200
800
400
2
4
6
8
10
12
14
16
207Pb/206Pb
238U/206Pb

Appendix B8: Zircon element concentrations (based on referenced isotope), concentration uncertainty and limit of detection (LOD) in ppm

ID	Ti_ppm_m49	Ti_ppm_m49_Int2SE	Ti_ppm_m49_LOD	Y_ppm_m89	Y_ppm_m89_Int2SE	Y_ppm_m89_LOD	Nb_ppm_m93	Nb_ppm_m93_Int2SE	Nb_ppm_m93_LOD
Primary standard									
G_NIST612_1	43.9	2.1	3.6	38.14	0.52	0.026	40.01	0.46	0.023
G_NIST612_2	43.3	2.4	2.9	37.54	0.4	0.027	39.47	0.47	0.023
G_NIST612_3	43.7	2.4	3.7	38.06	0.41	0.032	40.11	0.48	0.021
G_NIST612_4	45	1.6	3.2	38.19	0.46	0.022	40.36	0.41	0.018
G_NIST612_5	42.9	2	3.5	38.17	0.43	0.026	40.12	0.47	0.019
G_NIST612_6	45.7	2.5	3.2	38.05	0.5	0.035	39.88	0.44	0.018
G_NIST612_7	44.3	2.4	3.3	38.03	0.52	0.035	39.97	0.58	0.021
G_NIST612_8	40.8	2.1	3.2	38.13	0.52	0.027	39.79	0.47	0.02
G_NIST612_9	46.1	2.2	3.7	38.21	0.47	0.037	40.29	0.52	0.022
G_NIST612_10	44.5	1.9	2.8	37.72	0.46	0.033	39.98	0.58	0.017
G_NIST612_11	44	1.8	3.6	38.25	0.56	0.037	40.34	0.52	0.021
G_NIST612_12	42	2.2	3.4	37.61	0.48	0.039	39.5	0.56	0.017
G_NIST612_13	45.2	1.9	2.7	38.13	0.44	0.04	40.07	0.51	0.019
Secondary standard									
91500 - 1	5	1.7	3.4	135.3	1.2	0.033	0.796	0.035	0.024
91500 - 2	5.4	1.5	3.4	133.7	1.4	0.038	0.833	0.037	0.024
91500 - 3	4.5	1.5	3.2	137.4	1.3	0.042	0.806	0.039	0.02
91500 - 4	Below LOD	Below LOD	4.1	138.3	1.3	0.036	0.858	0.039	0.023
Average	**4.97**			**136.18**			**0.82**		
Published	**4.77**			**141.21**			**1.21**		

Variation	**1.04**			**0.96**			**0.68**		
GJ1 - 1	4.1	1.8	3.6	294.8	3	0.027	1.767	0.048	0.022
GJ1 - 2	4.8	1.3	3.3	290.7	2.8	0.036	1.69	0.055	0.02
GJ1 - 3	3.5	1.4	3	288.5	3	0.036	1.69	0.054	0.018
GJ1 - 4	3.5	1.6	3.2	295.8	3.3	0.028	1.791	0.061	0.023
Average	**3.98**			**292.45**			**1.73**		
Published	**4.39**			**211.21**			**1.27**		
Variation	**0.90**			**1.38**			**1.36**		

Appendix B8 *continued*

ID	Ce_ppm_m140	Ce_ppm_m140_Int2SE	Ce_ppm_m140_LOD	Nd_ppm_m146	Nd_ppm_m146_Int2SE	Nd_ppm_m146_LOD	Sm_ppm_m147	Sm_ppm_m147_Int2SE	Sm_ppm_m147_LOD
Primary standard									
G_NIST612_1	38.83	0.42	0.021	35.82	0.57	0.06	38.08	0.65	0.097
G_NIST612_2	38.51	0.5	0.018	35.09	0.55	0.064	38.11	0.7	0.095
G_NIST612_3	38.57	0.42	0.015	35.57	0.65	0.062	38.2	0.77	0.076
G_NIST612_4	38.89	0.47	0.024	36.63	0.47	0.069	38.03	0.6	0.094
G_NIST612_5	38.68	0.39	0.026	35.61	0.56	0.065	38.13	0.59	0.084
G_NIST612_6	38.65	0.57	0.023	36.33	0.73	0.066	38.13	0.7	0.085
G_NIST612_7	38.72	0.55	0.019	36.58	0.65	0.069	38.01	0.66	0.089
G_NIST612_8	38.89	0.47	0.023	37.05	0.6	0.053	38.24	0.7	0.065
G_NIST612_9	38.58	0.47	0.023	35.4	0.62	0.064	38.07	0.57	0.09
G_NIST612_10	38.34	0.5	0.021	34.7	0.5	0.075	38.01	0.71	0.092
G_NIST612_11	39.22	0.49	0.025	36.13	0.6	0.045	38.24	0.8	0.094
G_NIST612_12	38.28	0.52	0.024	35.45	0.67	0.075	38.06	0.55	0.087

G_NIST612_13	38.84	0.47	0.024	36.46	0.51	0.047	38.12	0.67	0.07
Secondary standard									
91500 - 1	2.675	0.067	0.022	0.153	0.042	0.068	0.319	0.056	0.074
91500 - 2	2.657	0.079	0.026	0.194	0.054	0.066	0.383	0.058	0.085
91500 - 3	2.648	0.067	0.032	0.162	0.046	0.078	0.492	0.079	0.1
91500 - 4	2.67	0.064	0.027	0.194	0.046	0.083	0.395	0.067	0.083
Average	**2.66**			**0.18**			**0.40**		
Published	**2.89**			**0.30**			**0.46**		
Variation	**0.92**			**0.59**			**0.86**		
GJ1 - 1	19.31	0.27	0.021	0.856	0.08	0.075	2.07	0.15	0.065
GJ1 - 2	19.05	0.27	0.028	0.909	0.081	0.082	2.01	0.12	0.095
GJ1 - 3	18.82	0.23	0.019	0.817	0.091	0.075	2	0.13	0.094
GJ1 - 4	19.3	0.25	0.02	0.838	0.088	0.054	2.05	0.15	0.087
Average	**19.12**			**0.86**			**2.03**		
Published	**15.91**			**0.72**			**1.24**		
Variation	**1.20**			**1.19**			**1.64**		

Appendix B8 *continued*

ID	Eu_ppm_m153	Eu_ppm_m153_Int2SE	Eu_ppm_m153_LOD	Gd_ppm_m157	Gd_ppm_m157_Int2SE	Gd_ppm_m157_LOD	Tb_ppm_m159	Tb_ppm_m159_Int2SE	Tb_ppm_m159_LOD
Primary standard									
G_NIST612_1	35.26	0.39	0.028	37.04	0.69	0.086	36.23	0.42	0.0064
G_NIST612_2	34.65	0.41	0.026	36.39	0.6	0.086	35.81	0.39	0.011
G_NIST612_3	34.83	0.45	0.027	36.17	0.57	0.092	35.74	0.42	0.0052
G_NIST612_4	35.22	0.41	0.023	37.26	0.51	0.061	36.31	0.45	0.0073
G_NIST612_5	34.97	0.45	0.023	36.65	0.66	0.087	36	0.37	0.0094

G_NIST612_6	35.04	0.53	0.029	36.74	0.62	0.065	36.07	0.43	0.0093
G_NIST612_7	34.72	0.46	0.022	36.2	0.65	0.095	35.56	0.46	0.0097
G_NIST612_8	35.46	0.38	0.031	37.69	0.71	0.098	36.75	0.39	0.0063
G_NIST612_9	34.66	0.53	0.027	36.53	0.69	0.098	35.39	0.51	0.0072
G_NIST612_10	34.44	0.55	0.026	36.08	0.64	0.11	35.38	0.45	0.0086
G_NIST612_11	35.35	0.49	0.026	37.06	0.6	0.11	36.76	0.49	0.0077
G_NIST612_12	34.72	0.47	0.024	36.31	0.67	0.085	35.61	0.42	0.0095
G_NIST612_13	35.13	0.37	0.024	37	0.67	0.092	36.25	0.45	0.0067
Secondary standard									
91500 - 1	0.215	0.026	0.029	2.01	0.13	0.079	0.762	0.03	0.0078
91500 - 2	0.216	0.022	0.032	1.99	0.13	0.099	0.759	0.032	0.0089
91500 - 3	0.203	0.024	0.032	1.99	0.14	0.13	0.781	0.032	0.0078
91500 - 4	0.251	0.021	0.03	2.08	0.13	0.11	0.791	0.031	0.0075
Average	**0.22**			**2.02**			**0.77**		
Published	**0.23**			**2.05**			**0.80**		
Variation	**0.95**			**0.98**			**0.97**		
GJ1 - 1	1.337	0.048	0.018	9.45	0.24	0.092	2.336	0.052	0.01
GJ1 - 2	1.316	0.053	0.03	9.09	0.33	0.12	2.369	0.062	0.011
GJ1 - 3	1.274	0.056	0.026	8.57	0.26	0.099	2.335	0.055	0.011
GJ1 - 4	1.32	0.054	0.029	9.11	0.3	0.13	2.398	0.061	0.008
Average	**1.31**			**9.06**			**2.36**		
Published	**0.95**			**5.77**			**1.66**		
Variation	**1.39**			**1.57**			**1.42**		

Appendix B8 *continued*

ID	Dy_ppm_m163	Dy_ppm_m163_Int2SE	Dy_ppm_m163_LOD	Ho_ppm_m165	Ho_ppm_m165_Int2SE	Ho_ppm_m165_LOD	Er_ppm_m166	Er_ppm_m166_Int2SE	Er_ppm_m166_LOD
Primary standard									
G_NIST612_1	36.11	0.51	0.036	38.01	0.41	0.0095	38.38	0.55	0.022
G_NIST612_2	35.83	0.65	0.031	37.99	0.45	0.011	37.49	0.58	0.027
G_NIST612_3	35.86	0.48	0.042	37.96	0.48	0.0088	37.94	0.59	0.019
G_NIST612_4	36.18	0.53	0.047	37.94	0.39	0.0087	38.07	0.47	0.023
G_NIST612_5	35.94	0.58	0.042	38.14	0.42	0.0089	38.04	0.48	0.018
G_NIST612_6	36.16	0.52	0.048	38	0.52	0.01	38.09	0.55	0.031
G_NIST612_7	35.63	0.57	0.035	37.76	0.45	0.0095	37.69	0.51	0.032
G_NIST612_8	36.79	0.63	0.032	38.65	0.45	0.0088	38.74	0.55	0.029
G_NIST612_9	35.75	0.54	0.041	37.56	0.53	0.01	37.65	0.6	0.027
G_NIST612_10	35.4	0.59	0.036	37.2	0.53	0.008	37.36	0.55	0.027
G_NIST612_11	36.54	0.53	0.041	38.7	0.46	0.0098	38.59	0.49	0.029
G_NIST612_12	35.78	0.62	0.044	37.69	0.44	0.01	37.7	0.57	0.022
G_NIST612_13	35.97	0.61	0.034	38.12	0.48	0.0082	38.02	0.48	0.025
Secondary standard									
91500 - 1	10.66	0.23	0.037	4.411	0.066	0.0093	24.47	0.34	0.022
91500 - 2	10.63	0.23	0.038	4.423	0.082	0.0095	24.31	0.32	0.03
91500 - 3	11	0.28	0.042	4.489	0.091	0.011	24.55	0.31	0.03
91500 - 4	11.14	0.22	0.05	4.532	0.091	0.0079	25	0.33	0.025
Average	**10.86**			**4.46**			**24.58**		
Published	**10.79**			**4.52**			**23.79**		
Variation	**1.01**			**0.99**			**1.03**		

GJ1 - 1	24.67	0.38	0.049	8.11	0.13	0.0083	35.6	0.44	0.019
GJ1 - 2	24.6	0.4	0.034	8.12	0.14	0.0082	35.63	0.5	0.032
GJ1 - 3	24.5	0.42	0.038	7.97	0.16	0.011	35.04	0.56	0.032
GJ1 - 4	25.77	0.47	0.048	8.2	0.12	0.011	36.35	0.62	0.026
Average	**24.89**			**8.10**			**35.66**		
Published	**17.10**			**5.84**			**25.19**		
Variation	**1.46**			**1.39**			**1.42**		

Appendix B8 *continued*

ID	Tm_ppm_m169	Tm_ppm_m169_Int2SE	Tm_ppm_m169_LOD	Yb_ppm_m172	Yb_ppm_m172_Int2SE	Yb_ppm_m172_LOD	Lu_ppm_m175	Lu_ppm_m175_Int2SE	Lu_ppm_m175_LOD
Primary standard									
G_NIST612_1	38.42	0.46	0.0055	39.58	0.62	0.029	37.21	0.45	0.0061
G_NIST612_2	37.8	0.38	0.0069	38.91	0.52	0.027	36.75	0.4	0.0068
G_NIST612_3	37.75	0.43	0.006	38.89	0.62	0.024	36.71	0.42	0.0068
G_NIST612_4	38.05	0.44	0.0065	39.4	0.61	0.021	36.92	0.33	0.0056
G_NIST612_5	38.14	0.43	0.0057	39.29	0.56	0.032	36.95	0.43	0.006
G_NIST612_6	38.01	0.49	0.0067	39.33	0.63	0.029	37.01	0.54	0.0062
G_NIST612_7	37.74	0.48	0.0071	38.93	0.6	0.029	36.63	0.48	0.0039
G_NIST612_8	38.69	0.5	0.0068	40.02	0.56	0.023	37.33	0.43	0.006
G_NIST612_9	37.35	0.57	0.007	38.58	0.64	0.029	36.72	0.5	0.0058
G_NIST612_10	37.42	0.57	0.0071	38.3	0.59	0.03	36.45	0.46	0.0041
G_NIST612_11	38.57	0.44	0.0086	40.23	0.6	0.02	37.51	0.52	0.0051
G_NIST612_12	37.65	0.48	0.0066	38.89	0.6	0.028	36.42	0.5	0.0077

G_NIST612_13	38.08	0.44	0.0054	39.2	0.59	0.019	37.14	0.46	0.0054
Secondary standard									
91500 - 1	6.139	0.096	0.0062	61.3	1	0.024	12.7	0.16	0.0046
91500 - 2	6.1	0.11	0.0062	62.23	0.87	0.025	12.68	0.17	0.0064
91500 - 3	6.105	0.097	0.0067	61.7	0.92	0.027	13.06	0.17	0.0062
91500 - 4	6.279	0.09	0.0041	63.49	0.89	0.021	12.92	0.17	0.0068
Average	**6.16**			**62.18**			**12.84**		
Published	**6.23**			**65.73**			**13.22**		
Variation	**0.99**			**0.95**			**0.97**		
GJ1 - 1	7.48	0.096	0.0088	68.78	0.8	0.031	14.51	0.17	0.0068
GJ1 - 2	7.4	0.12	0.0074	67.72	0.88	0.018	14.36	0.18	0.0076
GJ1 - 3	7.35	0.11	0.0066	65.81	0.95	0.029	14.18	0.17	0.0069
GJ1 - 4	7.55	0.13	0.0056	69	1.1	0.02	14.71	0.26	0.0063
Average	**7.45**			**67.83**			**14.44**		
Published	**5.38**			**54.75**			**10.93**		
Variation	**1.38**			**1.24**			**1.32**		

Appendix B8 *continued*

ID	Hf_ppm_m178	Hf_ppm_m178_Int 2SE	Hf_ppm_m178_LOD	Ta_ppm_m181	Ta_ppm_m181_Int 2SE	Ta_ppm_m181_LOD	Pb_ppm_m208	Pb_ppm_m208_Int 2SE	Pb_ppm_m208_LOD
Primary standard									
G_NIST612_1	35.33	0.49	0.022	40.27	0.45	0.008	39.02	0.58	0.031
G_NIST612_2	34.82	0.49	0.026	39.89	0.44	0.007	38.17	0.61	0.042
G_NIST612_3	34.83	0.47	0.021	39.79	0.43	0.0081	38.42	0.59	0.03
G_NIST612_4	34.99	0.47	0.025	40.03	0.4	0.0064	38.58	0.6	0.028
G_NIST612_5	35.02	0.49	0.023	40.01	0.42	0.0074	38.55	0.57	0.03

G_NIST612_6	35.15	0.6	0.027	40.06	0.55	0.0093	38.82	0.51	0.038
G_NIST612_7	34.64	0.54	0.026	39.74	0.6	0.0088	38.13	0.58	0.031
G_NIST612_8	35.7	0.49	0.09	40.53	0.46	0.008	39.09	0.53	0.025
G_NIST612_9	34.36	0.56	0.031	39.48	0.57	0.0099	38.1	0.47	0.04
G_NIST612_10	34.65	0.6	0.021	39.39	0.57	0.0092	38.63	0.57	0.038
G_NIST612_11	35.49	0.55	0.026	40.79	0.52	0.01	39.24	0.64	0.032
G_NIST612_12	34.84	0.5	0.025	39.62	0.52	0.0082	38.1	0.57	0.033
G_NIST612_13	35.03	0.44	0.025	40.07	0.51	0.0074	38.79	0.58	0.035
Secondary standard									
91500 - 1	5714	69	0.026	0.503	0.028	0.0077	3.04	0.13	0.031
91500 - 2	5787	60	0.11	0.491	0.029	0.0098	3.01	0.1	0.038
91500 - 3	5644	61	0.032	0.522	0.028	0.0091	3.07	0.12	0.043
91500 - 4	5693	67	0.18	0.487	0.024	0.0087	3.07	0.13	0.043
Average	**5709.50**			**0.50**			**3.05**		
Published	**6282.27**			**0.43**			**2.26**		
Variation	**0.91**			**1.16**			**1.35**		
GJ1 - 1	6160	75	0.03	0.443	0.025	0.0075	0.729	0.05	0.039
GJ1 - 2	6160	66	0.026	0.443	0.026	0.0079	0.787	0.051	0.031
GJ1 - 3	6130	81	0.042	0.427	0.022	0.0096	0.7	0.058	0.033
GJ1 - 4	6238	89	0.026	0.442	0.024	0.012	0.737	0.053	0.033
Average	**6172.00**			**0.44**			**0.74**		
Published	**6526.01**			**0.35**					
Variation	**0.95**			**1.26**					

Appendix B8 *continued*

ID	Th_ppm_m232	Th_ppm_m232_Int2SE	Th_ppm_m232_LOD	U_ppm_m238	U_ppm_m238_Int2SE	U_ppm_m238_LOD
Primary standard						
G_NIST612_1	37.86	0.43	0.0037	37.76	0.45	NaN
G_NIST612_2	37.64	0.46	0.0056	37.06	0.47	0.0043
G_NIST612_3	37.85	0.4	0.0032	37.28	0.53	0.0022
G_NIST612_4	37.79	0.42	0.0039	37.29	0.42	0.0042
G_NIST612_5	37.79	0.41	0.0032	37.45	0.44	NaN
G_NIST612_6	37.81	0.46	0.0024	37.52	0.56	0.0031
G_NIST612_7	37.75	0.61	0.0047	37.1	0.54	0.0021
G_NIST612_8	37.82	0.54	0.0049	37.92	0.49	0.0021
G_NIST612_9	37.76	0.52	0.0035	36.99	0.49	0.0023
G_NIST612_10	37.78	0.57	0.0048	36.97	0.5	NaN
G_NIST612_11	37.86	0.6	0.0033	38.25	0.56	0.0023
G_NIST612_12	37.7	0.42	0.0023	37.04	0.53	0.0022
G_NIST612_13	37.86	0.44	0.0022	37.41	0.45	0.0021
Secondary standard						
91500 - 1	29.43	0.33	0.0035	84.51	0.81	0.0033
91500 - 2	29.55	0.35	0.0034	85.53	0.83	0.0023
91500 - 3	31.2	0.36	0.0037	87.97	0.82	0.0042
91500 - 4	31.09	0.34	NaN	88.77	0.99	0.0041
Average	**30.32**			**86.70**		
Published	**27.83**			**73.25**		
Variation	**1.09**			**1.18**		
GJ1 - 1	12.9	0.19	0.008	310.6	3	0.0062
GJ1 - 2	12.78	0.19	NaN	312	3.1	0.0039
GJ1 - 3	12.72	0.21	0.005	310	3.8	0.0035
GJ1 - 4	13.36	0.22	0.0043	317.7	3.9	0.0075
Average	**12.94**			**312.58**		

Published	**11.16**			**294.88**		
Variation	**1.16**			**1.06**		

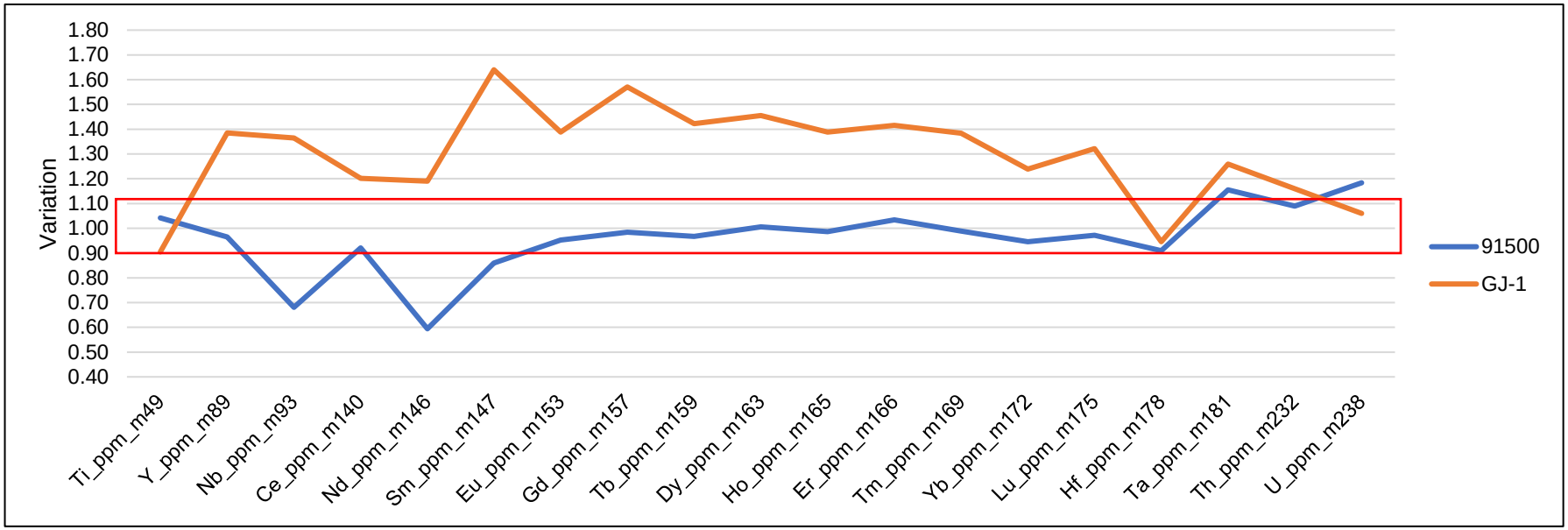

Appendix B9: U-Pb ages of the zircon primary standard (BB9)

Zircon primary standard				Common-lead uncorrected ratios					Final Ages (Ma)						
Id	U (ppm)	Th (ppm)	Th/U	$^{207}Pb/^{235}U$	±2σ	$^{206}Pb/^{238}U$	±2σ	Rho	$^{207}Pb/^{235}U$	±2σ	$^{206}Pb/^{238}U$	±2σ	$^{207}Pb/^{206}Pb$	±2σ	Concord-ance (%)
Z_BB9_1	270.8	62.8	0.2319	0.74	0.02	0.0918	0.0014	0.285	560	11	566	8	532	45	101
Z_BB9_2	269.8	63.4	0.2350	0.736	0.019	0.0903	0.0014	0.142	559	11	557	8	554	50	100
Z_BB9_3	269.5	62.9	0.2334	0.74	0.02	0.0910	0.0014	0.267	560	12	561	8	540	51	100
Z_BB9_4	269	63	0.2342	0.74	0.02	0.091	0.001	0.052	558	12	561	8	511	57	101
Z_BB9_5	271.8	63	0.2318	0.73	0.02	0.0903	0.0014	0.273	558	11	557	8	527	50	100
Z_BB9_6	269	63	0.2342	0.739	0.018	0.0902	0.0015	0.274	560	11	557	9	536	46	100
Z_BB9_7	270	63	0.2332	0.74	0.02	0.0906	0.0015	0.053	560	12	559	9	512	58	100
Z_BB9_8	270	63	0.2334	0.74	0.02	0.0906	0.0015	0.047	561	12	559	9	515	58	100
Z_BB9_9	270	63	0.2332	0.736	0.019	0.0909	0.0015	0.136	559	12	561	9	517	54	100
Z_BB9_10	270	63	0.2338	0.73	0.02	0.0895	0.0014	0.131	551	12	552	9	512	57	100
Z_BB9_11	270	63	0.2331	0.748	0.018	0.0919	0.0015	0.295	566	10	567	9	540	45	100
Z_BB9_12	270.9	63.1	0.2329	0.735	0.021	0.091	0.001	0.085	556	13	561	8	514	60	101
Z_BB9_13	269.7	62.9	0.2332	0.736	0.021	0.0910	0.0014	0.078	557	13	561	8	517	60	101
Z_BB9_14	270	63	0.2338	0.736	0.021	0.0908	0.0015	0.128	558	13	560	9	534	60	100
Z_BB9_1	267.7	63.3	0.2365	0.737	0.016	0.0917	0.0026	0.145	558	10	566	15	512	60	101
Z_BB9_2	275.6	65.4	0.2373	0.741	0.017	0.0909	0.0026	0.231	560	10	561	15	543	59	100
Z_BB9_3	268	62	0.2314	0.733	0.017	0.0903	0.0026	0.172	557	10	557	15	534	62	100
Z_BB9_4	269.8	61.9	0.2294	0.738	0.019	0.0898	0.0025	0.228	558	11	554	15	544	65	99
Z_BB9_5	269.9	61.4	0.2275	0.738	0.017	0.0915	0.0026	0.281	560	10	564	15	506	58	101
Z_BB9_6	270	63	0.2332	0.735	0.017	0.0900	0.0025	0.156	558	10	555	15	506	60	100
Z_BB9_7	270.1	64.9	0.2403	0.739	0.017	0.0912	0.0026	0.298	559	10	562	15	545	59	101
Z_BB9_8	269.8	62.9	0.2331	0.735	0.017	0.0915	0.0026	0.168	557	10	564	15	529	60	101
Z_BB9_9	270.1	61.6	0.2281	0.738	0.017	0.0905	0.0026	0.202	559	10	558	15	558	59	100
Z_BB9_10	270	63	0.2344	0.737	0.016	0.0918	0.0026	0.211	559	9	566	15	503	58	101

Z_BB9_11	269.8	61.8	0.2291	0.737	0.016	0.0897	0.0025	0.170	560	9	554	15	542	58	99
Z_BB9_12	270.2	65.1	0.2409	0.737	0.015	0.0898	0.0025	0.177	559	9	554	15	542	54	99
Z_BB9_13	270	63	0.2337	0.737	0.018	0.0923	0.0026	0.254	559	10	569	15	499	61	102
Z_BB9_14	269.9	61.9	0.2293	0.737	0.018	0.0909	0.0026	0.230	559	11	561	15	540	64	100
Z_BB9_15	270.1	64.4	0.2384	0.737	0.015	0.0910	0.0025	0.152	560	9	562	15	526	57	100
Z_BB9_16	270	61	0.2258	0.737	0.017	0.0897	0.0025	0.093	558	10	554	15	542	61	99
Z_BB9_17	270.1	65.9	0.2440	0.736	0.017	0.0910	0.0026	0.267	558	10	562	15	511	60	101
Z_BB9_18	270.2	62.9	0.2328	0.738	0.016	0.092	0.003	0.196	560	10	567	15	539	59	101
Z_BB9_19	269.6	63.2	0.2344	0.74	0.02	0.0908	0.0025	0.209	560	11	560	15	543	60	100
Z_BB9_20	270	62	0.2294	0.734	0.016	0.0899	0.0026	0.245	558	9	555	15	526	59	99
Z_BB9_1	276.3	65.2	0.2360	0.718	0.031	0.0905	0.0013	0.103	543	18	558	8	415	89	103
Z_BB9_2	263.6	60.8	0.2307	0.757	0.033	0.091	0.002	0.201	566	19	561	9	511	90	99
Z_BB9_3	265.9	61.6	0.2317	0.755	0.033	0.091	0.002	0.069	561	19	561	9	478	96	100
Z_BB9_4	273.9	64.1	0.2340	0.73	0.03	0.0909	0.0015	0.197	552	18	561	9	450	87	102
Z_BB9_5	272.5	63.9	0.2345	0.743	0.033	0.0909	0.0015	0.279	556	19	560	9	491	91	101
Z_BB9_6	265.1	61.6	0.2324	0.73	0.03	0.0904	0.0014	0.108	548	18	558	8	483	91	102
Z_BB9_7	274	64	0.2335	0.735	0.031	0.091	0.001	0.088	551	18	561	8	471	89	102
Z_BB9_8	265.9	61.7	0.2320	0.737	0.034	0.0907	0.0015	0.152	552	20	559	9	467	96	101
Z_BB9_9	279	66	0.2348	0.742	0.033	0.0912	0.0015	0.114	554	20	562	9	471	97	101
Z_BB9_10	268.8	62.2	0.2314	0.732	0.029	0.0905	0.0015	0.057	552	18	558	9	490	92	101
Z_BB9_11	263.6	61.9	0.2348	0.72	0.04	0.0906	0.0016	0.159	541	21	559	9	430	100	103
Z_BB9_12	263.5	61.4	0.2330	0.74	0.03	0.0912	0.0015	0.176	554	19	562	9	470	97	102
Z_BB9_13	279.3	64.7	0.2317	0.742	0.033	0.0903	0.0015	0.194	554	19	558	9	466	95	101
Z_BB9_14	274.2	62.6	0.2283	0.724	0.037	0.0912	0.0015	0.248	543	22	562	9	380	110	103
Z_BB9_15	275.8	66.2	0.2400	0.761	0.031	0.0905	0.0016	0.098	569	18	558	9	515	91	98
Z_BB9_16	266.1	62.7	0.2356	0.722	0.033	0.0911	0.0015	-0.019	551	19	562	9	390	100	102
Z_BB9_17	286	69	0.2416	0.74	0.03	0.0905	0.0015	0.190	555	20	558	9	477	94	101
Z_BB9_18	255.7	56.7	0.2217	0.74	0.03	0.0909	0.0015	0.098	556	20	561	9	480	97	101

Appendix B10: U-Pb ages of the zircon secondary standard (Plesovice)

Zircon secondary standard				Common-lead uncorrected ratios					Final Ages (Ma)						
Id	U (ppm)	Th (ppm)	Th/U	$^{207}Pb/^{235}U$	±2σ	$^{206}Pb/^{238}U$	±2σ	Rho	$^{207}Pb/^{235}U$	±2σ	$^{206}Pb/^{238}U$	±2σ	$^{207}Pb/^{206}Pb$	±2σ	Concord-ance (%)
PLESO - 1	548	37.52	0.068467	0.3862	0.0096	0.05401	0.00083	0.20666	331	7	339	5	263	46	102
PLESO - 3	584	40.97	0.070154	0.3803	0.0093	0.05342	0.00082	0.23852	327	7	335	5	246	46	103
PLESO - 4	577	42.12	0.072998	0.3851	0.0096	0.05377	0.00081	0.23645	330	7	338	5	252	47	102
PLESO - 5	570.1	39.02	0.068444	0.403	0.011	0.05443	0.00079	0.27583	343	8	342	5	335	50	100
PLESO - 1	559	38.64	0.069123	0.392	0.008	0.0534	0.0015	0.15425	335	6	335	9	317	57	100
PLESO - 2	529.4	37.03	0.069947	0.3859	0.0081	0.0540	0.0015	0.09609	331	6	339	9	273	58	103
PLESO - 3	539	36.13	0.067032	0.3876	0.0082	0.0529	0.0015	0.24432	332	6	332	9	291	55	100
PLESO - 4	568	37.97	0.066849	0.386	0.008	0.0538	0.0015	0.20393	331	6	338	9	288	56	102
PLESO - 5	546	36.88	0.067546	0.389	0.009	0.0535	0.0015	0.31134	333	7	336	9	292	58	101
PLESO - 6	559	38.5	0.068873	0.3968	0.0087	0.0544	0.0015	0.23029	338	6	342	9	320	56	101
PLESO - 2	522.8	34.91	0.066775	0.398	0.017	0.05359	0.00083	0.13851	338	12	336	5	311	90	100
PLESO - 4	560	38.19	0.068196	0.381	0.018	0.0545	0.0009	0.28796	326	13	342	6	178	91	105
PLESO - 5	501	33.02	0.065908	0.394	0.017	0.05471	0.00088	0.12928	333	13	343	5	199	92	103

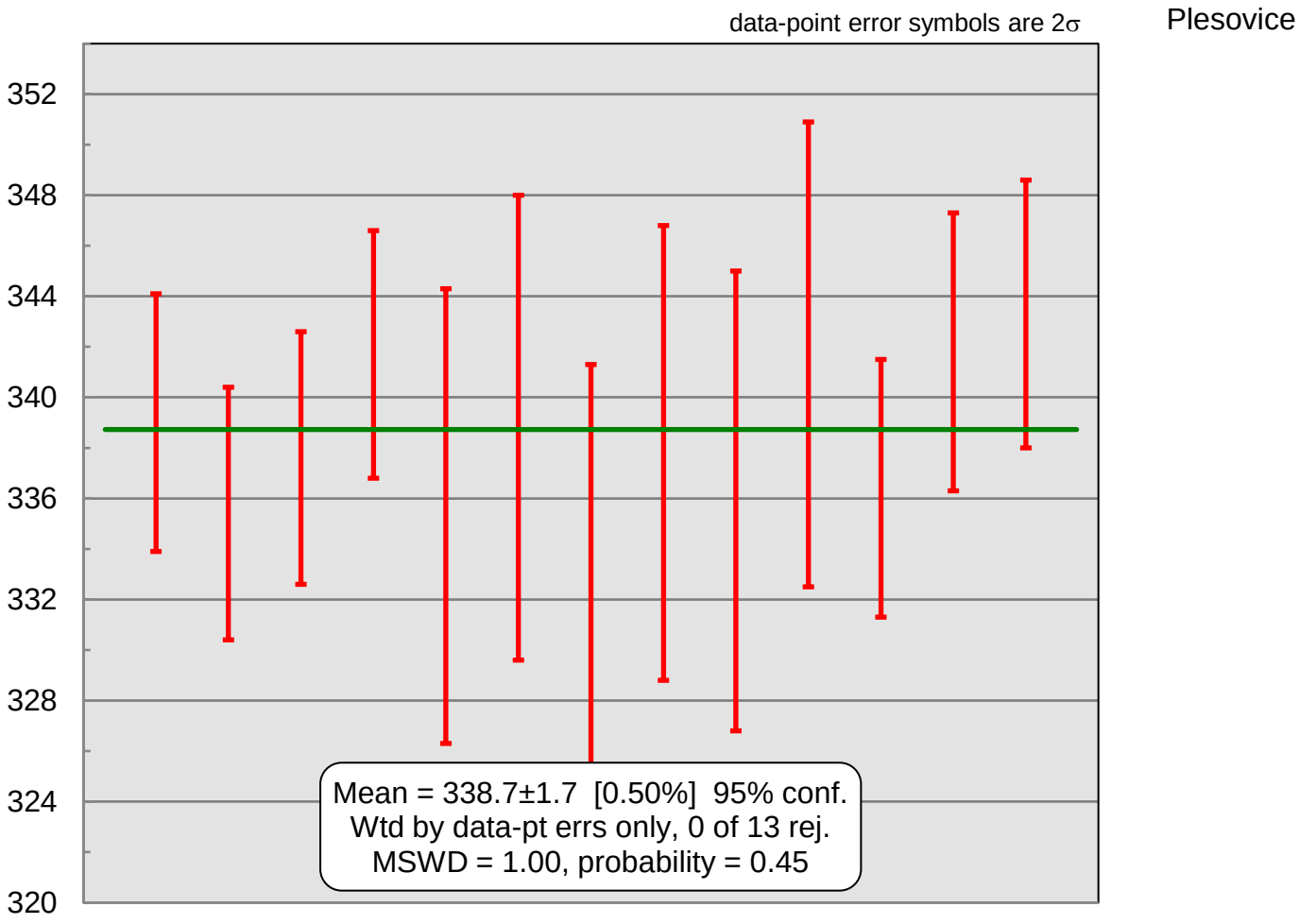
data-point error symbols are 2σ
Plesovice
352
348
344
340
336
332
328
324
320
Mean = 338.7±1.7 [0.50%] 95% conf.
Wtd by data-pt errs only, 0 of 13 rej.
MSWD = 1.00, probability = 0.45

Appendix B11: U-Pb ages of the zircon secondary standard (91500)

Zircon secondary standard				Common-lead uncorrected ratios					Final Ages (Ma)						
Id	U (ppm)	Th (ppm)	Th/U	$^{207}Pb/^{235}U$	±2σ	$^{206}Pb/^{238}U$	±2σ	Rho	$^{207}Pb/^{235}U$	±2σ	$^{206}Pb/^{238}U$	±2σ	$^{207}Pb/^{206}Pb$	±2σ	Concord-ance (%)
91500 - 1	71.6	18.2	0.25419	1.82	0.06	0.1788	0.0029	0.24329	1043	22	1060	16	985	61	102
91500 - 2	78.8	21.31	0.27043	1.861	0.062	0.177	0.003	0.06367	1056	22	1050	16	1015	67	99
91500 - 3	73.4	19.32	0.26322	1.818	0.058	0.178	0.003	0.09219	1042	21	1056	16	961	66	101
91500 - 4	72.2	19.14	0.26510	1.791	0.054	0.1777	0.0031	0.13948	1035	20	1054	17	961	62	102
91500 - 5	73.4	19.13	0.26063	1.869	0.058	0.1824	0.0031	0.15648	1064	21	1079	17	1014	63	101

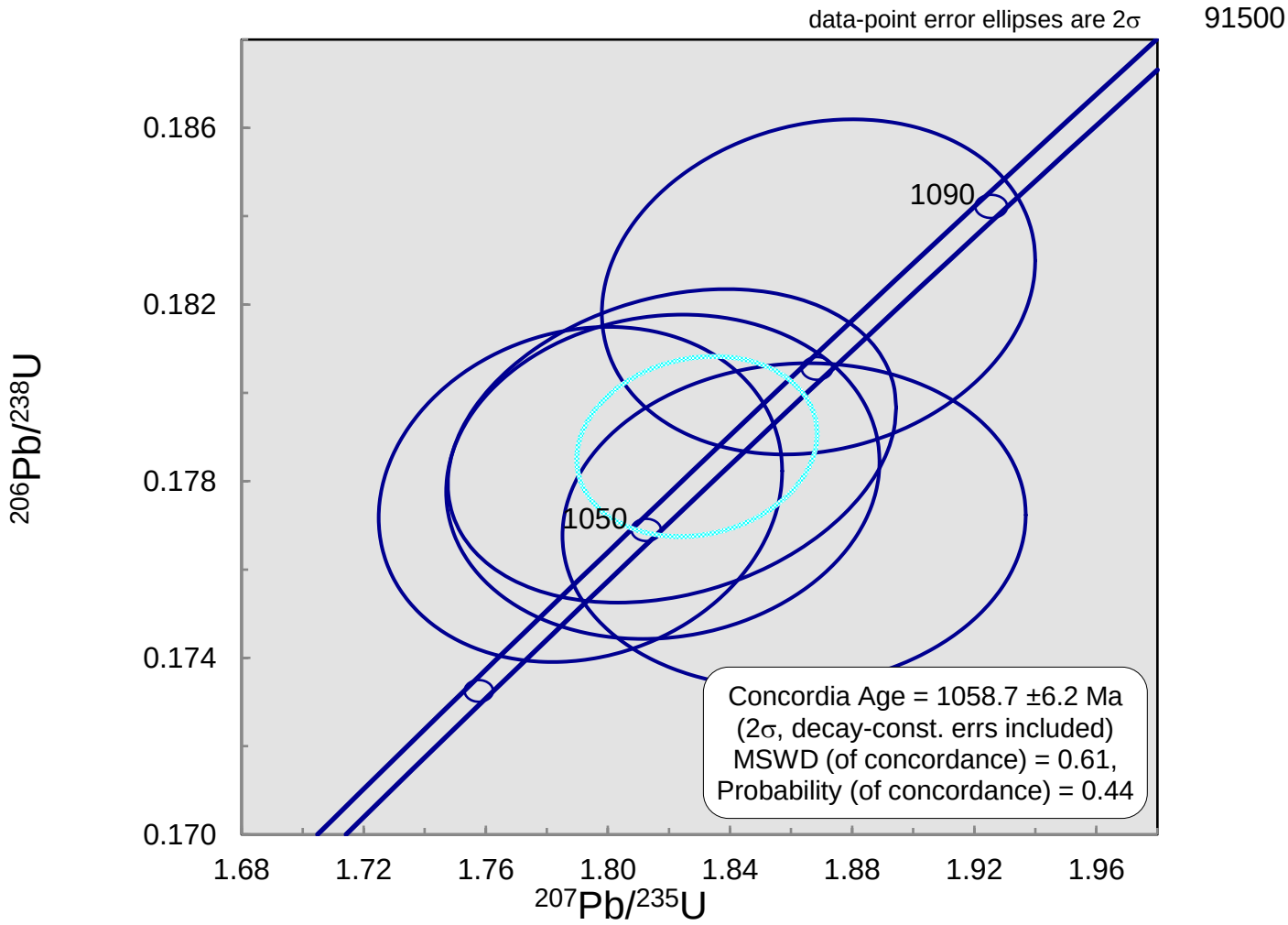
data-point error ellipses are 2σ
91500
0.186
0.182
0.178
0.174
0.170
1090
1050
Concordia Age = 1058.7 ±6.2 Ma
(2σ, decay-const. errs included)
MSWD (of concordance) = 0.61,
Probability (of concordance) = 0.44
1.68
1.72
1.76
1.80
1.84
1.88
1.92
1.96
206Pb/238U
207Pb/235U

Appendix B12: U-Pb ages of the zircon secondary standard (GJ-1)

Zircon secondary standard				Common-lead uncorrected ratios					Final Ages (Ma)						
Id	U (ppm)	Th (ppm)	Th/U	$^{207}Pb/^{235}U$	±2σ	$^{206}Pb/^{238}U$	±2σ	Rho	$^{207}Pb/^{235}U$	±2σ	$^{206}Pb/^{238}U$	±2σ	$^{207}Pb/^{206}Pb$	±2σ	Concord-ance (%)
GJ1 - 1	252.2	7.47	0.02962	0.804	0.022	0.0982	0.0016	0.2229	598	12	604	9	553	52	101
GJ1 - 2	235.9	7.47	0.03167	0.80	0.02	0.097	0.002	0.0908	594	12	596	9	534	54	100
GJ1 - 3	258.4	8.04	0.03111	0.785	0.019	0.0982	0.0015	0.0521	587	11	604	9	485	50	103
GJ1 - 4	249.9	7.89	0.03157	0.79	0.02	0.0972	0.0016	0.1535	587	11	598	9	514	50	102
GJ1 - 5	251.3	7.71	0.03068	0.833	0.021	0.0983	0.0016	0.2081	612	11	604	9	624	48	99
GJ1 - 1	245	7.55	0.03082	0.817	0.018	0.0980	0.0028	0.1711	603	10	602	16	598	60	100
GJ1 - 2	241.6	7.31	0.03026	0.806	0.018	0.0989	0.0028	0.2645	597	10	608	16	556	57	102
GJ1 - 3	245.4	7.25	0.02954	0.785	0.019	0.0954	0.0027	0.3036	586	10	587	16	534	59	100
GJ1 - 4	252.6	7.38	0.02922	0.829	0.019	0.0997	0.0028	0.2518	610	11	613	16	597	59	100
GJ1 - 5	241.5	7.13	0.02952	0.807	0.019	0.0984	0.0027	0.1922	598	11	605	16	542	60	101
GJ1 - 6	243.7	7.27	0.02983	0.794	0.018	0.0960	0.0027	0.1976	591	10	591	16	571	59	100
GJ1 - 1	220.5	6.51	0.02952	0.851	0.039	0.0974	0.0018	0.2309	614	22	599	10	578	96	98
GJ1 - 2	230.5	6.88	0.02985	0.813	0.038	0.0998	0.0017	0.0871	595	21	613	10	487	99	103
GJ1 - 5	242.8	7.07	0.02912	0.792	0.038	0.0969	0.0017	0.1813	582	22	596	10	450	100	102

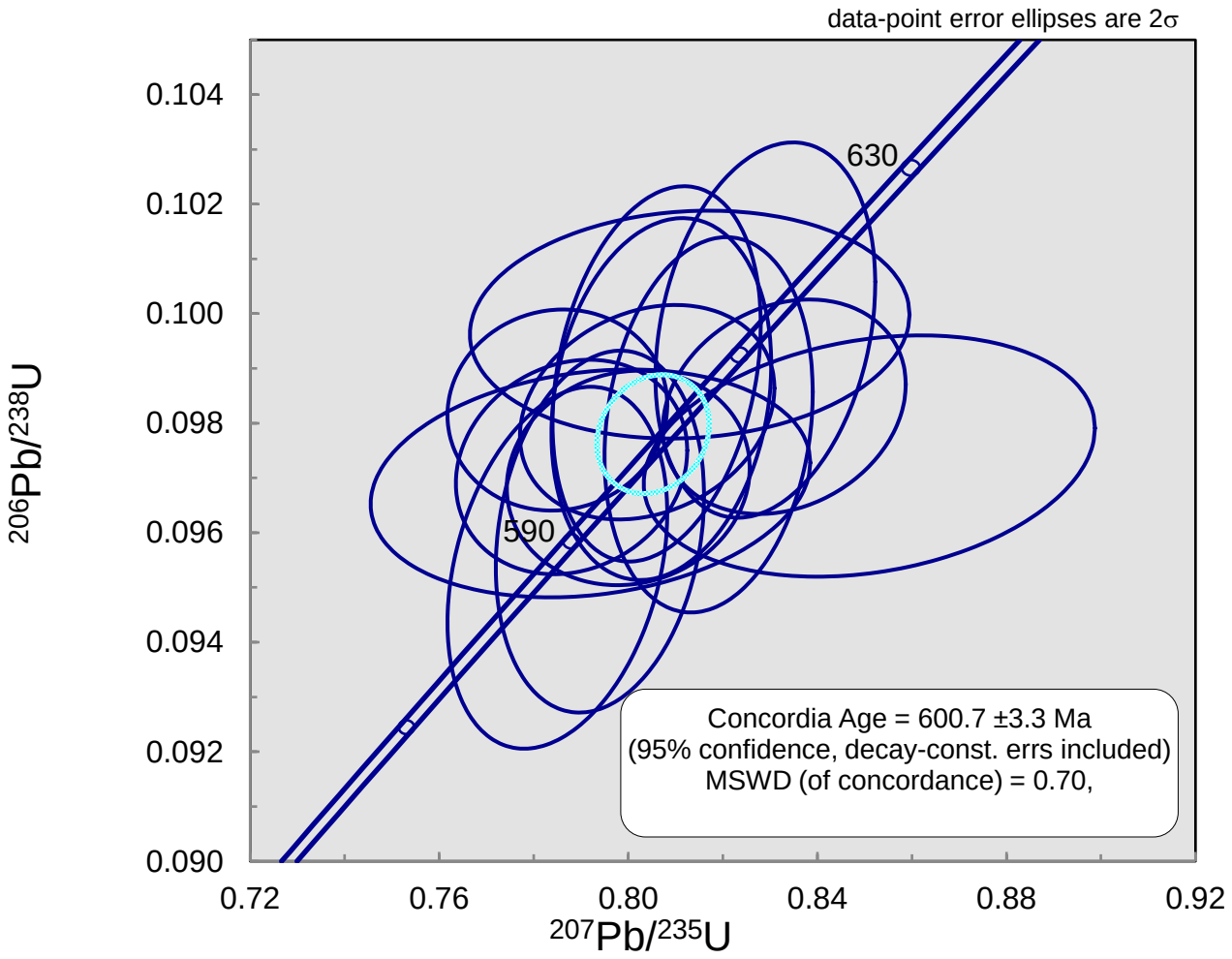
data-point error ellipses are 2σ
GJ-1
0.104
0.102
0.100
0.098
0.096
0.094
0.092
0.090
630
590
Concordia Age = 600.7 ±3.3 Ma
(95% confidence, decay-const. errs included)
MSWD (of concordance) = 0.70,
0.72
0.76
0.80
0.84
0.88
0.92
206Pb/238U
207Pb/235U

APPENDIX C – U-Pb data used in Chapter 5

Appendix C1 – LA-ICP-MS U–Pb zircon data of the Figueira de Castelo Rodrigo – Lumbrales Anatectic Complex granites

				Common-lead uncorrected					Final Ages (Ma)						
Id	U (ppm)	Th (ppm)	Th/U	$^{207}Pb/^{235}U$	±2σ	$^{206}Pb/^{238}U$	±2σ	Rho*	$^{207}Pb/^{235}U$	±2σ	$^{206}Pb/^{238}U$	±2σ	$^{207}Pb/^{206}Pb$	±2σ	Concordance (%)**
São Pedro-Vieiro granite (IIγ) Lat: 40.853; Long: -7.132															
M7_36_4c	273	94	0.34	0.336	0.016	0.0468	0.00089	0.0009	292	12	295	6	235	93	101
M7_36_11c	819	54	0.07	0.355	0.013	0.04742	0.00076	0.0008	308	10	299	5	354	71	97
M7_36_18c	377	104	0.28	0.344	0.015	0.0478	0.00086	0.0009	299	11	301	5	259	88	101
M7_36_5c	312	170	0.54	0.354	0.015	0.04826	0.00086	0.0009	307	11	304	5	295	86	99
M7_36_3e	383	125	0.33	0.341	0.021	0.0472	0.0012	0.03	293	16	297	7	230	130	102
Ribeira de Massueime-Galegos granite (IIIγ) Lat: 40.917; Long: -7.011															
M5_13_2b	1489	26	0.02	0.369	0.038	0.0502	0.0012	0.18	316	28	316	7	263	190	100
M5_13_1c	1163	39	0.03	0.370	0.038	0.0508	0.0012	0.29	317	28	320	7	252	180	101
M7_13_15e	1195	69	0.06	0.348	0.011	0.0489	0.0011	0.13	301	8	308	7	337	76	102
M5_13_2c	737	9	0.01	0.3684	0.0084	0.05	0.0007	0.0007	318	6	314	4	323	48	99
Chãs-Amargo granite (Vγ) Lat: 40.944; Long: -7.014															
M6_12_6e	1369	323	0.24	0.37	0.03	0.0516	0.0012	0.23	318	23	325	7	235	170	102
M6_12_2e	1285	6	0.005	0.36	0.03	0.0506	0.0012	0.18	313	22	318	8	248	180	102
M6_12_1c	1638	186	0.11	0.361	0.015	0.049	0.001	0.001	313	12	311	6	307	98	99
M6_12_19e	757	7	0.01	0.361	0.031	0.049	0.0012	0.33	310	23	308	8	280	180	99
M1_12_6	2479	24	0.01	0.382	0.015	0.05029	0.00058	0.0006	328	11	316	4	436	74	96
Mêda-Escalhão granite (IXγ) Lat: 40.923; Long: -6.91															
M6_45_3e	1158	152	0.13	0.363	0.029	0.0504	0.0012	0.25	313	22	317	7	258	180	101
M4_45_8c	10890	44	0.004	0.3658	0.0059	0.0505	0.0015	0.48	316	4	318	9	285	32	101
M4_45_2	2570	256	0.10	0.3678	0.0055	0.05082	0.00067	0.0007	318	4	320	4	303	27	100
M6_45_1c	1215	117	0.10	0.364	0.016	0.05	0.001	0.001	316	12	313	6	327	99	99
Sta. Comba-Algodres granite (Xγ) Lat: 40.911; Long: -7.11															
M6_34_15c	1624	327	0.20	0.364	0.015	0.049	0.001	0.001	314	11	307	6	364	97	98
M6_34_11c	1543	353	0.23	0.349	0.015	0.04894	0.00099	0.001	303	11	308	6	254	97	102
M6_34_15e	2304	629	0.27	0.364	0.0098	0.04901	0.00069	0.11	314	7	308	4	317	61	98
M6_34_10e	951	64	0.07	0.356	0.013	0.04919	0.00068	0.29	307	10	310	4	256	74	101
M6_34_29e	1662	220	0.13	0.351	0.028	0.0492	0.0011	0.16	305	21	310	7	253	180	102
M6_34_26c	815.2	159	0.19	0.381	0.017	0.049	0.001	0.001	327	12	311	6	426	100	95

M6_34_30e	1742	271	0.16	0.369	0.029	0.0495	0.0012	0.30	318	21	312	7	340	170	98
M6_34_1e	2146	15230	7.10	0.3789	0.0099	0.04964	0.00064	0.20	325	7	312	4	369	56	96
M6_34_11e	1471	191	0.13	0.35	0.01	0.04971	0.00068	0.21	300	8	313	4	195	63	104
M6_34_23c	1256	198	0.16	0.366	0.016	0.05	0.001	0.001	317	12	313	6	329	100	99
M6_34_10c	1882	38	0.02	0.382	0.016	0.05	0.001	0.001	328	12	313	6	426	97	95
M6_34_14e	1635	335	0.20	0.37	0.012	0.0498	0.0006	0.15	318	9	314	4	299	68	99
M6_34_14c	1195	90	0.08	0.364	0.016	0.05	0.001	0.001	315	12	315	6	295	98	100
M6_34_24e	2004	17	0.01	0.363	0.029	0.05	0.0012	0.31	313	21	315	7	288	170	100
M6_34_27c	1080	3950	3.66	0.373	0.016	0.05	0.001	0.001	321	12	315	6	348	99	98
M6_34_5e	1623	225	0.14	0.370	0.012	0.05038	0.00068	0.28	318	9	317	4	274	66	100
M6_34_25c	1254	2210	1.76	0.375	0.016	0.05	0.001	0.001	323	12	318	6	344	100	98
M6_34_13c	1508	249	0.16	0.364	0.016	0.051	0.001	0.001	316	11	318	6	272	98	101
M6_34_33c	908	165	0.18	0.379	0.017	0.051	0.001	0.001	325	13	318	6	357	100	98
M6_34_22c	1308	173	0.13	0.374	0.016	0.051	0.001	0.001	322	12	320	6	320	100	99

* Rho is calculated by Iolite package software and it corresponds to the correlation between the given errors of the $^{207}Pb/^{235}U$ and $^{206}Pb/^{238}U$ ratios.
**Concordance = ($^{206}Pb/^{238}U$ age) / ($^{207}Pb/^{235}U$ age) x 100

Appendix C2 – LA-ICP-MS U–Pb inherited zircon data of the Figueira de Castelo Rodrigo – Lumbrales Anatectic Complex granites

				Common-lead uncorrected					Final Ages (Ma)						
Id	U (ppm)	Th (ppm)	Th/U	$^{207}Pb/^{235}U$	±2σ	$^{206}Pb/^{238}U$	±2σ	Rho*	$^{207}Pb/^{235}U$	±2σ	$^{206}Pb/^{238}U$	±2σ	$^{207}Pb/^{206}Pb$	±2σ	Concordance (%)**
São Pedro-Vieiro granite (IIγ)															
M7_36_2c	537	28	0.05	0.531	0.023	0.0692	0.0019	0.002	429	15	431	11	409	70	100
M7_36_19c	552	126	0.23	0.589	0.021	0.0744	0.0013	0.001	469	14	463	8	474	71	99
M7_36_9c	282	106	0.38	0.573	0.023	0.0752	0.0013	0.001	458	15	468	8	385	80	102
M7_36_15c	690	344	0.50	0.602	0.021	0.0772	0.0014	0.001	477	13	479	8	452	69	100
M7_36_12c	578	158	0.27	0.659	0.023	0.0806	0.0013	0.001	512	14	500	8	547	69	98
M7_36_13c	1060	297	0.28	0.698	0.023	0.0866	0.0014	0.001	537	14	536	8	537	62	100
M7_36_1c	310	250	0.81	0.718	0.027	0.0901	0.0016	0.002	548	16	556	9	494	75	102
M7_36_14c	455	316	0.69	0.77	0.028	0.0908	0.0016	0.002	578	16	560	10	635	71	97
M7_36_8c	504	314	0.62	0.751	0.026	0.0913	0.0016	0.002	568	15	564	10	574	64	99

M7_36_10c	317	128	0.40	0.82	0.031	0.0999	0.0017	0.002	605	17	614	10	552	73	101
M7_36_14e	146	90	0.62	6.25	0.19	0.3821	0.0099	0.43	1997	26	2082	46	1907	54	109
Ribeira de Massueime-Galegos granite (IIIγ)															
M7_13_11e	365	66	0.18	0.582	0.032	0.0782	0.0024	0.28	457	20	485	14	370	110	106
M7_13_6c	336	101	0.30	0.725	0.027	0.0861	0.0015	0.002	553	16	532	9	612	74	96
M7_13_7c	1101	314	0.28	0.71	0.023	0.0872	0.0014	0.001	544	14	539	8	553	60	99
M7_13_12c	469	250	0.53	0.716	0.026	0.0884	0.0015	0.002	547	15	546	9	531	70	100
M5_13_4	690	512	0.74	0.853	0.085	0.0997	0.0024	0.002	623	46	613	14	605	180	98
Chãs-Amargo granite (Vγ)															
M6_12_18e	647	1	0.002	0.512	0.042	0.0656	0.0016	0.11	417	28	409	10	424	180	98
M6_12_15e	412	84	0.20	0.479	0.044	0.0669	0.0023	0.42	398	32	417	14	265	190	105
M6_12_20e	1199	177	0.15	0.5	0.04	0.0669	0.0016	0.19	414	27	418	10	366	170	101
M6_12_5e	1043	132	0.13	0.507	0.041	0.0678	0.0017	0.35	415	28	423	10	346	180	102
M6_12_15c	457	35	0.08	0.567	0.027	0.0714	0.0015	0.002	456	17	444	9	472	110	98
M1_12_8	263	256	0.97	0.666	0.031	0.0843	0.0012	0.001	516	20	522	7	486	94	101
M1_12_1a	556	226	0.41	0.755	0.032	0.0925	0.0012	0.001	569	19	570	7	485	82	100
M1_12_7	97	84	0.87	0.76	0.045	0.0928	0.0017	0.002	566	26	572	10	510	120	101
M6_12_21e	788	213	0.27	0.821	0.066	0.0953	0.0023	0.30	605	36	587	13	656	170	97
M1_12_2	150	142	0.95	0.808	0.044	0.0971	0.0015	0.002	593	25	597	9	496	110	101
M6_12_11c	335	282	0.84	0.798	0.037	0.098	0.002	0.002	594	21	600	12	542	100	101
M6_12_19c	527	336	0.64	0.82	0.036	0.098	0.002	0.002	607	21	603	12	600	100	99
M6_12_23c	1653	130	0.08	0.832	0.034	0.099	0.002	0.002	614	19	606	12	634	92	99
M6_12_17c	186	104	0.56	0.837	0.041	0.1015	0.0023	0.002	616	23	623	13	550	110	101
M6_12_16c	342	129	0.38	1.232	0.054	0.1349	0.0028	0.003	814	24	815	16	784	94	100
M6_12_14c	162	112	0.69	12.35	0.52	0.4769	0.0098	0.010	2629	38	2512	43	2704	71	93
Mêda-Escalhão granite (IXγ)															
M6_45_6e	1385	2	0.001	0.609	0.048	0.0766	0.0017	0.22	481	30	476	10	479	170	99
M4_45_8a	611	169	0.28	0.766	0.029	0.094	0.003	0.003	572	17	578	17	521	79	101

M4_45_1	162	55	0.34	0.796	0.024	0.097	0.0016	0.002	592	13	596	9	561	64	101
M4_45_3	221	113	0.51	0.891	0.024	0.1057	0.0016	0.002	643	13	648	9	599	59	101
M4_45_5	151	75	0.50	1.015	0.062	0.1249	0.0042	0.004	692	32	758	24	450	130	110
Sta. Comba-Algodres granite (Xγ)															
M6_34_8c	238	129	0.54	0.813	0.039	0.0976	0.0021	0.002	601	21	600	12	564	100	100
M6_34_12c	263	389	1.48	0.926	0.039	0.1061	0.0017	0.02	654	21	650	10	609	95	99
M6_34_29c	73	36	0.49	1.03	0.06	0.1197	0.0029	0.003	713	30	728	17	613	130	102

*Rho is calculated by Iolite package software and it corresponds to the correlation between the given errors of the $^{207}Pb/^{235}U$ and $^{206}Pb/^{238}U$ ratios.
**Concordance = ($^{206}Pb/^{238}U$ age) / ($^{207}Pb/^{235}U$ age) x 100 – for ages <900 Ma
= ($^{206}Pb/^{238}U$ age) / ($^{207}Pb/^{206}Pb$ age) x 100 – for ages >900 Ma

Appendix C3 – LA-ICP-MS U–Pb apatite data of the Figueira de Castelo Rodrigo – Lumbrales Anatectic Complex granites

									Final Ages (Ma)**			
Id	U (ppm)	Pb (ppm)	$^{206}Pb_{cm}$	$^{238}U/^{206}Pb$	±2σ	$^{207}Pb/^{206}Pb$	±2σ	Rho*	$^{207}Pb/^{235}U$	±2σ	$^{206}Pb/^{238}U$	±2σ
São Pedro-Vieiro granite (IIγ)												
M4_36_1	111	10	0.36	13.4	0.29	0.3393	0.0029	0.56	1523	17	464	10
M4_36_10	299	11	0.18	16.98	0.37	0.1991	0.0021	0.46	978	15	369	8
M4_36_2	99	10	0.38	13.22	0.30	0.3572	0.0048	0.32	1574	20	470	10
M4_36_3	246	10	0.19	16.96	0.37	0.2073	0.0018	0.31	1002	14	369	8
M4_36_4	79	12	0.50	11.13	0.26	0.4357	0.0052	0.54	1879	20	554	12
M4_36_5	51	9	0.54	10.18	0.23	0.472	0.005	0.63	2029	20	604	13
M4_36_6	359	13	0.18	17.32	0.36	0.195	0.0012	0.40	951	13	362	8
M4_36_7	311	11	0.16	17.39	0.36	0.1892	0.0014	0.32	930	13	361	8
M4_36_8	262	13	0.23	16.19	0.34	0.2352	0.0016	0.43	1116	15	386	8
M4_36_9	65	9	0.48	11.15	0.25	0.4212	0.0045	0.37	1852	20	554	12
M4_36_11	116	11	0.25	15.45	0.24	0.2587	0.0024	0.38	1213	12	404	6
M4_36_12	181	10	0.22	16.36	0.25	0.2267	0.0021	0.32	1084	11	383	6
M4_36_13	88	9	0.51	9.94	0.16	0.4691	0.0056	0.51	2043	15	618	10

M4_36_14	225	12	0.64	7.91	0.13	0.5522	0.0072	0.53	2395	17	767	12
M4_36_16	293	13	0.19	17.14	0.26	0.1979	0.0016	0.32	967	10	366	5
M4_36_17	54	10	0.22	16.36	0.25	0.222	0.002	0.29	1068	11	382	6
M4_36_18	42	11	0.35	13.63	0.20	0.3369	0.0032	0.54	1505	13	456	7
M4_36_19	317	11	0.39	12.48	0.19	0.3743	0.0032	0.51	1660	13	497	7
M4_36_20	295	13	0.38	12.23	0.19	0.3763	0.0037	0.54	1680	14	507	8
Ribeira de Massueime-Galegos granite (IIIγ)												
M5_13_1	62	10	0.19	10.55	0.23	0.4309	0.0072	0.58	1919	19	584	12
M5_13_2	59	9	0.20	10.85	0.24	0.431	0.009	0.60	1893	19	568	12
M5_13_3	61	12	0.22	9.05	0.20	0.4806	0.0094	0.21	2150	22	675	15
M5_13_4	36	12	0.25	7.09	0.16	0.5756	0.0102	0.56	2536	20	851	18
M5_13_5	70	9	0.17	11.49	0.25	0.4034	0.0066	0.40	1792	19	538	11
M5_13_6	48	12	0.23	8.48	0.19	0.52	0.01	0.53	2281	20	719	15
M5_13_8	61	9	0.18	10.64	0.27	0.4409	0.0152	0.53	1930	22	579	14
M5_13_9	89	11	0.17	11.64	0.26	0.3950	0.0062	0.49	1762	18	531	11
M5_13_12	87	11	0.16	12.53	0.20	0.3827	0.0076	0.19	1674	15	495	8
M5_13_13	78	10	0.14	14.03	0.22	0.326	0.007	0.42	1458	13	444	7
M5_13_14	67	10	0.26	8.01	0.15	0.558	0.0132	0.09	2393	20	759	13
M5_13_15	497	100	0.15	13.56	0.22	0.3492	0.0064	0.39	1536	13	459	7
M5_13_16	75	11	0.16	13.72	0.23	0.3542	0.0098	0.39	1536	15	454	7
M5_13_17	80	10	0.14	13.59	0.31	0.3518	0.0186	-0.60	1530	34	458	10
M5_13_20	61	9	0.20	10.46	0.18	0.4589	0.0116	0.61	1979	15	588	10
Chãs-Amargo granite (Vγ)												
M1_12_1	98	20	0.55	9.42	0.20	0.4846	0.0029	0.54	2121	19	650	13
M1_12_10	92	10	0.40	12.41	0.28	0.372	0.0037	-0.06	1659	20	500	11
M1_12_2	94	11	0.38	12.47	0.26	0.361	0.003	0.50	1630	18	497	10
M1_12_3	106	15	0.49	11.58	0.25	0.445	0.004	0.55	1869	19	534	12
M1_12_4	176	15	0.33	13.78	0.28	0.3137	0.0019	0.40	1442	17	452	9

M1_12_5	155	13	0.31	13.87	0.29	0.3076	0.0022	0.33	1421	17	449	9
M1_12_6	95	19	0.54	9.38	0.20	0.4878	0.0031	0.40	2132	19	653	13
M1_12_7	95	18	0.53	9.6	0.20	0.4811	0.0029	0.36	2097	19	639	13
M1_12_8	69	7	0.36	12.86	0.28	0.3544	0.0031	0.49	1592	18	483	10
M1_12_9	59	13	0.58	9.0	0.20	0.4985	0.0041	0.10	2188	21	679	14
M1_12_11	89	20	0.55	8.78	0.20	0.5123	0.0048	0.57	2233	21	695	15
M1_12_12	84	16	0.52	9.62	0.22	0.4794	0.0053	0.47	2095	21	639	15
M1_12_13	98	11	0.40	12.37	0.29	0.3652	0.0041	0.32	1647	20	501	11
M1_12_14	12	23	0.94	1.62	0.04	0.781	0.0082	0.21	4277	26	3104	61
M1_12_15	85	15	0.51	9.94	0.23	0.4665	0.0047	0.50	2039	21	618	14
M1_12_16	80	12	0.50	10.5	0.24	0.4421	0.0043	0.53	1944	20	586	13
M1_12_17	90	12	0.45	11.16	0.25	0.413	0.004	0.61	1834	20	553	12
M1_12_18	94	14	0.46	10.7	0.24	0.4301	0.0038	0.46	1906	20	576	13
M1_12_19	130	18	0.45	10.94	0.29	0.401	0.005	-0.22	1824	26	564	14
M1_12_20	90	12	0.42	11.38	0.26	0.3918	0.0039	0.56	1773	20	543	12
M1_12_21	99	17	0.43	10.05	0.27	0.463	0.008	0.56	2018	24	611	16
M1_12_22	85	24	0.57	7.63	0.20	0.557	0.0082	0.55	2436	25	794	20
M1_12_23	97	15	0.42	10.42	0.28	0.4501	0.0075	0.31	1959	25	591	15
M1_12_24	83	15	0.47	9.77	0.27	0.485	0.008	0.58	2082	25	628	16
M1_12_25	84	15	0.64	9.98	0.29	0.4779	0.0092	0.57	2049	26	615	17
Mêda-Escalhão granite (IXγ)												
M4_45_1	141	11	0.32	13.92	0.29	0.3122	0.0024	0.39	1429	17	447	9
M4_45_10	141	16	0.41	12.44	0.26	0.376	0.0022	0.40	1668	18	498	10
M4_45_2	114	15	0.41	11.75	0.25	0.4012	0.0027	0.54	1767	18	527	11
M4_45_3	139	12	0.34	13.54	0.29	0.325	0.0024	0.55	1481	17	459	10
M4_45_4	140	18	0.43	11.87	0.25	0.3946	0.0024	0.48	1746	18	522	11
M4_45_5	138	14	0.37	12.68	0.27	0.356	0.0024	0.43	1606	18	489	10
M4_45_6	138	18	0.42	11.72	0.25	0.3958	0.0022	0.58	1759	18	528	11

M4_45_7	115	15	0.42	11.75	0.25	0.3977	0.0027	0.55	1760	18	526	11
M4_45_8	146	15	0.36	12.79	0.28	0.3564	0.0027	0.41	1600	18	485	10
M4_45_9	136	14	0.39	12.88	0.28	0.356	0.0025	0.26	1594	18	482	10
M4_45_11	159	14	0.44	11.67	0.18	0.4123	0.0036	0.56	1796	13	530	8
M4_45_14	126	17	0.40	11.66	0.18	0.3791	0.0035	0.51	1725	14	530	8
M4_45_15	128	15	0.67	6.49	0.13	0.6188	0.0075	0.08	2684	21	924	17
M4_45_16	33	12	0.40	12.6	0.19	0.3699	0.0036	0.51	1641	13	492	7
M4_45_18	135	13	0.34	13.25	0.21	0.35	0.0036	0.51	1558	13	469	7
M4_45_19	282	18	0.25	15.08	0.23	0.2729	0.0023	0.51	1269	11	414	6
M4_45_20	130	14	0.41	12.58	0.19	0.374	0.0034	0.53	1653	13	493	7
M4_45_21	153	15	0.39	13.07	0.34	0.3421	0.0054	0.57	1545	22	475	12
M4_45_22	55	8	0.62	10.88	0.32	0.431	0.011	0.45	1884	28	567	16
M4_45_23	123	19	0.49	10.17	0.28	0.4232	0.0067	0.46	1930	25	604	16
M4_45_24	149	15	0.40	12.7	0.34	0.3512	0.0052	0.49	1589	22	488	13
M4_45_25	138	16	0.38	12.11	0.32	0.3784	0.0054	0.41	1690	23	511	13
Sta. Comba-Algodres granite (Xγ)												
M4_34_1	38.24	8.359	0.57	9.08	0.20	0.5113	0.0057	0.57	2201	20	673	14
M4_34_10	44.61	8.646	0.53	9.62	0.21	0.4816	0.0047	0.51	2097	20	638	14
M4_34_2	35.45	8.788	0.60	8.36	0.18	0.5302	0.0055	0.57	2308	20	728	15
M4_34_3	53.08	8.5	0.46	10.63	0.24	0.4365	0.0043	0.70	1924	19	580	12
M4_34_4	54.59	8.46	0.45	10.7	0.24	0.4217	0.0041	0.46	1890	19	576	12
M4_34_5	57.54	8.24	0.48	11.24	0.24	0.419	0.004	0.51	1839	19	549	11
M4_34_6	54.41	9.529	0.49	10.19	0.22	0.4586	0.0037	0.43	2003	19	603	13
M4_34_7	43.07	8.873	0.55	9.35	0.20	0.4952	0.0047	0.66	2146	20	655	14
M4_34_8	54.15	8.225	0.49	10.89	0.24	0.4298	0.0043	0.50	1889	19	566	12
M4_34_9	48.22	8.475	0.52	10.14	0.23	0.4604	0.0049	0.64	2010	19	606	13
M4_34_12	55.07	8.82	0.68	6.86	0.11	0.595	0.006	0.54	2600	16	877	13
M4_34_13	52.78	8.571	0.74	5.63	0.09	0.6467	0.0063	0.59	2864	16	1053	16

M4_34_14	48.76	8.42	0.75	5.56	0.10	0.6421	0.0074	0.57	2869	16	1065	17
M4_34_15	52.77	8.349	0.72	6.62	0.11	0.6046	0.0063	0.55	2649	16	907	14
M4_34_16	45.28	8.54	0.35	13.41	0.22	0.3476	0.0039	0.10	1542	16	464	7
M4_34_17	38.68	9.23	0.26	15.75	0.25	0.259	0.0034	0.06	1202	14	397	6
M4_34_19	51.81	8.844	0.37	12.6	0.21	0.3749	0.0043	0.45	1653	14	492	8
M4_34_20	53.53	8.96	0.24	15.87	0.24	0.2465	0.0024	0.21	1160	12	394	6
M4_34_21	54.86	8.97	0.49	10.5	0.30	0.4455	0.0091	0.60	1940	25	586	16
M4_34_22	39.26	8.8	0.51	8.94	0.26	0.519	0.012	0.57	2214	28	683	19
M4_34_23	40.62	8.34	0.45	9.48	0.28	0.498	0.011	0.56	2127	28	647	19
M4_34_24	54.88	9.63	0.56	10.07	0.28	0.4551	0.0086	0.49	1998	26	610	17

*Rho is calculated by Iolite package software and it corresponds to the correlation between the given errors of the $^{238}U/^{206}Pb$ and $^{207}Pb/^{206}Pb$ ratios.
**Pb_{cm} not corrected

APPENDIX D – Calculation of uncertainties associated with the cooling rates

The cooling rate uncertainty is defined as:

$$\text{maximum cooling rate} - \text{minimum cooling rate} / 2$$

where maximum and minimum cooling rate is calculated following the respective expressions:

$$\text{maximum cooling rate: } [(X+x) - (Y-y)] / [(A-a) - (B+b)]$$

$$\text{minimum cooling rate: } [(X-x) - (Y+y)] / [(A+a) - (B-b)]$$

When the difference of the mineral ages, used in the calculations of the maximum cooling rate, is negative it is necessary apply the following expression to obtain the maximum cooling rate:

$$[(X-Y) / (A-B)] - [(X-x) - (Y+y)] / [(A+a) - (B-b)]$$

Where:

X – Zircon closure temperature;

x – Zircon closure temperature error;

Y – Apatite closure temperature;

y – Apatite closure temperature error;

A – Zircon age;

a – Zircon age error;

B – Apatite age;

b – Apatite age error.

For zircon closure temperature we consider Ti-in-zircon estimates using Watson et al. (2006), with an estimated error based on maximum and minimum temperatures / 2.

For the apatite closure temperature, we consider published values from Cherniak et al. (1991) compiled by Hodges (2003). The estimated error is calculated using the difference between the published value and the internal calibration for the equation using the spreadsheet from Maeda et al. (2011) divided by 2.

APPENDIX E - U-Pb data used in Chapter 6

Appendix E1: LA-ICP-MS U–Pb zircon data of the Figueira de Castelo Rodrigo – Lumbrales Anatectic Complex migmatites

				Common-lead uncorrected					Final Ages (Ma)						
Id	U (ppm)	Th (ppm)	Th/U	$^{207}Pb/^{235}U$	±2σ	$^{206}Pb/^{238}U$	±2σ	Rho	$^{207}Pb/^{235}U$	±2σ	$^{206}Pb/^{238}U$	±2σ	$^{207}Pb/^{206}Pb$	±2σ	Concord-ance (%)*
Metatexite (JTJ-25)															
M2_25_2	1378	4.5	0.0032	0.373	0.012	0.0503	0.0015	0.002	321	9	316	9	319	70	99
M2_25_1	1455	4.4	0.0030	0.3699	0.0061	0.05073	0.00068	0.001	319	5	319	4	321	30	100
M6_25_2c	1382	3.9	0.0028	0.361	0.016	0.050	0.001	0.001	312	12	314	6	283	97	101
M6_25_3c	1289	5.2	0.0040	0.359	0.016	0.050	0.001	0.001	312	12	315	6	272	98	101
M6_25_5c	1252	4.0	0.0032	0.360	0.016	0.050	0.001	0.001	312	12	315	6	275	98	101
M6_25_4c	1458	4.3	0.0030	0.359	0.015	0.050	0.001	0.001	311	11	315	6	275	99	101
M6_25_6c	2027	5.6	0.0028	0.362	0.015	0.050	0.001	0.001	313	11	317	6	276	97	101
M6_25_1c	1394	5.6	0.0040	0.356	0.015	0.050	0.001	0.001	309	11	316	6	263	97	102
M6_25_10c	1392	4.2	0.0030	0.355	0.015	0.050	0.001	0.001	308	11	315	6	246	98	102
M6_25_7c	1047	3.4	0.0033	0.361	0.016	0.0510	0.0011	0.001	313	12	320	7	253	99	102
M6_25_10e	1281	3.9	0.0030	0.357	0.011	0.04929	0.00064	0.287	309	8	310	4	263	62	100
M6_25_1e	1550	3.9	0.0025	0.366	0.011	0.0497	0.0006	0.205	315	8	313	4	307	63	99
M6_25_2e	1873	3.9	0.0021	0.3685	0.0099	0.04953	0.00063	0.254	317	7	312	4	326	58	98
Diatexite (JTJ-24A)															
M1_24A_48	12370	29	0.002	0.4004	0.0057	0.0547	0.0016	0.002	342	4	344	10	317	29	101
M1_24A_38	10900	31	0.003	0.413	0.007	0.0546	0.0016	0.002	350	5	343	10	361	34	98
M1_24A_5	8790	7	0.001	0.4002	0.0066	0.0539	0.0015	0.002	341	5	338	9	344	33	99
Diatexite (JTJ-43)															
M7_43_12e	5640	5.2	0.001	0.3822	0.0069	0.0527	0.0011	0.39	328	5	331	7	281	50	101
M7_43_1e	748	8.2	0.011	0.383	0.018	0.0523	0.0013	0.08	325	13	328	8	271	100	101
M7_43_10e	1137	8.3	0.007	0.395	0.016	0.0517	0.0012	0.21	335	11	325	7	331	86	97
Diatexite (JTJ-55)															

M6_55_12c	1103	14.1	0.0128	0.367	0.016	0.0511	0.0011	0.001	317	12	321	7	270	100	101
M6_55_30e	2817	2.6	0.0009	0.38	0.03	0.0511	0.0011	0.25	324	22	321	7	317	170	99
M6_55_8e	2427	2.0	0.0008	0.39	0.03	0.0510	0.0012	0.27	330	22	320	7	376	180	97
M6_55_10e	1174	15.0	0.0128	0.371	0.031	0.0510	0.0012	0.23	320	23	321	7	281	180	100
M6_55_27e	3286	2.9	0.0009	0.374	0.029	0.0507	0.0012	0.38	322	22	319	7	316	180	99
M6_55_12e	2534	3.3	0.0013	0.370	0.029	0.0506	0.0012	0.34	319	22	318	7	305	180	100
M6_55_22e	3108	2.6	0.0008	0.360	0.028	0.0495	0.0011	0.35	311	21	312	7	289	180	100

*Concordance = ($^{206}Pb/^{238}U$ age) / ($^{207}Pb/^{235}U$ age) x 100

Appendix E2: LA-ICP-MS U–Pb apatite data of the Figueira de Castelo Rodrigo – Lumbrales Anatectic Complex migmatites

									Final Ages (Ma)			
Id	U (ppm)	Pb (ppm)	$^{206}Pb_{cm}$	$^{238}U/^{206}Pb$	±2σ	$^{207}Pb/^{206}Pb$	±2σ	Rho	$^{207}Pb/^{235}U$	±2σ	$^{206}Pb/^{238}U$	±2σ
Metatexite (JTJ-20)												
M1_20_1	115	11	0.35	12.91823	0.28370	0.3494	0.0027	0.55	1577	18	481	10
M1_20_3	164	15	0.33	13.47527	0.29053	0.325	0.002	0.40	1487	17	461	9.6
M1_20_6	168	13	0.29	14.15228	0.30043	0.304	0.002	0.47	1397	16	440	9.1
M1_20_7	178	15	0.32	13.71366	0.28210	0.3225	0.0023	0.51	1466	17	454	9.3
M1_20_11	199	11	0.24	15.21375	0.34719	0.2505	0.0024	0.42	1201	17	410	9
M1_20_12	246	11	0.19	15.95914	0.35657	0.219	0.002	0.53	1077	15	392	8.6
M1_20_13	135	15	0.37	12.3472	0.2744	0.3627	0.0034	0.51	1642	19	502	11
M1_20_15	186	17	0.33	13.34401	0.30271	0.3322	0.0025	0.44	1511	18	466	10
Metatexite (JTJ-25)												
M2_25_1	109	13	0.41	12.22344	0.25400	0.3832	0.0027	0.51	1696	18	507	10
M2_25_10	80	16	0.53	9.372071	0.202022	0.4859	0.0031	0.57	2129	19	654	13
M2_25_2	102	14	0.43	11.54734	0.25335	0.4079	0.0029	0.53	1797	17	535	11
M2_25_3	103	28	0.60	7.880221	0.167664	0.549	0.003	0.43	2397	20	770	16
M2_25_4	96	15	0.47	10.84011	0.23502	0.4328	0.0032	0.46	1900	19	569	12

M2_25_5	96	13	0.43	11.30327	0.242751	0.4132	0.0028	0.46	1825	18	546	11
M2_25_6	91	24	0.61	8.145976	0.172528	0.5424	0.0034	0.54	2355	19	746	15
M2_25_7	110	21	0.53	9.845427	0.213251	0.4811	0.0029	0.52	2077	19	624	13
M2_25_8	105	21	0.52	9.568462	0.201422	0.487	0.003	0.59	2112	19	641	13
M2_25_9	114	18	0.46	10.62586	0.22582	0.4387	0.0027	0.47	1930	18	580	12
M2_25_11	107	19	0.52	9.925558	0.22659	0.4709	0.004	0.38	2049	21	619	14
M2_25_12	79	24	0.61	7.429421	0.17111	0.5702	0.0046	0.50	2484	21	814	18
M2_25_13	93	15	0.50	10.47889	0.24158	0.4513	0.0044	0.53	1965	20	588	13
M2_25_14	3	29	0.95	0.382995	0.01012	0.8543	0.0075	0.27	5868	27	8260	120
M2_25_15	80	21	0.60	8.230453	0.18967	0.5423	0.0054	0.61	2344	21	739	16
M2_25_16	116	20	0.48	10.19472	0.22865	0.4592	0.004	0.49	2004	20	603	13
M2_25_17	59	26	0.74	5.627462	0.12667	0.6499	0.0052	0.50	2871	22	1054	22
M2_25_18	114	15	0.43	11.54068	0.26637	0.4113	0.0037	0.51	1801	20	536	12
M2_25_19	124	15	0.41	11.92606	0.27024	0.3878	0.0036	0.58	1724	19	519	11
M2_25_20	79	16	0.53	9.424182	0.213157	0.4929	0.0046	0.47	2136	21	650	14
M2_25_21	95	13	0.39	11.22334	0.30231	0.4249	0.0074	0.48	1852	25	550	14
M2_25_22	91	16	0.46	9.97009	0.26839	0.4739	0.0082	0.61	2044	25	617	16
M2_25_23	32	16	0.71	5.181347	0.147655	0.657	0.011	0.60	2955	27	1138	30
M2_25_24	83	13	0.52	10.44932	0.28389	0.449	0.008	0.58	1960	25	590	16
M2_25_25	108	15	0.44	11.27396	0.29233	0.413	0.006	0.43	1821	24	548	14
Metatexite (JTJ-48B)												
M3_48B_1	46	18	0.70	6.301197	0.142938	0.6148	0.0065	0.69	2711	21	950	20
M3_48B_10	29	15	0.75	5.117707	0.112621	0.6635	0.0051	0.63	2978	21	1150	23
M3_48B_2	25	14	0.72	4.826255	0.107147	0.6734	0.0063	0.64	3053	21	1214	25
M3_48B_3	43	17	0.68	6.22665	0.13570	0.6163	0.0045	0.53	2724	21	961	20
M3_48B_4	37	16	0.70	5.875441	0.131179	0.6387	0.0054	0.55	2813	21	1013	21
M3_48B_5	99	15	0.47	10.85187	0.23553	0.4331	0.0029	0.48	1901	18	568	12
M3_48B_6	33	17	0.72	5.159959	0.111826	0.6582	0.0048	0.49	2966	21	1142	23

M3_48B_7	29	17	0.71	4.528986	0.102559	0.6849	0.0069	0.67	3130	21	1286	26
M3_48B_9	28	14	0.76	5.235602	0.117870	0.6586	0.0065	0.57	2951	22	1127	23
M3_48B_11	69	21	0.63	7.401377	0.169819	0.5743	0.0046	0.44	2498	22	817	17
M3_48B_12	42	19	0.69	5.614823	0.132410	0.6437	0.0061	0.57	2863	22	1056	23
M3_48B_13	46	23	0.73	5.285412	0.120123	0.6571	0.0054	0.52	2940	22	1117	23
M3_48B_18	42	19	0.60	7.315289	0.117730	0.5754	0.0056	0.47	2507	16	826	13
M3_48B_19	31	14	0.79	4.5106	0.0753	0.6925	0.0069	0.45	3144	16	1292	19
M3_48B_20	51	18	0.84	3.894081	0.068237	0.7135	0.0074	0.45	3314	17	1473	23
M3_48B_21	28	14	0.76	5.313496	0.155283	0.667	0.014	0.63	2934	28	1110	30
M3_48B_22	68	19	0.64	7.727975	0.209026	0.555	0.009	0.50	2423	27	785	20
M3_48B_23	21	16	0.81	3.755163	0.108580	0.711	0.012	0.50	3343	29	1520	39
M3_48B_24	28	16	0.87	4.666356	0.137182	0.695	0.013	0.59	3107	28	1250	33
M3_48B_25	54	19	0.57	6.802721	0.189736	0.60	0.01	0.59	2612	25	884	23
Diatexite (JTJ-24A)												
M1_24A_1	150	8	0.23	15.93372	0.33005	0.2403	0.0021	0.14	1141	16	392	8
M1_24A_10	218	13	0.26	15.14234	0.32101	0.263	0.002	0.37	1241	15	412	8
M1_24A_2	177	10	0.25	15.1676	0.3221	0.2536	0.0021	0.29	1213	16	412	9
M1_24A_4	137	8	0.25	15.39883	0.33197	0.2589	0.0022	0.44	1217	16	406	8
M1_24A_5	192	12	0.29	15.07841	0.34104	0.2822	0.0038	-0.36	1291	22	414	9
M1_24A_7	234	11	0.21	16.14987	0.33906	0.2249	0.0017	0.47	1087	15	387	8
M1_24A_8	139	7	0.21	16.34788	0.34743	0.2326	0.0022	0.51	1101	15	383	8
M1_24A_11	197	7	0.17	17.36111	0.39183	0.1946	0.0023	0.41	947	15	361	8
M1_24A_12	168	8	0.20	16.42845	0.37785	0.2295	0.0026	0.30	1087	16	381	9
M1_24A_13	186	11	0.25	15.48467	0.33569	0.2569	0.0027	0.23	1207	17	403	9
M1_24A_14	15	10	0.77	4.355401	0.111920	0.69	0.01	0.48	3173	25	1332	31
M1_24A_15	234	11	0.20	16.16554	0.36585	0.2267	0.0022	0.35	1090	16	387	9
M1_24A_16	255	11	0.19	16.42036	0.37748	0.2161	0.0019	0.28	1050	15	381	8
M1_24A_17	175	11	0.27	15.07613	0.34093	0.2693	0.0028	0.48	1258	17	414	9

M1_24A_21	100	7	0.22	14.36782	0.41287	0.3013	0.0063	0.46	1370	23	434	12
M1_24A_22	84	6	0.22	14.36782	0.41287	0.3096	0.0078	0.45	1385	25	433	12
M1_24A_23	190	9	0.25	15.94134	0.40660	0.236	0.004	0.34	1128	20	392	10
M1_24A_24	111	6	0.26	15.5135	0.4332	0.261	0.006	0.48	1210	23	403	11
M1_24A_25	61	5	0.30	13.7931	0.4185	0.343	0.011	0.44	1493	29	451	13
Diatexite (JTJ-43)												
M2_43_1	22	7.7	0.64	6.872852	0.155879	0.5898	0.0064	0.55	2587	21	875	18
M2_43_10	31	6.9	0.51	9.199632	0.220046	0.4972	0.0081	0.54	2161	22	665	15
M2_43_2	18	6.4	0.61	6.906077	0.186006	0.59	0.01	0.66	2582	25	872	22
M2_43_3	39	7.9	0.49	9.526531	0.208736	0.481	0.005	0.54	2101	20	643	14
M2_43_4	50	8.1	0.47	10.755	0.231	0.4379	0.0044	0.57	1915	19	573	12
M2_43_5	50	8.2	0.48	10.63038	0.23731	0.4383	0.0042	0.58	1926	19	580	12
M2_43_6	39	7.2	0.49	10.08065	0.22356	0.4737	0.0052	0.66	2040	19	610	13
M2_43_7	50	9.2	0.51	10.15332	0.22680	0.459	0.005	0.62	2006	19	606	13
M2_43_8	33	7.6	0.55	8.992806	0.202176	0.5078	0.0048	0.53	2202	20	680	14
M2_43_9	18	6.8	0.64	6.72495	0.15376	0.6071	0.0068	0.54	2636	22	894	19
M2_43_11	28	8.1	0.65	7.674597	0.188478	0.549	0.006	0.60	2415	22	789	18
M2_43_12	29	6.8	0.49	9.0009	0.2187	0.5175	0.0074	0.62	2218	22	679	16
M2_43_13	46	7.4	0.50	10.84363	0.25869	0.4334	0.0053	0.51	1900	21	569	13
M2_43_14	39	7.4	0.46	9.80873	0.23091	0.471	0.006	0.53	2058	22	626	14
M2_43_15	33	8.2	0.55	8.503401	0.202462	0.5221	0.0068	0.58	2278	22	717	16
M2_43_16	15	7.0	0.69	5.640158	0.143151	0.65	0.01	0.60	2865	24	1052	24
M2_43_17	33	7.7	0.53	9.041591	0.220726	0.5129	0.0074	0.54	2206	22	676	16
M2_43_18	62	8.9	0.40	11.38563	0.27223	0.402	0.005	0.46	1792	21	543	12
M2_43_19	21	6.8	0.66	7.27802	0.17480	0.578	0.008	0.57	2515	23	830	19
M2_43_20	39	8.1	0.52	9.505703	0.225896	0.4949	0.0063	0.61	2130	21	645	15
M2_43_21	42	5.6	0.47	11.8624	0.3799	0.401	0.012	0.44	1749	32	521	16
M2_43_22	51	8.2	0.23	10.88139	0.31969	0.4305	0.0098	0.56	1888	27	567	16

M2_43_23	58	8.6	0.51	10.97695	0.31328	0.4217	0.0095	0.66	1858	25	562	16
M2_43_24	21	7.8	0.62	6.570302	0.211528	0.62	0.02	0.57	2663	31	912	27
M2_43_25	18	7.0	0.87	6.293266	0.209908	0.618	0.018	0.65	2692	32	949	29
Diatexite (JTJ-55)												
M3_55_1	131	7.3	0.26	15.74059	0.34687	0.2559	0.0026	0.36	1192	16	397	8
M3_55_10	115	10.5	0.37	13.44267	0.28913	0.3354	0.0027	0.54	1514	17	463	10
M3_55_2	157	9.8	0.26	15.18834	0.32296	0.2702	0.0022	0.34	1257	16	411	9
M3_55_3	78	8.9	0.39	12.47038	0.26437	0.3829	0.0033	0.51	1679	18	497	10
M3_55_4	123	8.6	0.27	14.71887	0.32497	0.2887	0.0028	0.26	1328	17	424	9
M3_55_5	108	9.2	0.33	13.77031	0.30339	0.3219	0.0027	0.46	1462	17	452	9
M3_55_6	148	10.7	0.30	14.49485	0.31515	0.2949	0.0024	0.50	1355	16	430	9
M3_55_7	132	8.7	0.29	14.97679	0.31403	0.2847	0.0024	0.41	1306	16	417	9
M3_55_8	123	9.7	0.32	14.18239	0.30171	0.3107	0.0026	0.45	1412	17	439	9
M3_55_9	138	10.0	0.31	14.4655	0.3139	0.296	0.002	0.48	1361	16	431	9
M3_55_11	133	9.2	0.28	14.45713	0.33441	0.2884	0.0031	0.46	1341	17	431	10
M3_55_12	163	10.4	0.29	14.94992	0.33525	0.2782	0.0026	0.40	1289	18	417	9
M3_55_13	101	9.1	0.36	13.51534	0.31053	0.3401	0.0039	0.41	1517	19	460	10
M3_55_14	120	11.3	0.37	13.28551	0.30006	0.3452	0.0038	0.51	1544	19	468	10
M3_55_15	132	7.7	0.24	15.63233	0.36655	0.2693	0.0033	0.48	1232	17	400	9
M3_55_16	146	9.7	0.29	15.04664	0.33960	0.2864	0.0031	0.51	1305	18	415	9
M3_55_17	129	9.8	0.31	14.49696	0.33626	0.3094	0.0034	0.40	1391	18	430	10
M3_55_18	151	9.6	0.26	15.19988	0.34655	0.2781	0.0028	0.38	1275	17	411	9
M3_55_19	109	11.7	0.39	12.69358	0.29003	0.3688	0.0038	0.48	1632	19	489	11
M3_55_20	145	10.9	0.32	14.22071	0.32357	0.301	0.003	0.49	1385	18	438	10
M3_55_21	99	8.5	0.29	13.89082	0.38591	0.329	0.006	0.51	1468	23	448	12
M3_55_22	156	9.5	0.23	14.98127	0.40399	0.2678	0.0048	0.49	1255	21	417	11
M3_55_23	138	10.3	0.28	14.48436	0.37763	0.304	0.005	0.51	1374	22	431	11
M3_55_24	91	6.3	0.19	15.06251	0.43107	0.3029	0.0072	0.45	1339	23	414	11

M3_55_25	145	10.5	0.24	14.44878	0.39666	0.299	0.005	0.49	1362	22	431	11

*Pb_{cm} not corrected

Appendix E3: LA-ICP-MS U–Pb inherited zircon of the Figueira de Castelo Rodrigo – Lumbrales Anatectic Complex migmatites

				Common-lead uncorrected					Final Ages (Ma)						
Id	U (ppm)	Th (ppm)	Th/U	$^{207}Pb/^{235}U$	±2σ	$^{206}Pb/^{238}U$	±2σ	Rho	$^{207}Pb/^{235}U$	±2σ	$^{206}Pb/^{238}U$	±2σ	$^{207}Pb/^{206}Pb$	±2σ	Concord-ance (%)*
Metatexites															
M1_20_10I	587	267	0.45	0.853	0.016	0.1023	0.0015	0.0015	626	9	628	9	628	40	100
M1_20_12	456	353	0.77	0.89	0.02	0.1063	0.0015	0.0015	644	10	651	9	616	41	101
M1_20_13	485	295	0.61	1.008	0.018	0.1165	0.0017	0.0017	707	9	710	10	686	36	100
M1_20_15	2159	529	0.25	0.850	0.012	0.1020	0.0014	0.0014	624	6	626	8	619	21	100
M1_20_16	770	561	0.73	0.798	0.016	0.094	0.001	0.0014	594	9	579	8	641	33	97
M1_20_18	324	170	0.52	0.784	0.019	0.0954	0.0014	0.0014	585	11	587	8	549	49	100
M1_20_19	765	237	0.31	0.716	0.013	0.0888	0.0013	0.0013	547	8	549	7	531	34	100
M1_20_20	240	69	0.29	1.076	0.026	0.1202	0.0018	0.0018	738	13	732	10	727	49	99
M1_20_21	826	533	0.64	0.851	0.015	0.1015	0.0014	0.0014	624	8	624	8	609	33	100
M1_20_22	258	58	0.23	0.74	0.02	0.0911	0.0014	0.0014	558	12	562	9	508	60	101
M1_20_23	80	31	0.39	1.23	0.05	0.1304	0.0028	0.0028	804	21	789	16	819	75	98
M1_20_4	184	56	0.30	0.761	0.025	0.0925	0.0015	0.0015	570	14	570	9	539	70	100
M1_20_6	45	13	0.28	0.856	0.054	0.1078	0.0023	0.0023	611	30	659	13	370	130	108
M1_20_7	86	26	0.30	7.03	0.13	0.38	0.006	0.0059	2113	17	2075	28	2144	28	97
M1_20_8	542	186	0.34	0.725	0.015	0.0895	0.0013	0.0013	552	9	553	8	546	42	100
M1_20_9	179	67	0.37	0.794	0.024	0.0978	0.0017	0.0017	590	13	602	10	523	63	102
M1_20_1	665	469	0.70	0.932	0.014	0.1105	0.0024	0.0024	668	7	676	14	656	64	101
M1_20_11	952	271	0.28	0.692	0.012	0.0851	0.0019	0.0019	533	7	527	11	559	69	99
M1_20_2	356	123	0.35	1.269	0.022	0.1363	0.0031	0.0031	831	10	824	17	855	65	99
M1_20_24	2563	409	0.16	0.7136	0.0086	0.0867	0.0019	0.0019	546	5	536	11	581	62	98

M1_20_25	312	328	1.05	0.858	0.019	0.1021	0.0023	0.0023	627	10	626	13	599	76	100
M1_20_27	205	67	0.33	0.79	0.02	0.0935	0.0022	0.0022	589	12	576	13	607	82	98
M1_20_3	319	206	0.64	0.72	0.02	0.0888	0.0021	0.0021	548	12	549	12	519	85	100
M1_20_30	178	92	0.52	0.748	0.023	0.093	0.002	0.0022	563	13	573	13	471	87	102
M1_20_32F	1116	294	0.26	0.583	0.011	0.0715	0.0016	0.0016	465	7	445	10	543	69	96
M1_20_32I	984	404	0.41	0.73	0.02	0.0874	0.0026	0.0026	557	12	540	15	600	77	97
M1_20_34	469	93	0.20	0.714	0.015	0.089	0.002	0.002	545	9	548	12	504	75	101
M1_20_35	201	176	0.88	1.227	0.029	0.134	0.003	0.0032	810	13	811	18	792	78	100
M1_20_36	707	215	0.30	0.741	0.013	0.091	0.002	0.002	561	8	558	12	572	67	99
M1_20_37	505	146	0.29	0.929	0.016	0.1084	0.0024	0.0024	665	8	663	14	668	69	100
M1_20_38	169	96	0.57	0.941	0.032	0.1034	0.0024	0.0024	668	17	634	14	762	92	95
M1_20_39	1164	332	0.29	0.839	0.012	0.0996	0.0022	0.0022	618	7	612	13	648	62	99
M1_20_40	640	303	0.47	0.766	0.013	0.094	0.002	0.002	578	7	576	12	572	69	100
M1_20_41	4432	892	0.20	0.7471	0.0078	0.093	0.002	0.002	566	5	572	12	545	61	101
M1_20_42	1390	129	0.09	0.8315	0.0098	0.1003	0.0022	0.0022	614	6	616	13	612	62	100
M1_20_43	422	222	0.53	0.742	0.015	0.0912	0.0021	0.0021	562	9	562	12	540	74	100
M1_20_44	2205	141	0.06	1.33	0.02	0.1348	0.003	0.003	858	7	815	17	975	56	95
M1_20_45	568	225	0.40	0.772	0.015	0.0943	0.0021	0.0021	579	9	581	13	567	68	100
M1_20_47	222	64	0.29	0.755	0.019	0.0934	0.0022	0.0022	568	11	575	13	515	80	101
M1_20_48	402	113	0.28	0.737	0.014	0.091	0.002	0.002	559	8	559	12	536	73	100
M1_20_49	132	189	1.43	0.888	0.029	0.1056	0.0026	0.0026	640	15	647	15	577	94	101
M1_20_52	861	181	0.21	0.658	0.011	0.0796	0.0018	0.0018	513	7	494	11	584	69	96
M1_20_53	1675	565	0.34	0.84	0.01	0.1009	0.0022	0.0022	621	6	620	13	622	62	100
M1_20_54	168	148	0.88	0.804	0.025	0.0966	0.0022	0.0022	596	14	594	13	565	85	100
M1_20_55	571	238	0.42	0.754	0.013	0.092	0.002	0.002	569	8	566	12	574	68	99
M1_20_57	1678	686	0.41	0.823	0.011	0.0973	0.0021	0.0021	609	6	598	12	676	61	98
M1_20_58	199	106	0.53	0.74	0.02	0.0926	0.0022	0.0022	563	12	571	13	537	83	101
M1_20_61	183	106	0.58	0.879	0.022	0.1045	0.0024	0.0024	637	12	640	14	605	82	101

M1_20_62	197	130	0.66	0.757	0.019	0.0918	0.0021	0.0021	569	11	566	12	559	80	99
M1_20_63	2057	550	0.27	0.8262	0.0093	0.0984	0.0021	0.0021	611	5	605	13	623	62	99
M1_20_64	430	142	0.33	0.746	0.015	0.091	0.002	0.002	564	9	564	12	553	73	100
M1_20_65	741	246	0.33	0.736	0.013	0.090	0.002	0.002	559	8	552	12	577	67	99
M1_20_66	315	171	0.54	0.73	0.02	0.089	0.002	0.002	554	10	552	12	549	74	100
M1_20_68	614	264	0.43	0.724	0.013	0.090	0.002	0.002	552	8	554	12	547	71	100
M1_20_69a	1992	671	0.34	0.748	0.073	0.089	0.002	0.002	564	42	551	12	595	180	98
M1_20_70a	376	396	1.05	0.881	0.093	0.1075	0.0027	0.0027	632	50	658	16	496	190	104
M1_20_71a	2178	1564	0.72	0.779	0.076	0.097	0.002	0.0022	584	42	597	13	529	180	102
M1_20_72	429	214	0.50	0.871	0.092	0.1069	0.0027	0.0027	627	50	654	16	500	190	104
M1_20_73a	350	171	0.49	0.746	0.081	0.0944	0.0025	0.0025	557	49	581	15	410	200	104
M1_20_74a	149	43	0.29	0.85	0.11	0.1003	0.0035	0.0035	588	60	615	21	380	230	105
M1_20_77a	765	291	0.38	0.723	0.074	0.0923	0.0022	0.0022	547	45	569	13	409	190	104
M1_20_79a	1931	2860	1.48	0.698	0.068	0.083	0.002	0.002	535	41	516	12	580	180	96
M1_20_80a	2295	835	0.36	0.747	0.073	0.0926	0.0021	0.0021	564	42	571	12	524	180	101
M1_20_5	236	274	1.16	5.618	0.084	0.3342	0.0047	0.0047	1917	13	1858	23	1982	21	94
M1_20_51	60	40	0.66	0.684	0.028	0.0786	0.0019	0.0019	524	17	487	11	656	110	93
M1_20_75a	1728	355	0.21	0.661	0.065	0.077	0.002	0.0018	512	40	478	11	633	180	93
M4_60A_1	432	214	0.50	1.351	0.024	0.141	0.002	0.002	866	11	850	11	899	33	98
M4_60A_2	513	617	1.20	0.874	0.018	0.1037	0.0016	0.002	637	10	636	9	616	38	100
M4_60A_3	297	342	1.15	0.837	0.022	0.0991	0.0015	0.002	614	12	609	9	597	56	99
M4_60A_4	344	214	0.62	0.90	0.02	0.1052	0.0016	0.002	653	11	645	9	654	46	99
M4_60A_5	342	221	0.65	0.863	0.018	0.1022	0.0015	0.002	630	10	627	9	611	45	100
M4_60A_6	321	196	0.61	1.684	0.031	0.1666	0.0024	0.002	1000	12	993	13	1000	32	99
M4_60A_7	125	74	0.59	7.65	0.12	0.4019	0.0062	0.006	2187	14	2176	28	2185	23	100
M4_60A_10	406	169	0.42	0.719	0.031	0.0896	0.0028	0.003	545	19	553	17	434	94	101
M4_60A_13a	310	202	0.65	1.128	0.053	0.127	0.004	0.004	754	26	772	23	610	100	102
M4_60A_14a	383	453	1.18	0.846	0.041	0.1023	0.0032	0.003	612	23	627	19	470	110	102

M4_60A_15a	2039	225	0.11	1.327	0.024	0.1386	0.0041	0.004	857	11	837	23	903	30	98
M4_60A_17	396	343	0.87	0.914	0.042	0.1085	0.0035	0.004	648	22	664	20	601	99	102
M4_60A_19	695	636	0.92	0.815	0.028	0.101	0.003	0.003	599	16	622	18	539	73	104
M4_60A_20	458	530	1.16	0.789	0.028	0.0997	0.0031	0.003	586	16	613	18	508	82	105
M4_60A_8	254	268	1.06	0.857	0.055	0.1081	0.0036	0.004	613	31	661	21	350	130	108
M4_60A_9	423	540	1.28	0.839	0.036	0.1016	0.0032	0.003	609	20	624	19	473	95	102
M7_60A_10c	330	312	0.95	0.833	0.031	0.0966	0.0019	0.002	613	17	594	11	668	73	97
M7_60A_12c	147	176	1.20	0.803	0.036	0.0954	0.0019	0.002	593	20	588	11	570	91	99
M7_60A_13c	683	592	0.87	0.807	0.028	0.0965	0.0016	0.002	599	16	594	9	612	64	99
M7_60A_14c	570	516	0.90	0.744	0.026	0.0908	0.0015	0.002	563	15	560	9	556	68	99
M7_60A_15c	861	637	0.74	0.799	0.026	0.0958	0.0015	0.002	596	15	590	9	620	62	99
M7_60A_17c	1163	628	0.54	0.775	0.025	0.0902	0.0014	0.001	582	15	557	8	669	60	96
M7_60A_19c	237	211	0.89	0.714	0.029	0.0862	0.0016	0.002	544	17	533	9	566	81	98
M7_60A_1c	290	163	0.56	0.704	0.028	0.0872	0.0016	0.002	538	17	539	9	502	78	100
M7_60A_22c	859	206	0.24	0.749	0.025	0.0920	0.0015	0.002	567	14	567	9	553	63	100
M7_60A_24c	325	144	0.44	0.749	0.029	0.092	0.002	0.002	565	17	567	9	535	75	100
M7_60A_26c	445	389	0.88	0.784	0.028	0.0949	0.0016	0.002	586	16	584	9	578	68	100
M7_60A_28c	242	154	0.64	0.829	0.032	0.1004	0.0018	0.002	610	18	617	10	556	79	101
M7_60A_29c	1099	511	0.46	0.752	0.025	0.0927	0.0015	0.002	569	14	571	9	550	61	100
M7_60A_2c	531	460	0.87	0.816	0.028	0.0948	0.0015	0.002	605	16	584	9	671	63	96
M7_60A_30c	716	586	0.82	0.648	0.022	0.0784	0.0013	0.001	506	14	486	8	585	67	96
M7_60A_5c	914	407	0.44	0.78	0.03	0.0946	0.0015	0.002	585	15	583	9	582	62	100
M7_60A_7c	202	327	1.62	0.73	0.03	0.0903	0.0017	0.002	555	18	557	10	508	85	100
M7_60A_11c	567	113	0.20	0.712	0.025	0.0816	0.0014	0.001	544	15	506	8	707	62	93
M7_60A_21c	287	143	0.50	1.02	0.04	0.1077	0.0024	0.002	708	20	659	14	854	68	93
M7_60A_8c	381	72	0.19	0.749	0.034	0.0841	0.0023	0.002	562	20	520	14	717	73	93
M7_60A_9c	200	149	0.74	21.28	0.67	0.5898	0.0097	0.010	3149	30	2987	39	3253	42	92
Diatexites															

M6_55_37c	694	10	0.01	0.589	0.026	0.0730	0.0015	0.002	469	17	455	9	535	99	97
M6_55_36c	395	133	0.34	0.576	0.027	0.0742	0.0016	0.002	460	17	461	10	449	110	100
M6_55_38c	475	11	0.02	0.594	0.027	0.0748	0.0016	0.002	473	18	465	9	498	100	98
M6_55_13c	326	26	0.08	0.6	0.03	0.0761	0.0017	0.002	475	18	473	10	451	100	100
M6_55_7c	308	73	0.24	0.62	0.03	0.0776	0.0017	0.002	487	19	482	10	487	110	99
M6_55_18c	373	46	0.12	0.632	0.029	0.0802	0.0017	0.002	495	18	497	10	463	100	100
M6_55_27c	440	83	0.19	0.678	0.031	0.0815	0.0017	0.002	524	19	505	10	610	100	96
M1_24A_18	2980	67	0.02	0.651	0.016	0.0847	0.0013	0.001	508	10	524	8	437	36	103
M1_24A_39	602	161	0.27	0.704	0.031	0.085	0.003	0.003	535	19	527	18	522	96	99
M6_55_41c	2665	957	0.36	0.73	0.03	0.0874	0.0018	0.002	556	18	540	10	633	90	97
M1_24A_22a	773	754	0.98	0.75	0.02	0.0919	0.0013	0.001	567	11	567	8	549	47	100
M1_24A_20	803	288	0.36	0.742	0.018	0.0920	0.0013	0.001	563	11	567	8	524	41	101
M1_24A_12	433	176	0.41	0.754	0.022	0.0930	0.0014	0.001	570	12	573	8	522	54	101
M7_43_8c	405	365	0.90	0.779	0.028	0.0939	0.0016	0.002	584	16	578	9	576	71	99
M1_24A_30	246	544	2.21	0.78	0.03	0.0946	0.0015	0.002	583	15	582	9	555	63	100
M1_24A_7	298	157	0.53	0.778	0.038	0.0957	0.0014	0.001	581	21	589	8	547	93	101
M1_24A_28	398	88	0.22	0.794	0.022	0.0961	0.0014	0.001	591	12	591	8	574	52	100
M7_43_3c	627	189	0.30	0.817	0.029	0.0976	0.0016	0.002	605	16	600	9	602	67	99
M1_24A_27	141	140	1.00	0.79	0.03	0.0977	0.0016	0.002	589	17	601	9	517	79	102
M6_55_24c	411	275	0.67	0.839	0.038	0.098	0.002	0.002	617	21	602	12	667	100	98
M7_43_2c	377	119	0.31	0.85	0.03	0.0993	0.0017	0.002	621	16	610	10	639	70	98
M7_43_1c	228	421	1.85	0.815	0.033	0.0996	0.0018	0.002	603	18	612	10	536	79	102
M1_24A_9	128	198	1.55	0.826	0.033	0.0998	0.0018	0.002	607	18	613	10	531	80	101
M1_24A_16	313	324	1.04	0.831	0.027	0.1005	0.0017	0.002	611	15	617	10	553	62	101
M1_24A_31	422	373	0.88	0.857	0.024	0.1015	0.0015	0.002	626	13	623	9	625	51	100
M1_24A_26	280	322	1.15	0.848	0.028	0.1028	0.0016	0.002	622	15	630	9	564	61	101
M1_24A_44a	1225	914	0.75	0.928	0.024	0.1041	0.0031	0.003	664	12	638	18	740	52	96
M1_24A_47a	666	720	1.08	0.961	0.032	0.1055	0.0031	0.003	679	17	646	18	749	74	95

M7_43_5c	388	302	0.78	0.992	0.035	0.1132	0.0018	0.002	698	18	691	11	707	65	99
M7_43_4c	490	184	0.38	0.967	0.033	0.1132	0.0018	0.002	687	17	691	10	660	63	101
M6_55_28c	409	321	0.79	1.314	0.059	0.1261	0.0033	0.003	850	25	765	19	1096	89	90
M1_24A_10	336	116	0.34	5.67	0.12	0.3407	0.0047	0.005	1925	19	1889	22	1957	26	97
M1_24A_24	267	98	0.37	5.97	0.13	0.361	0.005	0.005	1970	20	1986	24	1953	28	102
M6_55_22c	61	26	0.43	7.0	0.3	0.3766	0.0081	0.008	2101	40	2059	38	2152	80	96
M1_24A_46	242	152	0.63	6.99	0.15	0.3933	0.012	0.012	2103	19	2135	56	2082	37	103
M1_24A_8	574	386	0.67	7.38	0.28	0.3954	0.0047	0.005	2157	34	2147	22	2178	55	99
M1_24A_21	453	230	0.51	9.9	0.2	0.4457	0.006	0.006	2425	19	2375	27	2462	22	96
M7_43_14c	237	95	0.40	11.99	0.37	0.4857	0.0077	0.008	2603	29	2551	33	2643	42	97
M1_24A_3	145	68	0.47	12.84	0.48	0.5089	0.0067	0.007	2666	36	2650	29	2668	52	99
M1_24A_45a	1372	1987	1.45	15.07	0.25	0.526	0.016	0.016	2820	15	2719	69	2907	17	94

*Concordance = ($^{206}Pb/^{238}U$ age) / ($^{207}Pb/^{235}U$ age) x 100 – for ages <1000 Ma

= ($^{206}Pb/^{238}U$ age) / ($^{207}Pb/^{206}Pb$ age) x 100 – for ages >1000 Ma

Appendix E4: LA-ICP-MS U–Pb detrital zircon data of the Douro-Beiras Supergroup

				Common-lead uncorrected					Final Ages (Ma)						
Id	U (ppm)	Th (ppm)	Th/U	$^{207}Pb/^{235}U$	±2σ	$^{206}Pb/^{238}U$	±2σ	Rho	$^{207}Pb/^{235}U$	±2σ	$^{206}Pb/^{238}U$	±2σ	$^{207}Pb/^{206}Pb$	±2σ	Con-cord-ance (%)*
Douro-Beiras Supergroup North (DBSG N)															
M18_49_65r - 1	267	185	0.69	0.662	0.033	0.0845	0.0016	0.15	508	20	523	9	410	100	103
M18_49_19c - 1	1050	1517	1.44	0.7437	0.0094	0.0868	0.0024	0.35	564	5	537	14	675	41	95
M18_49_79c - 1	91	56	0.61	0.72	0.07	0.0912	0.0024	0.08	530	46	562	14	320	200	106
M18_49_101c - 1	83	41	0.50	0.775	0.079	0.092	0.002	0.19	539	47	566	13	270	200	105
M18_49_102c - 1	244	56	0.23	0.774	0.034	0.0929	0.0015	0.07	576	19	572	9	493	95	99
M18_49_95c - 1	290	293	1.01	0.793	0.035	0.0932	0.0016	0.16	587	20	574	10	545	90	98

M18_49_39c - 1	171	138	0.80	0.823	0.044	0.0935	0.0018	0.09	594	25	576	11	550	120	97
M18_49_45c - 1	50	15	0.30	0.85	0.11	0.0937	0.0027	0.14	556	65	577	16	290	250	104
M18_49_23c - 1	2039	282	0.14	0.7742	0.0073	0.0937	0.0025	0.48	582	4	577	15	577	37	99
M18_49_62c - 1	512	547	1.07	0.772	0.031	0.094	0.002	0.37	577	17	579	10	542	79	100
M18_49_97c - 1	96	92	0.96	0.755	0.071	0.0948	0.0024	0.05	535	43	583	14	220	190	109
M18_49_100c - 1	846	637	0.75	0.81	0.02	0.0949	0.0012	0.29	601	11	584	7	593	54	97
M18_49_89c - 1	182	49	0.27	0.768	0.042	0.095	0.002	0.09	569	26	585	12	440	120	103
M18_49_34c - 1	117	205	1.76	0.75	0.03	0.0957	0.0029	0.07	563	17	589	17	466	94	105
M18_49_3c - 1	899	366	0.41	0.82	0.02	0.0957	0.0015	0.44	607	9	589	9	664	32	97
M18_49_6c - 1	147	49	0.33	0.786	0.027	0.0959	0.0016	0.27	585	15	590	10	528	66	101
M18_49_58c - 1	79	60	0.76	0.74	0.08	0.0959	0.0025	0.14	518	49	591	15	180	210	114
M18_49_84c - 1	138	54	0.39	0.752	0.051	0.0961	0.0019	0.02	554	30	591	11	340	140	107
M18_49_11c - 1	261	316	1.21	0.791	0.021	0.0966	0.0015	0.30	590	12	594	9	552	48	101
M18_49_48c - 1	463	470	1.02	0.818	0.025	0.0968	0.0014	0.18	605	14	595	8	594	67	98
M18_49_82c - 1	542	289	0.53	0.821	0.028	0.0968	0.0014	0.35	609	16	595	8	639	68	98
M18_49_66c - 1	133	148	1.11	0.804	0.062	0.0969	0.0023	0.09	577	35	597	14	400	150	103
M18_49_30c - 1	611	228	0.37	0.804	0.011	0.0972	0.0027	0.28	599	7	598	16	581	44	100
M18_49_50c - 1	452	488	1.08	0.831	0.025	0.0973	0.0014	0.38	614	13	598	8	634	61	97
M18_49_73c - 1	150	113	0.75	0.825	0.053	0.0975	0.0019	0.11	605	29	599	11	520	130	99
M18_49_38c - 1	921	452	0.49	0.882	0.021	0.0976	0.0015	0.30	641	12	600	9	740	51	94
M18_49_83c - 1	114	81	0.71	0.794	0.063	0.0976	0.0023	0.16	567	37	600	13	370	160	106
M18_49_105c - 1	571	141	0.25	0.952	0.028	0.0992	0.0015	0.37	675	15	609	9	834	61	90
M18_49_53c - 1	759	277	0.36	0.832	0.037	0.0996	0.0023	0.47	611	21	612	13	643	82	100
M18_49_86c - 1	355	259	0.73	0.82	0.03	0.0997	0.0017	0.24	602	17	612	10	523	81	102
M18_49_108c - 1	404	447	1.11	0.829	0.026	0.0999	0.0015	0.21	608	15	614	9	538	69	101
M18_49_81c - 1	762	325	0.43	0.84	0.02	0.1001	0.0014	0.36	616	11	615	8	611	51	100
M18_49_60c - 1	68	52	0.76	0.9	0.1	0.1005	0.0032	0.18	620	58	618	18	490	230	100
M18_49_61c - 1	430	685	1.59	0.86	0.03	0.1007	0.0016	0.19	627	15	619	9	643	72	99

M18_49_46r - 1	124	41	0.33	0.89	0.06	0.1014	0.0022	0.14	625	33	622	13	520	140	100
M18_49_54c - 1	827	32	0.04	0.842	0.021	0.1015	0.0015	0.29	617	12	623	9	628	52	101
M18_49_74c - 1	158	109	0.69	0.832	0.053	0.1015	0.002	0.21	597	30	623	12	430	130	104
M18_49_88c - 1	824	521	0.63	0.885	0.023	0.1018	0.0015	0.27	641	13	625	9	660	57	98
M18_49_59c - 1	684	294	0.43	0.854	0.021	0.102	0.002	0.31	623	11	626	9	605	53	100
M18_49_94c - 1	144	133	0.93	0.872	0.056	0.1023	0.0025	0.07	621	31	627	14	490	140	101
M18_49_27c - 1	160	213	1.33	0.866	0.024	0.1024	0.0029	0.15	630	13	629	17	604	69	100
M18_49_35c - 1	339	155	0.46	0.833	0.016	0.1025	0.0028	0.14	614	9	629	17	571	55	102
M18_49_90c - 1	462	301	0.65	0.866	0.026	0.1025	0.0014	0.20	630	14	629	8	577	68	100
M18_49_72c - 1	408	253	0.62	0.872	0.033	0.1027	0.0016	0.31	628	18	630	10	599	76	100
M18_49_42c - 1	584	555	0.95	0.928	0.024	0.1027	0.0015	0.30	664	13	630	9	731	52	95
M18_49_56c - 1	166	78	0.47	0.841	0.047	0.1033	0.0019	0.07	603	26	633	11	460	120	105
M18_49_98c - 1	123	79	0.64	0.828	0.063	0.1036	0.0021	0.00	598	36	635	12	310	160	106
M18_49_96c - 1	118	83	0.70	0.91	0.07	0.104	0.002	0.27	624	37	637	13	450	150	102
M18_49_16c - 1	292	153	0.52	0.892	0.022	0.1039	0.0016	0.21	646	12	637	9	677	44	99
M18_49_69c - 1	438	530	1.21	0.938	0.033	0.1055	0.0017	0.27	667	17	646	10	703	73	97
M18_49_22c - 1	447	202	0.45	0.896	0.016	0.106	0.003	0.24	648	8	649	18	623	50	100
M18_49_21c - 1	362	234	0.65	0.888	0.017	0.1059	0.0029	0.29	643	9	649	17	595	51	101
M18_49_26c - 1	1002	266	0.27	0.907	0.012	0.106	0.003	0.56	655	6	649	17	658	38	99
M18_49_76c - 1	145	94	0.65	0.859	0.065	0.106	0.003	0.01	615	36	649	16	440	170	106
M18_49_77c - 1	529	792	1.50	0.947	0.033	0.106	0.002	0.37	671	18	649	11	748	70	97
M18_49_4c - 1	964	588	0.61	0.879	0.015	0.1068	0.0015	0.36	640	8	654	9	583	25	102
M18_49_71c - 1	2357	191	0.08	0.938	0.014	0.1084	0.0013	0.50	670	8	663	8	693	30	99
M18_49_91c - 1	1684	1063	0.63	0.937	0.015	0.1085	0.0013	0.42	671	8	664	8	655	34	99
M18_49_5c - 1	188	162	0.86	0.886	0.037	0.1086	0.0023	0.02	640	20	664	13	515	94	104
M18_49_36c - 1	252	314	1.25	0.92	0.05	0.1085	0.0031	0.18	656	27	664	18	600	130	101
M18_49_31c - 1	81	55	0.68	0.90	0.05	0.1098	0.0036	0.13	647	28	671	21	530	130	104
M18_49_103c - 1	302	44	0.15	0.963	0.035	0.1102	0.0017	0.32	680	18	673	10	605	77	99

M18_49_1c - 1	566	478	0.85	1.087	0.046	0.1102	0.0018	0.15	740	21	674	10	912	78	91
M18_49_51c - 1	70	13	0.18	0.901	0.082	0.1104	0.0028	0.01	622	44	674	16	320	180	108
M18_49_92c - 1	357	79	0.22	0.971	0.036	0.1115	0.0019	0.29	680	19	681	11	595	77	100
M18_49_78c - 1	919	168	0.18	0.986	0.023	0.1135	0.0013	0.45	693	12	693	8	698	44	100
M18_49_12c - 1	289	184	0.64	1.076	0.027	0.120	0.002	0.33	739	13	732	12	760	44	99
M18_49_87c - 1	140	70	0.50	1.066	0.068	0.1236	0.0027	0.31	721	35	751	15	530	130	104
M18_49_49c - 1	346	98	0.28	1.292	0.037	0.1361	0.0023	0.26	839	17	822	13	869	62	98
M18_49_32c - 1	144	121	0.84	1.253	0.027	0.141	0.004	0.25	823	12	850	22	744	55	103
M18_49_63c - 1	498	1319	2.65	1.433	0.052	0.1462	0.0033	0.63	902	21	879	18	938	61	97
M18_49_106c - 1	529	415	0.78	1.435	0.036	0.15	0.002	0.25	898	15	901	11	856	50	100
M18_49_67c - 1	154	36	0.23	1.432	0.066	0.1517	0.0028	0.23	892	28	910	16	793	98	102
M18_49_64c - 1	119	81	0.68	1.595	0.079	0.1539	0.0026	0.15	944	31	922	15	930	110	98
M18_49_70c - 1	400	347	0.87	1.484	0.055	0.1549	0.0034	0.21	918	23	928	19	881	88	101
M18_49_2c - 1	205	72	0.35	1.563	0.045	0.162	0.003	0.23	952	18	968	17	902	55	102
M18_49_44c - 1	156	97	0.62	1.66	0.06	0.1621	0.0026	0.17	978	24	968	15	953	78	99
M18_49_14c - 1	2001	197	0.10	1.655	0.025	0.1629	0.0023	0.61	991	9	973	13	1034	15	98
M18_49_68c - 1	185	267	1.45	1.586	0.064	0.1636	0.0028	0.26	955	25	976	16	869	86	102
M18_49_70r - 1	71	23	0.33	1.68	0.11	0.1658	0.0036	0.15	956	43	989	20	790	140	103
M18_49_24c - 1	295	356	1.21	1.651	0.035	0.1677	0.0049	0.37	990	14	999	27	956	55	101
M18_49_10c - 1	456	300	0.66	1.70	0.03	0.1693	0.0025	0.38	1006	11	1008	14	1000	25	101
M18_49_85c - 1	128	40	0.31	1.72	0.08	0.1711	0.0034	0.21	999	30	1017	18	911	97	112
M18_49_80r - 1	192	117	0.61	1.75	0.06	0.1743	0.0027	0.25	1019	23	1035	15	975	71	106
M18_49_80c - 1	250	284	1.14	1.845	0.058	0.1818	0.0029	0.36	1053	21	1076	16	1022	64	105
M18_49_18c - 1	82	23	0.28	2.232	0.066	0.1978	0.0034	0.30	1182	21	1163	18	1212	54	96
M18_49_99c - 1	171	57	0.33	3.372	0.088	0.2618	0.0045	0.29	1493	21	1497	23	1435	53	100
M18_49_47c - 1	100	46	0.46	4.73	0.16	0.3023	0.0055	0.44	1756	28	1700	27	1814	55	94
M18_49_15c - 1	235	29	0.12	5.103	0.085	0.3173	0.0047	0.44	1836	14	1776	23	1908	19	93
M18_49_55c - 1	227	210	0.92	5.07	0.11	0.3176	0.0049	0.35	1832	18	1776	24	1904	39	93

M18_49_25c - 1	266	112	0.42	5.85	0.07	0.3512	0.0098	0.49	1951	10	1939	47	1948	33	100
M18_49_57c - 1	284	183	0.64	5.83	0.13	0.353	0.006	0.46	1955	19	1947	28	1967	36	99
M18_49_8c - 1	329	103	0.31	6.7	0.1	0.3723	0.0067	0.52	2070	19	2040	31	2100	28	97
M18_49_104c - 1	105	112	1.07	7.87	0.18	0.3839	0.0063	0.39	2206	21	2092	29	2276	39	92
M18_49_43c - 1	1279	599	0.47	7.3	0.1	0.385	0.005	0.63	2145	12	2100	23	2166	20	97
M18_49_52c - 1	264	85	0.32	7.3	0.1	0.3893	0.0052	0.51	2145	17	2118	24	2165	29	98
M18_49_29c - 1	2455	515	0.21	7.11	0.05	0.393	0.011	0.70	2125	6	2138	49	2101.4	27	102
M18_49_107c - 1	113	35	0.31	22.44	0.45	0.634	0.012	0.54	3196	20	3166	46	3209	29	99
Douro-Beiras Supergroup South (DBSG S)															
M18_41b_56c - 1	745	164	0.22	0.722	0.012	0.0817	0.0023	0.32243	551	7	506	13	718	46	92
M18_41b_100c - 1	247	106	0.43	0.665	0.017	0.0831	0.0023	0.23265	515	11	515	14	508	66	100
M18_41b_18c - 1	318	156	0.49	0.679	0.019	0.0846	0.0014	0.18664	524	11	523	8	476	55	100
M18_41b_105c - 1	524	135	0.26	0.693	0.012	0.0856	0.0024	0.45093	534	8	529	14	566	46	99
M18_41b_68c - 1	170	60	0.36	0.68	0.02	0.0866	0.0025	0.095396	524	12	535	15	473	71	102
M18_41b_107c - 1	589	150	0.25	0.694	0.013	0.0866	0.0025	0.15677	534	8	536	15	527	55	100
M18_41b_39c - 1	486	138	0.28	0.699	0.018	0.087	0.002	0.22749	537	11	538	9	514	53	100
M18_41b_95c - 1	1061	157	0.15	0.738	0.011	0.0875	0.0025	0.3929	561	6	541	15	646	44	97
M18_41b_88c - 1	460	89	0.19	0.707	0.012	0.0883	0.0024	0.24708	543	7	545	14	507	49	100
M18_41b_87c - 1	241	69	0.28	0.716	0.023	0.0891	0.0026	0.23831	548	14	550	15	500	76	100
M18_41b_108c - 1	252	57	0.23	0.71	0.02	0.0892	0.0025	0.23108	543	10	551	15	505	61	101
M18_41b_8c - 1	132	55	0.42	0.718	0.029	0.0895	0.0017	0.19256	543	17	552	10	459	82	102
M18_41b_89c - 1	528	209	0.40	0.726	0.011	0.0894	0.0025	0.37759	553	6	552	15	541	44	100
M18_41b_34c - 1	1315	266	0.20	0.738	0.013	0.0895	0.0013	0.39232	561	8	553	8	575	25	99
M18_41b_8r - 1	365	20	0.06	0.736	0.017	0.0896	0.0014	0.28209	558	10	553	8	546	43	99
M18_41b_46c - 1	1199	409	0.34	0.720	0.012	0.0904	0.0013	0.44021	550	7	558	8	499	25	101
M18_41b_101c - 1	1962	183	0.09	0.727	0.007	0.0904	0.0025	0.511	554	4	558	15	556	36	101
M18_41b_47c - 1	344	73	0.21	0.723	0.017	0.0905	0.0014	0.12489	552	11	558	8	497	48	101
M18_41b_63c - 1	627	94	0.15	0.756	0.011	0.0906	0.0025	0.23135	571	6	559	15	591	45	98

M18_41b_22c - 1	325	135	0.41	0.74	0.02	0.0906	0.0014	0.20713	561	12	559	9	537	54	100
M18_41b_48c - 1	1045	206	0.20	0.745	0.017	0.0907	0.0014	0.20144	564	10	560	8	569	43	99
M18_41b_49c - 1	1315	251	0.19	0.737	0.012	0.0907	0.0013	0.40918	561	7	560	8	553	25	100
M18_41b_6c - 1	806	124	0.15	0.748	0.017	0.0908	0.0017	0.26957	566	10	560	10	578	44	99
M18_41b_36c - 1	2417	1047	0.43	0.750	0.012	0.0908	0.0013	0.50714	568	7	560	8	585	19	99
M18_41b_50c - 1	1716	505	0.29	0.731	0.012	0.0911	0.0013	0.39655	557	7	562	8	518	24	101
M18_41b_15r - 1	40	11	0.27	0.699	0.064	0.091	0.002	-0.11018	516	37	563	12	230	170	109
M18_41b_67c - 1	271	83	0.31	0.737	0.018	0.0913	0.0025	0.22785	558	10	563	15	525	60	101
M18_41b_14r - 1	153	48	0.32	0.773	0.028	0.0916	0.0017	0.24745	576	16	565	10	558	73	98
M18_41b_96c - 1	767	104	0.14	0.737	0.009	0.0916	0.0025	0.32023	560	5	565	15	543	42	101
M18_41b_62c - 1	225	62	0.28	0.772	0.019	0.0917	0.0026	0.10499	578	11	565	15	582	61	98
M18_41b_120c - 1	2870	353	0.12	0.7422	0.0067	0.0917	0.0025	0.49308	563	4	566	15	552	36	100
M18_41b_94c - 1	2561	780	0.30	0.7426	0.0067	0.0919	0.0025	0.49023	564	4	567	15	560	36	101
M18_41b_52r - 1	457	98	0.21	0.758	0.013	0.0921	0.0025	0.19105	571	8	568	15	573	50	99
M18_41b_24c - 1	1101	81	0.07	0.737	0.014	0.0922	0.0014	0.36272	560	8	568	8	490	32	102
M18_41b_52c - 1	1044	356	0.34	0.81	0.01	0.0922	0.0025	0.37225	603	6	569	15	733	39	94
M18_41b_81c - 1	1275	202	0.16	0.7414	0.0076	0.0929	0.0025	0.43119	563	5	572	15	512	38	102
M18_41b_58c - 1	278	102	0.37	0.773	0.019	0.0929	0.0026	0.26437	579	11	572	15	550	61	99
M18_41b_118c - 1	816	58	0.07	0.74	0.01	0.0929	0.0026	0.31335	564	6	573	15	519	44	102
M18_41b_115c - 1	3284	1365	0.42	0.746	0.006	0.0929	0.0025	0.58811	565	4	573	15	544	35	101
M18_41b_102c - 1	160	43	0.26	0.766	0.024	0.093	0.003	0.11646	572	14	573	16	545	77	100
M18_41b_14c - 1	111	32	0.29	0.756	0.029	0.0932	0.0016	0.16345	565	17	574	9	485	76	102
M18_41b_15c - 1	172	94	0.54	0.775	0.027	0.0934	0.0015	0.044542	579	15	575	9	527	72	99
M18_41b_72c - 1	554	139	0.25	0.738	0.012	0.0936	0.0026	0.30637	560	7	577	15	501	47	103
M18_41b_16r - 1	1040	258	0.25	0.787	0.014	0.0936	0.0014	0.38504	589	8	577	8	600	28	98
M18_41b_19c - 1	1162	244	0.21	0.759	0.014	0.0937	0.0014	0.3641	573	8	578	9	517	30	101
M18_41b_16c - 1	1108	245	0.22	0.757	0.013	0.0938	0.0014	0.27341	572	8	578	8	513	27	101
M18_41b_1c - 1	214	37	0.17	0.766	0.024	0.094	0.002	0.22464	574	14	579	10	529	64	101

M18_41b_64c - 1	265	77	0.29	0.767	0.027	0.094	0.003	0.1353	575	16	579	17	532	90	101
M18_41b_21c - 1	168	366	2.18	0.766	0.025	0.0942	0.0016	0.19773	573	14	580	9	481	65	101
M18_41b_65c - 1	168	56	0.33	0.772	0.021	0.0943	0.0027	0.23244	578	12	581	16	536	67	101
M18_41b_106c - 1	145	52	0.36	0.765	0.024	0.0946	0.0027	0.12815	573	14	583	16	517	74	102
M18_41b_73c - 1	163	35	0.22	0.745	0.021	0.0948	0.0026	0.17204	561	13	584	16	454	71	104
M18_41b_110c - 1	830	327	0.39	0.782	0.012	0.0950	0.0026	0.38168	586	7	585	15	585	42	100
M18_41b_112c - 1	324	117	0.36	0.761	0.014	0.0948	0.0026	0.36394	574	8	585	16	526	51	102
M18_41b_103c - 1	474	81	0.17	0.771	0.012	0.0951	0.0026	0.20858	579	7	585	15	566	47	101
M18_41b_82c - 1	126	23	0.19	0.764	0.027	0.0953	0.0028	0.25812	572	15	587	16	459	80	103
M18_41b_71c - 1	461	100	0.22	0.797	0.019	0.0955	0.0028	0.30998	595	11	588	16	629	61	99
M18_41b_28c - 1	209	33	0.16	0.77	0.03	0.0956	0.0015	0.15449	577	14	588	9	472	70	102
M18_41b_116c - 1	353	103	0.29	0.781	0.013	0.0956	0.0026	0.28715	585	7	589	16	573	49	101
M18_41b_113c - 1	279	91	0.33	0.836	0.019	0.0956	0.0027	0.14592	615	11	589	16	699	60	96
M18_41b_119c - 1	302	46	0.15	0.777	0.018	0.0962	0.0027	0.30803	581	10	592	16	523	57	102
M18_41b_83c - 1	248	63	0.26	0.781	0.025	0.0964	0.0028	0.28829	583	14	593	16	497	72	102
M18_41b_80c - 1	375	61	0.16	0.771	0.014	0.0965	0.0027	0.36078	580	8	594	16	502	50	102
M18_41b_9c - 1	287	31	0.11	0.79	0.02	0.0966	0.0017	0.2766	589	13	594	10	553	59	101
M18_41b_43c - 1	359	93	0.26	0.796	0.018	0.0970	0.0015	0.20497	593	11	597	9	549	44	101
M18_41b_104c - 1	1174	572	0.49	0.7877	0.0093	0.0970	0.0027	0.47337	590	5	597	16	573	40	101
M18_41b_7c - 1	322	119	0.37	0.799	0.022	0.0971	0.0016	0.25305	594	12	597	9	564	52	101
M18_41b_77c - 1	96	19	0.20	0.795	0.032	0.0973	0.0028	0.13917	587	18	599	16	490	92	102
M18_41b_99c - 1	747	96	0.13	0.803	0.014	0.0979	0.0028	0.43114	599	8	602	16	593	46	101
M18_41b_37c - 1	1381	544	0.39	0.791	0.015	0.0984	0.0015	0.47829	591	9	605	9	513	30	102
M18_41b_11c - 1	484	383	0.79	0.834	0.019	0.0985	0.0016	0.25994	616	11	606	9	627	40	98
M18_41b_38c - 1	183	93	0.51	0.828	0.026	0.0987	0.0016	0.073538	610	15	607	9	575	68	99
M18_41b_69c - 1	164	36	0.22	0.786	0.025	0.0988	0.0028	0.14002	588	14	607	17	483	78	103
M18_41b_85c - 1	2672	1912	0.72	0.82	0.01	0.0989	0.0028	0.47665	607	6	608	16	578	41	100
M18_41b_53c - 1	2980	2331	0.78	0.8262	0.0084	0.0992	0.0027	0.54589	611	5	610	16	614	37	100

M18_41b_45c - 1	2176	817	0.38	0.821	0.014	0.0995	0.0016	0.66029	608	8	611	9	585	20	101
M18_41b_98c - 1	149	59	0.39	0.807	0.022	0.0996	0.0028	0.11493	601	13	612	16	551	69	102
M18_41b_66c - 1	999	252	0.25	0.8366	0.0098	0.0997	0.0027	0.015427	617	5	612	16	624	41	99
M18_41b_109c - 1	702	1154	1.64	0.86	0.02	0.1003	0.0028	0.37189	630	11	616	17	690	53	98
M18_41b_23c - 1	872	240	0.28	0.85	0.02	0.1003	0.0016	0.24662	623	10	616	9	622	36	99
M18_41b_30c - 1	1856	592	0.32	0.834	0.013	0.1005	0.0015	0.55896	615	7	617	9	588	18	100
M18_41b_55c - 1	540	695	1.29	0.856	0.014	0.1007	0.0028	0.30866	627	7	619	16	646	46	99
M18_41b_51c - 1	389	173	0.45	0.84	0.02	0.1010	0.0016	0.34182	617	10	620	9	588	36	100
M18_41b_84c - 1	1510	1700	1.13	0.845	0.012	0.101	0.003	0.48689	621	7	620	17	606	44	100
M18_41b_25c - 1	336	170	0.51	0.97	0.03	0.1012	0.0016	0.30229	684	15	622	10	851	57	91
M18_41b_97c - 1	440	193	0.44	0.825	0.014	0.1013	0.0028	0.3006	609	8	622	16	574	49	102
M18_41b_33c - 1	229	107	0.47	0.858	0.022	0.1016	0.0017	0.19063	629	12	623	10	627	50	99
M18_41b_27c - 1	355	549	1.55	0.855	0.022	0.1021	0.0016	0.26895	626	12	627	9	590	48	100
M18_41b_75c - 1	184	105	0.57	0.85	0.02	0.1029	0.0029	0.15152	621	12	631	17	579	65	102
M18_41b_61c - 1	621	200	0.32	0.935	0.018	0.1031	0.003	0.47708	670	10	633	17	749	49	94
M18_41b_41c - 1	319	97	0.31	0.855	0.019	0.1034	0.0016	0.29452	625	11	634	9	571	41	101
M18_41b_31c - 1	277	47	0.17	0.882	0.021	0.1044	0.0016	0.22907	641	11	640	10	621	45	100
M18_41b_70c - 1	329	76	0.23	0.86	0.02	0.105	0.003	0.18253	628	9	644	17	576	52	103
M18_41b_121c - 1	133	98	0.74	0.897	0.041	0.1053	0.0032	0.17449	643	22	645	19	590	110	100
M18_41b_79c - 1	149	166	1.12	0.894	0.024	0.106	0.003	0.22821	645	13	651	18	607	66	101
M18_41b_74c - 1	470	265	0.56	0.861	0.014	0.107	0.003	0.32548	631	8	652	17	564	47	103
M18_41b_11r - 1	1989	293	0.15	0.899	0.014	0.1065	0.0015	0.5056	651	8	652	9	623	19	100
M18_41b_44c - 1	238	121	0.51	0.915	0.024	0.1078	0.0017	0.24524	656	12	660	10	612	49	101
M18_41b_111c - 1	285	191	0.67	0.888	0.017	0.1099	0.0031	0.26246	643	9	672	18	548	53	104
M18_41b_90c - 1	274	118	0.43	0.951	0.018	0.1116	0.0031	0.079004	677	10	682	18	644	55	101
M18_41b_86c - 1	301	119	0.40	1.019	0.025	0.117	0.0033	0.30866	711	13	711	19	671	61	100
M18_41b_33r - 1	3609	140	0.04	0.97	0.02	0.1191	0.0019	0.6553	688	9	726	11	528	23	105
M18_41b_26c - 1	197	79	0.40	1.056	0.027	0.120	0.002	0.29039	728	14	732	11	677	48	101

M18_41b_32c - 1	380	124	0.33	1.276	0.027	0.1376	0.0023	0.36958	834	12	831	13	820	36	100
M18_41b_114c - 1	211	76	0.36	1.295	0.056	0.1461	0.0047	0.54026	839	24	879	26	738	86	105
M18_41b_57c - 1	319	212	0.66	1.623	0.025	0.1626	0.0045	0.36723	978	10	971	25	973	43	99
M18_41b_5c - 1	161	53	0.33	1.648	0.038	0.1669	0.0026	0.37577	985	15	995	14	947	39	101
M18_41b_92c - 1	183	175	0.96	1.71	0.03	0.1698	0.0047	0.24744	1010	11	1011	26	1007	49	100
M18_41b_13c - 1	204	108	0.53	6.40	0.11	0.3646	0.0055	0.5819	2030	15	2003	26	2041	17	98
M18_41b_3c - 1	178	61	0.34	6.3	0.1	0.3647	0.0056	0.44616	2012	14	2003	26	2013	19	100
M18_41b_13r - 1	710	102	0.14	6.487	0.097	0.369	0.005	0.67675	2043	13	2024	25	2041	11	99
M18_41b_117c - 1	1535	366	0.24	6.3	0.05	0.37	0.01	0.61582	2018	7	2029	48	2005	28	101
M18_41b_91r - 1	283	40	0.14	10.36	0.11	0.445	0.012	0.60643	2466	9	2372	54	2548	28	93
M18_41b_40c - 1	578	273	0.47	13	0.19	0.5297	0.0076	0.7229	2679	14	2739	32	2624	9.6	104
M18_41b_2c - 1	88	46	0.52	13.7	0.2	0.5332	0.0083	0.52104	2729	15	2753	35	2701	17	102
M18_41b_17c - 1	178	102	0.57	22.63	0.34	0.6491	0.0098	0.64338	3211	15	3223	38	3186	12	101
M18_41b_10c - 1	865	131	0.15	30.06	0.73	0.723	0.018	0.71707	3486	24	3505	66	3450	23	102

APPENDIX F – Whole-rock geochemistry: Methods and detection limits of the elemental analyses

Analyte Symbol	Unit Symbol	Detection Limit	Analysis Method
SiO_2	%	0.01	FUS-ICP
Al_2O_3	%	0.01	FUS-ICP
Fe_2O_3(T)	%	0.01	FUS-ICP
MnO	%	0.001	FUS-ICP
MgO	%	0.01	FUS-ICP
CaO	%	0.01	FUS-ICP
Na_2O	%	0.01	FUS-ICP
K_2O	%	0.01	FUS-ICP
TiO_2	%	0.001	FUS-ICP
P_2O_5	%	0.01	FUS-ICP
LOI	%		FUS-ICP
Total	%	0.01	FUS-ICP
Sc	ppm	1	FUS-ICP
Be	ppm	1	FUS-ICP
V	ppm	5	FUS-ICP
Ba	ppm	2	FUS-ICP
Sr	ppm	2	FUS-ICP
Y	ppm	1	FUS-ICP
Zr	ppm	2	FUS-ICP
Cr	ppm	20	FUS-MS
Co	ppm	1	FUS-MS
Ni	ppm	20	FUS-MS
Cu	ppm	10	FUS-MS
Zn	ppm	30	FUS-MS
Ga	ppm	1	FUS-MS
Ge	ppm	1	FUS-MS
As	ppm	5	FUS-MS
Rb	ppm	2	FUS-MS
Nb	ppm	1	FUS-MS
Mo	ppm	2	FUS-MS
Ag	ppm	0.5	FUS-MS
In	ppm	0.2	FUS-MS
Sn	ppm	1	FUS-MS
Sb	ppm	0.5	FUS-MS
Cs	ppm	0.5	FUS-MS
La	ppm	0.1	FUS-MS
Ce	ppm	0.1	FUS-MS
Pr	ppm	0.05	FUS-MS
Nd	ppm	0.1	FUS-MS
Sm	ppm	0.1	FUS-MS
Eu	ppm	0.05	FUS-MS

Gd	ppm	0.1	FUS-MS
Tb	ppm	0.1	FUS-MS
Dy	ppm	0.1	FUS-MS
Ho	ppm	0.1	FUS-MS
Er	ppm	0.1	FUS-MS
Tm	ppm	0.05	FUS-MS
Yb	ppm	0.1	FUS-MS
Lu	ppm	0.01	FUS-MS
Hf	ppm	0.2	FUS-MS
Ta	ppm	0.1	FUS-MS
W	ppm	1	FUS-MS
Tl	ppm	0.1	FUS-MS
Pb	ppm	5	FUS-MS
Bi	ppm	0.4	FUS-MS
Th	ppm	0.1	FUS-MS
U	ppm	0.1	FUS-MS

APPENDIX G – Geochemical data used in Chapter 7

Appendix G1 – Whole-rock geochemical composition of phyllites, quartzphyllites (qtzphyllites) and FCR-LAC rocks (metatexites, diatexites, and granites). Major elements in weight percentage (wt. %) and the trace elements expressed in parts per million (ppm).

Lithology	Phyllite N		Phyllite S		Qtzphyllite N	Qtzphyllite S
Sample	JTJ-2	JTJ-6	JTJ-18	JTJ-19	JTJ-49	JTJ-41b
SiO_2	61.02	54.64	63.82	66.63	68.39	65.71
Al_2O_3	18.02	23.40	17.68	14.94	14.18	16.15
$Fe_2O_3^T$	6.95	7.34	4.91	5.36	4.55	6.24
FeO^T	6.25	6.60	4.42	4.82	4.09	5.61
MnO	0.06	0.07	0.05	0.04	0.06	0.08
MgO	2.40	2.06	1.75	1.67	1.65	2.00
CaO	1.36	0.30	0.10	0.15	2.36	0.44
Na_2O	1.75	1.14	1.18	1.35	2.52	1.75
K_2O	3.40	4.49	4.34	2.86	3.68	3.03
TiO_2	0.87	0.82	0.76	0.86	0.76	0.89
P_2O_5	0.14	0.13	0.11	0.07	0.15	0.15
LOI	3.65	5.09	4.22	5.02	1.01	3.60
Total	99.62	99.45	98.92	98.95	99.31	100.00
Sc	15.00	18.00	15.00	14.00	11.00	15.00
V	91.00	115.00	123.00	94.00	67.00	98.00
Ba	737.00	780.00	764.00	608.00	660.00	608.00
Sr	209.00	110.00	64.00	49.00	243.00	82.00
Y	32.00	29.00	28.00	34.00	28.00	33.00
Zr	203.00	133.00	211.00	218.00	386.00	285.00
Cr	90.00	110.00	90.00	80.00	60.00	90.00
Ni	40.00	40.00	20.00	30.00	20.00	20.00
Ga	25.00	32.00	23.00	20.00	19.00	21.00

Rb	154.00	184.00	174.00	116.00	154.00	110.00
Nb	15.00	14.00	11.00	12.00	13.00	12.00
Cs	4.90	9.90	7.60	4.80	8.80	2.10
La	51.00	53.90	42.80	46.40	50.90	38.60
Ce	92.40	104.00	83.00	93.20	103.00	77.60
Pr	11.30	11.90	10.30	10.70	11.40	9.28
Nd	40.10	43.30	37.90	40.80	41.60	34.30
Sm	7.60	8.40	7.30	8.10	7.60	7.10
Eu	1.55	1.69	1.41	1.65	1.67	1.42
Gd	6.30	6.80	6.00	7.40	6.30	6.70
Tb	1.00	1.00	0.90	1.20	1.00	1.10
Dy	6.00	5.90	5.50	6.90	5.70	6.30
Ho	1.10	1.10	1.10	1.30	1.10	1.20
Er	3.30	3.20	3.10	3.70	3.10	3.70
Tm	0.47	0.48	0.46	0.54	0.45	0.53
Yb	3.10	3.20	3.10	3.50	3.10	3.50
Lu	0.46	0.47	0.46	0.51	0.47	0.55
Hf	5.40	3.60	5.20	5.50	9.30	7.00
Ta	1.30	1.20	1.10	1.30	1.20	1.00
Pb	23.00	21.00	10.00	11.00	22.00	15.00
Th	17.10	16.90	12.00	10.20	16.70	13.40
U	3.50	6.50	3.60	3.80	3.20	3.80
REE	225.68	245.34	203.33	225.90	237.39	191.88
LREE	202.40	221.50	181.30	199.20	214.50	166.88
HREE	23.28	23.84	22.03	26.70	22.89	25.00
LREE/HREE	8.69	9.29	8.23	7.46	9.37	6.68
La/Yb_N	11.08	11.34	9.30	8.93	11.06	7.43
La/Sm_N	4.22	4.03	3.69	3.60	4.21	3.42

Dy/Yb_N	1.26	1.20	1.15	1.28	1.19	1.17
Tb/Yb_N	1.42	1.38	1.28	1.51	1.42	1.38
Eu/Eu*	0.68	0.68	0.65	0.65	0.74	0.63

Appendix G1 *continued*

Lithology	Metatexite										
Sample	JTJ-8	JTJ-20	JTJ-22B	JTJ-24B	JTJ-25	JTJ-37	JTJ-48B	JTJ-53	JTJ-54B	JTJ-56A	JTJ-60A
SiO_2	58.57	66.85	63.74	74.73	60.94	69.23	59.31	64.82	58.51	69.93	71.14
Al_2O_3	20.42	16.58	17.78	12.47	18.57	15.08	18.69	15.58	20.42	14.10	15.38
$Fe_2O_3^T$	8.10	5.51	5.61	3.78	6.52	4.76	7.32	5.90	6.79	4.47	2.50
FeO^T	7.29	4.96	5.05	3.40	5.87	4.28	6.59	5.31	6.11	4.02	2.25
MnO	0.09	0.06	0.05	0.12	0.04	0.07	0.10	0.10	0.09	0.09	0.08
MgO	2.43	1.74	2.01	1.25	2.24	1.84	2.70	2.16	2.73	1.69	0.73
CaO	0.55	0.79	0.35	0.76	0.51	1.13	0.54	0.23	0.69	0.74	0.60
Na_2O	1.57	2.30	1.18	2.18	1.40	2.65	1.21	1.45	1.82	2.80	3.04
K_2O	3.92	3.48	3.84	3.41	4.16	3.27	4.42	2.84	3.67	3.41	4.34
TiO_2	0.84	0.86	0.70	0.58	0.78	0.64	0.82	0.70	0.74	0.60	0.32
P_2O_5	0.13	0.11	0.14	0.17	0.17	0.19	0.15	0.14	0.17	0.16	0.24
LOI	3.72	2.25	3.69	1.23	4.51	1.53	4.43	4.72	4.75	1.63	1.37
Total	100.30	100.50	99.08	100.70	99.84	100.40	99.68	98.63	100.40	99.62	99.74
Sc	18.00	15.00	15.00	8.00	16.00	12.00	17.00	15.00	17.00	13.00	7.00
V	112.00	92.00	111.00	59.00	111.00	79.00	109.00	136.00	124.00	72.00	36.00
Ba	735.00	497.00	615.00	683.00	921.00	664.00	738.00	1038.00	1005.00	361.00	286.00
Sr	118.00	149.00	79.00	156.00	114.00	189.00	111.00	74.00	169.00	107.00	79.00
Y	29.00	22.00	24.00	21.00	26.00	29.00	28.00	33.00	29.00	26.00	14.00
Zr	142.00	188.00	162.00	274.00	142.00	200.00	140.00	155.00	140.00	240.00	114.00
Cr	100.00	80.00	80.00	50.00	90.00	70.00	100.00	100.00	90.00	70.00	40.00

Ni	50.00	30.00	20.00	< 20	30.00	< 20	40.00	50.00	30.00	30.00	< 20
Ga	29.00	22.00	23.00	16.00	25.00	19.00	26.00	23.00	28.00	21.00	22.00
Rb	189.00	167.00	180.00	186.00	170.00	150.00	234.00	170.00	281.00	279.00	260.00
Nb	15.00	13.00	11.00	8.00	12.00	10.00	14.00	11.00	12.00	16.00	19.00
Cs	16.30	12.60	33.30	20.60	9.30	9.40	28.50	13.30	44.10	58.40	42.00
La	61.10	34.70	34.50	43.60	46.40	38.20	45.90	44.70	46.90	40.80	17.70
Ce	114.00	73.00	69.20	91.10	92.10	78.50	90.60	88.30	92.80	82.70	35.00
Pr	13.20	8.22	8.26	9.82	10.90	8.68	10.00	10.30	10.40	9.44	4.03
Nd	46.60	31.00	30.00	35.50	40.90	31.60	37.50	38.40	38.40	34.00	14.00
Sm	8.50	6.20	6.10	6.60	7.90	6.40	7.00	7.40	7.40	6.80	2.90
Eu	1.67	1.23	1.22	1.10	1.50	1.36	1.39	1.47	1.53	1.10	0.54
Gd	6.60	5.20	5.40	5.50	6.60	5.60	6.10	6.80	6.10	5.50	2.50
Tb	1.00	0.80	0.90	0.80	1.00	0.90	1.00	1.00	1.00	0.90	0.50
Dy	6.00	4.50	5.00	4.50	5.60	5.60	5.40	6.00	5.70	5.00	2.70
Ho	1.10	0.80	0.90	0.80	1.00	1.10	1.00	1.20	1.10	1.00	0.50
Er	3.10	2.50	2.80	2.30	2.90	3.40	3.00	3.40	3.10	2.80	1.40
Tm	0.46	0.37	0.41	0.33	0.40	0.51	0.43	0.49	0.43	0.41	0.21
Yb	2.90	2.60	2.90	2.20	2.70	3.40	2.90	3.20	2.90	2.80	1.40
Lu	0.45	0.40	0.45	0.34	0.42	0.53	0.43	0.51	0.44	0.43	0.22
Hf	3.70	4.80	4.20	6.00	3.50	5.00	3.80	3.80	3.80	6.10	2.80
Ta	1.20	1.50	2.10	1.00	0.90	1.10	1.40	0.90	1.00	2.40	4.90
Pb	25.00	20.00	17.00	28.00	21.00	29.00	22.00	22.00	25.00	17.00	21.00
Th	17.20	10.80	10.50	15.30	12.70	11.90	13.20	12.20	13.20	12.80	5.50
U	4.20	5.10	6.60	3.50	4.50	3.90	6.40	43.70	9.40	7.10	3.80
REE	266.68	171.52	168.04	204.49	220.32	185.78	212.65	213.17	218.20	193.68	83.60
LREE	243.40	153.12	148.06	186.62	198.20	163.38	191.00	189.10	195.90	173.74	73.63
HREE	23.28	18.40	19.98	17.87	22.12	22.40	21.65	24.07	22.30	19.94	9.97
LREE/HREE	10.46	8.32	7.41	10.44	8.96	7.29	8.82	7.86	8.78	8.71	7.39

La/Yb_N	14.19	8.99	8.01	13.35	11.57	7.57	10.66	9.41	10.89	9.81	8.51
La/Sm_N	4.52	3.52	3.56	4.15	3.69	3.75	4.12	3.80	3.98	3.77	3.84
Dy/Yb_N	1.34	1.12	1.12	1.33	1.35	1.07	1.21	1.22	1.28	1.16	1.25
Tb/Yb_N	1.52	1.35	1.37	1.60	1.63	1.16	1.52	1.38	1.52	1.41	1.57
Eu/Eu*	0.68	0.66	0.65	0.56	0.63	0.69	0.65	0.63	0.70	0.55	0.61

Appendix G1 *continued*

Lithology	Diatexite Type-1								Diatexite Type-2							
Sample	JTJ-27	JTJ-30	JTJ-31C	JTJ-43	JTJ-48A	JTJ-52	JTJ-55	JPC-48	JTJ-23A	JTJ-24A	JTJ-26	JTJ-28A	JTJ-51	JTJ-56B	JTJ-60B	JPC-45
SiO2	72.92	72.29	74.46	68.32	72.75	72.33	73.30	69.83	73.53	74.24	74.82	75.14	75.24	74.98	72.95	74.55
Al2O3	13.92	14.17	14.07	15.60	15.37	14.94	14.72	15.62	14.35	13.93	13.27	14.96	12.87	12.91	15.25	14.11
$Fe2O3^T$	0.97	1.38	0.90	2.90	1.29	1.52	1.13	2.15	1.12	0.75	0.81	0.18	2.67	1.01	0.98	0.81
FeO^T	0.87	1.24	0.81	2.61	1.16	1.37	1.02	1.93	1.01	0.67	0.73	0.16	2.40	0.91	0.88	0.73
MnO	0.01	0.01	0.02	0.03	0.03	0.02	0.03	0.03	0.03	0.03	0.01	0.01	0.05	0.03	0.02	0.02
MgO	0.21	0.31	0.25	0.84	0.27	0.41	0.29	0.67	0.18	0.17	0.16	0.06	0.90	0.36	0.49	0.44
CaO	0.59	0.63	0.54	0.95	0.61	0.74	0.88	0.62	0.46	0.59	0.60	0.42	0.65	0.48	0.44	0.21
Na2O	3.07	3.12	3.13	2.80	3.39	2.98	3.56	2.91	3.57	3.66	3.15	2.57	2.31	3.16	3.89	2.96
K2O	5.31	5.64	5.50	5.71	4.82	5.44	4.18	5.93	4.28	4.97	4.50	6.16	3.77	4.55	3.91	5.27
TiO2	0.12	0.20	0.13	0.75	0.19	0.24	0.15	0.40	0.07	0.07	0.11	0.02	0.39	0.12	0.10	0.12
P2O5	0.36	0.47	0.30	0.44	0.42	0.39	0.25	0.40	0.24	0.25	0.18	0.34	0.14	0.17	0.24	0.20
LOI	1.10	0.93	0.83	1.41	1.05	1.15	1.21	1.23	1.35	0.72	0.98	0.81	1.47	1.50	1.20	1.19
Total	98.58	99.14	100.10	99.74	100.20	100.20	99.68	101.72	99.18	99.38	98.58	100.70	100.50	99.25	99.46	100.61
Sc	4.00	2.00	1.00	3.00	2.00	3.00	3.00	<7	4.00	3.00	5.00	< 1	8.00	3.00	3.00	<7
V	< 5	< 5	< 5	29.00	6.00	8.00	< 5	13.00	< 5	< 5	< 5	< 5	38.00	9.00	9.00	5.00
Ba	196.00	217.00	232.00	640.00	205.00	282.00	468.00	353.00	146.00	203.00	200.00	358.00	582.00	482.00	187.00	220.00
Sr	57.00	56.00	61.00	150.00	50.00	74.00	139.00	89.00	43.00	79.00	63.00	111.00	128.00	115.00	69.00	82.00

Y	12.00	11.00	4.00	11.00	8.00	12.00	9.00	14.00	9.00	8.00	12.00	4.00	24.00	9.00	7.00	10.00
Zr	47.00	79.00	45.00	415.00	74.00	100.00	48.00	163.00	28.00	42.00	35.00	25.00	159.00	42.00	39.00	37.00
Cr	< 20	< 20	< 20	< 20	< 20	< 20	< 20	19.00	< 20	< 20	< 20	< 20	40.00	< 20	< 20	6.00
Ni	< 20	< 20	< 20	< 20	< 20	< 20	< 20	7.00	< 20	< 20	< 20	< 20	< 20	< 20	< 20	<7
Ga	18.00	21.00	19.00	26.00	24.00	20.00	17.00	23.00	16.00	12.00	16.00	17.00	16.00	12.00	15.00	14.00
Rb	239.00	303.00	275.00	331.00	315.00	282.00	143.00	290.00	238.00	170.00	183.00	234.00	165.00	154.00	145.00	205.00
Nb	6.00	7.00	4.00	6.00	10.00	7.00	6.00	10.37	9.00	4.00	3.00	< 1	7.00	5.00	5.00	4.98
Cs	10.20	8.60	6.60	7.80	20.30	17.10	14.00	-	34.80	9.70	5.00	6.00	10.10	8.60	6.00	-
La	7.20	15.60	5.90	145.00	14.70	20.40	21.00	36.96	3.50	3.60	4.60	1.10	36.60	7.70	6.80	3.79
Ce	15.40	35.10	13.40	368.00	32.20	44.70	41.70	79.12	7.80	7.20	9.60	2.20	74.20	15.20	13.10	7.77
Pr	1.85	4.23	1.65	46.50	3.78	5.19	4.80	9.79	0.88	0.79	1.11	0.28	8.21	1.64	1.49	0.95
Nd	6.70	16.00	6.10	175.00	14.40	19.50	17.10	36.54	3.40	2.90	4.10	1.10	29.20	6.60	5.20	3.46
Sm	1.80	4.10	1.80	25.40	3.90	5.10	4.10	8.99	0.80	0.70	1.10	0.40	5.90	1.30	1.00	0.98
Eu	0.41	0.45	0.39	1.06	0.33	0.55	0.79	0.61	0.25	0.40	0.44	0.55	1.08	0.56	0.34	0.43
Gd	1.90	3.60	1.80	9.50	3.50	4.70	3.30	6.86	1.00	0.80	1.30	0.50	4.80	1.30	0.90	1.12
Tb	0.40	0.60	0.30	0.80	0.50	0.70	0.50	0.85	0.30	0.20	0.30	0.10	0.80	0.20	0.20	0.24
Dy	2.20	2.90	1.10	3.10	2.10	3.10	2.10	3.52	1.70	1.30	2.00	0.60	4.70	1.40	1.10	1.70
Ho	0.40	0.40	0.20	0.40	0.20	0.40	0.30	0.49	0.30	0.30	0.40	0.10	0.90	0.20	0.20	0.35
Er	1.10	0.70	0.30	0.90	0.50	0.80	0.60	1.10	0.90	0.80	1.20	0.30	2.50	0.70	0.70	1.07
Tm	0.14	0.08	0.05	0.12	0.06	0.11	0.08	0.15	0.14	0.14	0.20	0.05	0.37	0.10	0.11	0.18
Yb	0.90	0.40	0.20	0.70	0.40	0.60	0.50	1.00	1.00	1.10	1.40	0.30	2.30	0.80	0.90	1.27
Lu	0.12	0.01	0.01	0.09	0.05	0.10	0.06	0.14	0.15	0.17	0.22	0.04	0.36	0.13	0.13	0.20
Hf	1.40	2.10	1.30	10.00	2.10	2.80	1.50	2.32	0.80	1.20	0.90	0.90	4.10	1.00	1.30	<0.06
Ta	0.70	0.80	0.60	0.50	1.90	0.90	1.10	1.03	1.90	1.30	0.30	< 0.1	0.90	1.00	1.40	0.37
Pb	32.00	33.00	33.00	41.00	27.00	36.00	36.00	39.00	36.00	41.00	31.00	43.00	28.00	37.00	28.00	38.00
Th	2.50	7.50	2.90	133.00	6.90	8.10	6.90	20.62	0.90	0.90	1.30	< 0,1	12.30	2.30	1.80	1.54
U	5.50	9.30	6.10	10.30	10.00	7.80	5.90	13.48	6.80	12.80	3.30	1.50	5.40	3.00	7.10	3.38
REE	40.52	84.17	33.20	776.57	76.62	105.95	96.93	186.13	22.12	20.40	27.97	7.62	171.92	37.83	32.17	23.52

LREE	32.95	75.03	28.85	759.90	68.98	94.89	88.70	171.40	16.38	15.19	20.51	5.08	154.11	32.44	27.59	16.96
HREE	7.57	9.14	4.35	16.67	7.64	11.06	8.23	14.73	5.74	5.21	7.46	2.54	17.81	5.39	4.58	6.57
LREE/HREE	4.35	8.21	6.63	45.58	9.03	8.58	10.78	11.64	2.85	2.92	2.75	2.00	8.65	6.02	6.02	2.58
La/Yb_N	5.39	26.27	19.87	139.50	24.75	22.90	28.29	24.80	2.36	2.20	2.21	2.47	10.72	6.48	5.09	2.01
La/Sm_N	2.51	2.39	2.06	3.59	2.37	2.51	3.22	2.58	2.75	3.23	2.63	1.73	3.90	3.72	4.27	2.43
Dy/Yb_N	1.59	4.71	3.57	2.88	3.41	3.36	2.73	2.28	1.10	0.77	0.93	1.30	1.33	1.14	0.79	0.87
Tb/Yb_N	1.96	6.60	6.60	5.03	5.50	5.13	4.40	3.72	1.32	0.80	0.94	1.47	1.53	1.10	0.98	0.83
Eu/Eu*	0.68	0.36	0.66	0.21	0.27	0.34	0.66	0.24	0.85	1.63	1.12	3.76	0.62	1.32	1.10	1.26

Appendix G1 c*ontinued*

Lithology	Granite															
Sample	JTJ-31A	JTJ-32	JTJ-34	JTJ-40	JPC-49	JPC-56	JPC-57	JTJ-9	JTJ-10	JTJ-44	JTJ-45	JTJ-47	JTJ-50	JTJ-62	JPC-51	JPC-52
SiO2	73.04	71.18	70.97	74.07	71.66	72.13	71.99	73.37	71.55	71.54	73.60	70.78	72.76	73.31	71.53	71.37
Al2O3	15.07	14.88	15.14	14.33	14.95	14.88	15.02	14.56	14.70	15.20	14.40	14.89	14.50	15.40	14.92	15.19
$Fe2O3^T$	1.04	1.91	2.36	0.51	1.94	1.56	1.50	1.28	1.45	1.56	1.36	1.90	1.32	0.92	1.48	1.41
FeO^T	0.94	1.72	2.12	0.46	1.75	1.40	1.35	1.15	1.30	1.40	1.22	1.71	1.19	0.83	1.33	1.27
MnO	0.02	0.03	0.02	0.01	0.02	0.02	0.02	0.02	0.03	0.02	0.02	0.03	0.03	0.04	0.02	0.02
MgO	0.26	0.46	0.57	0.09	0.60	0.65	0.65	0.25	0.29	0.43	0.32	0.48	0.23	0.10	0.71	0.60
CaO	0.55	0.71	0.88	0.34	0.45	0.36	0.36	0.53	0.62	0.60	0.55	0.71	0.57	0.44	0.34	0.33
Na2O	2.90	2.51	2.61	1.99	2.67	3.14	3.03	2.98	3.30	3.04	2.79	2.83	3.15	3.92	3.87	3.04
K2O	5.24	5.43	5.98	7.57	5.61	5.38	5.54	4.99	5.02	5.34	5.28	5.56	5.01	4.05	5.47	6.09
TiO2	0.15	0.29	0.54	0.06	0.32	0.27	0.25	0.19	0.19	0.27	0.21	0.33	0.16	0.08	0.22	0.27
P2O5	0.38	0.48	0.41	0.55	0.33	0.37	0.39	0.36	0.40	0.44	0.41	0.35	0.35	0.45	0.38	0.33
LOI	0.94	1.28	1.20	0.90	1.34	1.09	1.13	1.61	0.96	1.25	1.30	1.11	0.96	1.23	0.98	1.19
Total	99.59	99.15	100.70	100.40	101.64	101.25	101.23	100.10	98.52	99.67	100.20	98.96	99.01	99.95	101.25	101.11
Sc	1.00	3.00	2.00	< 1	<7	<7	<7	2.00	2.00	2.00	3.00	2.00	2.00	2.00	<7	<7
V	8.00	10.00	17.00	< 5	11.00	7.00	8.00	7.00	5.00	11.00	7.00	13.00	< 5	< 5	7.00	8.00

Ba	211.00	279.00	357.00	143.00	258.00	235.00	217.00	243.00	225.00	262.00	206.00	263.00	139.00	46.00	213.00	261.00
Sr	60.00	68.00	84.00	54.00	69.00	67.00	62.00	57.00	57.00	64.00	54.00	80.00	48.00	27.00	62.00	79.00
Y	5.00	17.00	10.00	9.00	12.00	10.00	12.00	7.00	7.00	10.00	7.00	7.00	6.00	6.00	10.00	9.00
Zr	57.00	137.00	287.00	23.00	129.00	108.00	104.00	64.00	70.00	106.00	84.00	117.00	64.00	40.00	96.00	114.00
Cr	< 20	< 20	< 20	< 20	8.00	8.00	7.00	< 20	< 20	< 20	< 20	< 20	< 20	< 20	5.00	5.00
Ni	< 20	< 20	< 20	< 20	<7	<7	<7	< 20	< 20	< 20	< 20	< 20	< 20	< 20	<7	<7
Ga	23.00	24.00	27.00	22.00	22.00	22.00	22.00	22.00	22.00	22.00	22.00	27.00	23.00	26.00	20.00	23.00
Rb	325.00	316.00	376.00	401.00	284.00	343.00	311.00	311.00	342.00	330.00	338.00	416.00	419.00	521.00	339.00	371.00
Nb	5.00	9.00	7.00	3.00	10.54	11.26	11.68	9.00	9.00	7.00	9.00	9.00	14.00	15.00	10.08	8.87
Cs	20.30	18.40	11.50	13.60	-	-	-	13.30	27.00	15.20	18.90	17.80	26.60	37.50	-	-
La	10.80	31.80	97.30	2.90	37.13	24.76	22.92	15.50	15.90	21.40	19.80	36.00	15.00	8.00	21.82	31.72
Ce	25.00	75.50	248.00	7.80	85.76	54.74	52.13	34.00	34.60	50.80	47.50	84.10	34.10	17.90	50.56	71.00
Pr	3.08	9.37	31.50	1.05	11.01	6.94	6.70	4.01	3.98	6.28	5.85	10.30	4.08	2.13	6.57	9.03
Nd	12.40	35.40	119.00	4.30	41.49	26.35	25.79	14.80	15.20	24.10	22.40	38.50	14.50	7.80	25.37	34.11
Sm	3.10	8.10	20.50	1.50	8.33	6.07	6.00	3.70	3.80	5.80	4.50	8.50	3.60	1.90	5.77	7.68
Eu	0.41	0.54	0.78	0.33	0.42	0.42	0.40	0.34	0.36	0.51	0.38	0.62	0.33	0.13	0.37	0.54
Gd	2.30	6.20	9.30	1.50	5.12	4.50	4.59	3.40	3.50	4.60	3.20	5.40	2.80	1.60	3.96	5.16
Tb	0.30	0.90	0.80	0.30	0.63	0.54	0.63	0.50	0.50	0.60	0.40	0.60	0.40	0.30	0.51	0.58
Dy	1.20	4.00	2.90	1.70	2.75	2.18	2.82	1.90	2.00	2.40	1.80	2.00	1.80	1.30	2.29	2.18
Ho	0.20	0.60	0.30	0.30	0.39	0.29	0.38	0.20	0.20	0.30	0.20	0.20	0.20	0.20	0.32	0.29
Er	0.40	1.30	0.70	0.70	0.84	0.58	0.78	0.40	0.40	0.60	0.60	0.60	0.50	0.50	0.70	0.56
Tm	0.05	0.15	0.09	0.08	0.09	0.07	0.10	0.06	0.05	0.07	0.07	0.06	0.06	0.06	0.08	0.07
Yb	0.30	0.80	0.50	0.50	0.60	0.38	0.55	0.30	0.30	0.40	0.40	0.30	0.30	0.40	0.47	0.43
Lu	0.01	0.10	0.07	0.06	0.08	0.05	0.06	0.04	0.04	0.06	0.06	0.04	0.04	0.06	0.06	0.06
Hf	1.50	3.70	7.00	1.00	1.55	<0.06	1.50	1.70	1.90	2.80	2.20	3.10	1.80	1.50	1.31	3.02
Ta	0.90	1.10	0.80	0.40	0.58	1.14	1.14	1.80	1.90	1.20	1.50	1.00	3.30	4.90	1.20	0.86
Pb	28.00	36.00	39.00	43.00	38.00	35.00	35.00	27.00	27.00	31.00	29.00	36.00	32.00	16.00	36.00	43.00
Th	6.80	22.20	107.00	1.20	39.25	22.16	20.21	6.90	7.20	13.90	15.60	28.50	9.10	5.10	20.86	33.69

U	6.70	12.60	10.70	3.50	16.30	11.93	14.03	5.10	9.40	8.70	11.10	15.00	13.70	4.50	10.69	5.84
REE	59.55	174.76	531.74	23.02	194.63	127.86	123.85	79.15	80.83	117.92	107.16	187.22	77.71	42.28	118.85	163.41
LREE	54.38	160.17	516.30	17.55	183.71	118.86	113.54	72.01	73.48	108.38	100.05	177.40	71.28	37.73	110.09	153.54
HREE	5.17	14.59	15.44	5.47	10.92	9.00	10.31	7.14	7.35	9.54	7.11	9.82	6.43	4.55	8.76	9.88
LREE/HREE	10.52	10.98	33.44	3.21	16.83	13.20	11.01	10.09	10.00	11.36	14.07	18.07	11.09	8.29	12.57	15.55
La/Yb_N	24.24	26.77	131.06	3.91	41.48	43.79	27.82	34.80	35.69	36.03	33.34	80.82	33.67	13.47	31.35	49.25
La/Sm_N	2.19	2.47	2.98	1.22	2.80	2.56	2.40	2.63	2.63	2.32	2.77	2.66	2.62	2.65	2.38	2.59
Dy/Yb_N	2.60	3.25	3.77	2.21	2.96	3.72	3.30	4.11	4.33	3.90	2.92	4.33	3.90	2.11	3.18	3.27
Tb/Yb_N	4.40	4.95	7.04	2.64	4.57	6.24	5.00	7.33	7.33	6.60	4.40	8.80	5.87	3.30	4.82	5.83
Eu/Eu*	0.47	0.23	0.17	0.67	0.20	0.24	0.24	0.29	0.30	0.30	0.31	0.28	0.32	0.23	0.24	0.26

Appendix G1 *continued*

Lithology	Granite													
Sample	JPC-53	JTJ-35	JPC-50	JTJ-11	JTJ-12	JPC-55	JTJ-59	JTJ-13	JPC-19	JPC-24	JPC-59	JPC-54	JTJ-36	JTJ-58
SiO2	71.62	70.63	71.41	71.13	71.39	70.32	71.96	71.78	70.64	72.31	75.24	73.33	72.64	73.41
Al2O3	15.20	15.10	15.05	14.71	15.01	15.51	14.50	14.60	15.15	14.64	13.95	14.72	14.91	14.81
$Fe2O3^T$	1.72	2.14	1.51	1.64	1.84	2.15	1.66	1.63	1.73	1.89	0.70	1.19	1.34	0.82
FeO^T	1.55	1.93	1.36	1.48	1.66	1.93	1.49	1.47	1.56	1.70	0.63	1.07	1.21	0.74
MnO	0.02	0.02	0.02	0.02	0.02	0.03	0.04	0.02	0.02	0.03	0.02	0.02	0.02	0.03
MgO	0.70	0.59	0.55	0.43	0.41	0.75	0.54	0.36	0.63	0.64	0.36	0.48	0.31	0.19
CaO	0.40	0.72	0.26	0.73	0.61	0.58	1.01	0.58	0.46	0.37	0.09	0.24	0.63	0.55
Na2O	3.02	2.57	2.99	3.06	2.72	3.16	3.54	2.66	2.63	2.80	3.48	2.98	3.25	3.27
K2O	5.53	5.37	5.93	5.43	5.39	5.32	4.86	5.71	6.91	5.39	4.33	5.20	4.97	4.59
TiO2	0.31	0.44	0.22	0.28	0.28	0.42	0.28	0.28	0.40	0.31	0.10	0.19	0.19	0.10
P2O5	0.37	0.48	0.47	0.37	0.40	0.39	0.29	0.49	0.31	0.36	0.30	0.30	0.44	0.35
LOI	0.95	1.51	1.44	0.94	1.06	1.21	1.02	1.21	0.84	1.01	1.32	1.21	1.11	1.67
Total	101.39	99.58	101.21	98.71	99.14	101.77	99.70	99.31	101.28	101.45	100.52	100.93	99.82	99.78

Sc	<7	3.00	<7	2.00	2.00	<7	3.00	2.00	<7	<7	<7	<7	2.00	3.00
V	8.00	19.00	<5	11.00	9.00	18.00	17.00	10.00	8.00	9.00	<5	5.00	7.00	< 5
Ba	240.00	376.00	183.00	283.00	235.00	287.00	491.00	268.00	407.00	172.00	134.00	146.00	274.00	201.00
Sr	76.00	93.00	47.00	80.00	63.00	74.00	142.00	76.00	106.00	49.00	42.00	46.00	74.00	61.00
Y	10.00	10.00	14.00	9.00	11.00	10.00	8.00	8.00	9.00	11.00	5.00	6.00	9.00	7.00
Zr	123.00	211.00	86.00	112.00	116.00	198.00	130.00	113.00	193.00	130.00	35.00	72.00	74.00	46.00
Cr	9.00	< 20	6.00	< 20	< 20	11.00	< 20	< 20	6.00	7.00	<5	5.00	< 20	< 20
Ni	<7	< 20	<7	< 20	< 20	<7	< 20	< 20	<7	<7	<7	<7	< 20	< 20
Ga	24.00	25.00	23.00	22.00	22.00	25.00	23.00	25.00	23.00	24.00	20.00	22.00	23.00	18.00
Rb	371.00	358.00	403.00	334.00	357.00	369.00	276.00	381.00	305.00	378.00	277.00	293.00	288.00	281.00
Nb	11.61	7.00	14.99	8.00	10.00	9.94	10.00	8.00	4.32	15.97	12.91	7.92	10.00	9.00
Cs	-	10.60	-	14.80	18.30	-	19.10	13.00	-	-	-	-	17.00	18.90
La	33.65	65.40	16.95	26.60	30.40	64.65	38.80	31.20	61.40	37.77	5.03	14.98	12.40	8.50
Ce	75.62	162.00	39.29	60.00	72.70	151.70	77.60	72.00	135.11	87.83	11.04	33.71	26.90	17.70
Pr	9.74	20.40	5.00	7.08	8.82	19.91	8.80	8.88	16.41	11.35	1.36	4.24	3.27	2.09
Nd	36.91	75.60	18.49	26.50	33.50	75.41	30.80	33.80	61.23	43.58	5.09	15.65	12.40	7.50
Sm	8.17	12.90	3.94	6.30	7.00	12.56	5.50	7.40	13.18	9.40	1.22	3.56	3.30	2.20
Eu	0.50	0.74	0.25	0.57	0.45	0.59	0.75	0.56	0.79	0.46	0.11	0.23	0.34	0.51
Gd	5.30	6.40	2.91	4.50	5.10	6.18	3.70	4.80	7.47	5.84	1.20	2.62	3.00	2.10
Tb	0.61	0.70	0.50	0.60	0.70	0.68	0.40	0.60	0.70	0.72	0.19	0.34	0.50	0.30
Dy	2.43	2.80	2.66	2.20	2.80	2.60	1.90	2.10	2.39	2.92	0.95	1.46	2.30	1.80
Ho	0.30	0.40	0.41	0.30	0.40	0.38	0.30	0.30	0.30	0.43	0.15	0.18	0.30	0.30
Er	0.60	0.80	0.91	0.60	0.80	0.82	0.60	0.60	0.69	0.95	0.32	0.40	0.60	0.60
Tm	0.07	0.11	0.11	0.07	0.10	0.10	0.09	0.07	0.06	0.11	0.04	0.04	0.08	0.08
Yb	0.39	0.60	0.64	0.40	0.50	0.62	0.60	0.30	0.46	0.66	0.27	0.26	0.50	0.50
Lu	0.05	0.09	0.08	0.06	0.07	0.08	0.09	0.05	0.05	0.07	0.04	0.03	0.06	0.07
Hf	2.21	5.10	0.48	2.80	3.10	5.09	3.40	2.90	2.18	2.09	1.06	<0.06	2.10	1.50
Ta	1.05	0.80	1.61	1.10	1.60	1.27	1.40	0.90	0.52	1.23	2.09	1.07	2.10	2.50

Pb	39.00	34.00	34.00	36.00	33.00	36.00	34.00	37.00	53.00	34.00	21.00	33.00	26.00	42.00
Th	32.41	57.10	21.08	14.00	22.30	66.13	17.00	24.60	38.52	36.34	2.48	14.02	4.90	3.40
U	19.28	11.60	12.44	9.90	10.70	13.69	10.30	10.60	10.11	13.20	3.67	13.15	5.70	5.80
REE	174.34	348.94	92.13	135.78	163.34	336.28	169.93	162.66	300.24	202.10	27.00	77.70	65.95	44.25
LREE	164.08	336.30	83.67	126.48	152.42	324.23	161.50	153.28	287.33	189.93	23.74	72.14	58.27	37.99
HREE	10.26	12.64	8.46	9.30	10.92	12.05	8.43	9.38	12.91	12.17	3.27	5.56	7.68	6.26
LREE/HREE	15.99	26.61	9.89	13.60	13.96	26.90	19.16	16.34	22.27	15.61	7.27	12.98	7.59	6.07
La/Yb_N	58.29	73.41	17.92	44.79	40.95	69.91	43.55	70.04	90.16	38.33	12.66	38.24	16.70	11.45
La/Sm_N	2.59	3.19	2.70	2.65	2.73	3.23	4.43	2.65	2.93	2.53	2.60	2.64	2.36	2.43
Dy/Yb_N	4.06	3.03	2.71	3.57	3.64	2.71	2.06	4.55	3.39	2.86	2.31	3.58	2.99	2.34
Tb/Yb_N	6.94	5.13	3.45	6.60	6.16	4.82	2.93	8.80	6.72	4.78	5.69	3.12	4.40	2.64
Eu/Eu*	0.23	0.25	0.23	0.33	0.23	0.20	0.51	0.29	0.24	0.19	0.28	0.23	0.33	0.73

Appendix G2 – Apatite trace element composition (ppm) from the host rocks (phyllites) and FCR-LAC rocks (metatexites, diatexites, and granites).

Lithology	Phyllite			Metatexite				
Sample	M1_2_1	M1_2_2	M1_2_3	M1_20_1	M2_25_1	M3_8_1	M4_60A_1	M5_53_1
Sr	317	1471	333	167	243	487	113	183
Y	854	480	697	1973	1915	837	1618	1457
Th	27	97	18	1	1	50	1	0
U	8	34	18	223	32	17	91	46
La	386	1585	897	162	167	405	159	126
Ce	1124	2019	1672	547	559	921	503	425
Pr	175	174	179	91	97	107	83	74
Nd	931	630	747	513	565	455	457	435
Sm	253	94	143	216	245	120	190	195

Eu	21	21	19	17	26	29	16	17
Gd	252	98	158	301	350	145	255	278
Tb	33	16	22	60	67	27	50	52
Dy	169	100	130	386	410	166	316	320
Ho	29	18	25	77	78	31	61	60
Er	67	42	60	199	190	78	155	146
Tm	8	5	8	28	25	11	22	19
Yb	51	33	46	183	148	73	145	120
Lu	7	4	7	25	19	9	19	16
LREE	2870	4503	3638	1529	1632	2008	1391	1255
HREE	638	338	474	1275	1311	569	1039	1028
REE	3508	4841	4112	2804	2943	2577	2431	2283
Eu/Eu*	0.25	0.67	0.39	0.20	0.27	0.67	0.22	0.22
La/Yb_N	5.1	32.6	13.0	0.6	0.8	3.7	0.7	0.7
La/Sm_N	1.0	10.6	3.9	0.5	0.4	2.1	0.5	0.4
Dy/Yb_N	2.1	2.0	1.8	1.4	1.8	1.5	1.4	1.7

Appendix G2 *continued*

Lithology	Diatexite Type-1				Diatexite Type-2	Granite X	Granite IX	Granite VIII	Granite V	Granite III	Granite II
Sample	M2_43_1	M2_43_2	M3_55_1	M3_55_2	M1_24A_1	M4_34_1	M3_10_1	M2_35_1	M1_12_1	M5_13_1	M4_36_1
Sr	112	115	144	131	86	78	99	96	74	76	133
Y	847	852	1569	1634	2026	908	542	1026	1546	1083	212
Th	15	21	1	0	1	7	5	5	19	5	4
U	33	47	135	123	185	49	51	62	74	75	81
La	496	538	192	169	214	391	330	344	380	340	276
Ce	1848	1924	654	557	574	1404	879	1230	1289	1129	561
Pr	329	336	114	96	79	241	120	214	215	181	66

Nd	1760	1808	643	533	348	1282	514	1115	1114	899	259
Sm	491	502	321	261	142	432	168	377	414	363	67
Eu	10	10	14	14	11	10	17	13	8	11	22
Gd	315	321	444	361	194	334	160	318	392	345	59
Tb	39	39	82	69	48	45	28	47	66	54	10
Dy	181	184	404	378	341	205	124	226	327	255	46
Ho	29	30	55	58	67	31	15	35	49	36	6
Er	68	68	101	130	192	64	31	75	104	73	12
Tm	9	9	11	17	32	8	4	9	13	8	2
Yb	52	53	64	111	231	41	24	53	70	46	10
Lu	7	7	8	14	31	5	3	6	8	5	1
LREE	4924	5108	1923	1615	1357	3750	2011	3279	3413	2911	1229
HREE	709	720	1183	1153	1147	742	407	783	1036	833	168
REE	5633	5829	3106	2768	2504	4493	2418	4062	4448	3744	1397
Eu/Eu*	0.07	0.08	0.12	0.14	0.19	0.08	0.33	0.11	0.06	0.09	1.06
La/Yb_N	6.4	6.8	2.0	1.0	0.6	6.5	9.1	4.3	3.7	5.0	19.1
La/Sm_N	0.6	0.7	0.4	0.4	0.9	0.6	1.2	0.6	0.6	0.6	2.6
Dy/Yb_N	2.3	2.2	4.1	2.2	1.0	3.3	3.3	2.8	3.0	3.6	3.1

Appendix G3 – Zircon trace element composition (ppm) from FCR-LAC rocks (metatexites, diatexites, and granites).

Lithology	Metatexite											Diatexite Type-1		Diatexite Type-2
Sample	M1T_20_11c - 1	M1T_20_25c - 1	M1T_20_46c - 1	M1T_20_57c - 1	M1T_20_78c - 1	M6T_25_1c - 1	M6T_25_2c - 1	M6T_25_3c - 1	M6T_25_4c - 1	M6T_25_5c - 1	M6T_25_7c - 1	M6T_55_10c - 1	M6T_55_12c - 1	M1T_24A_17c - 1
Hf	10140	11080	8180	12530	10000	14300	13290	13260	13300	14410	14360	12750	11060	11810
U	1152	341	97	2171	851	1310	1137	1261	1378	1213	1239	475	1514	321
Th	419	288	57	520	253	4	3	6	4	4	5	28	117	37
Th/U	0.36	0.85	0.58	0.24	0.30	0.003	0.003	0.005	0.003	0.003	0.004	0.06	0.08	0.12
Y	-	-	677	-	120	-	-	-	-	-	2074	-	-	610
La	56	0.2	<LOD	14	3	<LOD	<LOD	<LOD	<LOD	<LOD	1	0.1	11	0.2
Ce	95	23	22	70	29	0.1	0.1	0.1	0.1	0.1	5	1	54	15
Pr	8	0.2	0.1	12	3	<LOD	<LOD	0.02	<LOD	<LOD	1	0.1	11	0.3
Nd	34	3	2	79	21	0.2	0.2	0.2	0.1	0.2	6	1	68	2
Sm	18	6	3	57	18	1	1	1	1	1	5	2	47	2
Eu	4	1	1	15	4	0.2	0.2	0.2	0.2	0.2	2	0.2	9	0.5
Gd	57	30	15	131	54	12	10	12	12	10	24	14	144	12
Tb	18	10	5	33	16	7	6	8	8	7	11	7	48	4
Dy	201	128	58	327	182	139	111	143	143	127	177	98	489	54
Ho	69	48	21	94	62	64	52	65	66	59	73	38	120	20
Er	309	230	105	391	288	388	320	394	407	354	419	188	369	101
Tm	63	49	23	77	62	112	94	112	118	103	115	44	55	23
Yb	534	439	215	647	552	1305	1090	1284	1368	1193	1307	434	381	225
Lu	104	92	48	122	116	297	248	290	309	269	295	91	64	48
LREE	212	32	27	232	73	1	1	1	1	1	19	4	190	19
HREE	1357	1026	490	1837	1334	2324	1930	2308	2430	2122	2423	915	1679	488
REE	1569	1059	517	2069	1407	2325	1931	2309	2432	2124	2442	919	1869	507

Yb/Gd_N	11.64	18.19	17.93	6.11	12.73	138.14	140.38	127.71	144.81	141.15	67.50	38.07	3.27	23.07
Ce/Yb_N	0.05	0.01	0.03	0.03	0.01	0.00003	0.00002	0.00002	0.00001	0.00001	0.001	0.001	0.04	0.02
Eu/Eu*	0.34	0.30	0.51	0.52	0.43	0.17	0.17	0.16	0.17	0.17	0.44	0.14	0.33	0.26
Ce/Ce*	1.09	26.09	-	1.30	2.49	-	-	-	-	-	1.15	3.77	1.22	14.55

Appendix G3 *continued*

Lithology	Granite X							Granite IX	Granite V
Sample	M6T_34_10c - 1	M6T_34_15c - 1	M6T_34_23c - 1	M6T_34_24c - 1	M6T_34_26c - 1	M6T_34_27c - 1	M6T_34_3c - 1	M6T_45_1 - 1	M6T_12_1c - 1
Hf	12850	11660	11990	12070	12430	12670	12650	10280	11950
U	734	1258	1182	1603	1480	1000	190	898	2770
Th	84	314	284	398	7400	980	68	214	16300
Th/U	0.11	0.25	0.24	0.25	5.00	0.98	0.36	0.24	5.88
Y	469	855	797	1199	985	592	799	-	-
La	0.1	2	4	22	731	64	<LOD	2	-
Ce	2	17	38	260	-	64	5	17	-
Pr	0.3	4	9	33	377	115	0.1	4	-
Nd	3	31	70	209	1920	950	1	27	-
Sm	6	26	50	90	1170	153	2	25	3440
Eu	0.1	1	2	5	7	2	0.1	1	18
Gd	23	49	70	106	450	89	13	75	1380
Tb	6	12	14	20	40	13	5	19	115
Dy	58	106	111	158	196	97	76	168	457
Ho	15	28	26	39	38	24	29	45	71
Er	55	104	91	136	124	89	131	180	200

Tm	10	19	16	24	21	17	26	35	31
Yb	80	146	118	178	157	132	214	296	231
Lu	14	25	20	30	27	23	39	58	38
LREE	11	80	170	614	4198	1346	8	75	3440
HREE	261	490	468	696	1058	486	533	877	2540
REE	272	570	638	1310	5256	1832	542	952	5980
Yb/Gd_N	4.25	3.65	2.08	2.08	0.43	1.83	19.91	4.89	0.21
Ce/YbN	0.01	0.03	0.08	0.4	-	0.1	0.01	0.01	-
Eu/Eu*	0.03	0.09	0.12	0.16	0.03	0.04	0.04	0.07	0.02
Ce/Ce*	2.43	1.39	1.52	2.34	-	0.18	-	1.43	-

Appendix G4 – Whole-rock Sr, Nd, Hf and Pb isotopic data for the host rocks (phyllites) and FCR-LAC rocks (metatexites, diatexites, and granites).

Lithology	Phyllite N	Phyllite S	Metatexite					Diatexite Type-1		Diatexite Type-2
Sample	JTJ-2	JTJ-19	JTJ-20	JTJ-25	JTJ-48B	JTJ-53	JTJ-60A	JTJ-43	JTJ-55	JTJ-24A
$^{87}Sr/^{86}Sr$	0.7250	0.7402	0.7245	0.7321	0.7318	0.7403	0.7489	0.7364	0.7340	0.7447
±2σ	0.000013	0.000016	0.000019	0.000016	0.000013	0.000017	0.000034	0.000018	0.000065	0.000020
$^{87}Sr/^{86}Sr_{320}$	0.7153	0.7089	0.7097	0.7124	0.7039	0.7099	0.7053	0.7072	0.7204	0.7162
$^{143}Nd/^{144}Nd$	0.5119	0.5126	0.5122	0.5121	0.5120	0.5121	0.5121	0.5120	0.5123	0.5122
±2σ	0.000011	0.000006	0.000009	0.000010	0.000007	0.000009	0.000009	0.000009	0.000011	0.000007
εNd	-13.42	0.15	-8.30	-10.91	-12.28	-10.57	-10.99	-12.77	-7.16	-8.28
εNd_{320}	-10.07	3.28	-5.21	-7.65	-8.86	-7.30	-8.08	-8.32	-5.05	-6.21
Nd T_{DM2} (Ma)[a]	1826	779	1445	1637	1731	1609	1670	1524	1690	1433
$^{176}Hf/^{177}Hf$	0.2823	0.2824	0.2825	0.2824	0.2824	0.2825	0.2824	0.2824	0.2825	0.2824
±2σ	0.000005	0.000005	0.000004	0.000009	0.000005	0.000004	0.000005	0.000005	0.000005	0.000007
εHf	-18.14	-11.40	-8.98	-11.41	-12.09	-9.44	-12.82	-14.92	-9.25	-12.02
εHf_{320}	-13.68	-7.16	-4.45	-7.99	-8.47	-6.45	-8.16	-8.16	-3.42	-9.25
Hf T_{DM2} (Ma)[b]	2160	1747	1574	1800	1830	1701	1810	1880	1810	1508
$^{208}Pb/^{204}Pb$	38.7956	38.6236	38.6820	38.8925	39.2638	38.6856	38.4898	39.9730	38.4068	38.2375
±2σ	0.0021	0.0023	0.0023	0.0021	0.0018	0.0013	0.0022	0.0022	0.0026	0.0024
$^{206}Pb/^{204}Pb$	18.3550	19.0401	18.7160	18.6505	18.6196	19.0338	18.5718	18.5110	18.4268	18.2206
±2σ	0.0009	0.0010	0.0011	0.0010	0.0009	0.0005	0.0011	0.0010	0.0011	0.0009
$^{207}Pb/^{204}Pb$	15.6924	15.6746	15.6434	15.6434	15.6485	15.6848	15.6502	15.6483	15.6407	15.6246
±2σ	0.0008	0.0008	0.0009	0.0008	0.0007	0.0005	0.0009	0.0008	0.0010	0.0008
$^{208}Pb/^{206}Pb$	2.1136	2.0285	2.0668	2.0853	2.1087	2.0325	2.0724	2.1594	2.0843	2.0986
±2σ	0.000029	0.000033	0.000037	0.000046	0.000034	0.000027	0.000037	0.000041	0.000032	0.000037
$^{207}Pb/^{206}Pb$	0.8549	0.8232	0.8358	0.8388	0.8404	0.8241	0.8427	0.8453	0.8488	0.8575
±2σ	0.000011	0.000011	0.000013	0.000016	0.000010	0.000008	0.000011	0.000014	0.000010	0.000010

$^{206}Pb/^{204}Pb_{320}$	17.8770	17.9549	17.9149	17.9774	17.7057	12.7938	18.0033	17.7218	17.9120	17.2398
$^{207}Pb/^{204}Pb_{320}$	15.6671	15.6173	15.6011	15.6079	15.6002	15.3554	15.6201	15.6067	15.6135	15.5728
$^{208}Pb/^{204}Pb_{320}$	38.0388	37.6798	38.1323	38.2769	38.6531	38.1212	38.2232	36.6712	38.2117	38.2151

Appendix G4 *continued*

Lithology	Granite X	Granite IX	Granite VIII	Granite V	Granite II
Sample	JTJ-34	JTJ-45	JTJ-35	JTJ-12	JTJ-36
$^{87}Sr/^{86}Sr$	0.7648	0.7893	0.7636	0.7774	0.7578
±2σ	0.000015	0.000024	0.000025	0.000013	0.000021
$^{87}Sr/^{86}Sr_{320}$	0.7055	0.7062	0.7126	0.7022	0.7063
$^{143}Nd/^{144}Nd$	0.5120	0.5121	0.5120	0.5120	0.5123
±2σ	0.000009	0.000008	0.000009	0.000012	0.000012
εNd	-12.66	-11.06	-12.18	-11.51	-7.49
$εNd_{320}$	-8.89	-7.99	-8.36	-8.64	-6.03
Nd T_{DM2} (Ma)[a]	1714	1734	1693	1664	1510
$^{176}Hf/^{177}Hf$	0.2823	0.2824	0.2824	0.2824	0.2825
±2σ	0.000006	0.000006	0.000005	0.000004	0.000005
εHf	-15.16	-13.99	-14.21	-14.06	-10.16
$εHf_{320}$	-8.43	-7.78	-7.71	-7.70	-3.99
Hf T_{DM2} (Ma)[b]	1781	1828	1781	1786	1544
$^{208}Pb/^{204}Pb$	42.1802	38.6802	39.2789	38.9877	38.3497
±2σ	0.0022	0.0021	0.0017	0.0014	0.0023
$^{206}Pb/^{204}Pb$	19.0352	18.6156	18.6437	18.6888	18.6227
±2σ	0.0009	0.0010	0.0007	0.0006	0.0009
$^{207}Pb/^{204}Pb$	15.6830	15.6541	15.6583	15.6631	15.6618
±2σ	0.0008	0.0008	0.0007	0.0005	0.0008
$^{208}Pb/^{206}Pb$	2.2159	2.0778	2.1068	2.0862	2.0593

±2σ	0.000030	0.000046	0.000039	0.000045	0.000086
$^{207}Pb/^{206}Pb$	0.8239	0.8409	0.8399	0.8381	0.8410
±2σ	0.000010	0.000015	0.000010	0.000015	0.000024
$^{206}Pb/^{204}Pb_{320}$	18.1733	17.4132	17.5719	17.6702	17.9340
$^{207}Pb/^{204}Pb_{320}$	15.6375	15.5907	15.6017	15.6093	15.6254
$^{208}Pb/^{204}Pb_{320}$	39.3876	38.1326	37.5695	38.2999	38.1579

[a]$T_{DM2} = 1/\lambda \times \ln(^{143}Nd/^{144}Nd-(e^{\lambda t}-1) \times (^{147}Sm/^{144}Nd-^{147}Sm/^{144}Nd_{CC})-^{143}Nd/^{144}Nd_{DM} / (^{147}Sm/^{144}Nd_{CC}-^{147}Sm/^{144}Nd_{DM})+1)$

[b]$T_{DM2} = 1/\lambda \times \ln(^{176}Hf/^{177}Hf-(e^{\lambda t}-1) \times (^{176}Lu/^{177}Hf-^{176}Lu/^{177}Hf_{CC})-^{176}Hf/^{177}Hf_{DM} / (^{176}Lu/^{177}Hf_{CC}-^{176}Lu/^{177}Hf_{DM}) +1)$

λRb - Steiger and Jäger (1977)

λSm - Lugmair and Marti (1978)

λLu - Söderlund et al. (2004)

λU and λTh - Steiger and Jäger (1977)

$^{147}Sm/^{144}Nd_{CHUR}$ and $^{143}Nd/^{144}Nd_{CHUR}$ - Jacobsen and Wasserburg (1980)

$^{147}Sm/144Nd_{DM}$,143Nd/$^{144}Nd_{DM}$, and $^{147}Sm/^{144}Nd_{CC}$ - Liew and Hofmann (1988)

$^{176}Lu/^{177}Hf_{CHUR}$ and $^{176}Hf/^{177}Hf_{CHUR}$ - Blichert-Toft and Albarède (1997)

$^{176}Lu/^{177}Hf_{DM}$ and $^{176}Hf/^{177}Hf_{DM}$ - Vervoort and Blichert-Toft (1999)

$^{176}Lu/^{177}Hf_{CC}$ - Griffin et al. (2002)

APPENDIX H – PhD outputs

Publications:

Ferreira, J.A., Mata, J., Bento dos Santos, T., Pereira, I. 2020. The role of melting on the geochemical evolution and isotopic variability of an anatectic complex in the Iberian Variscides. Lithos, 378-379. https://doi.org/10.1016/j.lithos.2020.105769

Ferreira, J.A., Bento dos Santos, T., Pereira, I., Mata, J., 2019. Tectonically assisted exhumation and cooling of Variscan granites in an anatectic complex of the Central Iberian Zone, Portugal: constraints from LA - ICP - MS zircon and apatite U – Pb ages. Int. J. Earth Sci. https://doi.org/10.1007/s00531-019-01755-1

Ferreira, J.A., Pereira, I., Bento dos Santos, T., Mata, J., *submitted*. U-Pb age constraints on the source, cooling and exhumation of a Variscan middle crust migmatite complex from Central Iberian Zone. Precambrian Research

Conferences communications:

2019 – XII Congresso Ibérico de Geoquímica / XX Semana da Geoquímica, Évora, Portugal, Zircon and apatite U-Pb age constraints on the exhumation of middle crust granites and migmatites during orogenesis: a case from the Central Iberian Zone, Ferreira, J.A., Bento dos Santos, T., Pereira, I., Mata, J.

2019 – XII Congresso Ibérico de Geoquímica / XX Semana da Geoquímica, Évora, Portugal, Comparison between the U-Pb detrital zircon ages of the Douro-Beiras Supergroup and the Figueira de Castelo Rodrigo – Lumbrales Anatectic Complex (Central Iberian Zone, Portugal): geodynamic implications, Ferreira, J.A., Bento dos Santos, T., Pereira, I., Mata, J.

2019 – Goldschmidt Conference, Barcelona, Spain, Isotopic disequilibrium between migmatites and granites in an anatectic complex, Ferreira, J.A., Mata, J., Bento dos Santos, T.

2019 – Goldschmidt Conference, Barcelona, Spain, U-Pb ages and cooling rates of variscan migmatites from the Central Iberian Zone: geodynamic implications, Ferreira, J.A., Bento dos Santos, T., Pereira, I., Mata, J.

2019 – EGU General Assembly, Viena, Austria, Exhumation and cooling rates of Variscan granites in an anatectic complex of the Central Iberian Zone, Portugal: constraints from LA-ICP-MS Zircon and Apatite U-Pb ages, Joana Ferreira., Telmo Bento dos Santos., Inês Pereira., João Mata

2018 – XIV Congresso de Geoquímica dos Países de Língua Portuguesa e XIX Semana de Geoquímica, Vila Real, Portugal, U-Pb Crystallization Ages and Cooling Rates of the Figueira de Castelo Rodrigo-Lumbrales Anatectic Complex Granites, Central Iberian Zone (Portugal), Ferreira, J.A., Pereira, I., Bento dos Santos, T., Mata, J.

2017 – Goldschmidt Conference, Paris, France, The link between diatexites and syn-tectonic granites of an Iberian Variscan anatectic complex, Ferreira, J.A., Bento dos Santos, T., Mata, J., Pereira, I

2016 – VI CJIG, LEG 2016, Estremoz, Migmatitos da Zona Centro-Ibérica: comparação entre o complexo migmatítico do Pedregal e o Complexo Anatéctico de Figueira de Castelo-Rodrigo – Lumbrales, Ferreira, J., Pereira, I., Bento dos Santos, T., Mata, J., Dias, R., Ribeiro, M.A., Martins, H.C.B.